Quantum Master Equation Approaches for Open System Chemical Dynamics in Driven and Multi-Bath Systems

by

Callie R. Wilson

A dissertation submitted in partial fulfillment
of the requirements for the degree of
Doctor of Philosophy
(Chemistry)
in The University of Michigan
2026

Doctoral Committee:

Professor Eitan Geva, Chair
Assistant Professor Yuki Kobayashi
Professor Roseanne Sension
Professor Dominika Zgid

Callie R. Wilson
jcallie@umich.edu
ORCID iD: 0000-0003-0727-0065

© Callie R. Wilson 2026

DEDICATION

To my husband, for being my steady state in a dynamic world.

ACKNOWLEDGEMENTS

This thesis would not be possible without the help of many wonderful, supportive people in my life. First and foremost, I would like to thank my advisor, Eitan Geva, for his continuous support and guidance throughout my time at Michigan. His mentorship has played a tremendous role in becoming the researcher and scientist I am today. Research rarely follows a straight path, and many of the projects outlined in this work have involved many roadblocks and changing directions over the years, and I am so grateful to have had an advisor that allowed me the space to work independently through many of the challenges that research brings, while also still being readily available to provide guidance and direction when I often needed it. I would also like to thank my committee members, Dominika Zgid, Roseanne Sension, and Yuki Kobayashi for their insightful feedback and helpful conversations throughout my time at Michigan.

I would like to thank all of my group members that I crossed paths with, both past and present: Dr. Ellen Mulvihill, Dr. Yifan Lai, Dr. Yudan Liu, Dr. Miriam Lenn, Dr. Max Saller, Dalia Hassan, Dr. Pouya Khazaei, Zongwei Huang, Esther Adelson, and Kyle Haggard. I would especially like to thank Dr. Ellen Mulvihill, whom I considered an additional mentor throughout my time at Michigan. Ellen played a significant role in my development as a researcher, not only by providing guidance in the theoretical foundations of the GQME, but also by helping me develop many of the programming skills required for this work. Although our overlapping time in the group was brief, she was always willing to answer questions or meet for clarification, even years after her time at Michigan ended, and for that I am deeply grateful. I would like to thank Zongwei, who played an important role in the driven OD-QME project, helping to develop the code framework while I was still in the beginning stages of learning programming, and I am grateful for our collaboration on this project. I would also like to thank the collaborators at Yale University who played a supportive role in the two-bath project, especially Dr. Dan Xiaohan, whose insight and perspective was invaluable as the project evolved into many different directions.

I would like to thank my friends for their support throughout my graduate studies. This includes the friends I met within the physical chemistry cluster, especially Dr. Zahra Gandhi, whom I grew especially close with while teaching introductory chemistry lab in our first year. Zahra has consistently been someone I could turn to whether navigating degree requirements,

sharing the joys of cat parenthood, or facing the many highs and lows of graduate school. I would also like to acknowledge the many wonderful individuals I met during my time in the Army Reserve, whose mentorship, encouragement, and friendship helped shape me both personally and professionally throughout my time in service.

I would like to thank several of my former professors at Alma College who fostered my love for chemistry and research, and encouraged me to pursue graduate school. This includes, Dr. James Mazzuca, my former physical chemistry professor, and the person that inspired me to pursue theory at Michigan, as well as Dr. Joel Dopke and Dr. Nancy Dopke, two professors who became like an extension of family to me throughout my time at Alma and whom I am forever grateful to have met through pursuing chemistry.

To my family, for their unwavering support throughout my time in graduate school. To my nana and papa, you are loved and missed every single day, and I could not be more proud to join you both in being a Michigan Wolverine. I carry you in my heart in everything that I do. To my dad, who has taught me so much and whether it be at a race, celebrating major life milestones, or anything in between, you have always been one of the loudest voices cheering me on across any finish line. To my mom, for her unconditional love and for always lending a listening ear on many phone calls while I walked back and forth to campus, thank you for always answering and for believing in me every step of the way. Your love and grounding stability mean more to me than you will ever know. To Libbey, for being one of my biggest cheerleaders, someone I have always looked up to, and my best friend for my whole life, you are the greatest sister and role model I could ever ask for.

And to my husband, DeMarco, words cannot express my gratitude for the person you are. None of this would be possible without your endless love and the unwavering support you have provided to me as we build our life together. You ground me and encourage me to strive toward my goals, and have never failed to support me through all of my endeavors. I cannot thank you enough for walking alongside me every step of the way on every path life takes us. I dedicate this work to you.

TABLE OF CONTENTS

DEDICATION ii

ACKNOWLEDGEMENTS iii

LIST OF FIGURES viii

LIST OF TABLES xiii

LIST OF APPENDICES xiv

LIST OF ACRONYMS xv

ABSTRACT xvi

CHAPTER

1 Introduction 1

1.1 Motivation: Open System Chemical Dynamics 1
1.1.1 The Wavefunction Formalism 2
1.1.2 The Density Operator Formalism 3
1.2 Quantum Master Equations 4
1.2.1 The Generalized Quantum Master Equation 4
1.2.2 Redfield Quantum Master Equations 6
1.2.3 Off-Diagonal Quantum Master Equations 8
1.3 Non-Equilibrium Dynamics 10
1.4 Overview of this Dissertation 11

2 Quantum Master Equations for Systems Off-Diagonally Driven by a Time-Dependent External Field[1] 14

2.1 Introduction 14
2.2 Theory 16
2.2.1 Preliminary Considerations 16
2.2.2 Populations-Only OD-QMEs for a Donor-Acceptor System Off-Diagonally Driven by a Time-Dependent External Field 19
2.2.3 P-Tcl-OD-QMEs for a Donor-Acceptor System Subject to a CW Driving Field within the Condon Approximation 24
2.2.4 Asymptotic Behavior and the Marcus Theory Limit 26

2.3 Results and Discussion . . . 29
2.4 Summary and Concluding Remarks . . . 39

3 Memory Kernel Non-Additivity in the GQME for a System Coupled to Multiple Heat Baths[2] . . . 41

3.1 Introduction . . . 41
3.2 Theory . . . 45
3.2.1 Preliminary Considerations . . . 45
3.2.2 The Generalized Quantum Master Equation (GQME) . . . 47
3.2.3 The Non-Additivity of the Effect of the Individual Baths on the System's Dynamics . . . 50
3.2.4 The Limits of Weak System-Bath Coupling, Markovian Dynamics and the Secular Approximation . . . 52
3.3 A Demonstrative Application to a Two-Level System Linearly Coupled to Hot and Cold Harmonic Baths . . . 55
3.3.1 Model Hamiltonian . . . 55
3.3.2 Computational Details . . . 57
3.3.3 Results and Discussion . . . 57
3.4 Concluding Remarks . . . 63

4 Reduced-Dimensionality Generalized Quantum Master Equations for a System Coupled to Multiple Heat Baths[3] . . . 67

4.1 Introduction . . . 67
4.2 Theory . . . 69
4.2.1 Preliminary Considerations . . . 69
4.2.2 The Nakajima-Zwanzig Equation . . . 71
4.2.3 Projection-Dependent Breakdown of Kernel and Inhomogeneous Term Additivity . . . 79
4.3 Application to a Two-Level System Linearly Coupled to Hot and Cold Harmonic Baths . . . 81
4.3.1 Results . . . 84
4.4 Concluding Remarks . . . 89

5 A Mixed Quantum-Classical Generalized Quantum Master Equation for a System Coupled to Multiple Heat Baths[4] . . . 99

5.1 Introduction . . . 99
5.2 Theory . . . 100
5.2.1 The GQME: Memory Kernel and Projection-Free Inputs . . . 100
5.2.2 Ehrenfest Method for Obtaining Projection-Free Inputs . . . 102
5.3 Application to a Two-Level System Linearly Coupled to a Hot and Cold Harmonic Bath . . . 104
5.3.1 Results . . . 106
5.4 Concluding Remarks . . . 107

6 Conclusion . . . 112

6.1 Summary . . . 112

6.2 Outlook 114

APPENDICES 117

BIBLIOGRAPHY 139

LIST OF FIGURES

FIGURE

1.1 Representative examples of realistic, molecular systems that motivate the study of open system quantum dynamics. (a) A linear carotenoid-porphyrin-C_{60} molecular triad in tetrahydrofuran (THF), which serves as a model system for photosynthetic charge separation, where the charge transfer dynamics depend on the conformational state of the triad. (b) The Fenna-Matthews-Olson (FMO) complex, a photosynthetic light-harvesting complex that mediates excitation energy transfer between chromophores. Images adapted from Refs. 132, 81. 2

1.2 Schematic illustrating two extensions of the conventional single-bath model without an external driving field: (top) a driven two-level system coupled to a single bath and an external time-dependent driving field, (bottom) a two-level system simultaneously coupled to hot and cold thermal baths. 12

2.1 A schematic view of the GOA-type models A and B discussed in the text, which represent donor-to-acceptor downhill CT reactions in the normal and inverted regions, respectively. The donor (blue) and acceptor (orange) free energy surfaces along the primary mode coordinate, representing the solvation coordinate, are shown (note that the primary mode is coupled to a bath of secondary modes which are not shown in the figure). Also shown are the donor-to-acceptor (U_{AD}, green) and acceptor-to-donor (U_{DA}, red) vertical transition energies. It should be noted that U_{AD} is positive in the normal region and negative in the inverted region, while U_{DA} is positive in both regions. 28

2.2 The effect of the driving field's intensity and frequency on the CT dynamics within models A (top panel) and B (bottom panel), which was simulated at $T = 300$K based on p-tcl-OD-QME, Eq. (2.21). The difference between the populations of the donor and acceptor states, $\langle\hat{\sigma}_z\rangle = \langle D|\hat{\sigma}|D\rangle - \langle A|\hat{\sigma}|A\rangle$ is plotted as a function of time for different combinations of $\chi^0_{DA}/\Lambda = \{0.1, 0.5, 1.0, 2.0\}$ and $\omega/|\omega_v| = \{0.1, 0.5, 1.0, 2.0\}$. 34

2.3 The donor-to-acceptor E-FGR rate constant as a function of the driving field's amplitude (measured by χ^0_{DA}/Λ) and frequency (measured by $\omega/|\omega_v|$) for models A (top panel) and B (bottom panel). 35

2.4 A semi-log plot of the E-FGR (solid lines and full circles) and Marcus (dashed line and blank circles) donor-to-acceptor CT rate constants as a function of $|\Delta E|$, for different driving field amplitudes (measured by χ^0_{DA}/Λ). The results in this plot were obtained for $E_r = 650$meV and $\Lambda = 10$meV, and the field frequencies, ω are in resonance with the vertical transition frequencies, ω_v. Vertical lines indicate the values of $|\Delta E|$ that correspond to models A (red) and B (blue). . . . 37
2.5 The effect of temperature on the field-free and field-driven CT dynamics. The figure is formatted similarly to Fig. 2.2, with results shown at $T = 300$K (light blue) and $T = 77$K (dark blue). 38

3.1 $\sigma_x(t)$, $\sigma_y(t)$ and $\sigma_z(t)$ as a function of time for models 1-3 (top panel) and models 4-6 (bottom panel) in Table 4.2. Shown are exact HEOM-based results (dotted red line), GQME-based results with the exact memory kernel $\mathcal{K}(\tau)$, Eq. (4.12), calculated from HEOM-based PFIs (solid blue line), GQME-based results with the approximate additive memory kernal $\mathcal{K}_h(\tau) + \mathcal{K}_c(\tau)$, Eqs. (3.25) and (3.28), calculated from HEOM-based PFIs (dashed blue line), results based on the Markovian and secular Redfield quantum master equation, Eq. (3.36) (dashed green line), and results based on the non-Markovian and secular Redfield quantum master equation, Eq. (3.32) (dashed orange line). 58
3.2 A comparison of the four independent and non-vanishing matrix elements $[(01, 00), (01, 01), (01, 10), (01, 11)]$ of $\mathcal{K}(\tau)$ vs. $\mathcal{K}_h(\tau) + \mathcal{K}_c(\tau)$, for the six spin-boson models under consideration. Shown are the real (solid blue line) and imaginary (solid green line) parts of $\mathcal{K}(\tau)$ vs. the real (dashed red line) and imaginary (dashed orange line) parts of $\mathcal{K}_h(\tau) + \mathcal{K}_c(\tau)$. 59
3.3 The real (top panels) and imaginary (lower panels) parts of the $(01, 00)$, $(01, 01)$, $(01, 10)$ and $(01, 11)$ nonvanishing matrix elements of $\Delta\mathcal{K}(\tau) = \mathcal{K}(\tau) - \mathcal{K}_h(\tau) - \mathcal{K}_c(\tau)$, for the six spin-boson models under consideration. 60

4.1 $\sigma_z(t)$, $\sigma_y(t)$, $\sigma_x(t)$ as a function of time for model 5 in Table 4.2. Shown are exact results calculated using HEOM (red dotted line), and four variations of GQME-based results with the exact memory kernel $\mathcal{K}(\tau)$: (1) the full GQME (solid blue line with diamonds), (2) a combination of single-population scalar GQMEs for $\sigma_{DD}(t)$, $\sigma_{AA}(t)$, $\sigma_{DA}(t)$, and $\sigma_{AD}(t)$ (solid green line with squares), (3) a coherences-only GQME (orange solid line with square), and (4) a populations-only GQME (solid purple line with circles). 84
4.2 $\sigma_x(t)$, $\sigma_y(t)$ and $\sigma_z(t)$ as a function of time for models 1-3 (top panel) and models 4-6 (bottom panel) in Table 4.2. Shown are exact results calculated using HEOM (red dotted line), four variations of GQME-based results with the approximate additive memory kernel $\mathcal{K}_h(\tau)+\mathcal{K}_c(\tau)$: (1) the full GQME (dashed blue line), (2) a combination of single-population scalar GQMEs for $\sigma_{DD}(t)$, $\sigma_{AA}(t)$, $\sigma_{DA}(t)$, and $\sigma_{AD}(t)$ (dashed green line), (3) a coherences-only GQME (orange dashed line), (4) a populations-only GQME (purple dashed line). 86

4.3 A comparison of the independent and non-vanishing matrix elements of $\mathcal{K}^{proj}(\tau)$ vs. $\mathcal{K}_h^{proj}(\tau) + \mathcal{K}_c^{proj}(\tau)$, for Model 1 (see Table 4.2). The independent matrix elements are projection dependent. For $\mathcal{K}^{full}(\tau)$, the four independent nonzero elements are (01,00), (01,01), (01,10), (01,11). For $\mathcal{K}^{pop}(\tau)$, the two independent elements are: (00,00), (00,11), and for $\mathcal{K}^{coh}(\tau)$, the two independent elements are: (01,01), (10,01). For $\mathcal{K}^{scalar}(\tau)$ the two population independent elements are: (00,00), (11,11), and the two coherence elements are: (01,01), (10,10). . . . 90
4.4 A comparison of the independent and non-vanishing matrix elements of $\mathcal{K}^{proj}(\tau)$ vs. $\mathcal{K}_h^{proj}(\tau) + \mathcal{K}_c^{proj}(\tau)$, for Model 2 (see Table 4.2). The independent matrix elements are projection dependent. For $\mathcal{K}^{full}(\tau)$, the four independent nonzero elements are (01,00), (01,01), (01,10), (01,11). For $\mathcal{K}^{pop}(\tau)$, the two independent elements are: (00,00), (00,11), and for $\mathcal{K}^{coh}(\tau)$, the two independent elements are: (01,01), (10,01). For $\mathcal{K}^{scalar}(\tau)$ the two population independent elements are: (00,00), (11,11), and the two coherence elements are: (01,01), (10,10). . . . 91
4.5 A comparison of the independent and non-vanishing matrix elements of $\mathcal{K}^{proj}(\tau)$ vs. $\mathcal{K}_h^{proj}(\tau) + \mathcal{K}_c^{proj}(\tau)$, for Model 3 (see Table 4.2). The independent matrix elements are projection dependent. For $\mathcal{K}^{full}(\tau)$, the four independent nonzero elements are (01,00), (01,01), (01,10), (01,11). For $\mathcal{K}^{pop}(\tau)$, the two independent elements are: (00,00), (00,11), and for $\mathcal{K}^{coh}(\tau)$, the two independent elements are: (01,01), (10,01). For $\mathcal{K}^{scalar}(\tau)$ the two population independent elements are: (00,00), (11,11), and the two coherence elements are: (01,01), (10,10). . . . 92
4.6 A comparison of the independent and non-vanishing matrix elements of $\mathcal{K}^{proj}(\tau)$ vs. $\mathcal{K}_h^{proj}(\tau) + \mathcal{K}_c^{proj}(\tau)$, for Model 4 (see Table 4.2). The independent matrix elements are projection dependent. For $\mathcal{K}^{full}(\tau)$, the four independent nonzero elements are (01,00), (01,01), (01,10), (01,11). For $\mathcal{K}^{pop}(\tau)$, the two independent elements are: (00,00), (00,11), and for $\mathcal{K}^{coh}(\tau)$, the two independent elements are: (01,01), (10,01). For $\mathcal{K}^{scalar}(\tau)$ the two population independent elements are: (00,00), (11,11), and the two coherence elements are: (01,01), (10,10). . . . 93
4.7 A comparison of the independent and non-vanishing matrix elements of $\mathcal{K}^{proj}(\tau)$ vs. $\mathcal{K}_h^{proj}(\tau) + \mathcal{K}_c^{proj}(\tau)$, for Model 5 (see Table 4.2). The independent matrix elements are projection dependent. For $\mathcal{K}^{full}(\tau)$, the four independent nonzero elements are (01,00), (01,01), (01,10), (01,11). For $\mathcal{K}^{pop}(\tau)$, the two independent elements are: (00,00), (00,11), and for $\mathcal{K}^{coh}(\tau)$, the two independent elements are: (01,01), (10,01). For $\mathcal{K}^{scalar}(\tau)$ the two population independent elements are: (00,00), (11,11), and the two coherence elements are: (01,01), (10,10). . . . 94
4.8 A comparison of the independent and non-vanishing matrix elements of $\mathcal{K}^{proj}(\tau)$ vs. $\mathcal{K}_h^{proj}(\tau) + \mathcal{K}_c^{proj}(\tau)$, for Model 6 (see Table 4.2). The independent matrix elements are projection dependent. For $\mathcal{K}^{full}(\tau)$, the four independent nonzero elements are (01,00), (01,01), (01,10), (01,11). For $\mathcal{K}^{pop}(\tau)$, the two independent elements are: (00,00), (00,11), and for $\mathcal{K}^{coh}(\tau)$, the two independent elements are: (01,01), (10,01). For $\mathcal{K}^{scalar}(\tau)$ the two population independent elements are: (00,00), (11,11), and the two coherence elements are: (01,01), (10,10). . . . 95

4.9 The real parts of the non-vanishing, independent kernel matrix elements of $\Delta\mathcal{K}^{proj}(\tau) = \mathcal{K}^{proj}(\tau) - \mathcal{K}_h^{proj}(\tau) - \mathcal{K}_c^{proj}(\tau)$ for the full GQME, populations-only and coherences-only GQMEs and the scalar population/coherence GQMEs, for the six spin-boson models under consideration. The number of independent kernel matrix elements are projection-dependent. 96
4.10 Shown are the real and imaginary parts of the independent non-zero inhomogeneous terms, $I_{11}^{scalar}(t)$, $I_{01}^{scalar}(t)$, and $I_{01}^{coh}(t)$ from Eqs. (4.20), (4.21), (4.30) for the six spin-boson models under consideration. 97

5.1 A comparison of the two projection-free input matrix elements, $\mathcal{F}_{0000}(\tau)$ and $\mathcal{F}_{0011}(\tau)$, used to construct the populations-only GQME memory kernel for the six spin-boson models under consideration. The exact HEOM results are shown in blue, while the Ehrenfest results are shown in magenta, with solid lines denoting the real parts and dotted lines denoting the imaginary parts of $\mathcal{F}(\tau)$. 108
5.2 A comparison of the two projection-free input matrix elements, $\dot{\mathcal{F}}_{0000}(\tau)$ and $\dot{\mathcal{F}}_{0011}(\tau)$, used to construct the populations-only GQME memory kernel for the six spin-boson models under consideration. The exact HEOM results are shown in blue, while the numerical derivatives of the Ehrenfest PFIs are shown in magenta, with solid lines denoting the real parts and dotted lines denoting the imaginary parts of $\dot{\mathcal{F}}(\tau)$. 109
5.3 A comparison of the real and imaginary parts of two memory kernel matrix elements, $\mathcal{K}_{0000}(\tau)$ and $\mathcal{K}_{0011}(\tau)$, used in the populations-only GQME for the six spin-boson models under consideration. The real parts (solid blue line) and imaginary parts (solid green line) of the exact HEOM memory kernels are shown, while the real parts (dashed red line) and imaginary parts (dashed green line) of the Ehrenfest-based memory kernels are also shown. 110
5.4 $\sigma_z(t)$ as a function of time for models 1-3 (top panel) and models 4-6 (bottom panel) in Table 3.1. Shown are exact HEOM-based results (dotted red line), populations-only GQME-based results with the exact memory kernel, $\mathcal{K}(\tau)$, calculated from HEOM-based PFIs (solid blue line), populations-only MF-GQME results using an approximate memory kernel constructed from Ehrenfest-based PFIs (solid green line), and results from direct propagation of Ehrenfest (MF) dynamics (dashed magenta line). 111

A.1 The effect of the driving field's intensity and frequency on the CT dynamics within models A (top panel) and B (bottom panel), simulated at $T = 300$K based on four different OD-QMEs (p-tcl-OD-QME, p-tc-OD-QME, f-tcl-OD-QME and f-tc-OD-QME). The difference between the populations of the donor and acceptor states, $\langle\hat{\sigma}_z\rangle = \langle D|\hat{\sigma}|D\rangle - \langle A|\hat{\sigma}|A\rangle$ is plotted as a function of time for different combinations of $\chi_{DA}^0/\Lambda = \{0.1, 0.5, 1.0, 2.0\}$ and $\omega/|\omega_v| = \{0.1, 0.5, 1.0, 2.0\}$. . . 120

B.1 Shown are the real parts of the exact single-bath memory kernels, $\mathcal{K}_h^{proj}(\tau)$ (red dotted line) and $\mathcal{K}_c^{proj}(\tau)$ (blue dotted line), and the exact two-bath memory kernel, $\mathcal{K}^{proj}(\tau)$ for Model 1 (see Tab. 4.2). 126

B.2 Shown are the real parts of the exact single-bath memory kernels, $\mathcal{K}_h^{proj}(\tau)$ (red dotted line) and $\mathcal{K}_c^{proj}(\tau)$ (blue dotted line), and the exact two-bath memory kernel, $\mathcal{K}^{proj}(\tau)$ for Model 2 (see Tab. 4.2). 127
B.3 Shown are the real parts of the exact single-bath memory kernels, $\mathcal{K}_h^{proj}(\tau)$ (red dotted line) and $\mathcal{K}_c^{proj}(\tau)$ (blue dotted line), and the exact two-bath memory kernel, $\mathcal{K}^{proj}(\tau)$ for Model 3 (see Tab. 4.2). 128
B.4 Shown are the real parts of the exact single-bath memory kernels, $\mathcal{K}_h^{proj}(\tau)$ (red dotted line) and $\mathcal{K}_c^{proj}(\tau)$ (blue dotted line), and the exact two-bath memory kernel, $\mathcal{K}^{proj}(\tau)$ for Model 4 (see Tab. 4.2). 129
B.5 Shown are the real parts of the exact single-bath memory kernels, $\mathcal{K}_h^{proj}(\tau)$ (red dotted line) and $\mathcal{K}_c^{proj}(\tau)$ (blue dotted line), and the exact two-bath memory kernel, $\mathcal{K}^{proj}(\tau)$ for Model 5 (see Tab. 4.2). 130
B.6 Shown are the real parts of the exact single-bath memory kernels, $\mathcal{K}_h^{proj}(\tau)$ (red dotted line) and $\mathcal{K}_c^{proj}(\tau)$ (blue dotted line), and the exact two-bath memory kernel, $\mathcal{K}^{proj}(\tau)$ for Model 6 (see Tab. 4.2). 131
B.7 Shown are the real (top) and imaginary (bottom) contributions of the convolution of the memory kernel, $\int_0^t \mathcal{K}^{coh}(\tau)\sigma(t-\tau)$ (red line), the inhomogeneous term for the coherences-only GQME, $I_{01}^{coh}(t)$ (see Eq. 4.29) (blue line), and the sum of the two contributions (purple line) for Model 1 (see Tab. 4.2). 133
B.8 Shown are the real (top) and imaginary (bottom) contributions of the convolution of the memory kernel, $\int_0^t \mathcal{K}^{coh}(\tau)\sigma(t-\tau)$ (red line), the inhomogeneous term for the coherences-only GQME, $I_{01}^{coh}(t)$ (see Eq. 4.29) (blue line), and the sum of the two contributions (purple line) for Model 2 (see Tab. 4.2). 134
B.9 Shown are the real (top) and imaginary (bottom) contributions of the convolution of the memory kernel, $\int_0^t \mathcal{K}^{coh}(\tau)\sigma(t-\tau)$ (red line), the inhomogeneous term for the coherences-only GQME, $I_{01}^{coh}(t)$ (see Eq. 4.29) (blue line), and the sum of the two contributions (purple line) for Model 3 (see Tab. 4.2). 135
B.10 Shown are the real (top) and imaginary (bottom) contributions of the convolution of the memory kernel, $\int_0^t \mathcal{K}^{coh}(\tau)\sigma(t-\tau)$ (red line), the inhomogeneous term for the coherences-only GQME, $I_{01}^{coh}(t)$ (see Eq. 4.29) (blue line), and the sum of the two contributions (purple line) for Model 4 (see Tab. 4.2). 136
B.11 Shown are the real (top) and imaginary (bottom) contributions of the convolution of the memory kernel, $\int_0^t \mathcal{K}^{coh}(\tau)\sigma(t-\tau)$ (red line), the inhomogeneous term for the coherences-only GQME, $I_{01}^{coh}(t)$ (see Eq. 4.29) (blue line), and the sum of the two contributions (purple line) for Model 5 (see Tab. 4.2). 137
B.12 Shown are the real (top) and imaginary (bottom) contributions of the convolution of the memory kernel, $\int_0^t \mathcal{K}^{coh}(\tau)\sigma(t-\tau)$ (red line), the inhomogeneous term for the coherences-only GQME, $I_{01}^{coh}(t)$ (see Eq. 4.29) (blue line), and the sum of the two contributions (purple line) for Model 6 (see Tab. 4.2). 138

LIST OF TABLES

TABLE

2.1 Parameters of the GOA Model 31

3.1 Spin-Boson Model Parameters 57

4.1 Types of GQMEs, the corresponding projection operators used in their construction, and the subsets of reduced system dynamics associated with each projection. 79

4.2 Spin-Boson Model Parameters 83

LIST OF APPENDICES

APPENDIX

A Driven OD-QMEs: Additional Driven OD-QME Variations and Discussion of Experimental Validity 117

B Reduced-Dimensionality GQMEs: Proofs of Memory Kernels and Inhomogeneous Terms 123

LIST OF ACRONYMS

QME Quantum Master Equation

OD-QME Off-Diagonal Quantum Master Equation

CT Charge Transfer

CW Continuous Wave

DOF Degree of Freedom

p-tcl-OD-QME Populations-Only Time-Convolutionless Off-Diagonal Quantum Master Equation

p-tc-OD-QME Populations-Only Time-Convolution Off-Diagonal Quantum Master Equation

f-tcl-OD-QME Full Electronic Time-Convolutionless Off-Diagonal Quantum Master Equation

f-tc-OD-QME Full Electronic Time-Convolution Off-Diagonal Quantum Master Equation

NE-FGR Non-Equilibrium Fermi's Golden Rule

E-FGR Equilibrium Fermi's Golden Rule

GOA Garg-Onuchic-Ambegaokar

GQME Generalized Quantum Master Equation

PFI Projection-Free Input

HEOM Hierarchical Equations of Motion

MF Mean Field

LSC Linearized Semiclassical

ABSTRACT

The simulation of chemical dynamics is important for understanding energy and charge transfer processes in chemical, biological, and technological systems. Realistic chemical systems often operate under nonequilibrium conditions, such as interacting with external driving fields or multiple bath environments. These conditions introduce complex interactions among a large number of system and bath degrees of freedom, making their accurate simulation computationally challenging. As a result, quantum master equation approaches have been developed as powerful frameworks for providing effective, reduced descriptions of system dynamics in complex environments. However, extending these approaches to accurately describe nonequilibrium quantum systems presents challenges due to the complexity introduced by time-dependent driving, as well as non-additive effects that emerge when systems interact with multiple bath environments.

In the second chapter, we present off-diagonal quantum master equations (OD-QMEs) for systems with time-dependent electronic coupling terms, which can be accomplished by driving the system with a time-dependent external field. We also present an asymptotic analysis that shows how the dynamics described by the OD-QMEs for a charge transfer (CT) system driven by a continuous wave (CW) field turns into rate kinetics governed by field-modified Marcus theory rate constants at long times and high temperatures (when Gaussian statistics is assumed). The ability of off-diagonal driving to open up new CT pathways that can compete with non-radiative pathways is demonstrated in the case of the Garg–Onuchic–Ambegaokar CT model driven by a CW field.

In the third chapter, we investigate whether the memory kernel for a system coupled simultaneously to multiple independent baths can be expressed as a sum of single-bath memory kernels. We show that additivity holds in the weak system-bath coupling limit, where the second-order memory kernel separates into independent bath contributions. Beyond this limit, however, the baths become dynamically correlated through their mutual coupling to the system, and the exact multi-bath memory kernel is no longer equal to the sum of exact single-bath memory kernels. We demonstrate this non-additivity for a two-level system linearly coupled to hot and cold harmonic baths, using the hierarchical equations of motion (HEOM) method to construct the memory kernels.

In the fourth chapter, we describe a formally exact generalized quantum master equation (GQME) framework for describing the dynamics of arbitrary subsets of reduced density matrix elements. Within this framework, the influence of both the bath degrees of freedom and any projected-out system reduced density matrix elements is captured through a memory kernel and an inhomogeneous term whose dimensionalities are determined by the subspace one projects onto. Using the HEOM method to construct these quantities for a two-level system linearly coupled to hot and cold harmonic baths, we investigate bath additivity across reduced-dimensionality GQMEs. The results reveal that the types of reduced-dimensionality GQMEs under consideration exhibit non-additivity even in the weak system-bath coupling limit, suggesting additivity can be tied to the choice of projection operator and the resulting reduced description of the system dynamics.

In the fifth chapter, the Ehrenfest method, a mixed quantum-classical approach is outlined and extended to a two-bath system. The approximate method's accuracy is assessed through its ability to reproduce the projection-free inputs needed to construct the two-bath populations-only GQME memory kernel. Direct application of Ehrenfest to obtain the population dynamics of a two-bath system is compared as well. The results are benchmarked against exact dynamics obtained via HEOM propagation.

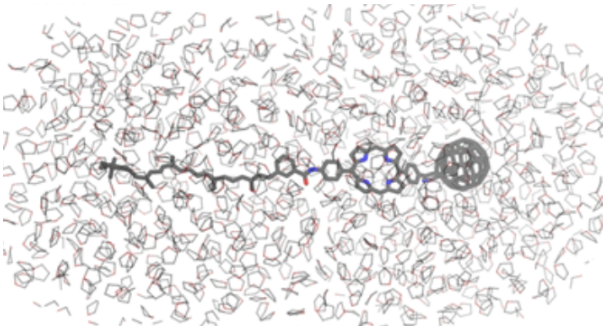
CHAPTER 1

Introduction

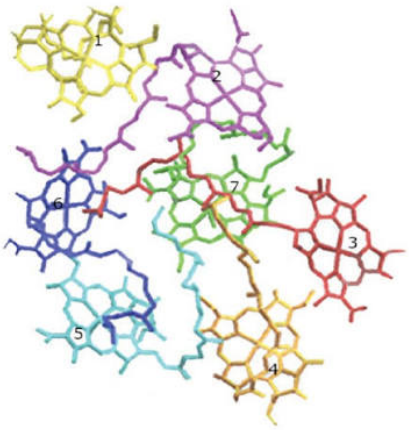
1.1 Motivation: Open System Chemical Dynamics

In classical mechanics, the dynamics of a system of particles is fully determined once their positions and momenta are known. With these initial conditions known, Newton's laws of motion can predict the system's trajectory forward in time. At the atomistic level, however, this classical picture breaks down, and quantum-mechanical phenomena such as superposition, tunneling, and coherence become non-negligible contributions such that a quantum-mechanical treatment is necessary to accurately describe a system's evolution. Broadly defined, chemical dynamics is the study of time-dependent processes that involve charge transfer, energy transfer, and chemical reactivity, and it is in these processes that quantum-mechanical effects are often most dominant.

There are many examples in which these processes play an important role in chemically, biologically, and technologically relevant phenomena. For example, excitation energy transfer plays a crucial role in photosynthetic light-harvesting complexes such as the Fenna-Matthews-Olson (FMO) complex.[18,87] Similarly, photo-induced charge transfer is a key process in both natural and artificial photosynthetic systems such as carotenoid–porphyrin–C_{60} molecular triads, as well as in many emerging technologies, such as organic photovoltaics and molecular junctions.[132,39,63,64] Representative examples of these processes are shown in Fig. 1.1.



(a) Carotenoid-Porphyrin-C_{60} Triad in Tetrahydrofuran (THF)[132]



(b) Fenna-Matthews-Olson (FMO) complex[81]

Figure 1.1: Representative examples of realistic, molecular systems that motivate the study of open system quantum dynamics. (a) A linear carotenoid-porphyrin-C_{60} molecular triad in tetrahydrofuran (THF), which serves as a model system for photosynthetic charge separation, where the charge transfer dynamics depend on the conformational state of the triad. (b) The Fenna-Matthews-Olson (FMO) complex, a photosynthetic light-harvesting complex that mediates excitation energy transfer between chromophores. Images adapted from Refs. 132, 81.

As these processes often occur in condensed-phase environments where quantum dynamical effects can strongly influence the dynamics, their theoretical description remains one of the most significant computational challenges.[91,76] Developing accurate methods for the simulation of these quantum dynamical processes is therefore essential not only for understanding natural phenomena, but also as a way to enable the design and control of chemical processes and technologies.

1.1.1 The Wavefunction Formalism

In many formulations of quantum dynamics, the state of a system is described using a time-dependent wavefunction represented by a state vector, $|\psi(t)\rangle$, in Hilbert space. The evolution of this state is governed by the Schrödinger equation,

$$i\hbar\frac{d}{dt}|\psi(t)\rangle = \hat{H}|\psi(t)\rangle \ , \tag{1.1}$$

where $\hat{H}$ is the Hamiltonian of the system. In principle, the Schrödinger equation provides a complete description of the dynamics of any quantum system, including a molecular system and its surrounding environment.

In practice, however, directly solving for the wavefunction of a system of interest is only feasible for very small systems. This limitation arises because the dimensionality of the Hilbert space grows exponentially with the number of degrees of freedom, causing the computational cost of storing and propagating the many-body wavefunction to increase exponentially as well. For many realistic chemical systems, such as the carotenoid-porphyrin-C_{60} molecular triad in tetrahydrofuran shown in Fig. 1.1a, the Hilbert space is so large that the full many-body wavefunction cannot be represented or propagated using any existing supercomputer. Consequently, direct wavefunction-based simulations quickly become computationally intractable for realistic condensed-phase molecular systems.

1.1.2 The Density Operator Formalism

Moreover, the time-dependent Schrödinger equation describes the unitary evolution of a closed quantum system. Most chemical, biological, and technological systems of interest, however, are not isolated, closed systems. Instead, real-life systems of interest freely interact continuously with one or more external environments, or baths. These bath interactions can significantly influence the system's dynamics, giving rise to processes such as relaxation, decoherence, and energy exchange, causing the subsystem of interest to evolve into a mixed state that can not be represented by a single wavefunction. Instead, the appropriate description is provided by the density operator,

$$\hat{\rho}(t) = \sum_k p_k(t) |\psi_k(t)\rangle\langle\psi_k(t)| \ , \tag{1.2}$$

where $p_k(t)$ gives the probability of finding the system in state $|\psi_k(t)\rangle$. The density operator has several important properties, including Hermiticity such that $\hat{\rho}(t) = \hat{\rho}^\dagger(t)$; the diagonal

elements of the density matrix are non-negative and have a trace of 1; the trace of the density operator squared is bound by $\mathrm{Tr}\{\hat{\rho}^2(\mathrm{t})\} \leq 1$, with equality only for the case the system is in a pure state.

While the density operator formalism naturally describes both pure and mixed states, representing the full density operator, Eq. (1.2), does not resolve the computational scaling challenge, as this description still corresponds to the combined system and bath degrees of freedom. For realistic condensed-phase systems, the dimensionality of the full density operator continues to scale exponentially with the total number of degrees of freedom, just as for the many-body wavefunction. However, since the primary interest is typically the dynamics of the subsystem rather than those of the bath, the relevant quantity of interest for an *open quantum system* is the reduced density operator, which acts only on the Hilbert space of the system and can be obtained by starting with the full density operator and tracing over the bath degrees of freedom,

$$\hat{\sigma}(t) = \mathrm{Tr}_{\mathrm{B}} \left\{\hat{\rho}(\mathrm{t})\right\} \ . \tag{1.3}$$

1.2 Quantum Master Equations

1.2.1 The Generalized Quantum Master Equation

The reduced density operator contains all information necessary to describe the dynamics of the subsystem of interest while still accounting for the influence of its environment. However, within this framework, the equation of motion is no longer governed by the Schrödinger equation for a state vector, but instead in terms of quantum master equations, equations of motion that describe the time-evolution of the reduced density operator. The derivation of quantum master equations begins with the equation of motion for the full system density

operator, known as the quantum Liouville equation,

$$\frac{d}{dt}\rho(t) = -\frac{i}{\hbar}\left[\hat{H}, \hat{\rho}(t)\right] \equiv -\frac{i}{\hbar}\mathcal{L}\hat{\rho}(t) \ , \tag{1.4}$$

where $\mathcal{L} \equiv [\hat{H}, \hat{A}]$ is the quantum Liouville superoperator. An important advantage of a reduced dynamics approach is the ability to focus on only a small subset of relevant degrees of freedom while the remaining degrees of freedom are accounted for through their influence on the subsystem. Mathematically, this separation can be achieved through the use of projection operator techniques. A projection superoperator $\mathcal{P}$ satisfies the idempotence property, $\mathcal{P}^2 = \mathcal{P}$, and is accompanied by a complimenatry projection superoperator, $\mathcal{Q} = 1 - \mathcal{P}$. Defining the following projection operator,

$$\mathcal{P}\hat{A} = \hat{\rho}_B(0) \otimes Tr_B\{\hat{A}\} \ , \tag{1.5}$$

and projecting onto the full density operator, yields the following formally exact Nakajima-Zwanzig equation for the reduced density matrix of the system,[90,151]

$$\frac{d}{dt}\hat{\sigma}(t) = -\frac{i}{\hbar}\langle\mathcal{L}\rangle\hat{\sigma}(t) - \int_0^t d\tau \mathcal{K}(\tau)\hat{\sigma}(t-\tau) + I(t) \ . \tag{1.6}$$

Here, $\langle\mathcal{L}\rangle(\hat{A}) = \mathrm{Tr}\left\{\hat{\rho}_{\mathrm{B}}(0)\mathcal{L}\right\}(\hat{\mathrm{A}})$, $\mathcal{K}(\tau)$ is the memory kernel superoperator, and $I(t)$ is the inhomogeneous term, which are explicitly given by:

$$\mathcal{K}(\tau) = \frac{1}{\hbar^2}\mathrm{Tr}_{\mathrm{B}}\left\{\mathcal{L}\mathrm{e}^{-\mathrm{i}\mathcal{Q}\mathcal{L}\tau/\hbar}\mathcal{Q}\mathcal{L}\hat{\rho}_{\mathrm{B}}(0)\right\} \ , \tag{1.7}$$

$$I(t) = -\frac{1}{\hbar}\mathrm{Tr}_{\mathrm{B}}\left\{\mathcal{L}\mathrm{e}^{-\mathrm{i}\mathcal{Q}\mathcal{L}\mathrm{t}/\hbar}\mathcal{Q}\hat{\rho}_{\mathrm{B}}(0)\right\} \ . \tag{1.8}$$

It is important to note that Eq. (1.6) is a formally exact equation of motion for the projected dynamics, and will be referred to as the generalized quantum master equation (GQME) throughout this dissertation. A key advantage of the GQME formalism is in its

flexibility, as the projection operator can be chosen arbitrarily to retain any subset of reduced density matrix elements of interest, while still corresponding to an exact equation of motion.

Another key feature of Eq. (1.6) is the fact that it is a *non-Markovian* equation of motion. In contrast to classical initial value problems where the future evolution is completely determined by the system's instantaneous position and momentum, the future evolution of an open quantum subsystem generally depends on its past history. The memory of past system-bath interactions arises from the complementary projection operator, $\mathcal{Q} = 1 - \mathcal{P}$, which accounts for the degrees of freedom eliminated by the defined projection. Their influence on the retained subsystem dynamics is captured through the memory kernel, Eq. (1.7), and when present, the inhomogeneous term, $I(t)$, Eq. (1.8). It is important to note the presence of a non-zero inhomogeneous term depends on both the choice of projection and the choice of the initial state of the system, and vanishes for commonly used choices, such as initially projected states satisfying $\mathcal{Q}\hat{\rho}(0) = 0$.

1.2.2 Redfield Quantum Master Equations

Despite its flexibility and exactness, because the exponential of the memory kernel contains the projection superoperator $\mathcal{Q}$, direct evaluation of this quantity is generally unfeasible for realistic chemical systems that contain a large quantity of coupled bath and system degrees of freedom. Therefore, a hierarchy of approximate quantum master equations (QMEs) have been developed to obtain descriptions of reduced quantum dynamics at a lower computational cost. One of the most widely used is the Redfield QME, which treats the system-bath interaction perturbatively to second-order.[102] The Redfield formalism begins by splitting the total Hamiltonian in system-bath form into a zero-order Hamiltonian and an interaction Hamiltonian,[35]

$$\begin{aligned} \hat{H}_0 &= \hat{H}_S + \hat{H}_B \ , \\ \hat{H}_I &= \hat{H}_{BS} \ . \end{aligned} \tag{1.9}$$

In the weak coupling limit, when the memory kernel in Eq. (1.7) is expanded to second order, the lowest non-vanishing order, it can be approximated such that:

$$\mathcal{K}_{WC}(\tau) = \frac{1}{\hbar^2}\mathrm{Tr_B}\left\{\mathcal{L}_{\mathrm{BS}}\exp\left[-\frac{\mathrm{i}}{\hbar}\mathcal{L}_{\mathrm{B}}\tau\right]\exp\left[-\frac{\mathrm{i}}{\hbar}\mathcal{L}_{\mathrm{S}}\tau\right]\mathcal{L}_{\mathrm{BS}}\hat{\rho}_{\mathrm{B}}^{\mathrm{eq}}\right\} . \tag{1.10}$$

Substituting Eq. (1.10) into Eq. (1.6), yields the *non-Markovian quantum master equation* in the limit of weak system-bath coupling:

$$\frac{d}{dt}\hat{\sigma}(t) = -\frac{i}{\hbar}\mathcal{L}_S\hat{\sigma}(t) - \int_0^t d\tau\mathcal{K}_{WC}(\tau)\hat{\sigma}(t-\tau) . \tag{1.11}$$

The non-Markovian form retains the memory kernel, allowing the instantaneous evolution of the reduced density operator to depend on its past history through finite bath memory effects. If the time scale of the bath-induced relaxation dynamics is much slower than the memory time, the memory kernel effectively becomes *local* in time and the corresponding equation of motion becomes *memory-less*, an approximation known as the *Markovian quantum master equation*:

$$\begin{aligned}\frac{d}{dt}\hat{\sigma}(t) &= -\frac{i}{\hbar}\mathcal{L}_s\hat{\sigma}(t) - \mathcal{D}\hat{\sigma}(t) ,\\ \mathcal{D} &= \frac{1}{\hbar^2}\int_0^\infty d\tau\mathrm{Tr_B}\left\{\mathcal{L}_{\mathrm{BS}}\exp\left[-\frac{\mathrm{i}}{\hbar}\mathcal{L}_{\mathrm{B}}\tau\right]\exp\left[-\frac{\mathrm{i}}{\hbar}\mathcal{L}_{\mathrm{S}}\tau\right]\mathcal{L}_{\mathrm{BS}}\exp\left[\frac{\mathrm{i}}{\hbar}\mathcal{L}_{\mathrm{S}}\tau\right]\hat{\rho}_{\mathrm{B}}^{\mathrm{eq}}\right\} .\end{aligned} \tag{1.12}$$

Another commonly used approximate form of the Redfield equation is the secular approximation, which neglects rapidly oscillating terms in the equation of motion. Specifically, terms oscillating at frequencies much larger than the characteristic relaxation rates are assumed to average to zero over the timescale of the system dynamics and are therefore omitted. The secular approximation is typically well justified in the limit of weak system-bath coupling where the coupling energy is assumed to be negligibly small compared to the system and bath energies. Applying the secular approximation to Eq. (1.12) yields a Lindblad-form QME, in which the dynamics of the system's populations, $\{\sigma_{jj}(t)\}$, and the coherences, $\{\sigma_{jk}(t)\}$, are

decoupled and can be described by:[4,69]

$$\begin{aligned}\frac{d}{dt}\sigma_{jj}(t) &= -\sum_{l\neq j} k_{l\leftarrow j}\sigma_{jj}(t) + \sum_{l\neq j} k_{j\leftarrow l}\sigma_{ll}(t) \ , \\ \frac{d}{dt}\sigma_{jk}(t) &= -(i\omega_{jk} + \gamma_{jk})\sigma_{jk}(t) \ .\end{aligned} \tag{1.13}$$

Here, $\{k_{l\leftarrow j}\}$ and $\{\gamma_{jk}\}$ are the population relaxation and dephasing rate constants, respectively:

$$\begin{aligned}k_{l\leftarrow j} &= \frac{1}{\hbar^2}\tilde{C}_{jl,lj}(\omega_{jl}) \ , \\ \gamma_{jk} &= \frac{1}{2}\left(\sum_{l\neq j} k_{l\leftarrow j} + \sum_{l\neq k} k_{l\leftarrow k}\right) + \frac{1}{2\hbar^2}\left[\tilde{C}_{jj,jj}(0) + \tilde{C}_{kk,kk}(0)\right] \ .\end{aligned} \tag{1.14}$$

In the above, $\hbar\omega_{jl} = E_j - E_l$. The population relaxation rates satisfy the detailed balance relation,

$$k_{l\leftarrow j}/k_{j\leftarrow l} = e^{\beta\hbar\omega_{jl}} \ , \tag{1.15}$$

and the Fourier transform of the bath correlation function is given by

$$\begin{aligned}\tilde{C}_{jl,lj}(\omega_{jl}) &= \int_{-\infty}^{\infty} d\tau e^{i\omega_{jl}\tau} C_{jl,lj}(\tau) \ , \\ C_{jl,lj}(\tau) &= \mathrm{Tr}_B\left[\hat{\rho}_B(0) e^{i\hat{H}_S\tau/\hbar}\hat{\Lambda}_{jl} e^{-i\hat{H}_S\tau/\hbar}\hat{\Lambda}_{lj}\right] \ .\end{aligned} \tag{1.16}$$

1.2.3 Off-Diagonal Quantum Master Equations

Another perturbative quantum master equation of interest is the *populations-only time-convolutionless off-diagonal QME (p-tcl-OD-QME)*, which will be discussed extensively throughout Chapter 2.[60] Unlike Redfield theory where the system-bath coupling is treated perturbatively, the OD-QME framework employs a perturbative expansion of the electronic couplings between diabatic states. Specifically, the zero-order Hamiltonian and interaction

Hamiltonian are now defined as:

$$\hat{H}_0 = \sum_j \hat{H}_j |j\rangle\langle j| \ , \tag{1.17}$$

$$\hat{H}_I(t) = \sum_{j \neq k} \hat{V}_{jk}(t) |j\rangle\langle k| \ . \tag{1.18}$$

Here, $\{|j\rangle\}$ are *diabatic* electronic states and $\{\hat{V}_{jk}\}$ are electronic couplings between the states.

The derivation is most conveniently performed in the interaction picture, where

$$\begin{aligned} \tilde{\rho}(t) &= e^{\frac{i}{\hbar}\hat{H}_0 t} \hat{\rho}(t) e^{-\frac{i}{\hbar}\hat{H}_0 t} = e^{\frac{i}{\hbar}\mathcal{L}_0 t} \hat{\rho}(t) \ , \\ \tilde{H}_I(t) &= e^{\frac{i}{\hbar}\hat{H}_0 t} \hat{H}_I e^{-\frac{i}{\hbar}\hat{H}_0 t} \ , \\ \frac{d}{dt}\tilde{\rho}(t) &= -\frac{i}{\hbar}[\tilde{H}_I(t), \tilde{\rho}(t)] \ . \end{aligned} \tag{1.19}$$

To obtain an equation of motion for the electronic populations, a projection operator defined as $\mathcal{P}(\hat{A}) = \sum_j |j\rangle\langle j||j\rangle\hat{A}\langle j|$ is introduced. Using this projection operator within the time-convolutionless (TCL) formalism yields the Shibata Equation, a formally exact equation of motion analagous to Eq. (1.6) with the exception of replacing $\sigma(t-\tau)$ with $\sigma(t)$. Truncating the resulting TCL expansion at second-order gives:

$$\begin{aligned} \frac{d}{dt}\tilde{\sigma}_{jj}(t) &= -\sum_{k \neq j} k'_{kj}(t)\tilde{\sigma}_{jj}(t) + \sum_{k \neq j} k'_{jk}(t)\tilde{\sigma}_{kk}(t) \ , \\ k'_{jk}(t) &= \frac{2}{\hbar^2}\mathrm{Re}\int_0^{\mathrm{t}} \mathrm{d}\tau \langle \hat{\mathrm{V}}_{\mathrm{kj}}(\mathrm{t})\hat{\mathrm{V}}_{\mathrm{jk}}(\tau)\rangle \ . \end{aligned} \tag{1.20}$$

Here, $k'_{jk}(t)$ are the time-dependent rate coefficients, equivalent to the *nonequilubrium Fermi's golden rule (NE-FGR) rate coefficients.*[127,128,129,131]

1.3 Non-Equilibrium Dynamics

The quantum master equation approaches described above have been extensively applied to simulate reduced quantum dynamics in systems coupled to a single thermal bath environment and in the absence of external driving fields. These studies have provided important benchmarks for assessing the accuracy and applicability of the quantum master equations under consideration. However, many experimentally-relevant systems operate under more complex, nonequilibrium conditions. For example, time-dependent external fields can activate transitions previously forbidden under equilibrium conditions and drive fundamental changes in transport pathways and rates. Additionally, a system coupled to multiple thermal environments at different temperatures can generate nonequilibrium steady states, a key feature underlying heat transport, as well as energy and charge transfer processes.

The extension to nonequilibrium quantum systems remains considerably less explored, and in many cases, non-trivial modifications are required to capture the resulting nonequilibrium dynamics that arise, particularly beyond the weak system-bath coupling regime. For example, the presence of a time-dependent external field introduces additional complexity because the driving field adds an explicit time-dependence into the Hamiltonian, fundamentally altering the coupled system-bath dynamics. Although the field directly drives the system out of equilibrium, its influence also extends to the environment by modifying the system-bath correlations and the pathways through which energy is exchanged with the bath. As a result, the effective relaxation dynamics and associated rates become both time-dependent and dependent on the external field, rather than being fixed quantities determined solely by the equilibrium bath interaction. Quantum master equations must therefore be extended to capture this explicit time dependence and accurately describe the interplay between external driving, system dynamics, and environmental fluctuations.

Similarly, quantum heat transport through systems coupled to multiple thermal environments presents challenges that extend beyond classical descriptions of heat flow. For example,

in classical, nonequilibrium thermodynamics, heat currents from independent thermal reservoirs can often be treated as additive contributions to the overall dynamics. However, for quantum systems, distinct thermal reservoirs can become coupled indirectly through their interaction with a quantum system, leading to collective bath effects and non-additive behavior that can no longer be described by a sum of independent bath contributions. Understanding the quantum collective effects between multiple thermal environments is therefore essential for accurately describing nonequilibrium heat flow and energy-transfer processes.

A central objective of this dissertation is to extend the quantum master equation approaches outlined in Sec. 1.2 beyond the single-bath, field-free frameworks previously studied. Specifically, the following chapters investigate the application of quantum master equation approaches to time-dependent, externally driven quantum systems and to quantum systems coupled to multiple heat baths. These extensions enable the study of a broad range of chemically, biologically, and technologically relevant phenomena, including light-driven dynamics, nonequilibrium energy and charge transfer, and heat flow. More broadly, these developments provide a framework for understanding how external driving fields and multi-bath environmental interactions influence quantum dynamical behavior, while establishing methodologies for accurately modeling and ultimately controlling charge transfer, relaxation, and energy transfer processes.

1.4 Overview of this Dissertation

The remainder of this dissertation is organized as follows. In Chapter 2, we present an extension of the OD-QME method for a system coupled to an external time-dependent driving field. We walk through the application of the driven OD-QME to a two-level GOA model coupled to a time-dependent external driving field as a demonstration. The simulation results are then compared to the results from the field-free OD-QME applied to the same model system. In Chapter 3, the GQME with exact projection-free inputs is described. We walk through the application of the GQME for a two-level spin-boson model linearly coupled

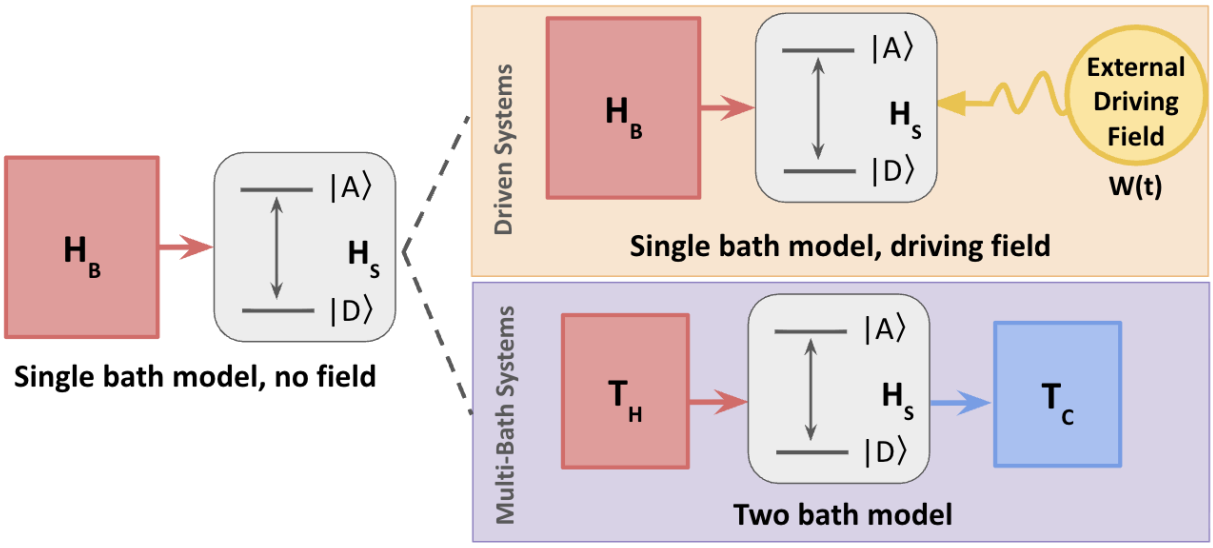


Figure 1.2: Schematic illustrating two extensions of the conventional single-bath model without an external driving field: (top) a driven two-level system coupled to a single bath and an external time-dependent driving field, (bottom) a two-level system simultaneously coupled to hot and cold thermal baths.

to a hot and a cold harmonic bath. The simulation results of the populations and coherence dynamics of the two-level spin-boson two-bath model are then presented and compared to the exact results generated with hierarchical equations of motion (HEOM), as well as an exploration of memory kernel non-additivity. In Chapter 4, four projection operators are investigated, each of which defines a corresponding reduced-dimensionality GQME. The results of the population and coherence dynamics, as well as an investigation of the memory kernel additivity for the four reduced-dimensionality GQMEs is demonstrated on the two-bath spin boson model outlined in Chapter 3. In Chapter 5, a mixed quantum-classical approximate method will be used both for direct propagation of reduced system dynamics, and as an input method to the populations-only GQME. The resulting approximate projection-free inputs, memory kernels, and population and coherence dynamics will be compared with the corresponding exact quantities in the context of the two-bath spin-boson model outlined in Chapter 3. Finally, a short summary of the dissertation and a discussion of several future directions of interest for the application of quantum master equations for non-equilibrium

systems will be given in Chapter 6. Additional results from Chapter 2 including three other variations of driven OD-QMEs, along with a discussion of the experimental relevance of the model parameters and an alternative derivation based on the rotating wave approximation are presented in Appendix A, while a mathematical proof and additional explanations of the reduced-dimensionality memory kernels and inhomogeneous terms from Chapter 4 are provided in Appendix B.

CHAPTER 2

Quantum Master Equations for Systems Off-Diagonally Driven by a Time-Dependent External Field[1]

2.1 Introduction

Charge transfer (CT) reactions underlie key dynamical processes that take place in complex systems of chemical, biological, and technological importance.[144,42,68,67,11,103,9,136,80,32,148,62,64,132,125,124,87] Modeling CT dynamics is typically based on treating the electronic degrees-of-freedom (DOF) of interest as an open quantum system (referred to as *the system*), and restricting the input regarding the remaining electronic and nuclear DOF (referred to as *the bath*) to the minimum necessary in order to account for their effect on the system. Following such an approach casts the impact of the bath on the system in terms of compact reduced quantities such as time correlation functions, spectral densities, memory kernels and influence functionals.[91,22,44,127,131,129,130,132,138,91,96,53,1,126,29,31,41,59,92,100,138,90,150,113,118,146,51,55,82,17,49,88,84,137,15]

[1] This work was conducted in collaboration with Zongwei Huang and Professor Eitan Geva.

This chapter is based on the following published work:

Callie Wilson†; Zongwei Huang†; Eitan Geva. *Quantum master equations for systems off-diagonally driven by a time-dependent external field.* *J. Chem. Phys.* **2025**, *163* (9), 094101. https://doi.org/10.1063/5.0287202.[143]

† These authors contributed equally to this work.

Callie Wilson developed the theoretical analysis, performed the simulations, analyzed and interpreted the results, prepared the figures, and contributed to the writing of the manuscript. Zongwei Huang developed the computational implementation used in this work, performed simulations, contributed to the analysis and interpretation of the results, and contributed to manuscript preparation. Professor Eitan Geva supervised the research, contributed to the interpretation of the results, and provided guidance and editorial feedback during manuscript preparation.

Quantum master equations (QMEs) provide a powerful, flexible and general-purpose framework for formulating the effect of the bath on the dynamics of the system. Different types of QMEs have been proposed over the years that range from the formally exact time-convolution Nakajima-Zwanzig generalized quantum master equation (GQME)[90,150,113,118,146,48,24,142,25,23,51,55,97,82,50,52,54,98,88,84,87] and its convolutionless analogue,[13,122,19,121] to Redfield and Lindblad QMEs, which rely on multiple assumptions, including treating the system-bath coupling as weak, assuming that the system dynamics is Markovian, and imposing the secular approximation.[102,100,99,79,31,40,45,9,4]

A type of QME which is particularly suitable for simulating charge transfer dynamics is based on treating the terms that couple different electronic states as a small perturbation (within the framework of second-order perturbation theory). Adopting the terminology of Ref. 60, we will refer to such QMEs as *off-diagonal QMEs (OD-QMEs)* for the remainder of this paper. This terminology stems from the fact that the aforementioned electronic coupling terms are off-diagonal when represented in terms of the basis of electronic states between which electronic transitions occur. It should be noted that the definitions of "diagonal" and "off-diagonal" depend on the choice of electronic basis. For example, *modified Redfield QMEs*,[61,147,145,92,138,45] are one type of such OD-QMEs which are based on an electronic basis that consists of the typically delocalized eigen-states of the system Hamiltonian, while another type of OD-QMEs (sometimes referred to as QMEs in the Förster regime) is based on an electronic basis that consists of localized excited states.[145,58,138]

Variations of OD-QMEs also differ with respect to the choice of electronic DOF of interest (e.g. electronic populations vs. the full electronic reduced density matrix) and whether they are of a *time-convolution* or *time-convolutionless* form.[60,138]

Previous studies that utilized OD-QMEs were based on the assumption that the overall Hamiltonian, including the off-diagonal coupling terms, is *time-independent*. In this chapter, we extend the range of applicability of OD-QMEs to systems whose Hamiltonian includes *time-dependent* off-diagonal coupling terms. For example, this can be experimentally real-

ized by driving the system with a laser field. Importantly, such explicitly time-dependent coupling terms in the Hamiltonian open up new charge transfer pathways that can effectively compete with the non-radiative ones even when the field-matter interaction is treated as a small perturbation. The fact that such time-dependent off-diagonal coupling terms are switchable and programmable (via modifications to the driving field's intensity and frequency profiles) opens the door to controlling and manipulating charge transfer dynamics in complex molecular systems.

The remainder of this chapter is organized as follows. OD-QMEs for off-diagonally driven systems are derived and their asymptotic behavior at various limits is explored in Sec. 2.2. The effect of off-diagonal driving is demonstrated on a benchmark Garg-Onuchic-Ambegaokar (GOA) CT model[33] driven by a CW field in Sec. 2.3. A summary of the main results and concluding remarks are provided in section 6. Results for three other driven OD-QMEs, a discussion of experimental feasibility, and a discussion on the rotating wave approximation (RWA) are shown in Appendix A.

2.2 Theory

2.2.1 Preliminary Considerations

We start out by considering a two-state system with the following *explicitly time-dependent Hamiltonian*:

$$\hat{H}(t) = \hat{H}_D|D\rangle\langle D| + \hat{H}_A|A\rangle\langle A| + \hat{V}_{DA}(t)(|D\rangle\langle A| + |A\rangle\langle D|) \tag{2.1}$$

Here, $\{|D\rangle, |A\rangle\}$ are *diabatic* donor (D) and acceptor (A) electronic states; $\{\hat{H}_D \equiv T(\hat{\mathbf{P}}) + V_D(\hat{\mathbf{R}}), \hat{H}_A \equiv T(\hat{\mathbf{P}}) + V_A(\hat{\mathbf{R}})\}$ are the Hamiltonians of the nuclear DOF when the system is in those diabatic states, with $T(\hat{\mathbf{P}})$ the kinetic energy and $V_{D/A}(\hat{\mathbf{R}})$ the potential energy; $\hat{\mathbf{R}} = (\hat{R}_1, \hat{R}_2, ..., \hat{R}_N)$ and $\hat{\mathbf{P}} = (\hat{P}_1, \hat{P}_2, ..., \hat{P}_N)$ are the coordinates and momenta of the N

nuclear DOF; $\{\hat{V}_{DA}(t) = \hat{V}_{AD}(t) \equiv V_{DA}(\hat{\mathbf{R}}, t)\}$ are coupling terms between the donor and acceptor states. In the above and in what follows, a hat over a symbol, e.g., $\hat{A}$, indicates that the quantity is an operator, vector quantities are boldfaced, e.g., $\mathbf{R}$, and calligraphic font, e.g., $\mathcal{L}$, indicates that the quantity is a superoperator.

Importantly, the time dependence of the Hamiltonian in Eq. (2.1) is restricted to the electronic coupling term, $\hat{V}_{DA}(t)$. One way to realize such a Hamiltonian is by subjecting a donor-acceptor system to an external time-dependent driving laser field. The Hamiltonian of the *field-free donor-acceptor system* in such a case is given by:

$$\hat{H}_M = \hat{H}_D|D\rangle\langle D| + \hat{H}_A|A\rangle\langle A| + \hat{V}_{DA}(|D\rangle\langle A| + |A\rangle\langle D|) \quad , \tag{2.2}$$

where $\hat{V}_{DA}$ is the *time-independent* non-radiative coupling between the donor and acceptor states [a real number in the Condon approximation ($\hat{V}_{DA} \to V_{DA}$) or a Hermitian nuclear operator in the non-Condon case [$\hat{V}_{DA} \to V_{DA}(\hat{\mathbf{R}})$]]. Subjecting such a system to a time-dependent driving laser field, $\boldsymbol{\epsilon}(t) = [\epsilon_x(t), \epsilon_y(t), \epsilon_z(t)]^T$, then gives rise to an additional field-matter coupling term of the following form:

$$\begin{aligned} \hat{W}(t) &= -\hat{\boldsymbol{\mu}} \cdot \boldsymbol{\epsilon}(t) \\ &= -\begin{pmatrix} \boldsymbol{\epsilon}(t) \cdot \hat{\boldsymbol{\mu}}_{DD}|D\rangle\langle D| + \boldsymbol{\epsilon}(t) \cdot \hat{\boldsymbol{\mu}}_{AA}|A\rangle\langle A| \\ +\boldsymbol{\epsilon}(t) \cdot \hat{\boldsymbol{\mu}}_{DA}|D\rangle\langle A| + \boldsymbol{\epsilon}(t) \cdot \hat{\boldsymbol{\mu}}_{AD}|A\rangle\langle D| \end{pmatrix} \end{aligned} \tag{2.3}$$

Here, $\hat{\boldsymbol{\mu}} = (\hat{\mu}_x, \hat{\mu}_y, \hat{\mu}_z)^T$ is the dipole operator of the system (an overall system operator); $\hat{\boldsymbol{\mu}}_{jj} = \langle j|\hat{\mu}|j\rangle$ corresponds to the *permanent dipole moment* of the molecular system in state $|j\rangle$ (a nuclear operator with $j = D, A$); $\hat{\boldsymbol{\mu}}_{jk}$ corresponds to the *transition dipole moment* between states $|j\rangle$ and $|k\rangle$ (a nuclear operator with $j, k = D, A$ and $j \neq k$).

Adding the driving term in Eq. (2.3) to the field-free molecular Hamiltonian in Eq. (2.2) and assuming that $\hat{\boldsymbol{\mu}}_{DA} = \hat{\boldsymbol{\mu}}_{AD}$ [which corresponds to choosing the donor and acceptor electronic wave functions to be real and is consistent with the fact that $\hat{V}_{AD} = \hat{V}_{DA}$ in Eq.

(2.2)], then gives rise to a Hamiltonian of the following form for the *field-driven system*:

$$\begin{aligned}\hat{H}(t) &= \hat{H}_M + \hat{W}(t) \\ &= \left[\hat{H}_D - \boldsymbol{\epsilon}(t)\cdot\hat{\boldsymbol{\mu}}_{DD}\right]|D\rangle\langle D| \\ &+ \left[\hat{H}_A - \boldsymbol{\epsilon}(t)\cdot\hat{\boldsymbol{\mu}}_{AA}\right]|A\rangle\langle A| \\ &+ \left[\hat{V}_{DA} - \boldsymbol{\epsilon}(t)\cdot\hat{\boldsymbol{\mu}}_{DA}\right](|D\rangle\langle A| + |A\rangle\langle D|).\end{aligned}$$

For typical driving field intensities and permanent dipoles of molecular systems, the permanent dipole terms, $\{\boldsymbol{\epsilon}(t)\cdot\hat{\boldsymbol{\mu}}_{jj}|j\rangle\langle j|\}$, would typically be negligible relative to the field-free terms, $\{\hat{H}_j\}$. At the same time, the transition dipole terms, $\{\boldsymbol{\epsilon}(t)\cdot\hat{\boldsymbol{\mu}}_{jk}|j\rangle\langle k|\}$, can be comparable to the non-radiative terms, $\hat{V}_{DA}$ (see Appendix A.3). Thus, neglecting the permanent dipole terms while keeping the transition dipole terms gives rise to a Hamiltonian in the form of Eq. (2.1):

$$\begin{aligned}\hat{H}(t) &= \hat{H}_D|D\rangle\langle D| + \hat{H}_A|A\rangle\langle A| \\ &+ \left(\hat{V}_{DA} + \hat{\chi}_{DA}(t)\right)(|D\rangle\langle A| + |A\rangle\langle D|)\end{aligned} \tag{2.4}$$

Here, $\hat{\chi}_{DA}(t) = -\boldsymbol{\epsilon}(t)\cdot\hat{\boldsymbol{\mu}}_{DA}$. Comparison of Eq. (2.4) to Eq. (2.1) reveals that $\hat{V}_{DA}(t)$ consists of two contributions:

$$\hat{V}_{DA}(t) = \hat{V}_{DA} + \hat{\chi}_{DA}(t) \quad . \tag{2.5}$$

Here, $\hat{V}_{DA}$ is the *time-independent non-radiative coupling term* between the donor and acceptor states and $\hat{\chi}_{DA}(t)$ is the *time-dependent radiative coupling term* between the donor and acceptor states.

For example, consider the case of a CW driving field of the form

$$\boldsymbol{\epsilon}(t) = 2\boldsymbol{\epsilon}_0 \cos(\omega t) = \boldsymbol{\epsilon}_0 \Big(e^{i\omega t} + e^{-i\omega t} \Big), \tag{2.6}$$

where ω is the field frequency and $\boldsymbol{\epsilon}_0$ is half the field amplitude (referred to as just the field amplitude throughout the remainder of this paper for the sake of simplicity). In this case,

$$\hat{\chi}_{DA}(t) = -\boldsymbol{\epsilon}_0 \cdot \hat{\boldsymbol{\mu}}_{DA} \Big(e^{i\omega t} + e^{-i\omega t} \Big) = \hat{\chi}^0_{DA} \Big(e^{i\omega t} + e^{-i\omega t} \Big) \ , \tag{2.7}$$

where $\hat{\chi}^0_{DA} = -\boldsymbol{\epsilon}_0 \cdot \hat{\boldsymbol{\mu}}_{DA}$. It should be noted that unlike the non-radiative donor-acceptor coupling term, the radiative coupling term is switchable, such that $\hat{V}_{DA}(t)$ can switch between $\hat{V}_{DA}$ and $\hat{V}_{DA} + \hat{\chi}_{DA}(t)$ by turning the driving field on and off (e.g., by applying a sequence of square-enveloped pulses with amplitudes, lengths, leading frequencies and inter-pulse intervals of one's choice).

2.2.2 Populations-Only OD-QMEs for a Donor-Acceptor System Off-Diagonally Driven by a Time-Dependent External Field

Adopting the terminology used in Ref. 60, *off-diagonal quantum master equations (OD-QMEs)* correspond to the equations of motion of the reduced electronic density matrix elements of choice when the off-diagonal coupling term in the Hamiltonian [Eq. (2.1)], $\hat{V}_{DA}(t)\,(|D\rangle\langle A| + |A\rangle\langle D|)$, is treated as a small perturbation, within the framework of second-order time-dependent perturbation theory.

The derivation of OD-QMEs for a system governed by a Hamiltonian of the form of Eq. (2.1) starts out similarly to the derivation outlined in Ref. 60 for the case where $\hat{V}_{DA}$ is assumed to be *time-independent*. More specifically, the Hamiltonian in Eq. (2.1) is written as a sum of a *time-independent zero-order Hamiltonian* and a *time-dependent interaction term* (λ is a book keeping real parameter used for keeping track of the order within perturbation

theory):

$$\hat{H}_0 = \hat{H}_D|D\rangle\langle D| + \hat{H}_A|A\rangle\langle A|, \tag{2.8}$$

$$\lambda\hat{H}_I(t) = \hat{V}_{DA}(t)(|D\rangle\langle A| + |A\rangle\langle D|). \tag{2.9}$$

Importantly, even though the derivation in Ref. 60 assumed that $\hat{V}_{DA}$ is *time-independent*, the fact that the interaction term is explicitly time-dependent in our case does not pose a problem since within the OD-QME formalism, this term is treated as a small perturbation. More specifically, time-dependent perturbation theory calls for working in the interaction picture, where the interaction term becomes time-dependent regardless of whether or not it was time-dependent in the Schrödinger picture. The difference compared to the field-free case is that the time dependence of the interaction Hamiltonian in the interaction picture now has two sources: (1) An explicit time dependence in the Schrödinger picture, and (2) An implicit time dependence due to the transformation to the interaction picture (see below).

In the next step, we note that the dynamics of the density operator of the overall system in the Schrödinger picture, $\hat{\rho}(t)$, is governed by the following Liouville equation:

$$\begin{aligned}\frac{d}{dt}\hat{\rho}(t) &= -\frac{i}{\hbar}[\hat{H}_0, \hat{\rho}(t)] - \frac{i}{\hbar}\lambda[\hat{H}_I(t), \hat{\rho}(t)] \\ &= -\frac{i}{\hbar}\mathcal{L}_0\hat{\rho}(t) - \frac{i}{\hbar}\lambda\mathcal{L}_I(t)\hat{\rho}(t).\end{aligned} \tag{2.10}$$

Here, $\mathcal{L}_0\hat{\rho}(t) \equiv [\hat{H}_0, \hat{\rho}(t)]$ and $\mathcal{L}_I(t)\hat{\rho}(t) \equiv [\hat{H}_I(t), \hat{\rho}(t)]$. We will also assume that the initial state of the overall system is of the form:

$$\hat{\rho}(0) = \sigma_{DD}(0)\hat{\rho}^{eq}_{n,D} \otimes |D\rangle\langle D| + \sigma_{AA}(0)\hat{\rho}^{eq}_{n,A} \otimes |A\rangle\langle A|. \tag{2.11}$$

Here, $\sigma_{jj}(0) = \langle j|\hat{\sigma}(0)|j\rangle$ $(j = D, A)$, are the initial populations of the donor and acceptor states, respectively ($\hat{\sigma}(0) = \mathrm{Tr}_n\left[\hat{\rho}(0)\right]$ is the electronic reduced density operator that describes the initial state of the electronic DOF), and $\hat{\rho}^{eq}_{n,j}$ are the corresponding nuclear

equilibrium density operators, which are given by

$$\hat{\rho}_{n,j}^{eq} = \frac{e^{-\beta \hat{H}_j}}{Z_j} \quad ; \quad Z_j = \mathrm{Tr}_n\left(e^{-\beta \hat{H}_j}\right). \tag{2.12}$$

(Tr_n corresponds to taking the partial trace over the nuclear Hilbert space).

Next, we define the overall system density operator in the interaction picture:

$$\tilde{\rho}(t) = e^{\frac{i}{\hbar}\hat{H}_0 t}\hat{\rho}(t)e^{-\frac{i}{\hbar}\hat{H}_0 t} = e^{\frac{i}{\hbar}\mathcal{L}_0 t}\hat{\rho}(t). \tag{2.13}$$

$\tilde{\rho}(t)$ should not be confused with $\hat{\rho}(t)$ (the latter is the overall system density operator in the *Schrödinger picture*). It should, however, be pointed out that $\tilde{\rho}(t)$ and $\hat{\rho}(t)$ coincide at $t = 0$, namely $\tilde{\rho}(0) = \hat{\rho}(0)$.

The equation of motion for $\tilde{\rho}(t)$ has the form of a Liouville equation:

$$\frac{d}{dt}\tilde{\rho}(t) = -\frac{i}{\hbar}\lambda[\tilde{H}_I(t), \tilde{\rho}(t)] = -\frac{i}{\hbar}\,\tilde{\mathcal{L}}_I(t)\tilde{\rho}(t). \tag{2.14}$$

Here, $\tilde{H}_I(t)$, which is the Hamiltonian that governs the overall system dynamics in the interaction picture, is given by:

$$\begin{aligned}
\tilde{H}_I(t) &= e^{i\hat{H}_0 t/\hbar}\hat{H}_I(t)e^{-i\hat{H}_0 t/\hbar} \\
&= e^{i\hat{H}_0 t/\hbar}\hat{V}_{DA}(t)\left[|D\rangle\langle A| + |A\rangle\langle D|\right]e^{-i\hat{H}_0 t/\hbar} \\
&= e^{i\hat{H}_D t/\hbar}\hat{V}_{DA}(t)e^{-i\hat{H}_A t/\hbar}|D\rangle\langle A| \\
&+ e^{i\hat{H}_A t/\hbar}\hat{V}_{DA}(t)e^{-i\hat{H}_D t/\hbar}|A\rangle\langle D| \\
&\equiv \tilde{V}_{DA}(t)|D\rangle\langle A| + \tilde{V}_{AD}(t)|A\rangle\langle D|.
\end{aligned} \tag{2.15}$$

$\tilde{V}_{DA}(t) \equiv e^{i\hat{H}_D t/\hbar}\hat{V}_{DA}(t)e^{-i\hat{H}_A t/\hbar}$ should not be confused with $\hat{V}_{DA}(t)$ (the latter is in the Schrödinger picture while the former is in the interaction picture). It should also be noted that $\tilde{V}_{DA}(t) \neq \tilde{V}_{AD}(t)$ even though $\hat{V}_{DA}(t) = \hat{V}_{AD}(t)$.

The remainder of the derivation of the OD-QMEs in this paper follows a procedure similar to that used in Ref. 60 to derive OD-QMEs in the field-free case. It should, however, be noted that the notation used is somewhat different since $\hat{V}_{kl}(t)$ defined in Eq. (27) of Ref. 60 is not the same as $\hat{V}_{kl}(t)$ defined in Eq. (2.1). More specifically, whereas $\hat{V}_{kl}(t)$ in Eq. (2.1) is already explicitly time-dependent in the Schrödinger picture, the time dependence of $\hat{V}_{kl}(t)$ in Eq. (27) of Ref. 60 only comes about from the transformation to the interaction picture, with $\hat{V}_{kl}$ starting out as *time-independent* in the Schrödinger picture.

To demonstrate this, we will outline the derivation of OD-QMEs for the populations of the donor and acceptor electronic states, which we will refer to as *populations-only OD-QMEs*. The derivation starts out by introducing the following projection superoperator:

$$\begin{aligned}\mathcal{P}\hat{\xi} = \mathrm{Tr}_n\Big(\langle D|\hat{\xi}|D\rangle\Big)\hat{\rho}^{eq}_{n,D}\otimes|D\rangle\langle D| \\ + \mathrm{Tr}_n\Big(\langle A|\hat{\xi}|A\rangle\Big)\hat{\rho}^{eq}_{n,A}\otimes|A\rangle\langle A|.\end{aligned} \tag{2.16}$$

Here, $\mathcal{P}$ is a projection superoperator operating on the overall system operator $\hat{\xi}$ (note that $\mathcal{P}$ is idempotent, i.e. $\mathcal{P}^2=\mathcal{P}$, which is necessary for it to be a projection). We also define the complimentary projection superoperator as $\mathcal{Q}=\mathcal{I}-\mathcal{P}$, where $\mathcal{I}$ is the unity superoperator.

Applying $\mathcal{P}$ to $\hat{\rho}(t)$ yields:

$$\begin{aligned}\mathcal{P}\hat{\rho}(t) &= \mathrm{Tr}_n\Big(\langle D|\hat{\rho}(t)|D\rangle\Big)\hat{\rho}^{eq}_{n,D}\otimes|D\rangle\langle D| \\ &+ \mathrm{Tr}_n\Big(\langle A|\hat{\rho}(t)|A\rangle\Big)\hat{\rho}^{eq}_{n,A}\otimes|A\rangle\langle A| \\ &= \sigma_{DD}(t)\hat{\rho}^{eq}_{n,D}\otimes|D\rangle\langle D| + \sigma_{AA}(t)\hat{\rho}^{eq}_{n,A}\otimes|A\rangle\langle A|.\end{aligned} \tag{2.17}$$

Here, we used the fact that $\mathrm{Tr}_n\Big(\langle j|\hat{\rho}(t)|j\rangle\Big)=\sigma_{jj}(t)$ is the population of electronic state $|j\rangle$ $(j=D,A)$. Since $\mathrm{Tr}_n\Big(\hat{\rho}^{eq}_{n,D}\Big)=\mathrm{Tr}_n\Big(\hat{\rho}^{eq}_{n,A}\Big)=1$, partially tracing $\mathcal{P}\hat{\rho}(t)$ over the nuclear DOF yields the projection of $\hat{\sigma}(t)$ onto the populations subspace [i.e. excluding the electronic

coherences $\sigma_{DA}(t)$ and $\sigma_{AD}(t)$]:

$$\mathrm{Tr}_n[\mathcal{P}\hat{\rho}(t)] = \sigma_{DD}(t)|D\rangle\langle D| + \sigma_{AA}(t)|A\rangle\langle A|. \tag{2.18}$$

Thus, using the projection superoperator in Eq. (2.16) yields an OD-QME for the populations of the donor and acceptor states. Importantly, this is still true when working in the interaction picture, since the donor and acceptor populations are invariant to the transformation to the interaction picture, i.e. $\tilde{\sigma}_{jj}(t) = \sigma_{jj}(t)$.

Following the procedure outlined in Ref. 60, with the projection superoperator in Eq. (2.16), leads to the following population-only time-convolution OD-QME (p-tc-OD-QME):

$$\begin{aligned}\frac{d}{dt}\sigma_{DD}(t) &= -\frac{d}{dt}\sigma_{AA}(t) \\ &= -\frac{2}{\hbar^2}Re\int_0^t d\tau C_{D\to A}(t,\tau)\sigma_{DD}(t-\tau) \\ &+ \frac{2}{\hbar^2}Re\int_0^t d\tau C_{A\to D}(t,\tau)\sigma_{AA}(t-\tau)\end{aligned} \tag{2.19}$$

where,

$$\begin{aligned}C_{D\to A}(t,\tau) &= \mathrm{Tr}_n\left[\tilde{V}_{DA}(t)\tilde{V}_{AD}(t-\tau)\hat{\rho}^{eq}_{n,D}\right] \\ &= \mathrm{Tr}_n\left[e^{i\hat{H}_D\tau/\hbar}\hat{V}_{DA}(t)e^{-i\hat{H}_A\tau/\hbar}\hat{V}_{DA}(t-\tau)\hat{\rho}^{eq}_{n,D}\right] \\ C_{A\to D}(t,\tau) &= \mathrm{Tr}_n\left[\tilde{V}_{AD}(t)\tilde{V}_{DA}(t-\tau)\hat{\rho}^{eq}_{n,A}\right] \\ &= \mathrm{Tr}_n\left[e^{i\hat{H}_A\tau/\hbar}\hat{V}_{DA}(t)e^{-i\hat{H}_D\tau/\hbar}\hat{V}_{DA}(t-\tau)\hat{\rho}^{eq}_{n,A}\right]\end{aligned} \tag{2.20}$$

The two forms of $C_{D\to A}(t,\tau)$ and $C_{A\to D}(t,\tau)$ in Eq. (2.20) are based on the identity $\tilde{V}_{jk}(t) = e^{i\hat{H}_j t/\hbar}\hat{V}_{jk}(t)e^{-i\hat{H}_k t/\hbar}$ and the fact that $[\hat{\rho}^{eq}_{j,n}, e^{-i\hat{H}_j t/\hbar}] = 0$. It should also be noted that $\frac{d}{dt}\sigma_{AA}(t) = -\frac{d}{dt}\sigma_{DD}(t)$ such that $\frac{d}{dt}[\sigma_{DD}(t) + \sigma_{AA}(t)] = 0$ (conservation of population).

A time-convolutionless version of Eq. (2.19), which we will refer to as the p-tcl-OD-QME,

corresponds to substituting $\sigma_{jj}(t)$ for $\sigma_{jj}(t-\tau)$, and is given by:[60]

$$\begin{aligned}\frac{d}{dt}\sigma_{DD}(t) &= -\frac{d}{dt}\sigma_{AA}(t) \\ &= -k_{D\to A}(t)\sigma_{DD}(t) + k_{A\to D}(t)\sigma_{AA}(t).\end{aligned} \tag{2.21}$$

Here, $k_{D\to A}(t)$ and $k_{A\to D}(t)$ are the donor-to-acceptor and acceptor-to-donor *nonequilubrium Fermi's golden rule (NE-FGR) rate coefficients*[22,131,130,60]

$$\begin{aligned}k_{D\to A}(t) &= \frac{2}{\hbar^2}Re\int_0^t d\tau C_{D\to A}(t,\tau) \\ k_{A\to D}(t) &= \frac{2}{\hbar^2}Re\int_0^t d\tau C_{A\to D}(t,\tau) \quad .\end{aligned} \tag{2.22}$$

2.2.3 P-Tcl-OD-QMEs for a Donor-Acceptor System Subject to a CW Driving Field within the Condon Approximation

Further insight into the p-tcl-OD-QME [Eqs. (2.21) and (2.22)], can be gained by considering the special case where $\hat{V}_{DA}(t)$ is given by Eq. (2.5), with the radiative donor-acceptor coupling term given by Eq. (2.7). For the sake of simplicity, we also make the Condon approximation with respect to both the radiative and non-radiative donor-acceptor coupling terms, such that $\hat{V}_{DA} \to V_{DA}$ and $\hat{\chi}_{DA} \to \chi_{DA}$, where V_{DA} and χ_{DA} are treated as numbers (as opposed to nuclear operators). It should also be noted that $\chi_{DA}/\hbar$ is often referred to as the *Rabi frequency*.

Substituting $V_{DA}(t) = V_{DA} + \chi^0_{DA}(e^{i\omega t} + e^{-i\omega t})$ into the expression for $C_{D\to A}(t)$ in Eq. (2.20), and then substituting it back into Eq. (2.22), and applying the rotating wave approximation (RWA), according to which terms containing $e^{\pm i\omega t}$ and $e^{\pm 2i\omega t}$ factors are negligible (see Appendix A.2), we obtain the following expression for $k_{D\to A}(t)$ [the analogous expression

for $k_{A\to D}(t)$ can be obtained by switching D and A]:

$$\begin{aligned} k_{D\to A}(t) &= k^0_{D\to A}(t) \\ &+ \left(\frac{\chi^0_{DA}}{V_{DA}}\right)^2 \left[k^0_{D\to A}(-\omega,t) + k^0_{D\to A}(\omega,t)\right] \quad . \end{aligned} \tag{2.23}$$

Here,

$$\begin{aligned} k^0_{D\to A}(t) &= \frac{2}{\hbar^2} Re \int_0^t d\tau C^0_{D\to A}(\tau), \\ k^0_{D\to A}(\pm\omega,t) &= \frac{2}{\hbar^2} Re \int_0^t d\tau e^{\pm i\omega\tau} C^0_{D\to A}(\tau), \\ C^0_{D\to A}(\tau) &= V^2_{DA} Tr_n \left[e^{i\hat{H}_D\tau/\hbar} e^{-i\hat{H}_A\tau/\hbar} \hat{\rho}^{eq}_{n,D}\right]. \end{aligned} \tag{2.24}$$

It should be noted that $k^0_{DA}(t) \equiv k^0_{DA}(\omega = 0, t)$ corresponds to the *field-free* NE-FGR rate coefficient. Thus, the second term on the RHS of Eq. (2.23) corresponds to an additive enhancement of the donor-to-acceptor CT rate brought about by adding a radiative donor-to-acceptor transition pathway (note that this enhancement vanishes when $\chi^0_{DA} \to 0$).

As expected, one factor that determines this enhancement is the ratio of the strengths of the radiative and non-radiative coupling coefficients, $(\chi^0_{DA}/V_{DA})^2$. More specifically, while both couplings are treated as small perturbations, $|\chi^0_{DA}|$ needs to be comparable to $|V_{DA}|$ for the radiative pathway to be competitive with the non-radiative pathway.

The other factor that determines the enhancement is $[k^0_{D\to A}(-\omega,t) + k^0_{D\to A}(\omega,t)]$. This factor accounts for the effect of the field frequency, ω [as opposed to the field intensity in the first factor, $(\chi^0_{DA})^2$]. As we show in Sec. 2.2.4, this term accounts for the fact that the enhancement is maximized when the frequency of the driving field is in resonance with the donor-to-acceptor vertical transition frequency. It is also noteworthy that $k^0_{DA}(\pm\omega,t)$ can be thought of as the NE-FGR rate coefficients for a dressed system with the donor PES shifted up (+) or down (-) by the absorption or emission of a photon with energy $\hbar\omega$, respectively.

2.2.4 Asymptotic Behavior and the Marcus Theory Limit

Eq. (2.21) describes the donor-acceptor CT dynamics in terms of *time-dependent rate coefficients* [$k_{D\to A}(t)$ and $k_{A\to D}(t)$]. However, the time dependence of $k_{D\to A}(t)$ and $k_{A\to D}(t)$ is transient and only relevant on the time scale determined by the lifetime of the correlation functions $C^0_{D\to A}(\tau)$ and $C^0_{A\to D}(\tau)$ [see Eqs. (2.23) and (2.24)]. Thus, given that the lifetime of $C^0_{D\to A}(\tau)$ and $C^0_{A\to D}(\tau)$ is τ_c, on timescales longer than τ_c, the upper limit of the time integral in Eq. (2.24) can be set to infinity, so that the donor-acceptor transition dynamics can be described by *equilibrium Fermi's golden rule (E-FGR) rate constants* (as opposed to time-dependent NE-FGR rate coefficients):

$$\begin{aligned}\frac{d}{dt}\sigma_{DD}(t) &= -\frac{d}{dt}\sigma_{AA}(t) \\ &\xrightarrow{t>\tau_c} -k_{D\to A}\sigma_{DD}(t) + k_{A\to D}\sigma_{AA}(t) \quad .\end{aligned} \tag{2.25}$$

Here,

$$\begin{aligned}k_{D\to A} &= k^0_{D\to A} \\ &+ \left(\frac{\chi^0_{DA}}{V_{DA}}\right)^2 \left[k^0_{D\to A}(-\omega) + k^0_{D\to A}(\omega)\right] \quad ,\end{aligned} \tag{2.26}$$

with

$$\begin{aligned}k^0_{D\to A} &= \frac{2}{\hbar^2} Re \int_0^\infty d\tau C^0_{D\to A}(\tau), \\ k^0_{D\to A}(\pm\omega) &= \frac{2}{\hbar^2} Re \int_0^\infty d\tau e^{\pm i\omega\tau} C^0_{D\to A}(\tau) \quad .\end{aligned} \tag{2.27}$$

Further insight can be obtained by considering the Marcus limit of E-FGR. More specifically, the E-FGR rate constant turns into the Marcus-like rate constant when $C_{D\to A}(\tau)$ is approximated by its short-time and high-temperature limit and the nuclear dynamics are assumed to satisfy Gaussian statistics.[127,91] In this limit, $C^0_{D\to A}(\tau)$ and $k^0_{D\to A}$ in Eq. (2.27)

can be replaced by

$$\begin{aligned} C^{M}_{D\to A}(\tau) &= V^2_{DA} e^{-i\langle U_{AD}\rangle_D \tau/\hbar - \frac{1}{2}\sigma^2\tau^2/\hbar^2} \\ k^{0}_{D\to A} &= \frac{1}{\hbar^2} V^2_{DA} \sqrt{\frac{2\pi}{\sigma^2}} e^{-\frac{\langle U_{AD}\rangle^2_D}{2\sigma^2}} \quad . \end{aligned} \tag{2.28}$$

Here, $U_{AD}(\mathbf{R}) = V_A(\mathbf{R}) - V_D(\mathbf{R})$ is the donor-to-acceptor vertical transition energy and the average $\langle \cdots \rangle_D$ corresponds to *classical* thermal equilibrium on the donor potential energy surface:

$$\langle U^n_{AD}\rangle_D = \frac{\int \mathbf{dR} e^{-\beta V_D(\mathbf{R})} U^n_{AD}(\mathbf{R})}{\int \mathbf{dR} e^{-\beta V_D(\mathbf{R})}} \quad . \tag{2.29}$$

Thus, $\langle U_{AD}\rangle_D$ is the average vertical transition energy and $\sigma^2 = \langle U^2_{AD}\rangle_D - \langle U_{AD}\rangle^2_D$ is the corresponding variance. It should be noted that $\langle U_{AD}\rangle_D$ and σ^2 can be related to the reaction energy, ΔE, and reorganization energy, E_r, as follows:[127]

$$\langle U_{AD}\rangle_D = \Delta E + E_r \qquad , \qquad E_r = \frac{\sigma^2}{2k_B T} \quad . \tag{2.30}$$

Importantly, $\langle U_{AD}\rangle_D$ can be positive or negative depending on whether the CT reaction is in the *normal region* or *inverted region*, respectively. More specifically, given that $\langle U_{AD}\rangle_D = \Delta E + E_r$, with $E_r > 0$ and $\Delta E < 0$ (assuming a downhill reaction), the normal region corresponds to $|\Delta E| = -\Delta E < E_r$ and therefore to $\langle U_{AD}\rangle_D = \Delta E + E_r > 0$, while the inverted region corresponds to $|\Delta E| = -\Delta E > E_r$ and therefore to $\langle U_{AD}\rangle_D = \Delta E + E_r < 0$. This implies that in the normal region, the radiative path involves energy *absorption* by the molecular system from the driving field, while in the inverted region it involves energy *emission* by the molecular system to the driving field (see Fig. 2.1).

The resonant nature of the rate enhancement term in Eq. (2.26) is revealed by substituting

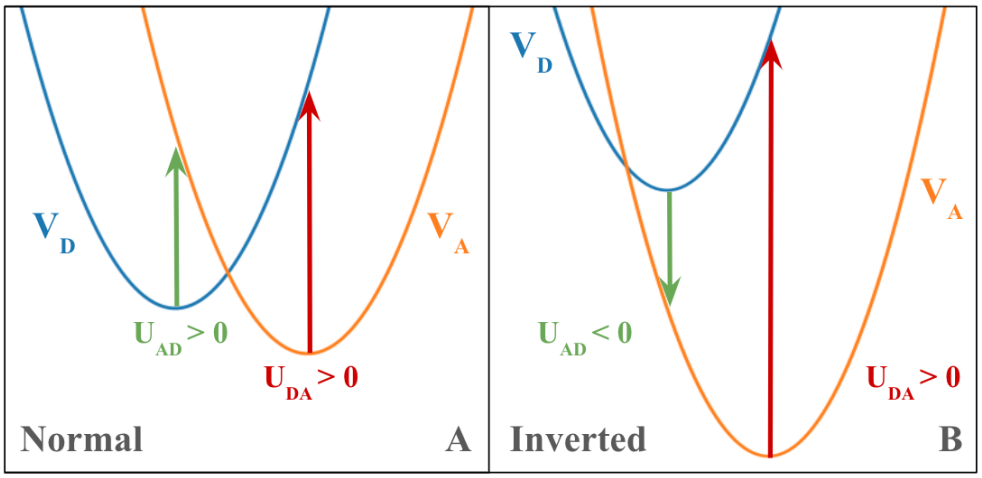


Figure 2.1: A schematic view of the GOA-type models A and B discussed in the text, which represent donor-to-acceptor downhill CT reactions in the normal and inverted regions, respectively. The donor (blue) and acceptor (orange) free energy surfaces along the primary mode coordinate, representing the solvation coordinate, are shown (note that the primary mode is coupled to a bath of secondary modes which are not shown in the figure). Also shown are the donor-to-acceptor (U_{AD}, green) and acceptor-to-donor (U_{DA}, red) vertical transition energies. It should be noted that U_{AD} is positive in the normal region and negative in the inverted region, while U_{DA} is positive in both regions.

Eq. (2.28) into Eq. (2.24), which yields:

$$\begin{aligned} k^0_{D\to A}(\pm\omega) &= \frac{1}{\hbar^2}V_{DA}^2\int_{-\infty}^{\infty} d\tau e^{-i(\langle U_{AD}\rangle_D/\hbar\mp\omega)\tau-\frac{1}{2}\sigma^2\tau^2/\hbar^2} \\ &= \frac{1}{\hbar^2}V_{DA}^2\sqrt{\frac{2\pi}{\sigma^2}}e^{-\frac{(\langle U_{AD}\rangle_D\mp\hbar\omega)^2}{2\sigma^2}} \end{aligned} \tag{2.31}$$

Given that the field frequency is positive, $\omega > 0$, we see that the field-induced enhancement is dominated by $k^0_{D\to A}(+\omega)$ in the normal region, since $\langle U_{AD}\rangle_D > 0$ in this case. In contrast, the field-induced enhancement is dominated by $k^0_{D\to A}(-\omega)$ in the inverted region, since $\langle U_{AD}\rangle_D < 0$ in this case. Thus,

$$k_{D\to A} = \begin{cases} k^0_{D\to A} + \left(\frac{\chi^0_{DA}}{V_{DA}}\right)^2 k^0_{D\to A}(\omega) & \text{normal region} \\ k^0_{D\to A} + \left(\frac{\chi^0_{DA}}{V_{DA}}\right)^2 k^0_{D\to A}(-\omega) & \text{inverted region} \end{cases} \tag{2.32}$$

Eq. (2.32) has a straightforward interpretation since $\left(\frac{\chi^0_{DA}}{V_{DA}}\right)^2 k^0_{D\to A}(\omega)$ and $\left(\frac{\chi^0_{DA}}{V_{DA}}\right)^2 k^0_{D\to A}(-\omega)$ can be shown to correspond to the equilibrium electronic absorption and emission spectra for a system that starts at equilibrium in the donor state and transitions to the acceptor state via either absorption (+) or stimulated emission (-) of light:

$$\begin{aligned}&\left(\frac{\chi^0_{DA}}{V_{DA}}\right)^2 k^0_{D\to A}(\pm\omega)\\&= \frac{1}{\hbar^2}(\chi^0_{DA})^2 \int_{-\infty}^{\infty} d\tau e^{\pm i\omega\tau} Tr_n\left[e^{i\hat{H}_D\tau/\hbar} e^{-i\hat{H}_A\tau/\hbar}\hat{\rho}^{eq}_{n,D}\right]\end{aligned} \tag{2.33}$$

As we have seen above, the radiative pathway is absorptive in the normal region and emissive in the inverted region. Thus, the equilibrium absorption and emission spectra correspond to the rate constants for field-induced transitions between the donor and acceptor electronic states in each of those regions.

Finally, it should be noted that the above discussion corresponds to the donor-to-acceptor reaction, which is assumed to be a *downhill* reaction (i.e. $\Delta E < 0$). The situation is somewhat different in the case of the inverse acceptor-to-donor *uphill* reaction. In this case, the vertical transition, $U_{AD}(\mathbf{R})$, needs to be replaced by $U_{DA}(\mathbf{R}) = V_D(\mathbf{R}) - V_A(\mathbf{R})$. Since, $\langle U_{DA}\rangle_A > 0$ for both normal and inverted regions, the radiative pathway for the inverse reaction is always absorptive (see Fig. 2.1).

2.3 Results and Discussion

In this section, we demonstrate the interplay between the non-radiative and radiative electronic CT pathways in the case of the Garg-Onuchic-Ambegaokar (GOA) model for CT in the condensed phase.[33] To this end, we present results obtained by simulating the CT dynamics based on the p-tcl-OD-QME for the GOA model in the presence of a CW driving field [see Eq. (2.21)].

Results based on three other variations of OD-QMEs, which utilize other projection su-

peroperators and/or involve time convolution are presented in Appendix A.1. The p-tcl-OD-QMEs were solved numerically using a fourth-order Runge-Kutta algorithm following the procedure outlined in Ref. 60. For solving the tcl-OD-QMEs shown in Eqs. (2.21) and (A.3), a Simpson's integration with fixed integration points, N_{points}, was used. For solving the tc-OD-QMEs, integration was performed via the Trapezoid rule with an adaptive number of integration points to accurately capture the memory effects of the system as tc-OD-QMEs involve an integral that is non-local in time. Additionally, a smaller timestep, δt, is required to achieve comparable accuracy to results obtained for tcl-OD-QMEs (see Appendix A.1). The choice to present only the results obtained via the p-tcl-OD-QME in the main text is motivated by the fact that the four types of OD-QMEs yield indistiguishable results for the model parameters under consideration, which were chosen to be consistent with typical CT reactions.

The p-tcl-OD-QME also emerges as the method of choice, because its computational cost is the lowest among the four OD-QMEs tested, and because it is the most straightforward to interpret (see Secs. 2.2.3 and 2.2.4).

The GOA model is based on the following Hamiltonian, which can be cast in the form of Eq. (2.1):

$$\begin{aligned}\hat{H}_{\mathrm{GOA}} = \Lambda\hat{\sigma}_x + \frac{\hbar\omega_{DA}}{2}\hat{\sigma}_z + \frac{\hat{P}_y^2}{2} + \frac{\Omega^2}{2}(\hat{y} + y_0\hat{\sigma}_z)^2 \\ + \sum_{j=1}^{N-1}\left[\frac{\hat{p}_j^2}{2} + \frac{\omega_j^2}{2}\left(\hat{x}_j + \frac{c_j\hat{y}}{\omega_j^2}\right)^2\right],\end{aligned} \tag{2.34}$$

Here, $\hat{\sigma}_x = |D\rangle\langle A| + |A\rangle\langle D|$ and $\hat{\sigma}_z = |D\rangle\langle D| - |A\rangle\langle A|$, where $|D\rangle$ and $|A\rangle$ are the donor and acceptor electronic states; $V_{DA} = \Lambda$ is the electronic coupling coefficient (constant within the Condon approximation); $\Delta E = -\hbar\omega_{DA}$ is the donor-to-acceptor CT reaction energy; $\hat{y}$, $\hat{P}_y$, and Ω are the mass-weighted primary mode coordinate, momentum, and frequency, respectively; $\{\hat{x}_j, \hat{p}_j, \omega_j | j = 1, ..., N-1\}$ are the mass-weighted coordinates, momenta and frequencies, respectively, of the secondary bath modes; $\{c_j | j = 1, ..., N-1\}$ are the coupling

Parameter	Description	Value (a.u.)	
		Model A	Model B
ω_{DA}	Energy difference	4.851×10^{-3}	4.292×10^{-2}
$\langle U_{AD}\rangle_D$	Vertical transition energy	1.903×10^{-2}	-1.903×10^{-2}
E_r	Reorganization energy	2.389×10^{-2}	
Λ	Electronic coupling coefficient	3.674×10^{-4}	
T	Temperature	300 (K)	
Ω	Primary mode frequency	3.507×10^{-4}	
y_0	Primary mode coordinate	3.116×10^{2}	
N	Number of bath modes	101	
ω_c	Cutoff frequency	3.507×10^{-4}	
η	Friction constant	1.066×10^{6}	

Table 2.1: Parameters of the GOA Model

coefficients between the secondary modes and the primary mode; $2y_0$ is the shift in equilibrium geometry of the primary mode between the donor and acceptor states, such that the reorganization energy is given by $E_r = 2\Omega^2 y_0^2$.

The GOA model also assumes that the secondary bath modes can be described by an Ohmic spectral density with exponential cutoff:

$$J(\omega) = \frac{\pi}{2}\sum_{j=1}^{N-1}\frac{c_j^2}{\omega_j}\delta(\omega-\omega_j) = \eta\omega e^{-\omega/\omega_c} \quad . \tag{2.35}$$

Here, η is the friction coefficient, which determines the coupling strength between the primary and secondary modes, and ω_c is the cutoff frequency. The values of the parameters used to obtain the results reported below are given in Table 2.1.

The form of the Hamiltonian in Eq. (2.34) requires representing the continuous spectral density in Eq. (2.35) in terms of a set of discrete secondary bath modes. To this end, we follow the procedure outlined in Refs. 72 and 21, with the number of secondary modes set to $N-1=100$.

The fact that the primary and secondary modes are bilineraly coupled implies that the nuclear coordinates can be cast in terms of the corresponding normal modes instead of in terms of the primary mode and secondary modes.[127,128] Doing so leads to the following

expressions for $\hat{H}_D$, $\hat{H}_A$ and $\hat{V}_{DA}(t)$ in Eq. (2.4):

$$\begin{aligned}
\hat{H}_D &= \hbar\omega_{DA} + \sum_{n=1}^{N}\left[\frac{1}{2}\hat{P}_n^2 + \frac{1}{2}\tilde{\omega}_n^2\tilde{q}_n^2\right], \\
\hat{H}_A &= \sum_{n=1}^{N}\left[\frac{1}{2}\hat{P}_n^2 + \frac{1}{2}\tilde{\omega}_n^2(\tilde{q}_n - R_n^{eq})^2\right], \\
\hat{V}_{DA}(t) &= V_{DA}(t) = \Lambda + \chi_{DA}^0(e^{i\omega t} + e^{-i\omega t}).
\end{aligned} \tag{2.36}$$

Here, $\{\tilde{q}_n, \hat{P}_n, \tilde{\omega}_n | n = 1, ..., N\}$ are the normal mode coordinates, momenta, and frequencies, and $\{R_n^{eq} | n = 1, ..., N\}$ are the equilibrium donor-to-acceptor shifts in the equilibrium geometry along the normal mode coordinates. The system is assumed to start at the donor state with the nuclear DOF in thermal equilibrium on the donor PES, such that $\hat{\rho}(0) = \hat{\rho}_D^{eq} \otimes |D\rangle\langle D|$, where $\hat{\rho}_D^{eq} = e^{-\beta\hat{H}_D}/Tr_n[e^{-\beta\hat{H}_D}]$.

Finally, we note that the quantum-mechanically exact $C_{D\to A}^0(\tau)$ can be obtained in closed form for the GOA model, and is given by:[60,91,83]

$$\begin{aligned}
C_{D\to A}^0(\tau) = \Lambda^2 e^{i\omega_{DA}(t-\tau)} & \\
\times \exp\Bigg\{ \sum_n \frac{\tilde{\omega}_n (R_n^{eq})^2}{2\hbar} \coth(\frac{1}{2}\beta\hbar\tilde{\omega}_n) & \\
\times [\cos(\tilde{\omega}_n(t-\tau)) - 1] \Bigg\} & \\
\times \exp\Bigg\{ -i \sum_n \frac{\tilde{\omega}_n (R_n^{eq})^2}{2\hbar} \sin(\tilde{\omega}_n(t-\tau)) \Bigg\}, &
\end{aligned} \tag{2.37}$$

We start by considering two GOA-type models, denoted A and B (see Table 2.1). The two models are identical, except for the value of $\hbar\omega_{DA} \equiv -\Delta E$. More specifically, both models have the same reorganization energy, $E_r = 650$meV, and electronic coupling, $\Lambda \equiv V_{DA} = 10$meV, which are within the range of typical values for CT reactions. Furthermore, the rates for both models are calculated at room temperature ($T = 300$K), which is also typical. The models vary with respect to the reaction energy. For model A, $\hbar\omega_{DA} \equiv -\Delta E = 132$meV,

which puts it in the normal region, while for model B, $\hbar\omega_{DA} \equiv -\Delta E = 1168$meV, which puts it in the inverted region. Importantly, those parameters are chosen so that the activation energy for the donor-to-acceptor reaction is the same for both models, and given by $E_a \equiv \frac{(\Delta E+E_r)^2}{4E_r} = 4k_BT = 102.8$meV. These choices guarantee that the donor-to-acceptor reaction is downhill for both models, with the same field-free Marcus theory rate constant (since the activation energy is the same). Finally, the donor-to-acceptor vertical transition energy for both models is defined by $\langle U_{AD}\rangle_D = \Delta E + E_r$ [see Eq. (2.30)]. We also define the vertical transition frequency as $\omega_v = \langle U_{AD}\rangle_D/\hbar$. Importantly, the magnitude of the vertical transition energy is the same for models A and B, $|\langle U_{AD}\rangle_D| = 518$meV. However, while $\langle U_{AD}\rangle_D = 518$meV is positive for model A, it is negative for model B, $\langle U_{AD}\rangle_D = -518$meV (see Fig. 2.1). This implies that the field-induced CT pathway is absorptive in the case of model A (normal region), and emissive in the case of model B (inverted region).

The effect of the driving field's intensity and frequency on the CT dynamics within models A and B, which was simulated based on p-tcl-OD-QME, Eq. (2.21), is shown in the top and bottom panels of Fig. 2.2, respectively. To this end, we show the difference between the populations of the donor and acceptor states, $\langle\hat{\sigma}_z\rangle = \langle D|\hat{\sigma}|D\rangle - \langle A|\hat{\sigma}|A\rangle$ as a function of time for different combinations of $\chi^0_{DA}/\Lambda = \{0.1, 0.5, 1.0, 2.0\}$ and $\omega/|\omega_v| = \{0.1, 0.5, 1.0, 2.0\}$.

As expected, the driving field is seen to enhance the charge-transfer rate (solid lines in Fig. 2.2) in comparison to the field-free case (dashed lines in Fig. 2.2). The rate enhancement is seen to increase with the field intensity, as well as with proximity to resonance between the driving field frequency, ω, and the vertical transition frequency $\omega_v = |\langle U_{AD}\rangle_D|/\hbar$. The CT dynamics is also seen to follow rate kinetics in both field-free and field-driven cases, which implies that the time scale of CT in models A and B is much slower than the lifetime of $C^0_{D\to A}(\tau)$ and $C^0_{A\to D}(\tau)$. Thus, the CT dynamics in models A and B is well described by the E-GFR [see Eq. (2.25)]. Finally, the fact that the CT dynamics in models A and B are indistinguishable in both the field-free and field-driven cases can be traced back to the fact that for those model parameters, the dynamics is well described by the Marcus limit [see Eq.

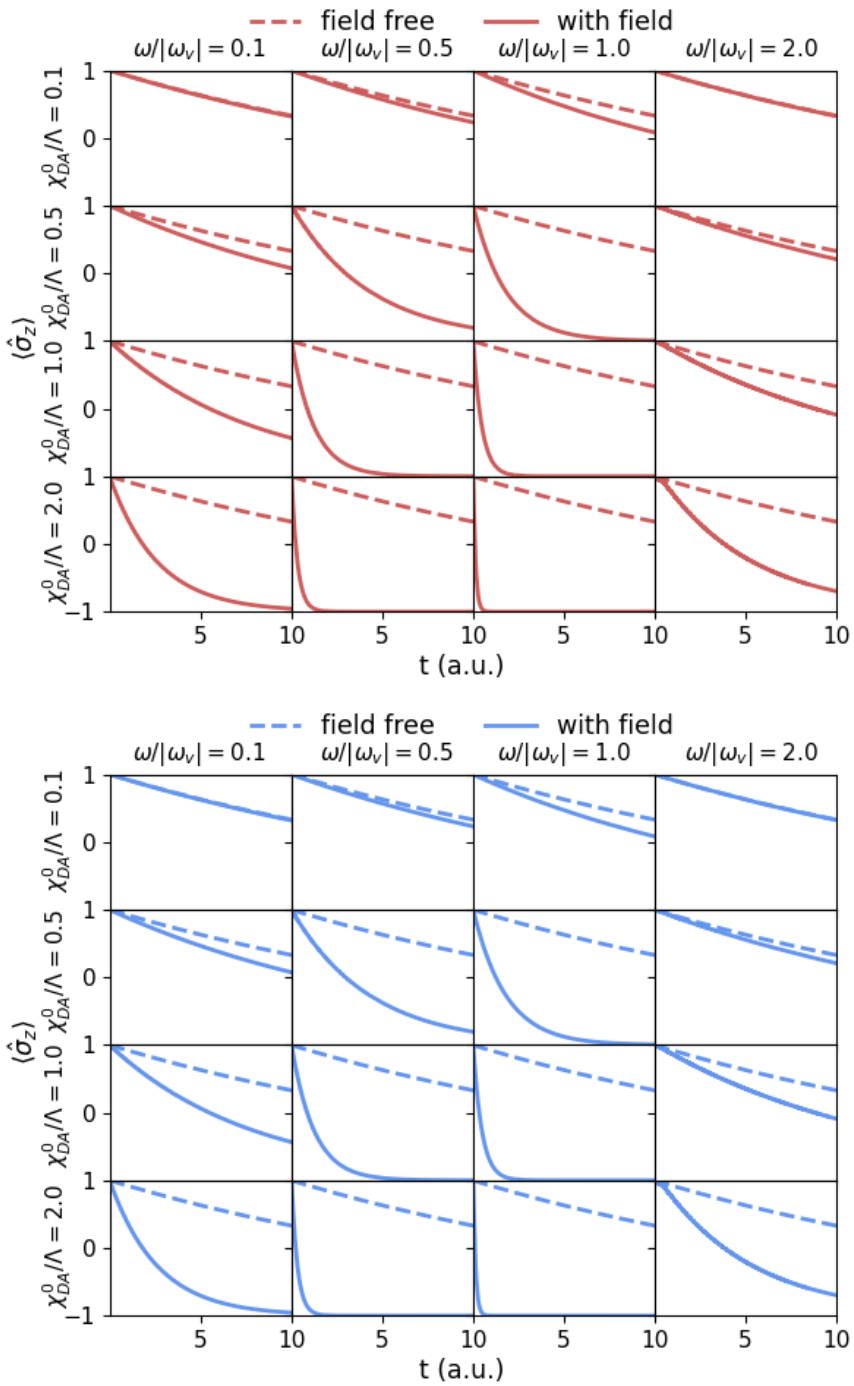


Figure 2.2: The effect of the driving field's intensity and frequency on the CT dynamics within models A (top panel) and B (bottom panel), which was simulated at $T = 300$K based on p-tcl-OD-QME, Eq. (2.21). The difference between the populations of the donor and acceptor states, $\langle\hat{\sigma}_z\rangle = \langle D|\hat{\sigma}|D\rangle - \langle A|\hat{\sigma}|A\rangle$ is plotted as a function of time for different combinations of $\chi^0_{DA}/\Lambda = \{0.1, 0.5, 1.0, 2.0\}$ and $\omega/|\omega_v| = \{0.1, 0.5, 1.0, 2.0\}$.

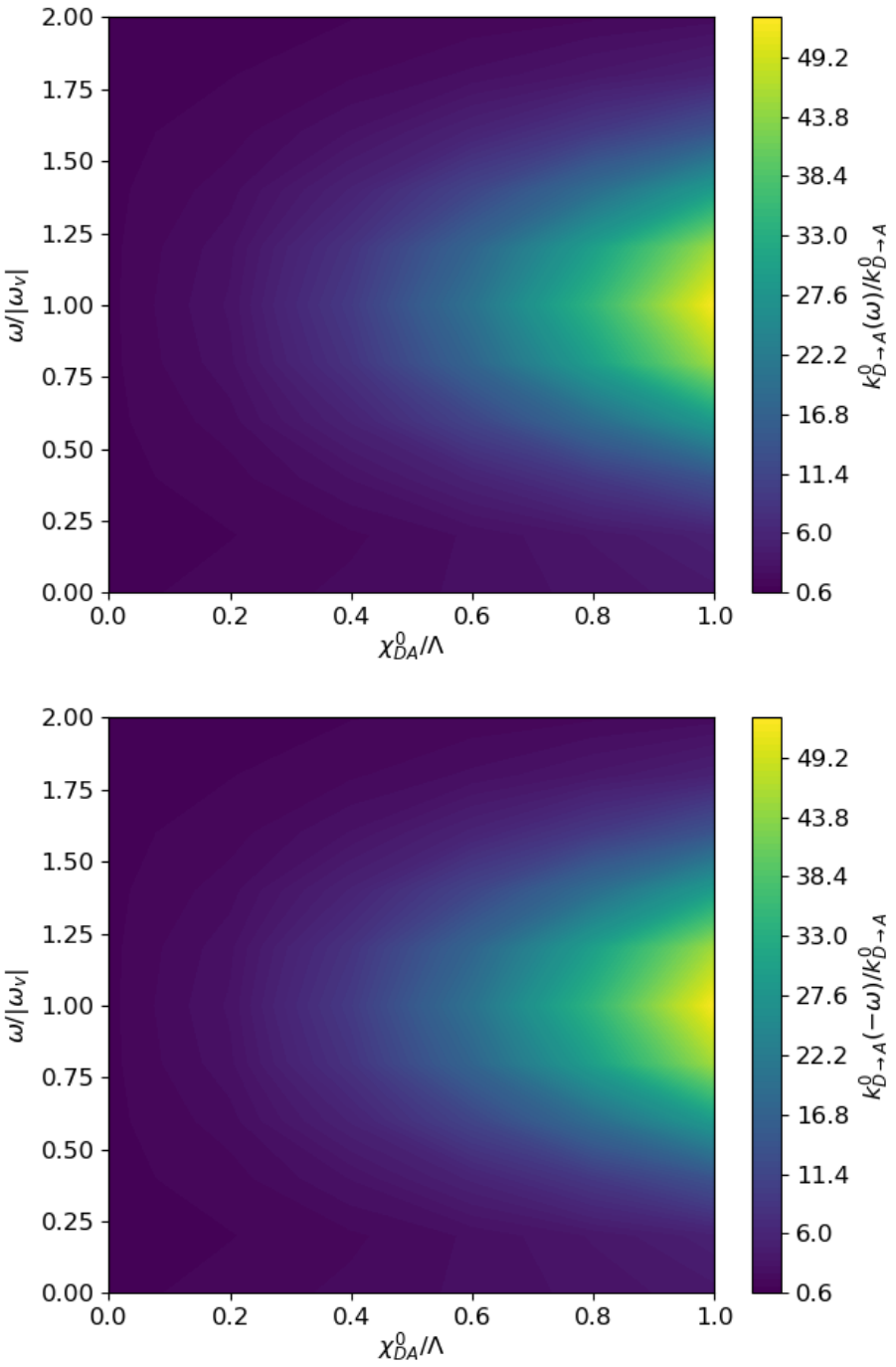


Figure 2.3: The donor-to-acceptor E-FGR rate constant as a function of the driving field's amplitude (measured by χ^0_{DA}/Λ) and frequency (measured by $\omega/|\omega_v|$) for models A (top panel) and B (bottom panel).

(2.31)]. This is because the field-free CT rate constant is dictated by the activation energy in this case, which is the same for models A and B. However, it should be noted that the

mechanism underlying the field-induced enhancement of the CT rate is different [absorptive for model A (normal region) and emissive for model B (inverted region), see Fig. 2.1].

The above analysis implies that the effect of the driving field on the CT dynamics can be described by the dependence of the E-FGR rate constants on the intensity and frequency of the driving field. This dependence for models A and B is shown in the top and bottom panels of Fig. 2.3, respectively. The results in Fig. 2.3 are consistent with those in Fig. 2.2. More specifically, the E-FGR rate constant is seen to increase with field intensity, as well as with proximity to resonance between the field frequency and vertical transition frequency. Also, the fact that the top and bottom panels of Fig. 2.3 are practically indistinguishable can be traced back to the fact that for those model parameters, the dynamics is well described by the Marcus limit, where the CT rate constant is dictated by the activation energy, which is the same for models A and B [see Eq. (2.31)].

Further insight can be gained by plotting the E-FGR and Marcus donor-to-acceptor rate constants as a function of ΔE for the same value of E_r as in models A and B, $E_r = 650$meV (see Fig. 2.4). In the field-free case, this plot shows the characteristic Marcus turnover inverted parabolic behavior (on a semi-log plot). The fact that the E-FGR and its Marcus limit coincide over the range of ΔE under consideration is testimony to the validity of the Marcus limit. Adding a driving field which is in resonance with the vertical transition energy leads to enhancement of the rate constant in comparison to the field-free case and a flattening of of the turnover curve. This can be traced back to the fact that the resonant field-induced enhancement is independent of $\langle U_{AD} \rangle_D = \Delta E + E_r$. Thus, the larger χ^0_{DA}/Λ, the bigger the contribution of the field-induced CT pathway and the flatter the Marcus curve. Importantly, the E-FGR and Marcus limit still coincide in the presence of the field, as predicted by Eq. (2.31).

Finally, we consider the effect of temperature on the field-induced enhancement of the CT rate. In Fig. 2.5, we compare the effect of the driving field's intensity and frequency on the CT dynamics within models A and B at two different temperatures, 300K and 77K. The

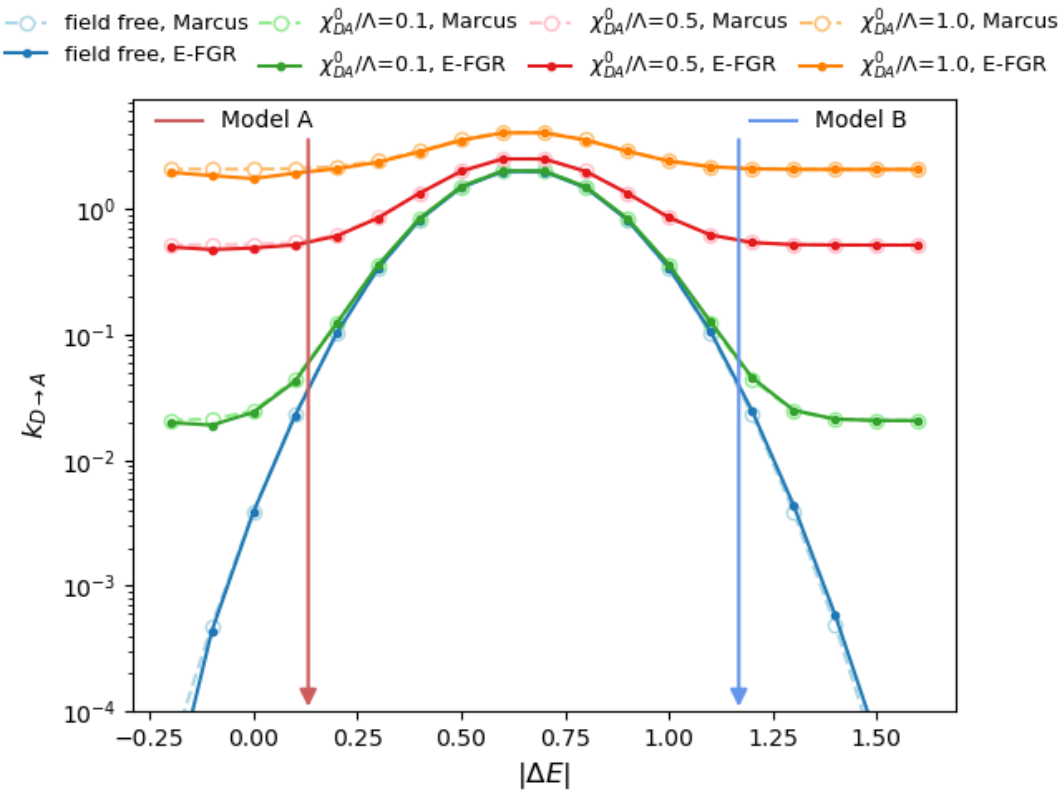


Figure 2.4: A semi-log plot of the E-FGR (solid lines and full circles) and Marcus (dashed line and blank circles) donor-to-acceptor CT rate constants as a function of $|\Delta E|$, for different driving field amplitudes (measured by χ^0_{DA}/Λ). The results in this plot were obtained for $E_r = 650$meV and $\Lambda = 10$meV, and the field frequencies, ω are in resonance with the vertical transition frequencies, ω_v. Vertical lines indicate the values of $|\Delta E|$ that correspond to models A (red) and B (blue).

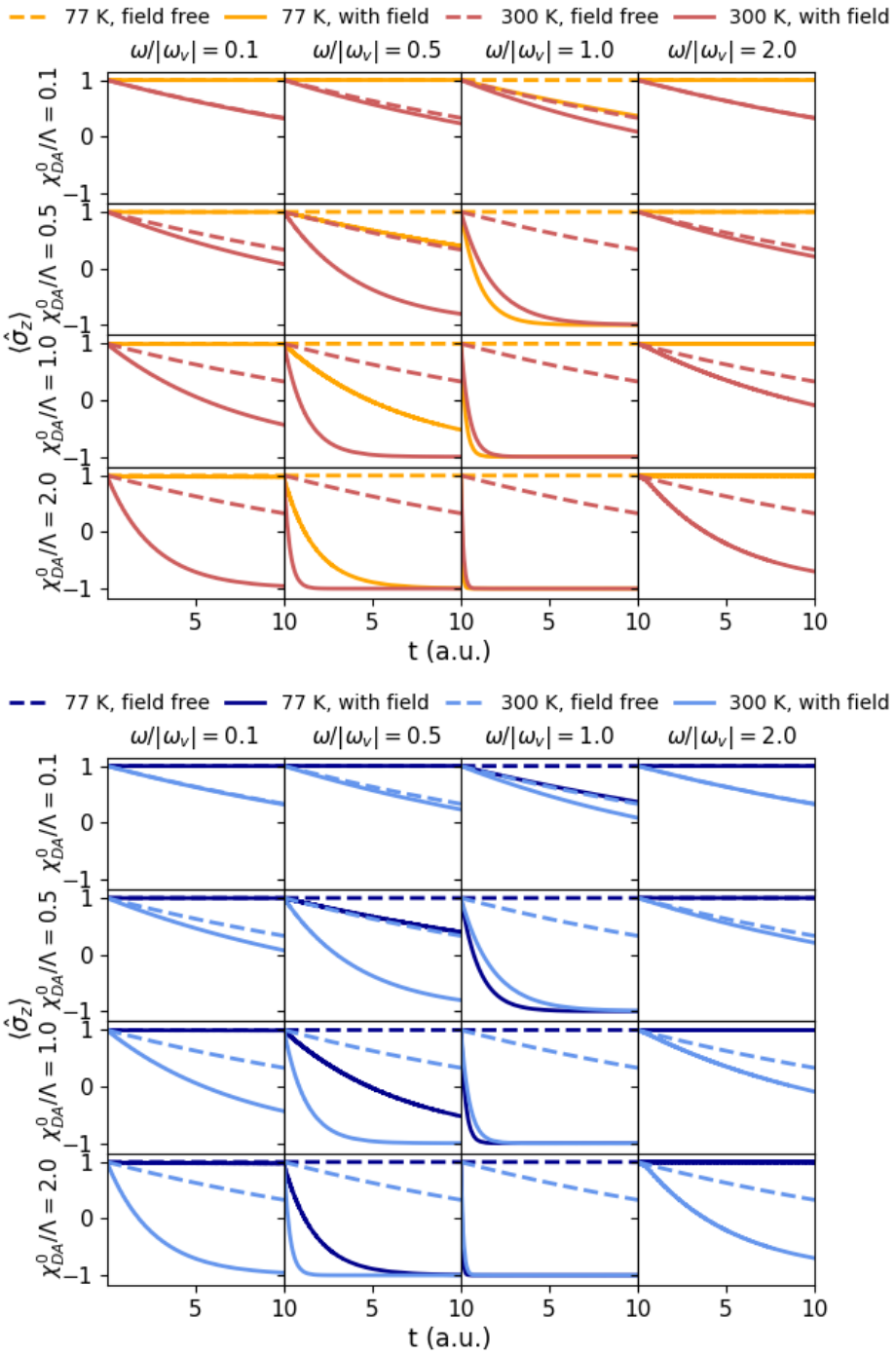


Figure 2.5: The effect of temperature on the field-free and field-driven CT dynamics. The figure is formatted similarly to Fig. 2.2, with results shown at $T = 300$K (light blue) and $T = 77$K (dark blue).

off-resonance CT dynamics at 77K is slower than that at 300K, which can be traced back to the fact that the non-radiative pathway is activated, and therefore faster with increasing temperature. In contrast, at resonance, the CT dynamics at 77K is observed to become faster than that at 300K. This behavior can be traced back to the fact that the absorption line-shape at 77K is narrower than that at 300K, which in turn gives rise to a sharper resonance.

2.4 Summary and Concluding Remarks

Marcus' theory is based on the key insight that, within the nonadiabatic regime, solution-phase CT reactions that occur in the dark are facilitated by spontaneous, yet rare, solvent fluctuations, which are necessary for achieving resonance between the donor and acceptor states and therefore satisfying energy conservation.[74] This is because the much higher energetic cost for direct electron transfer via a vertical transition when the solvent configuration corresponds to equilibrium at the donor state makes it highly unfavorable in comparison. However, this is not the case when the electronic coupling term is allowed to become time-dependent, e.g. by driving the donor-to-acceptor transition with a CW laser field. In such a case, the radiative vertical-transition-induced pathway can become competitive with the non-radiative solvent-fluctuations-induced pathway. Importantly, this is the case even if the light-matter interaction is weak, provided that the laser frequency is in resonance with the vertical transition between the donor and acceptor states.

In this chapter, we have shown how OD-QMEs offer a straightforward and yet general-purpose strategy for incorporating the possibility of time-dependent electronic coupling terms into the rate theory of CT reactions. This is because time-dependent perturbation theory calls for working in the interaction picture, where the interaction term becomes time-dependent regardless of whether or not it was time-dependent in the Schrödinger picture. The difference compared to the case of time-independent electronic coupling is that the time dependence of the interaction Hamiltonian in the interaction picture now has two sources: (1)

An explicit time dependence in the Schrödinger picture, and (2) An implicit time dependence due to the transformation to the interaction picture.

While the OD-QMEs can account for non-equilibrium and non-time-local effects, it can be shown to asymptotically coincide with rate kinetics governed by E-FGR rate constants, or Marcus theory rate constants. In this limit, the results presented in this paper can also be thought of as the classical limit of the recently reported E-FGR-based cavity-enhanced CT rate theory.[106]

A distinct advantage of the radiative electronic coupling term over the non-radiative one, is that the radiative coupling term is switchable and programmable. This suggests new ways of controlling CT rates and pathways by applying a sequence of pulses with amplitudes, lengths, leading frequencies and inter-pulse intervals of one's choice. Another advantage of the OD-QME-based formulation outlined in this chapter is that it is generalizable for systems with more than two states.

CHAPTER 3

Memory Kernel Non-Additivity in the GQME for a System Coupled to Multiple Heat Baths[1]

3.1 Introduction

Open quantum system dynamics is often modeled based on the assumption that the system is coupled to a single bath at thermal equilibrium with respect to a single well-defined temperature.[102,4,99,151,113,13] However, real systems often interact simultaneously with multiple baths composed of different subsets of degrees of freedom, each characterized by distinct thermodynamic conditions such as temperature or chemical potential, thereby driving the system out of equilibrium. Such situations arise, for example, in molecular junctions, quantum thermal transport setups, nanoscale heat engines, and driven condensed-phase systems.[36,37,123,28,27,111,110,104,109,75,30,7,8,65,34,20,89] The presence of multiple nonequilibrated environments raises a fundamental question: is the cumulative effect of the baths on the

[1]This work was conducted in collaboration with Dr. Xiaohan Dan, Professor Victor S. Batista, and Professor Eitan Geva.

This chapter is based on the following manuscript submitted for publication:

Callie Wilson[†]; Xiaohan Dan[†]; Victor S. Batista; Eitan Geva. Memory kernel non-additivity in the generalized quantum master equation for a system coupled to multiple heat baths. Submitted to *J. Chem. Phys.* (2026).

[†]These authors contributed equally to this work.

Callie Wilson developed the theoretical analysis, implemented the generalized quantum master equation and Redfield quantum master equation numerical frameworks, performed the simulations, analyzed and interpreted the results, prepared the figures, and wrote the initial manuscript. Dr. Xiaohan Dan performed the hierarchical equations of motion (HEOM) calculations used to generate the exact benchmark results and projection-free inputs for Models 1–6, and contributed to the interpretation of the results and manuscript preparation. Professors Victor S. Batista and Eitan Geva supervised the research, contributed to the interpretation of the results, and provided guidance and editorial feedback during manuscript preparation.

system dynamics equal to the sum of the effects that each bath would exert in isolation?

At the limit of weak system-bath coupling, the answer is yes. Specifically, when the system-bath coupling terms are treated as small perturbations within the framework of second-order time-dependent perturbation theory, the bath-induced contribution to the reduced dynamics is expressed in terms of equilibrium bath correlation functions of the individual baths.[102,4,151,99,13,113]

As a result, the second-order memory kernel separates into a sum of independent bath contributions, as discussed in Sec. 3.2.4. This additivity underlies standard weak-coupling quantum master equations, where relaxation rates can be written as sums of bath-resolved terms.

Beyond weak system-bath coupling, this additive structure no longer holds. Even when the baths are initially independent and there is no direct bath-bath interaction, the baths can become dynamically correlated through their mutual interaction with the system. Consequently, the effect of one bath on the system may depend on whether the other bath is also present. Deviations from additivity therefore provide a direct probe of bath-bath correlations generated indirectly through the system, as discussed in Sec. 3.2.3.

Additivity of the bath-induced impact on the system, or lack thereof, is also closely connected to the definition of heat flows between the system and the baths, which is important for understanding heat formation and distribution in quantum devices and molecular junctions.[36,37,6,10,123,28,27,111,110,104,109,75,30,89] In classical thermodynamics,[16] the heat flow between a system and multiple baths is assumed to be additive. For example, in the case of a system coupled to two heat baths, hot and cold, the rate of change of the system energy is assumed to be given by

$$\dot{U} = \dot{Q}_h + \dot{Q}_c \quad , \tag{3.1}$$

where U is the system energy, $\dot{Q}_h$ is the heat flux associated with the hot bath, and $\dot{Q}_c$ is the heat flux associated with the cold bath. In such an additive description, $\dot{Q}_h$ is assumed to be the same as it would have been in the absence of the cold bath, and $\dot{Q}_c$ is assumed to

be the same as it would have been in the absence of the hot bath. This decomposition is natural for macroscopic systems, where the interaction between the system and each bath occurs at the interface at the point of contact and is therefore weak compared with the bulk energies. For microscopic quantum systems strongly coupled to baths, however, the system-bath interaction energy can become comparable to the system energy, and a unique bath-resolved decomposition of heat flow is no longer obvious.

In this paper, we examine the additivity of bath-induced effects from the point of view of the generalized quantum master equation (GQME). The GQME provides an *exact* equation of motion for the reduced density operator of a quantum system coupled to one or more baths.[90,150,113,118,146,48,24,142,25,23,51,55,97,82,50,52,54,98,88,84,87,85,14,5,28,141,70,73,95] It is inherently non-Markovian and non-unitary, and can accommodate multiple baths that may or may not be in thermal equilibrium internally or relative to the other baths.

Within the GQME, all bath-induced effects are encoded in a memory kernel superoperator, $\mathcal{K}(t)$. Thus, for a system coupled to multiple baths, the question of additivity becomes the question of whether the exact multi-bath memory kernel can be decomposed into a sum of exact single-bath memory kernels. For example, in the case of a system coupled to two baths, hot and cold, this question can be written as

$$\mathcal{K}(t) \stackrel{?}{=} \mathcal{K}_h(t) + \mathcal{K}_c(t) \ , \tag{3.2}$$

where $\mathcal{K}(t)$ is the exact memory kernel for the system coupled simultaneously to both baths, while $\mathcal{K}_h(t)$ and $\mathcal{K}_c(t)$ are the exact memory kernels for the corresponding hot (h) and cold (c) single-bath problems, respectively. This comparison is stronger than simply testing the validity of the weak-coupling approximation: it asks whether the exact influence of two independent baths is equivalent to the sum of two exact one-bath influences.

We show that Eq. (3.2) holds in the weak system-bath coupling limit, but fails at stronger

coupling. The non-additive component,

$$\Delta\mathcal{K}(t) = \mathcal{K}(t) - \mathcal{K}_h(t) - \mathcal{K}_c(t) \ , \tag{3.3}$$

therefore quantifies the collective effect of coupling the system to both baths simultaneously. Importantly, this non-additivity is not uniform across the memory kernel. Different matrix elements of $\mathcal{K}(t)$ describe different bath-induced dynamical processes, including phase damping, population-to-coherence transfer, coherence-to-population transfer, and coherence-to-coherence transfer. As a result, the degree of non-additivity can depend on the specific process through which the baths affect the system dynamics.

We demonstrate these ideas for a two-level system linearly coupled to two harmonic baths held at different temperatures. The model is simple enough to allow a transparent analysis, but rich enough to exhibit non-Markovian dynamics, strong system-bath coupling effects, and nonequilibrium heat transport. The quantum-mechanically exact memory kernels are calculated via the hierarchical equations of motion (HEOM) method,[134,135,133,112] which allows us to compare the exact two-bath memory kernel directly with the sum of the exact one-bath memory kernels.

The results reveal three main trends. First, the GQME with the exact multi-bath memory kernel reproduces the exact HEOM dynamics, while the additive approximation $\mathcal{K}_h(t)+\mathcal{K}_c(t)$ becomes increasingly inaccurate as the system-bath coupling strength increases. Second, the breakdown of additivity is process dependent: the phase-damping-related kernel element remains comparatively well described by an additive form, whereas population-coherence and coherence-coherence transfer show pronounced non-additive behavior. Third, the non-additivity of the memory kernel sheds new light on why decomposing the system-energy change into independent bath-resolved heat currents becomes ambiguous beyond weak coupling. Bath-resolved currents can still be introduced by specifying how the system-bath interaction energy is assigned. As a result, such current decompositions are convention de-

pendent and cannot be uniquely inferred from the exact reduced system dynamics alone.[123]

The remainder of this chapter is organized as follows. The GQME formalism for a system coupled to multiple baths is outlined and discussed in Sec. 3.2, with emphasis on the additivity of the memory kernel, or lack thereof. A demonstrative application to a model of a two-level system linearly coupled to hot and cold harmonic baths is provided in Sec. 3.3. Finally, concluding remarks are presented in Sec. 3.4.

3.2 Theory

3.2.1 Preliminary Considerations

We consider a system coupled to multiple baths, described by the Hamiltonian

$$\hat{H} = \hat{H}_s + \hat{H}_b + \hat{H}_{bs} \quad , \tag{3.4}$$

where $\hat{H}_s$ is the system Hamiltonian, $\hat{H}_b$ is the multiple baths Hamiltonian, and $\hat{H}_{bs}$ represents the interaction between the system and the baths.

For the sake of simplicity, we focus on the case of two heat baths at different temperatures (hot and cold), noting that all conclusions can be straightforwardly generalized to an arbitrary number of baths:

$$\hat{H}_b = \hat{H}_h + \hat{H}_c \quad . \tag{3.5}$$

Here, $\hat{H}_h$ is the hot bath Hamiltonian and $\hat{H}_c$ is the cold bath Hamiltonian (each defined as a Hermitian operator in its own Hilbert space). The system-bath interactions can, without loss of generality, be expressed as a sum of tensor products of system and bath operators:

$$\hat{H}_{bs} = \hat{H}_{sh} + \hat{H}_{sc} = \sum_j \hat{B}_{hj} \otimes \hat{S}_j + \sum_j \hat{B}_{cj} \otimes \hat{S}_j. \tag{3.6}$$

Here, $\{\hat{S}_j\}$ are system operators, $\{\hat{B}_{hj}\}$ are hot bath operators and $\{\hat{B}_{cj}\}$ are cold bath

operators (the explicit forms of these operators is system-specific, and will be specified in Sec. 3.3 for the demonstrative model under consideration).

In what follows, we will also assume, without loss of generality, that

$$\mathrm{Tr}_h\left(\hat{\rho}_h^{eq}\hat{H}_{sh}\right) = \mathrm{Tr}_c\left(\hat{\rho}_c^{eq}\hat{H}_{sc}\right) = 0. \tag{3.7}$$

Here, Tr_h is the partial trace over the hot bath Hilbert space, Tr_c is the partial trace over the cold bath Hilbert space, and $\hat{\rho}_h^{eq}$ and $\hat{\rho}_c^{eq}$ are the density operators that correspond to the hot and cold baths being in thermal equilibrium:

$$\hat{\rho}_h^{eq} = \frac{e^{-\beta_h\hat{H}_h}}{Z_h} \quad ; \quad \hat{\rho}_c^{eq} = \frac{e^{-\beta_c\hat{H}_c}}{Z_c} \ , \tag{3.8}$$

where $\beta_h = 1/k_B T_h$ is the inverse temperature of the hot bath (k_B is the Boltzmann's constant), $\beta_c = 1/k_B T_c$ is the inverse temperature of the cold bath, $Z_h = \mathrm{Tr}_h(e^{-\beta_h\hat{H}_h})$ is the partition function of the hot bath and $Z_c = \mathrm{Tr}_c(e^{-\beta_c\hat{H}_c})$ is the partition function of the cold bath. The reason for why Eq. (3.7) is valid without loss of generality is because one can always make it valid by redefining the system-bath coupling and system Hamiltonians such that

$$\begin{aligned}
\hat{H}_{sh} &\rightarrow \hat{H}_{sh} - \mathrm{Tr}_h\left(\hat{\rho}_h^{eq}\hat{H}_{sh}\right) \ , \\
\hat{H}_{sc} &\rightarrow \hat{H}_{sc} - \mathrm{Tr}_c\left(\hat{\rho}_c^{eq}\hat{H}_{sc}\right) \ , \\
\hat{H}_{s} &\rightarrow \hat{H}_{s} + \mathrm{Tr}_h\left(\hat{\rho}_h^{eq}\hat{H}_{sh}\right) + \mathrm{Tr}_c\left(\hat{\rho}_c^{eq}\hat{H}_{sc}\right) \ .
\end{aligned} \tag{3.9}$$

Finally, we assume that the initial state of the overall system is given by a density operator of the following form:

$$\hat{\rho}(0) = \hat{\rho}_h^{eq} \otimes \hat{\rho}_c^{eq} \otimes \hat{\sigma}(0) \tag{3.10}$$

Here, $\hat{\rho}_h^{eq}$ and $\hat{\rho}_c^{eq}$ are defined as in Eq. (3.8), and $\hat{\sigma}(0)$ is the reduced density operator that

describes the initial state of the system. Note that the system and baths are assumed to start out unentangled, with the baths in thermal equilibrium at their respective temperatures. Even though this is a commonly used form of the initial state, other choices are possible. Importantly, our approach is not limited to this form and can be straightforwardly extended to other choices of initial state, including ones where the baths are initially in nonequilibrium states and entangled with the system.

It should be noted that the multiple-bath Hamiltonian in Eq. (3.4) can alternatively be viewed as a *system coupled to a single composite bath*. However, this composite bath possesses a specific structure: (1) it consists of two distinct sub-baths that are not in mutual thermal equilibrium, although each sub-bath is individually thermalized at its own temperature. (2) The system–bath interaction is given by a sum of couplings to the individual sub-baths and does not include terms of the form $\hat{S} \otimes \hat{B}_h \otimes \hat{B}_c$, which could directly couple the sub-baths.

3.2.2 The Generalized Quantum Master Equation (GQME)

Next, we outline the formalism underlying the GQME, with emphasis on its application to a system with the Hamiltonian of the form of Eq. (3.4). Since the overall system is closed, the dynamics of the overall system density operator $\hat{\rho}(t)$ is governed by the quantum Liouville equation:

$$\frac{d}{dt}\hat{\rho}(t) = -\frac{i}{\hbar}[\hat{H}, \hat{\rho}(t)] \equiv -\frac{i}{\hbar}\mathcal{L}\hat{\rho}(t) \tag{3.11}$$

In the next step, we define a projection superoperator $\mathcal{P}$ (an operator in the overall system's Liouville space), which satisfies $\mathcal{P}^2 = \mathcal{P}$. The equation of motion for the projection of $\hat{\rho}(t)$, $\mathcal{P}\hat{\rho}(t)$, is then given by the *Nakajima-Zwanzig equation*:[90,150]

$$\begin{aligned}\frac{d}{dt}\mathcal{P}\hat{\rho(t)} = &-\frac{i}{\hbar}\mathcal{P}\mathcal{L}\mathcal{P}\hat{\rho}(t) \\ &- \frac{1}{\hbar^2}\int_0^t d\tau \mathcal{P}\mathcal{L}e^{-i\mathcal{Q}\mathcal{L}\tau/\hbar}\mathcal{Q}\mathcal{L}\mathcal{P}\hat{\rho}(t-\tau) \\ &- \frac{i}{\hbar}\mathcal{P}\mathcal{L}e^{-i\mathcal{Q}\mathcal{L}t/\hbar}\mathcal{Q}\hat{\rho}(0) \quad ,\end{aligned} \tag{3.12}$$

where $\mathcal{Q}$ is the complementary projection operator defined by

$$\mathcal{Q} = \mathcal{I} - \mathcal{P} \quad , \tag{3.13}$$

where $\mathcal{I}$ is the unity superoperator in the overall system Liouville space.

The specific choice of projection operator $\mathcal{P}$ is dictated by the choice of *dynamical quantity of interest*. In what follows, we will focus on a commonly used choice of dynamical quantity of interest, which corresponds to the reduced density operator that describes the state of the system at time t:

$$\hat{\sigma}(t) = \mathrm{Tr}_b \left[\hat{\rho}(t)\right] \quad . \tag{3.14}$$

Here, $\mathrm{Tr}_b = \mathrm{Tr}_h \mathrm{Tr}_c$ (the partial trace over the Hilbert spaces of both baths) and $\hat{\rho}(t) = e^{-i\hat{H}t/\hbar}\hat{\rho}(0)e^{i\hat{H}t/\hbar} = e^{-i\mathcal{L}t/\hbar}\hat{\rho}(0)$.

Obtaining the equation of motion for $\hat{\sigma}(t)$ from Eq. (3.12) is facilitated by the following choice of projection operator:

$$\mathcal{P}\hat{A} = \hat{\rho}_h^{eq} \otimes \hat{\rho}_c^{eq} \otimes \mathrm{Tr}_b(\hat{A}) \tag{3.15}$$

Here, $\hat{\rho}_h^{eq}$ and $\hat{\rho}_c^{eq}$ are as in Eq. (3.8) and $\hat{A}$ is an overall system operator. Substituting $\mathcal{P}$ from Eq. (3.15) into Eq. (3.12) and partially tracing over the Hilbert spaces of both baths, we obtain:[113]

$$\frac{d}{dt}\hat{\sigma}(t) = -\frac{i}{\hbar}\mathcal{L}_s\hat{\sigma}(t) - \int_0^t d\tau \mathcal{K}(\tau)\hat{\sigma}(t-\tau) \quad . \tag{3.16}$$

Here, $\mathcal{L}_s\hat{\sigma}(t) \equiv [\hat{H}_s, \hat{\sigma}(t)]$ and $\mathcal{K}(\tau)$ is the memory kernel superoperator, which is explicitly given by:

$$\mathcal{K}(\tau) = \frac{1}{\hbar^2}\mathrm{Tr}_b\left\{\mathcal{L}e^{-i\mathcal{Q}\mathcal{L}\tau/\hbar}\mathcal{Q}\mathcal{L}\hat{\rho}_h^{eq} \otimes \hat{\rho}_c^{eq}\right\} \tag{3.17}$$

It should be noted that Eq. (3.16) is the *quantum-mechanically exact equation of motion*

for $\hat{\sigma}(t)$. In what follows, we will refer to Eq. (3.16) as the *GQME*. Importantly, other types of commonly used quantum master equations, such as the Lindblad[4] and Redfield quantum master equations,[102] correspond to approximate versions of the GQME which are based on assuming weak system-bath coupling and Markovity, and making the secular approximation (see Sec. 3.2.4).

Inspection of the GQME, Eq. (3.16), reveals that when $\mathcal{K}(\tau) \to 0$, the system can be treated as a *closed system*, whose dynamics is unitary and fully dictated by $\hat{H}_s$ via the quantum Liouville equation $d\hat{\sigma}(t)/dt = -i\mathcal{L}_s\hat{\sigma}(t)/\hbar$. Thus, $\mathcal{K}(\tau)$ fully captures the effect of the baths on the system's dynamics. The evaluation and analysis of $\mathcal{K}(\tau)$ therefore offers a useful pathway for understanding the effect of the baths on the system's dynamics, which turns it from a unitary closed system dynamics into a non-unitary open system dynamics.

The memory kernel, $\mathcal{K}(\tau)$, can be calculated from so-called *projection free inputs (PFIs)*, i.e. inputs that do not explicitly feature $\mathcal{P}$ or $\mathcal{Q}$, via a variety of pathways.[85] In what follows, we will focus on one such pathway, where the system's time evolution superoperator, $\mathcal{U}(t)$, serves as the PFI. $\mathcal{U}(t)$ is defined as follows:

$$\hat{\sigma}(t) = \mathcal{U}(t)\hat{\sigma}(0) = \mathrm{Tr}_b\left(e^{-i\mathcal{L}t/\hbar}\hat{\rho}_b^{eq} \otimes \hat{\rho}_c^{eq} \otimes \hat{\sigma}(0)\right) \quad . \tag{3.18}$$

Given $\mathcal{U}(t)$, $\mathcal{K}(\tau)$ can be obtained by numerically solving the following integral Volterra equation:[54,88,86]

$$\mathcal{K}(\tau) = -\ddot{\mathcal{U}}(\tau) - \frac{i}{\hbar}\dot{\mathcal{U}}(\tau)\mathcal{L}_s - \int_0^\tau d\tau' \dot{\mathcal{U}}(\tau - \tau')\mathcal{K}(\tau') \tag{3.19}$$

It should be noted that in practice, $\mathcal{U}(t)$ and $\mathcal{K}(\tau)$ are represented by $n^2 \times n^2$ matrices in terms of a basis of the system's Hilbert space of one's choice, where n is the dimension of the system's Hilbert space. More specifically, Eqs. (3.16) and (3.19) in matrix form are

given by

$$\begin{aligned}\frac{d}{dt}\sigma_{jk}(t) = &-\frac{i}{\hbar}\sum_{mn}\mathcal{L}_{s,jk,mn}\sigma_{mn}(t) \\ &-\sum_{mn}\int_0^t d\tau \mathcal{K}_{jk,mn}(\tau)\sigma_{mn}(t-\tau) \quad ,\end{aligned} \tag{3.20}$$

$$\begin{aligned}\mathcal{K}_{jk,mn}(\tau) = &-\ddot{\mathcal{U}}_{jk,mn}(\tau) - \frac{i}{\hbar}\sum_{pq}\dot{\mathcal{U}}_{jk,pq}(\tau)\mathcal{L}_{s,pq,mn} \\ &-\sum_{pq}\int_0^\tau d\tau' \dot{\mathcal{U}}_{jk,pq}(\tau-\tau')\mathcal{K}_{pq,mn}(\tau') \quad ,\end{aligned} \tag{3.21}$$

with $\sigma_{jk}(t) = \langle j|\hat{\sigma}(t)|k\rangle$ and the (jk,lm) matrix element of a system superoperator $\mathcal{A}(\tau)$ given by

$$\mathcal{A}_{jk,lm}(\tau) = \mathrm{Tr}\Big\{|j\rangle\langle k|^\dagger \mathcal{A}(\tau)|l\rangle\langle m|\Big\} \quad , \tag{3.22}$$

where $\mathrm{Tr} = \mathrm{Tr}_s\mathrm{Tr}_h\mathrm{Tr}_c$ is the trace over the overall system's Hilbert space, $\mathcal{A} = \mathcal{L}_s, \mathcal{K}(\tau), \mathcal{U}(\tau), \dot{\mathcal{U}}(\tau)$ and $j,k,m,l,n,p,q = 1,\ldots,n$.

3.2.3 The Non-Additivity of the Effect of the Individual Baths on the System's Dynamics

The GQME in Eq. (3.16) is the exact equation of motion for a system coupled to *two* baths. Within Eq. (3.16), the memory kernel, $\mathcal{K}(\tau)$, as given by Eq. (3.17), fully captures the effect of the two baths on the system's dynamics. Generally speaking, the effect of the two baths on the system's dynamics is *non-additive*, i.e. it is not generally true that $\mathcal{K}(\tau)$ can be written as a sum of two memory kernels.

To see this, consider the case where the system is only coupled to the hot bath. The overall Hamiltonian for such a system is then given by:

$$\hat{H}_\eta = \hat{H}_s + \hat{H}_h + \hat{H}_{sh} \quad , \tag{3.23}$$

Following a similar procedure to that followed in Sec. 3.2.2, one can derive the following

GQME for such a case:

$$\frac{d}{dt}\hat{\sigma}(t) = -\frac{i}{\hbar}\mathcal{L}_s\hat{\sigma}(t) - \int_0^t d\tau \mathcal{K}_h(\tau)\hat{\sigma}(t-\tau) \tag{3.24}$$

where

$$\mathcal{K}_h(\tau) = \frac{1}{\hbar^2}\mathrm{Tr}_h\left\{\mathcal{L}_{sh}e^{-i\mathcal{Q}_h\mathcal{L}_\eta\tau/\hbar}\mathcal{Q}_h\mathcal{L}_{sh}\hat{\rho}_h^{eq}\right\} \ . \tag{3.25}$$

Here, $\mathcal{L}_\eta\hat{A} = [\hat{H}_\eta, \hat{A}]$, $\mathcal{L}_{sh}\hat{A} = [\hat{H}_{sh}, \hat{A}]$, $\mathcal{P}_h\hat{A} = \hat{\rho}_h^{eq} \otimes \mathrm{Tr}_h(\hat{A})$ and $\mathcal{Q}_h = \mathcal{I} - \mathcal{P}_h$. Similarly, when the system is only coupled to the cold bath, the overall Hamiltonian is given by:

$$\hat{H}_\kappa = \hat{H}_s + \hat{H}_c + \hat{H}_{sc} \ , \tag{3.26}$$

and the corresponding GQME is:

$$\frac{d}{dt}\hat{\sigma}(t) = -\frac{i}{\hbar}\mathcal{L}_s\hat{\sigma}(t) - \int_0^t d\tau \mathcal{K}_c(\tau)\hat{\sigma}(t-\tau) \tag{3.27}$$

where

$$\mathcal{K}_c(\tau) = \frac{1}{\hbar^2}\mathrm{Tr}_c\left\{\mathcal{L}_{sc}e^{-i\mathcal{Q}_c\mathcal{L}_\kappa\tau/\hbar}\mathcal{Q}_c\mathcal{L}_{sc}\hat{\rho}_c^{eq}\right\} \ , \tag{3.28}$$

with $\mathcal{L}_\kappa\hat{A} = [\hat{H}_\kappa, \hat{A}]$, $\mathcal{L}_{sc}\hat{A} = [\hat{H}_{sc}, \hat{A}]$, $\mathcal{P}_c\hat{A} = \hat{\rho}_c^{eq} \otimes \mathrm{Tr}_c(\hat{A})$ and $\mathcal{Q}_c = \mathcal{I} - \mathcal{P}_c$.

The non-additivity of $\mathcal{K}(\tau)$ then implies that

$$\mathcal{K}(\tau) \neq \mathcal{K}_h(\tau) + \mathcal{K}_c(\tau) \ . \tag{3.29}$$

Importantly, the non-additivity of the memory kernel is a signature of strong system-bath coupling. As we will see in Sec. 3.2.4, $\mathcal{K}(\tau)$ is additive, namely $\mathcal{K}(\tau) = \mathcal{K}_h(\tau) + \mathcal{K}_c(\tau)$, in the limit of weak system-bath coupling. Thus, $\mathcal{K}(\tau) - \mathcal{K}_h(\tau) - \mathcal{K}_c(\tau)$ can be used as a measure of the collective strong coupling effect, where the effect of being coupled to two baths is not the same as the sum of effects due to being coupled to the individual baths.

3.2.4 The Limits of Weak System-Bath Coupling, Markovian Dynamics and the Secular Approximation

Further insight into the aforementioned GQME for a system coupled to two baths can be obtained by considering its weak system-bath coupling limit. The weak system-bath coupling limit corresponds to truncating the expansion of the memory kernel, $\mathcal{K}(\tau)$, in powers of the system-bath coupling terms, $\hat{H}_{bs}$, [see Eq. (3.6)] at the lowest non-vanishing order, which corresponds to second order for the Hamiltonian under consideration.[113] Doing so for the memory kernel in Eq. (3.17) leads to the following weak-coupling approximation for the memory kernel:

$$\mathcal{K}(\tau) \approx \mathcal{K}^{(2)}(\tau) = \mathcal{K}_h^{(2)}(\tau) + \mathcal{K}_c^{(2)}(\tau) \quad , \tag{3.30}$$

where

$$\begin{aligned} \mathcal{K}_h^{(2)}(\tau) &= \frac{1}{\hbar^2}\mathrm{Tr}_h\left\{\mathcal{L}_{sh}e^{-i\mathcal{L}_h\tau/\hbar}e^{-i\mathcal{L}_s\tau/\hbar}\mathcal{L}_{sh}\hat{\rho}_h^{eq}\right\} \quad , \\ \mathcal{K}_c^{(2)}(\tau) &= \frac{1}{\hbar^2}\mathrm{Tr}_c\left\{\mathcal{L}_{sc}e^{-i\mathcal{L}_c\tau/\hbar}e^{-i\mathcal{L}_s\tau/\hbar}\mathcal{L}_{sc}\hat{\rho}_c^{eq}\right\} \quad . \end{aligned} \tag{3.31}$$

Thus, the system dynamics in the limit of weak system-bath coupling is given by the following quantum master equation:

$$\begin{aligned} \frac{d}{dt}\hat{\sigma}(t) &= -\frac{i}{\hbar}\mathcal{L}_s\hat{\sigma}(t) - \int_0^t d\tau \mathcal{K}_h^{(2)}(\tau)\hat{\sigma}(t-\tau) \\ &- \int_0^t d\tau \mathcal{K}_c^{(2)}(\tau)\hat{\sigma}(t-\tau) \end{aligned} \tag{3.32}$$

Importantly, the effect of the two baths on the system dynamics is *additive* in the weak system-bath coupling limit. It consists of a sum of two terms, one which is solely due to the coupling to the hot bath, $-\int_0^t d\tau \mathcal{K}_h^{(2)}(\tau)\hat{\sigma}(t-\tau)$, and another, $-\int_0^t d\tau \mathcal{K}_c^{(2)}(\tau)\hat{\sigma}(t-\tau)$, which is solely due to the coupling to the cold bath.

Furthermore, $\mathcal{K}_h^{(2)}(\tau)$ and $\mathcal{K}_c^{(2)}(\tau)$ correspond to the weak coupling limit of $\mathcal{K}_h(\tau)$ and

$\mathcal{K}_c(\tau)$ in Eqs. (3.25) and (3.28), respectively. This implies that the effect of the hot (cold) bath on the system is the same as it would have been if the system was only coupled to the hot (cold) bath. Thus, the collective double-bath effect measured by $\mathcal{K}(\tau) - \mathcal{K}_h(\tau) - \mathcal{K}_c(\tau)$ vanishes in the limit of weak system-bath coupling.

Eq. (3.32) can be made Markovian if the time scale of the bath-induced relaxation dynamics is much slower than the memory time (i.e. the time scale on which $\mathcal{K}_h^{(2)}(\tau)$ and $\mathcal{K}_c^{(2)}(\tau)$ vanish). This corresponds to substituting $\hat{\sigma}(t-\tau)$ with $e^{i\mathcal{L}_s\tau/\hbar}\hat{\sigma}(t)$ and setting the upper limit of the time integrals to infinity in Eq. (3.32), and leads to a *Markovian quantum master equation* of the form

$$\frac{d}{dt}\hat{\sigma}(t) = -\frac{i}{\hbar}\mathcal{L}_s\hat{\sigma}(t) - \left[\mathcal{D}_h^{(2)} + \mathcal{D}_c^{(2)}\right]\hat{\sigma}(t) \quad , \tag{3.33}$$

where

$$\begin{aligned} D_h^{(2)}(\tau) &= \frac{1}{\hbar^2}\int_0^\infty d\tau \mathrm{Tr}_h\Big\{\mathcal{L}_{sh}e^{-i\mathcal{L}_h\tau/\hbar} \\ &\qquad \times e^{-i\mathcal{L}_s\tau/\hbar}\mathcal{L}_{sh}\hat{\rho}_{h,eq}e^{i\mathcal{L}_s\tau/\hbar}\Big\} \\ D_c^{(2)}(\tau) &= \frac{1}{\hbar^2}\int_0^\infty d\tau \mathrm{Tr}_c\Big\{\mathcal{L}_{sc}e^{-i\mathcal{L}_c\tau/\hbar} \\ &\qquad \times e^{-i\mathcal{L}_s\tau/\hbar}\mathcal{L}_{sc}\hat{\rho}_{c,eq}e^{i\mathcal{L}_s\tau/\hbar}\Big\} \end{aligned} \tag{3.34}$$

Casting, Eq. (3.34) in terms of the eigen-basis of $\hat{H}_s$, $\hat{H}_s|j\rangle = E_j|j\rangle$, the system-bath coupling terms can be written in the following form:

$$\hat{H}_{sh} = \sum_{j,k}\hat{\Lambda}_{h,jk}|j\rangle\langle k| \quad , \quad \hat{H}_{sc} = \sum_{j,k}\hat{\Lambda}_{c,jk}|j\rangle\langle k| \quad , \tag{3.35}$$

where $\{\hat{\Lambda}_{h,jk}\}$ and $\{\hat{\Lambda}_{c,jk}\}$ are hot bath and cold bath operators, respectively. Making the secular approximation,[91] the dynamics of the system's populations, $\{\sigma_{jj}(t)\}$, and coherences,

$\{\sigma_{jk}(t)\}$ $(j \neq k)$ can be described by:

$$\begin{aligned} \frac{d}{dt}\sigma_{jj}(t) &= -\sum_{l\neq j} k_{l\leftarrow j}\sigma_{jj}(t) + \sum_{l\neq j} k_{j\leftarrow l}\sigma_{ll}(t), \\ \frac{d}{dt}\sigma_{jk}(t) &= -(i\omega_{jk} + \gamma_{jk})\sigma_{jk}(t) \quad . \end{aligned} \tag{3.36}$$

$\{k_{l\leftarrow j}\}$ and γ_{jk} are the population relaxation and dephasing rate constants, respectively, which consist of sums of hot and cold bath contributions:

$$\begin{aligned} k_{l\leftarrow j} &= k^h_{l\leftarrow j} + k^c_{l\leftarrow j}, \\ \gamma_{jk} &= \gamma^h_{jk} + \gamma^c_{jk} \quad . \end{aligned} \tag{3.37}$$

Here,

$$k^h_{l\leftarrow j} = \frac{1}{\hbar^2}\tilde{C}^h_{jl,lj}(\omega_{jl}) \quad , \quad k^c_{l\leftarrow j} = \frac{1}{\hbar^2}\tilde{C}^c_{jl,lj}(\omega_{jl}) \quad ,$$

$$\begin{aligned} \gamma^h_{jk} &= \frac{1}{2}\left(\sum_{l\neq j} k^h_{l\leftarrow j} + \sum_{l\neq k} k^h_{l\leftarrow k}\right) \\ &\quad + \frac{1}{2\hbar^2}\left[\tilde{C}^h_{jj,jj}(0) + \tilde{C}^h_{kk,kk}(0)\right] \quad , \\ \gamma^c_{jk} &= \frac{1}{2}\left(\sum_{l\neq j} k^c_{l\leftarrow j} + \sum_{l\neq k} k^c_{l\leftarrow k}\right) \\ &\quad + \frac{1}{2\hbar^2}\left[\tilde{C}^c_{jj,jj}(0) + \tilde{C}^c_{kk,kk}(0)\right] \quad . \end{aligned} \tag{3.38}$$

In the above, $\hbar\omega_{jl} = E_j - E_l$, $k^h_{l\leftarrow j}/k^h_{j\leftarrow l} = e^{\beta_h\hbar\omega_{jl}}$, $k^c_{l\leftarrow j}/k^c_{j\leftarrow l} = e^{\beta_c\hbar\omega_{jl}}$ and

$$\begin{aligned} \tilde{C}^h_{jl,lj}(\omega_{jl}) &= \int_{-\infty}^{\infty} d\tau e^{i\omega_{jl}\tau} C^h_{jl,lj}(\tau) \\ C^h_{jl,lj}(\tau) &= \mathrm{Tr}_h\left[\hat{\rho}^{eq}_h e^{i\hat{H}_h\tau/\hbar}\hat{\Lambda}_{h,jl}e^{-i\hat{H}_h\tau/\hbar}\hat{\Lambda}_{h,lj}\right] \quad , \\ \tilde{C}^c_{jl,lj}(\omega_{jl}) &= \int_{-\infty}^{\infty} d\tau e^{i\omega_{jl}\tau} C^c_{jl,lj}(\tau) \quad , \\ C^c_{jl,lj}(\tau) &= \mathrm{Tr}_c\left[\hat{\rho}^{eq}_c e^{i\hat{H}_c\tau/\hbar}\hat{\Lambda}_{c,jl}e^{-i\hat{H}_c\tau/\hbar}\hat{\Lambda}_{c,lj}\right] \quad . \end{aligned} \tag{3.39}$$

In what follows, we will refer to the Markovian and secular quantum master equation in Eq. (3.36) as the *Redfield quantum master equation*. It should be noted that non-Markovian and/or nonsecular versions of the Redfield quantum master equation exist and can, in some cases, improve their accuracy (as long as treating the system-bath coupling as a small perturbation within second-order time-dependent perturbation theory is valid). Our choice to focus on the Markovian and secular quantum master equation as a reference is motivated by the fact that it has the Lindblad form, which is widely used and guarantees complete positivity.[69,4] Deviations between the predictions of the Redfield quantum master equation and the GQME [Eq. (3.16)] will be used as a measure of the effect of strong coupling, non-Markovity and non-secular terms.

3.3 A Demonstrative Application to a Two-Level System Linearly Coupled to Hot and Cold Harmonic Baths

3.3.1 Model Hamiltonian

In this section, we demonstrate the theoretical framework outlined in Sec. 3.2, and the insights that can be obtained from it, on a benchmark model that consists of a two-level system linearly coupled to hot and cold harmonic baths. To this end, we adopted a model Hamiltonian previously studied by Song and Shi in Ref. 123, which has the form of Eq. (3.4), with $\{\hat{H}_s, \hat{H}_h, \hat{H}_c, \hat{H}_{sh}, \hat{H}_{sc}\}$ given by

$$\begin{aligned}
\hat{H}_s &= \Delta\hat{\sigma}_x \\
\hat{H}_h &= \sum_{j=1}^{N}\left[\frac{\hat{P}_{hj}^2}{2} + \frac{\omega_{hj}^2\hat{R}_{hj}^2}{2}\right] \ , \ \hat{H}_c = \sum_{j=1}^{N}\left[\frac{\hat{P}_{cj}^2}{2} + \frac{\omega_{cj}^2\hat{R}_{cj}^2}{2}\right] \quad , \\
\hat{H}_{sh} &= \sum_{j=1}^{N} c_{hj}\hat{R}_{hj}\hat{\sigma}_z \ , \ \hat{H}_{sc} = \sum_{j=1}^{N} c_{cj}\hat{R}_{cj}\hat{\sigma}_z \quad .
\end{aligned} \tag{3.40}$$

Here, $\hat{\sigma}_x = |0\rangle\langle 1| + |1\rangle\langle 0|$, $\hat{\sigma}_y = -i(|0\rangle\langle 1| - |1\rangle\langle 0|)$ and $\hat{\sigma}_z = |0\rangle\langle 0| - |1\rangle\langle 1|$ are the Pauli operators, with $|0\rangle$ and $|1\rangle$ corresponding to the eigen states of $\hat{\sigma}_z$ with eigenvalues $+1$ and -1, respectively; $\{\hat{R}_{hj}, \hat{P}_{hj}, \omega_{hj}, c_{hj} | j = 1, \ldots, N\}$ and $\{\hat{R}_{cj}, \hat{P}_{cj}, \omega_{cj}, c_{cj} | j = 1, \ldots, N\}$ denote the mass-weighted coordinates, momenta, frequencies, and coupling coefficients of the hot and cold bath modes, respectively. It should be noted that for this model, the hot and cold baths' Hamiltonians are identical and coupled to the two-level system in the same way.

The values of $\{\omega_{hj}, c_{hj} | j = 1, \ldots, N\}$ and $\{\omega_{cj}, c_{cj} | j = 1, \ldots, N\}$ are extracted from spectral density functions, which are assumed to be identical for both baths and given by ($\alpha = h, c$):[123]

$$\begin{aligned} I_\alpha(\omega) &= \frac{\pi}{2} \sum_{j=1}^{N} \frac{c_{\alpha j}^2}{\omega_{\alpha j}} \delta(\omega - \omega_{\alpha j}) \\ &= \frac{\eta_\alpha \omega \gamma_{\alpha,1} \gamma_{\alpha,2} \gamma_{\alpha,3}}{(\omega^2 + \gamma_{\alpha,1}^2)(\omega^2 + \gamma_{\alpha,2}^2)(\omega^2 + \gamma_{\alpha,3}^2)} \quad . \end{aligned} \tag{3.41}$$

The initial state of the overall system is assumed to be given by Eq. (3.10), with $\hat{\sigma}(0) = |0\rangle\langle 0|$:

$$\hat{\rho}(0) = \hat{\rho}_h^{eq} \otimes \hat{\rho}_c^{eq} \otimes |0\rangle\langle 0| \quad . \tag{3.42}$$

Here, $\hat{\rho}_h^{eq}$ and $\hat{\rho}_c^{eq}$ are defined as in Eq. (3.8).

Calculations were performed for six realizations of this model that correspond to the values of the parameters in Table 3.1. The values of β_h, β_c, $\gamma_{\alpha,1}$, $\gamma_{\alpha,2}$ and $\gamma_{\alpha,3}$ are the same for all six models. The models differ with respect to the values of Δ ($\Delta = 0.1$ for models 1-3, while $\Delta = 0.5$ for models 4-6) and η_α ($\eta_\alpha = 0.01$ for models 1 and 4, $\eta_\alpha = 0.1$ for models 2 and 5, and $\eta_\alpha = 1.0$ for models 3 and 6). It should be noted that quantum-mechanically exact results obtained via the HEOM method were reported in Ref. 123 for models 2,3,5 and 6. Models 1 and 4 were added in this study since they correspond to weaker system-bath coupling, in order to demonstrate the more additive nature of the memory kernel in this case.

Table 3.1: Spin-Boson Model Parameters

Model #	Δ	β_h	β_c	η_α	$\gamma_{\alpha,1}$	$\gamma_{\alpha,2}$	$\gamma_{\alpha,3}$
1	0.1	0.5	1.5	0.01	0.5	1.0	1.5
2	0.1	0.5	1.5	0.1	0.5	1.0	1.5
3	0.1	0.5	1.5	1.0	0.5	1.0	1.5
4	0.5	0.5	1.5	0.01	0.5	1.0	1.5
5	0.5	0.5	1.5	0.1	0.5	1.0	1.5
6	0.5	0.5	1.5	1.0	0.5	1.0	1.5

3.3.2 Computational Details

Calculating the memory kernel, Eq. (3.17), for the GQME that describes the dynamics of the two-level system coupled to two baths, Eq. (3.16), requires solving the Volterra equation, Eq. (3.19), which requires $\mathcal{U}(\tau)$ as the PFI, Eq. (3.18). To this end, we calculated the 4×4 matrix that represents $\mathcal{U}(\tau)$ via the HEOM method, and its time derivatives, $\dot{\mathcal{U}}(\tau)$ and $\ddot{\mathcal{U}}(\tau)$, via the finite central difference method available in the NumPy Python library. The Volterra equation was then solved numerically via the iterative algorithm outlined in Refs. 88, 26, followed by propagation of the GQME using a fourth-order Runge–Kutta method.

It should be noted that while the results are presented in terms of the eigen-basis of $\hat{\sigma}_z$ ($\{|0\rangle, |1\rangle\}$, such that $\hat{\sigma}_z|0\rangle = |0\rangle$ and $\hat{\sigma}_z|1\rangle = -|1\rangle$), the Redfield quantum master equation, Eq. (3.36), is given in terms of the eigen-basis of $\hat{\sigma}_x$ (since the system Hamiltonian in this case is given by $\hat{H}_s = \Delta\hat{\sigma}_x$).

3.3.3 Results and Discussion

We start by demonstrating the effect of the system-bath coupling on the dynamics of the system. To this end, we compare and contrast the dynamics of the three components of the Bloch vector, $[\sigma_x(t), \sigma_y(t), \sigma_z(t)]$, where $\sigma_u(t) = \langle\hat{\sigma}_u\rangle(t)$, as obtained in four different ways: (1) The GQME, Eq. (3.16), with the *exact two-bath memory kernel*, Eq. (4.12); (2) The GQME, Eq. (3.16), with the *sum of exact single-bath memory kernels*, $\mathcal{K}(\tau) \approx \mathcal{K}_h(\tau) + \mathcal{K}_c(\tau)$,

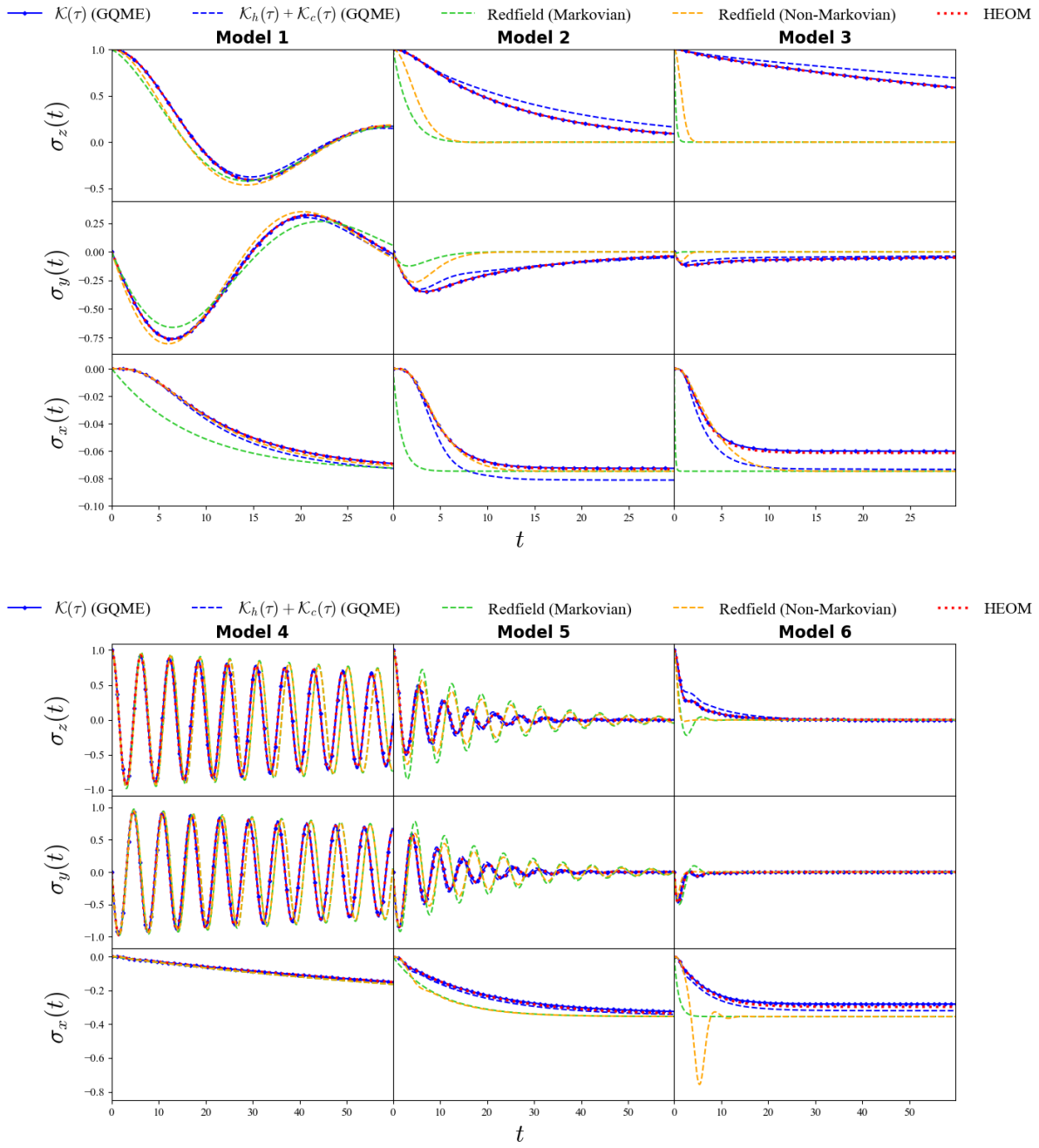


Figure 3.1: $\sigma_x(t)$, $\sigma_y(t)$ and $\sigma_z(t)$ as a function of time for models 1-3 (top panel) and models 4-6 (bottom panel) in Table 4.2. Shown are exact HEOM-based results (dotted red line), GQME-based results with the exact memory kernel $\mathcal{K}(\tau)$, Eq. (4.12), calculated from HEOM-based PFIs (solid blue line), GQME-based results with the approximate additive memory kernal $\mathcal{K}_h(\tau) + \mathcal{K}_c(\tau)$, Eqs. (3.25) and (3.28), calculated from HEOM-based PFIs (dashed blue line), results based on the Markovian and secular Redfield quantum master equation, Eq. (3.36) (dashed green line), and results based on the non-Markovian and secular Redfield quantum master equation, Eq. (3.32) (dashed orange line).

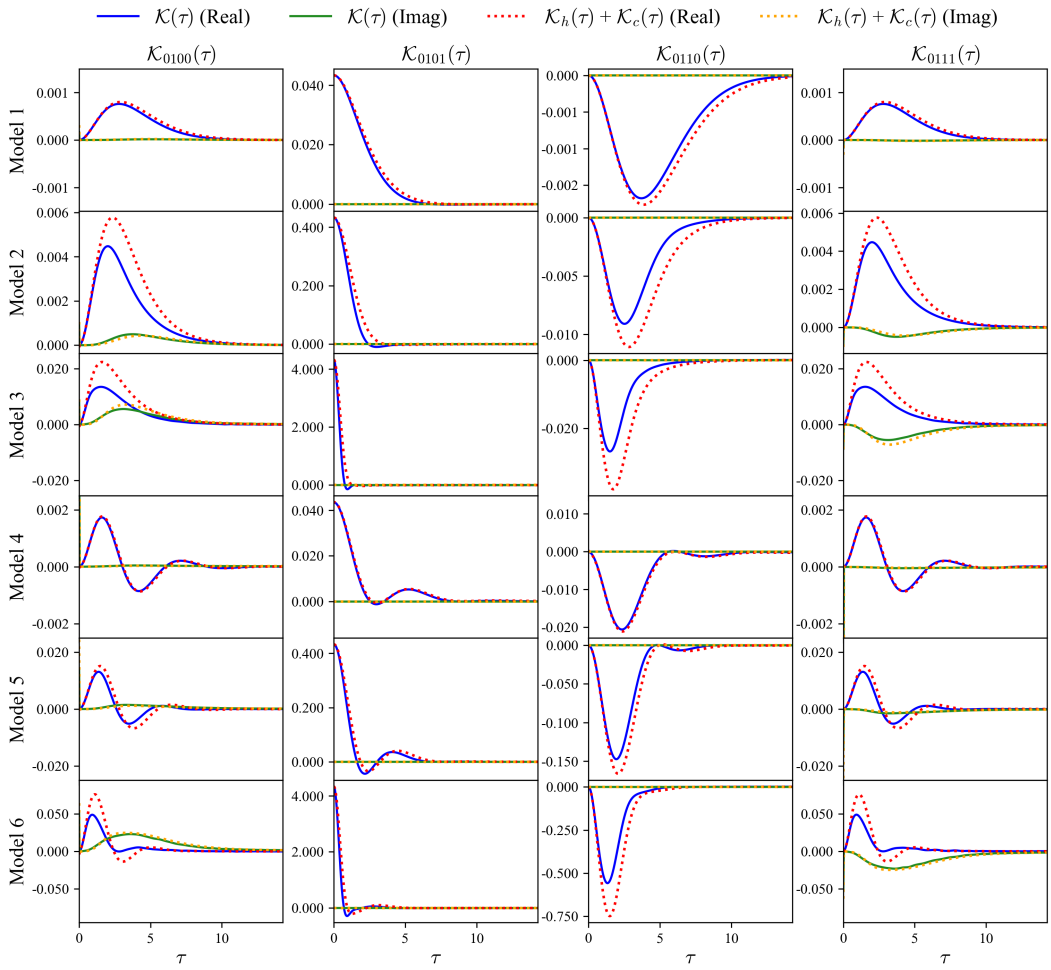


Figure 3.2: A comparison of the four independent and non-vanishing matrix elements $[(01,00),(01,01),(01,10),(01,11)]$ of $\mathcal{K}(\tau)$ vs. $\mathcal{K}_h(\tau)+\mathcal{K}_c(\tau)$, for the six spin-boson models under consideration. Shown are the real (solid blue line) and imaginary (solid green line) parts of $\mathcal{K}(\tau)$ vs. the real (dashed red line) and imaginary (dashed orange line) parts of $\mathcal{K}_h(\tau)+\mathcal{K}_c(\tau)$.

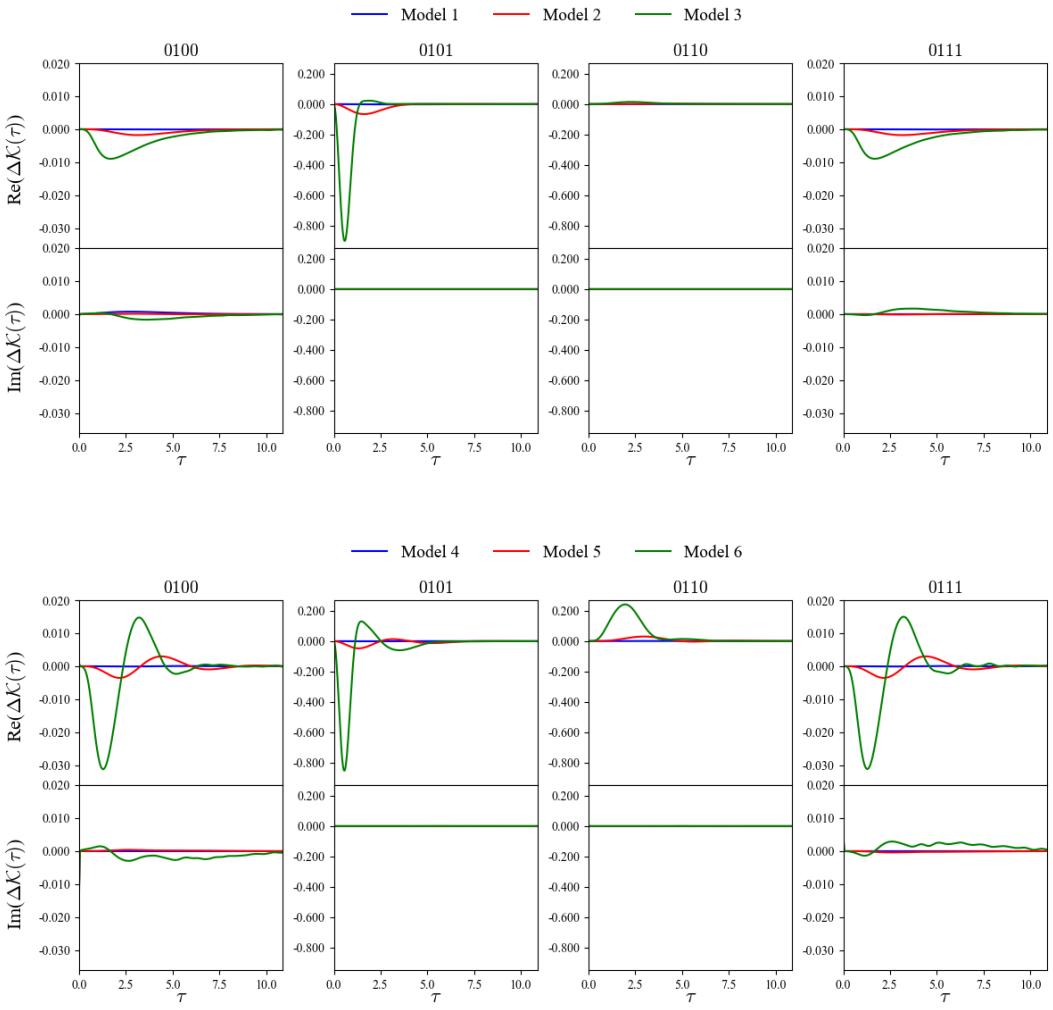


Figure 3.3: The real (top panels) and imaginary (lower panels) parts of the $(01, 00)$, $(01, 01)$, $(01, 10)$ and $(01, 11)$ nonvanishing matrix elements of $\Delta\mathcal{K}(\tau) = \mathcal{K}(\tau) - \mathcal{K}_h(\tau) - \mathcal{K}_c(\tau)$, for the six spin-boson models under consideration.

Eqs. (3.25) and (3.28); (3) The *secular and Markovian Redfield quantum master equation*, Eq. (3.36); (4) The *secular and non-Markovian Redfield quantum master equation*, Eq. (3.32). The results of this comparison for models 1-6 are shown in Fig 3.1.

We first note that the dynamics generated via the GQME with the HEOM-based exact memory kernel coincides with that obtained via direct use of the HEOM method. This is to be expected since, given the exact memory kernel, the GQME is the exact equation of motion for the system's density matrix.

Also as expected, the dynamics of σ_x (which correspond to energy relaxation) is seen to become increasingly more damped with increasing η_α, while the dynamics of σ_y and σ_z (which correspond to phase damping) is seen to go from under-damped to over-damped with increasing η_α. It should also be noted that while σ_y and σ_z are seen to vanish at steady state regardless of the value of η_α, the steady state value of σ_x is non-zero and strongly dependent on η_α. As η_α increases, the steady state value of σ_x is also seen to deviate more and more from the value predicted by the Redfield quantum master equation.

The increasing non-additivity of the memory kernel with increasing system-bath coupling strength (as measured by η_α) is manifested by the growing difference between the exact results and the results obtained by using the approximation $\mathcal{K}(\tau) \approx \mathcal{K}_h(\tau) + \mathcal{K}_c(\tau)$. The non-additive nature of the bath-induced effect is more pronounced for models 1-3 than for models 4-6. This behavior can be traced back to the increasing role of coherent Hamiltonian dynamics relative to dissipative dynamics with increasing Δ.

From the three components of the Bloch vector, σ_x and σ_z are seen to be more sensitive than σ_y to the non-additive nature of the bath-induced effect. This sensitivity manifests itself both in the transient dynamics and steady-state values, and can be traced back to the fact that the Hamiltonian in Eq. (3.40) is given in terms of $\hat{\sigma}_x$ and $\hat{\sigma}_z$, but not $\hat{\sigma}_y$.

Finally, while the dynamics generated by the secular and Markovian Redfield quantum master equation is seen to get closer to the exact dynamics with decreasing η_α, deviations are still observable even at the weakest system-bath coupling under consideration ($\eta_\alpha = 0.01$).

Those deviations are particularly manifest for σ_x in model 1, where they can be traced back to transient non-Markovian effects. Specifically, the onset of Markovian dynamics in this case occurs at $t \sim 5$, as opposed to at the initial time (as required by the assumption of Markovity). Thus, while the dynamics at $t > 5$ is exponential and parallels the exact dynamics, the delayed onset of Markovian dynamics leads to the observed deviation.

Further insight into the non-additivity of the bath-induced effect can be obtained by directly comparing $\mathcal{K}(\tau)$ with $\mathcal{K}_h(\tau) + \mathcal{K}_c(\tau)$. To this end, it should be remembered that $\mathcal{K}(\tau)$, $\mathcal{K}_h(\tau)$ and $\mathcal{K}_c(\tau)$ are superoperators, and therefore representable in terms of $n^2 \times n^2$ matrices (see Eq. (3.22)). For the spin-boson model under consideration, $n = 2$, which means that $\mathcal{K}(\tau)$, $\mathcal{K}_h(\tau)$ and $\mathcal{K}_c(\tau)$ are representable in terms of 4×4 matrices. However, represented in terms of the $\hat{\sigma}_z$ eigen-basis, $\{|0\rangle, |1\rangle\}$, the (jj, lm) matrix elements of $\mathcal{K}(\tau)$, $\mathcal{K}_h(\tau)$ and $\mathcal{K}_c(\tau)$ vanish for the spin-boson model.[88,71] Thus, eight of the sixteen matrix elements of $\mathcal{K}(\tau)$, $\mathcal{K}_h(\tau)$ and $\mathcal{K}_c(\tau)$ vanish (i.e. the ones for which $jj = 00, 11$ and $lm = 00, 01, 10, 11$).[88,71] For the remaining eight non-vanishing matrix elements, four can be shown to be the complex conjugates of the other four, since $\mathcal{K}_{jk,lm}(\tau) = \mathcal{K}^*_{kj,ml}(\tau)$, which means that the memory kernels can be determined by the values of the following four matrix elements: $\{\mathcal{K}_{0100}(\tau), \mathcal{K}_{0101}(\tau), \mathcal{K}_{0110}(\tau), \mathcal{K}_{0111}(\tau)\}$.[88,71]

A comparison of the aforementioned four independent and non-vanishing matrix elements of $\mathcal{K}(\tau)$ vs. $\mathcal{K}_h(\tau) + \mathcal{K}_c(\tau)$ is shown in Fig. 3.2 for the six spin-boson models under consideration (see Table. 3.1). The corresponding real and imaginary parts of the $(01, 00)$, $(01, 01)$, $(01, 10)$ and $(01, 11)$ matrix elements of $\mathcal{K}(\tau) - \mathcal{K}_h(\tau) - \mathcal{K}_c(\tau)$ are shown in Fig. 3.3.

The difference between $\mathcal{K}(\tau)$ and $\mathcal{K}_h(\tau) + \mathcal{K}_c(\tau)$ is seen to increase with increasing coupling strength between the system and the baths, as measured by η_α. Specifically, $\mathcal{K}_h(\tau) + \mathcal{K}_c(\tau)$ is seen to reproduce $\mathcal{K}(\tau)$ rather well when $\eta_\alpha = 0.01$ (models 1 and 4), which is consistent with the expectation that the memory kernel becomes additive in the limit of weak system-bath coupling (see Eq. (3.30)). However, the effect of the baths becomes increasingly non-additive as η_α increases, as is clearly evident from the growing deviation between $\mathcal{K}(\tau)$ and

$\mathcal{K}_h(\tau) + \mathcal{K}_c(\tau)$ as η_α is increased.

Interestingly, the non-additive nature of $\mathcal{K}(\tau)$ is dependent on the matrix element. Specifically, while $\mathcal{K}_{0101}(\tau)$ is well approximated by $\mathcal{K}_{h,0101}(\tau) + \mathcal{K}_{c,0101}(\tau)$, this is not the case for $\mathcal{K}_{0100}(\tau)$, $\mathcal{K}_{0111}(\tau)$ and $\mathcal{K}_{0110}(\tau)$. It should however be noted that the absolute error associated with assuming additivity is actually similar for all four matrix elements (see Fig. 3.3). However, this absolute error translates into a much smaller relative error in the case of $\mathcal{K}_{0101}(\tau)$, because it is so much larger than $\mathcal{K}_{0100}(\tau)$, $\mathcal{K}_{0111}(\tau)$ and $\mathcal{K}_{0110}(\tau)$.

It should be noted that $\mathcal{K}_{0101}(\tau)$, couples σ_{10} with itself. This term therefore gives rise to coherence damping in the $\{|0\rangle, |1\rangle\}$ representation. Thus, the fact that $\mathcal{K}_{0101}(\tau)$ can be well approximated as additive implies that this coherence damping process is relatively insensitive to the non-additive nature of the effects of the baths.

In contrast, $\mathcal{K}_{0100}(\tau)$ and $\mathcal{K}_{0111}(\tau)$ give rise to bath-induced coupling between populations and coherences in the $\{|0\rangle, |1\rangle\}$ representation, which can give rise to population-to-coherence and coherence-to-population transfer. Similarly, $\mathcal{K}_{0110}(\tau)$ gives rise to bath-induced coupling between different coherences, which can lead to coherence transfer.

Thus, unlike coherence damping, population-to-coherence, coherence-to-population and coherence-to-coherence transfer are seen to become strongly non-additive with increasing system-bath coupling. This is consistent with the fact that the emergence of those processes as non-negligible beyond the limit of weak system-bath coupling goes hand in hand with their non-additive nature, as signatures of strong system-bath coupling.

3.4 Concluding Remarks

The non-additivity of the memory kernel, as measured by the difference between $\mathcal{K}(\tau)$ and $\mathcal{K}_h(\tau) + \mathcal{K}_c(\tau)$, can serve as a test for the adequacy of methods that treat system-bath coupling as a weak perturbation. Generally speaking, $\mathcal{K}(\tau)$ can only be written in the additive form $\mathcal{K}_h(\tau) + \mathcal{K}_c(\tau)$ under weak system-bath coupling conditions. Beyond that, the difference between $\mathcal{K}(\tau)$ and $\mathcal{K}_h(\tau) + \mathcal{K}_c(\tau)$ grows with the strength of system-bath coupling.

This happens because the effect of the bath on a system is *non-local*. In other words, the cumulative effect of coupling to multiple baths is not the same as the sum of the effects of the individual baths.

The effect of non-additivity depends on the matrix element of $\mathcal{K}(\tau)$. Specifically, the *relative* error associated with approximating $\mathcal{K}_{jkmn}(\tau)$ by $\mathcal{K}_{h,jkmn}(\tau) + \mathcal{K}_{c,jkmn}(\tau)$ depends on (jk, mn), which in turn correspond to the dynamical coupling between $\sigma_{jk}(t)$ and $\sigma_{mn}(t)$. For example, we have shown that for the spin-boson models under consideration in this paper, coherence damping, which is associated with $\mathcal{K}_{0101}(\tau)$, is well approximated by $\mathcal{K}_{h,0101}(\tau) + \mathcal{K}_{c,j0101}(\tau)$, while coherence-to-coherence, coherence-to-population and population-to-coherence transfer, associated with $\mathcal{K}_{0110}(\tau)$, $\mathcal{K}_{0100}(\tau)$ and $\mathcal{K}_{0111}(\tau)$, show strong non-additive behavior. Thus, non-additivity is process-dependent.

The fact that the memory kernel becomes non-additive beyond the limit of weak system-bath coupling also suggests that it may not be possible to break down the heat flow between the system and the baths into a sum of heat flows between the system and the individual baths. More specifically, defining the energy of the system as the expectation value of $\hat{H}_s$ at time t, $\langle \hat{H}_s \rangle(t)$, it can be shown that:

$$\begin{aligned} \frac{d}{dt}\langle \hat{H}_s \rangle &= \mathrm{Tr}_s \left[\hat{H}_s \frac{d}{dt} \hat{\sigma}(t) \right] \\ &= -\int_0^t d\tau \mathrm{Tr}_s \left[\hat{H}_s \mathcal{K}(\tau) \hat{\sigma}(t-\tau) \right] \quad , \end{aligned} \tag{3.43}$$

where we used the fact that $\mathrm{Tr}_s[\hat{H}_s(t)\mathcal{L}_s\hat{\sigma}(t)] = 0$. According to Eq. (3.43), the only way for the energy of the system to change is by exchanging energy with the heat baths. It therefore seems reasonable to identify $d\langle \hat{H}_s \rangle / dt$ as the *overall* heat flow between the system and the baths, which we will denote $\dot{Q}$. Thus, $\dot{Q} = d\langle \hat{H}_s \rangle / dt$, such that $\dot{Q} > 0$ means heat transfer from the baths into the system and $\dot{Q} < 0$ means heat transfer from the system into the baths. It should also be noted that $\dot{Q} = 0$ at steady state.

Now, if $\mathcal{K}(\tau)$ is additive, namely $\mathcal{K}(\tau) = \mathcal{K}_h(\tau) + \mathcal{K}_c(\tau)$, then $\dot{Q}$ is also additive, such that

$\dot{Q} = \dot{Q}_h + \dot{Q}_c$, where $\dot{Q}_h$ and $\dot{Q}_c$ are the heat flows between the system and the hot and cold baths, respectively:

$$\begin{aligned} \dot{Q}_h &= -\int_0^t d\tau \mathrm{Tr}_s \left[\hat{H}_s \mathcal{K}_h(\tau)\hat{\sigma}(t-\tau)\right] \quad , \\ \dot{Q}_c &= -\int_0^t d\tau \mathrm{Tr}_s \left[\hat{H}_s \mathcal{K}_c(\tau)\hat{\sigma}(t-\tau)\right] \quad . \end{aligned} \tag{3.44}$$

However, $\mathcal{K}(\tau) = \mathcal{K}_h(\tau) + \mathcal{K}_c(\tau)$ only holds in the limit of weak system-bath coupling. Thus, there seems to be no clear way to define $\dot{Q}_h$ and $\dot{Q}_c$ beyond this limit. Indeed, previous studies of systems coupled to multiple baths found that different definitions for $\dot{Q}_h$ and $\dot{Q}_c$ gave rise to different results beyond the limit of weak-system bath coupling.[123]

The origin for the lack of consistent definitions for $\dot{Q}_h$ and $\dot{Q}_c$ can be traced back to the fact that energy of the overall system includes the expectation values of the system-bath coupling terms $\langle \hat{H}_{sh} \rangle + \langle \hat{H}_{sc} \rangle$. Only in the limit of weak system-bath coupling do those terms become negligible, such that $d\langle H_s \rangle/dt + d\langle H_h \rangle/dt + d\langle H_c \rangle/dt = 0$, with $\dot{Q}_h = -d\langle H_h \rangle/dt$ and $\dot{Q}_c = -d\langle H_c \rangle/dt$. Beyond weak system-bath coupling, $d\langle \hat{H}_s \rangle/dt + d\langle \hat{H}_h \rangle/dt + d\langle \hat{H}_c \rangle/dt = -d\langle \hat{H}_{sh} \rangle/dt - d\langle \hat{H}_{sc} \rangle/dt$. Since $\langle \hat{H}_{sh} \rangle$ and $\langle \hat{H}_{sc} \rangle$ cannot be identified as purely system or bath observables, there appears to be no obvious way of identifying them as contributions to the energies of the system or the baths, which gives rise to an inherent ambiguity in the definitions of $\dot{Q}_h$ and $\dot{Q}_c$.

The analysis presented in this chapter demonstrates the usefulness of the GQME formalism as a way of quantifying non-additive and non-local effects, and elucidating their signature on the system dynamics. Another advantage of the GQME approach is that it is not restricted to exact quantum methods like HEOM, and can be used with semiclassical and mixed quantum-classical methods for calculating the PFIs.[84,88,118,85] This in turn opens the door for applications to anharmonic all-atom models of complex molecular systems. Yet, another advantage of the GQME approach is that it is flexible with respect to the projection operator used, and therefore the dynamical quantity of interest.[86] For example, one can

derive the GQME for only the populations (the diagonal elements of $\hat{\sigma}$), only the coherences (the off-diagonal elements of $\hat{\sigma}$), or more generally, any subset of $\hat{\sigma}$ matrix elements. For each of those choices, there would be a separate GQME with its own memory kernel. The extent of non-additivity can therefore depend on the choice of quantity of interest and the memory kernel that comes with it. Other possible extensions correspond to models where there are more than two baths, the bath and system-bath coupling differ from one bath to another,[30] and the baths start out in nonequilibrium states or entangled with the system.

CHAPTER 4

Reduced-Dimensionality Generalized Quantum Master Equations for a System Coupled to Multiple Heat Baths[1]

4.1 Introduction

In this chapter, we build upon a previous approach for examining the additivity of bath-induced effects from the point of view of the generalized quantum master equation (GQME), outlined in Chapter 3.[90,150,113,118,146,48,24,142,25,23,51,55,97,82,50,52,54,98,88,84,87,85,14,5,28,141,70,73,95] The GQME provides an exact equation of motion for the reduced density operator of a quantum system coupled to one or more baths. It is inherently non-Markovian and non-unitary, and can accommodate multiple baths that may or may not be in thermal equilibrium internally or relative to one another.

Within the GQME framework, all bath-induced effects are encoded in a memory kernel superoperator, $\mathcal{K}(\tau)$. However, the GQME is not unique: it depends on the choice of

[1] This work was conducted in collaboration with Dr. Xiaohan Dan and Professor Eitan Geva.

This chapter is based on a manuscript currently in preparation with the following working title and authors: Callie Wilson; Xiaohan Dan; Eitan Geva. Reduced-dimensionality generalized quantum master equations for a system coupled to multiple heat baths. Manuscript in preparation. (2026).

Callie Wilson developed the theoretical analysis, implemented the reduced-dimensionality generalized quantum master equation numerical frameworks, performed the simulations, analyzed and interpreted the results, prepared the figures, and wrote the initial manuscript draft. Dr. Xiaohan Dan performed the hierarchical equations of motion (HEOM) calculations used to generate the exact benchmark results and projection-free inputs for Models 1–6, and contributed to the interpretation of the results. Professor Eitan Geva supervised the research, contributed to the interpretation of the results, and provided scientific guidance and editorial feedback during manuscript preparation.

projection operator used to define the reduced system dynamics. Different projection operators correspond to different representations of the system dynamics, ranging from the full electronic reduced density matrix to reduced-dimensional descriptions that retain only a selected subset of electronic reduced density matrix elements. As a result, the structure of the memory kernel depends explicitly on the choice of projection.

This introduces an additional layer to the question of additivity. For systems coupled to multiple baths, the decomposition of $\mathcal{K}(\tau)$ into bath-resolved contributions is not only a property of the underlying dynamics, but can also be influenced by the projection defining the reduced representation. Thus, the validity of the additive approximation for a multi-bath memory kernel does not depend exclusively on the strength of system-bath coupling, but must also be considered in conjunction with the dimensionality and resulting reduced description of the projected dynamics.

In this chapter, we explore how both the choice of projection operator and the presence of multiple baths impact the behavior of reduced-dimensionality GQMEs. In such formulations, reduced dimensionality generally introduces not only a modified memory kernel, but also an inhomogeneous term arising in order to capture the effect of the projected-out DOFs on the system DOF of interest. By comparing different projection operators, we assess the extent to which additive constructions based on the sum of single-bath memory kernels and inhomogeneous terms reproduce the full two-bath dynamics, and examine the regimes in which such additive approximations break down.

We demonstrate these ideas for a two-level system linearly coupled to two harmonic baths held initially at different temperatures. The quantum-mechanically exact dynamics are obtained using the hierarchical equations of motion (HEOM) method, from which we construct memory kernels and inhomogeneous terms associated with different projection operators. This allows us to compare the exact two-bath reduced-dimensional GQME quantities directly with additive approximations constructed from the corresponding sum of the exact single-bath contributions.

The remainder of the chapter is organized as follows. The GQME formalism for a system coupled to multiple baths is outlined in Sec. 4.2 with particular emphasis on formulations based on different projection operators, including those that give rise to reduced-dimensionality GQMEs. A demonstrative application to a model system linearly coupled to hot and cold harmonic baths is provided in Sec. 4.3. Concluding remarks are presented in Sec. 4.4. Additional details and proofs regarding the observed behaviors of the projection-dependent memory kernels and inhomogeneous terms is provided in Appendix B.

4.2 Theory

In this section, we outline the theoretical framework for GQMEs for a system coupled to multiple baths. To this end, we follow a convention, where a hat over a symbol, e.g. $\hat{A}$, indicates that the quantity is an operator and calligraphic font, e.g. $\mathcal{L}$, indicates that the quantity is a superoperator.

4.2.1 Preliminary Considerations

We consider a system coupled to multiple baths, described by the Hamiltonian

$$\hat{H} = \hat{H}_s + \hat{H}_b + \hat{H}_{bs} \quad , \tag{4.1}$$

where $\hat{H}_s$ is the system Hamiltonian, $\hat{H}_b$ is the multiple baths Hamiltonian, and $\hat{H}_{bs}$ represents the interaction between the system and the baths.

For the sake of simplicity, we focus on the case of two heat baths at different temperatures (hot and cold), noting that all conclusions can be straightforwardly generalized to an arbitrary number of baths:

$$\hat{H}_b = \hat{H}_h + \hat{H}_c \quad , \tag{4.2}$$

where $\hat{H}_h$ is the hot bath Hamiltonian and $\hat{H}_c$ is the cold bath Hamiltonian. The system-

bath interactions can, without loss of generality, be expressed as a sum of tensor products of system and bath operators:

$$\hat{H}_{bs} = \hat{H}_{sh} + \hat{H}_{sc} = \sum_j \hat{B}_{hj} \otimes \hat{S}_j + \sum_j \hat{B}_{cj} \otimes \hat{S}_j. \tag{4.3}$$

Here, $\{\hat{S}_j\}$ are system operators, $\{\hat{B}_{hj}\}$ are hot bath operators and $\{\hat{B}_{cj}\}$ are cold bath operators (the explicit forms of these operators is system-specific, and will be specified in Sec. 4.3, for the demonstrative model under consideration).

In what follows, we will also assume, without loss of generality, that

$$\mathrm{Tr}_h\left(\hat{\rho}_h^{eq}\hat{H}_{sh}\right) = \mathrm{Tr}_c\left(\hat{\rho}_c^{eq}\hat{H}_{sc}\right) = 0. \tag{4.4}$$

Here, Tr_h is the partial trace over the hot bath, Tr_c is the partial trace over the cold bath, and $\hat{\rho}_h^{eq}$ and $\hat{\rho}_c^{eq}$ are the density operators that correspond to the hot and cold baths being in thermal equilibrium:

$$\hat{\rho}_h^{eq} = \frac{e^{-\beta_h \hat{H}_h}}{Z_h} \qquad ; \qquad \hat{\rho}_c^{eq} = \frac{e^{-\beta_c \hat{H}_c}}{Z_c} \quad . \tag{4.5}$$

Here, $\beta_h = 1/k_B T_h$ is the inverse temperature of the hot bath (T_h is the hot bath temperature in K), $\beta_c = 1/k_B T_c$ is the inverse temperature of the cold bath (T_c is the cold bath temperature in K), $Z_h = \mathrm{Tr}_h(e^{-\beta_h \hat{H}_h})$ is the partition function of the hot bath and $Z_c = \mathrm{Tr}_c(e^{-\beta_c \hat{H}_c})$ is the partition function of the cold bath (k_B is the Boltzmann's constant).

Finally, we assume that the initial state of the overall system is given by the density operator:

$$\hat{\rho}(0) = \hat{\rho}_h^{eq} \otimes \hat{\rho}_c^{eq} \otimes \hat{\sigma}(0) \tag{4.6}$$

Here, $\hat{\rho}_h^{eq}$ and ρ_c^{eq} are defined as in Eq. (4.5), and $\hat{\sigma}(0)$ is the reduced density operator that describes the initial state of the system. Note that the system and baths are assumed to start out unentangled, with the baths in thermal equilibrium at their respective temperatures.

Even though this is a commonly used form of the initial state, other choices are possible. Importantly, our approach is not limited to this form and can be straightforwardly extended to other choices of initial state, including ones where the baths are initially in nonequilibrium states and entangled with the system.

It should be noted that the multiple-bath Hamiltonian in Eq. (4.1) can alternatively be viewed as a *system coupled to a single composite bath*. However, this composite bath possesses a specific structure: (1) it consists of two distinct sub-baths that are not in mutual thermal equilibrium, although each sub-bath is individually thermalized at its own temperature. (2) The system–bath interaction is given by a sum of couplings to the individual sub-baths and does not include terms of the form $\hat{S} \otimes \hat{B}_h \otimes \hat{B}_c$, which would simultaneously couple the system to both sub-baths.

4.2.2 The Nakajima-Zwanzig Equation

Next, we outline the formalism underlying the generalized quantum master equation (GQME), with emphasis on its application to a system with the Hamiltonian of the form of Eq. (4.1). We start out by assuming that the overall system is closed, which implies that the dynamics of the overall system density operator, $\hat{\rho}(t)$, is governed by the quantum Liouville equation:

$$\frac{d}{dt}\hat{\rho}(t) = -\frac{i}{\hbar}[\hat{H}, \hat{\rho}(t)] \equiv -\frac{i}{\hbar}\mathcal{L}\hat{\rho}(t) \tag{4.7}$$

In the next step, we define a projection superoperator $\mathcal{P}$ (an operator in the overall system's Liouville space). For any projection superoperator $\mathcal{P}$ which satisfies $\mathcal{P}^2 = \mathcal{P}$, the equation of motion for the projection of $\hat{\rho}(t)$, $\mathcal{P}\hat{\rho}(t)$, is then given by the *Nakajima-Zwanzig equation*:[90,149]

$$\begin{aligned}\frac{d}{dt}\mathcal{P}\hat{\rho(t)} = &-\frac{i}{\hbar}\mathcal{P}\mathcal{L}\mathcal{P}\hat{\rho}(t) \\ &- \frac{1}{\hbar^2}\int_0^t d\tau \mathcal{P}\mathcal{L}e^{-i\mathcal{Q}\mathcal{L}\tau/\hbar}\mathcal{Q}\mathcal{L}\mathcal{P}\hat{\rho}(t-\tau) \\ &- \frac{i}{\hbar}\mathcal{P}\mathcal{L}e^{-i\mathcal{Q}\mathcal{L}t/\hbar}\mathcal{Q}\hat{\rho}(0) \quad ,\end{aligned} \tag{4.8}$$

where $\mathcal{Q}$ is the complementary projection operator defined by

$$\mathcal{Q} = \mathcal{I} - \mathcal{P} \quad , \tag{4.9}$$

where $\mathcal{I}$ is the unity superoperator in the overall system Liouville space.

The specific choice of projection operator $\mathcal{P}$ is dictated by the choice of *dynamical quantity of interest* with each choice giving rise to a different equation of motion, or GQME, for the desired observable quantity of interest as defined by the choice of projection. In what follows, we will focus on four different choices of system observables of interest and the corresponding GQMEs that arise from each choice.

4.2.2.1 Full System Density Matrix GQME

The first choice of system observable of interest corresponds to the full reduced system density operator $\hat{\sigma}(t)$, which can be obtained by projecting out the bath DOFs, leading to an equation of motion for $\hat{\sigma}(t)$ based on the following choice of projection superoperator:

$$\mathcal{P}^{full}\hat{A} = \hat{\rho}_h^{eq} \otimes \hat{\rho}_c^{eq} \otimes \mathrm{Tr}_b(\hat{A}) \tag{4.10}$$

Here, $\mathrm{Tr}_b = \mathrm{Tr}_h\mathrm{Tr}_c$ (the partial trace over the Hilbert spaces of both baths) and $\hat{\rho}(t) = e^{-i\hat{H}t/\hbar}\hat{\rho}(0)e^{i\hat{H}t/\hbar} = e^{-i\mathcal{L}t/\hbar}\hat{\rho}(0)$ [see Eq. (4.7)].

Here, $\hat{\rho}_h^{eq}$ and $\hat{\rho}_c^{eq}$ are as in Eq. (4.5) and $\hat{A}$ is an overall system operator. Substituting $\mathcal{P}$ from Eq. (4.10) into Eq. (4.8) and partially tracing over the Hilbert spaces of both baths, we obtain:[113]

$$\frac{d}{dt}\hat{\sigma}(t) = -\frac{i}{\hbar}\mathcal{L}_s\hat{\sigma}(t) - \int_0^t d\tau \mathcal{K}^{full}(\tau)\hat{\sigma}(t-\tau) \quad . \tag{4.11}$$

Here, $\mathcal{L}_s\hat{\sigma}(t) \equiv [\hat{H}_s, \hat{\sigma}(t)]$ and $\mathcal{K}^{full}(\tau)$ is the memory kernel superoperator, which is explicitly

given by:

$$\mathcal{K}^{full}(\tau) = \frac{1}{\hbar^2}\mathrm{Tr}_b\left\{\mathcal{L}e^{-i\mathcal{Q}\mathcal{L}\tau/\hbar}\mathcal{Q}\mathcal{L}\hat{\rho}_h^{eq}\otimes\hat{\rho}_c^{eq}\right\} \tag{4.12}$$

It should be noted that Eq. (4.11) is the *quantum-mechanically exact equation of motion for* $\hat{\sigma}(t)$.

Inspection of the GQME, Eq. (4.11), reveals that when $\mathcal{K}^{full}(\tau) \to 0$, the system can be treated as a *closed system*, whose dynamics is unitary and fully dictated by $\hat{H}_s$ via the quantum Liouville equation $d\hat{\sigma}(t)/dt = -i\mathcal{L}_s\hat{\sigma}(t)/\hbar$. Thus, $\mathcal{K}^{full}(\tau)$ fully captures the effect of the baths on the system's dynamics. The evaluation and analysis of $\mathcal{K}^{full}(\tau)$ therefore offers a useful pathway for understanding the effect of the baths on the system's dynamics, which turns it from a unitary closed system dynamics into a non-unitary open system dynamics.

The memory kernel, $\mathcal{K}^{full}(\tau)$, can be calculated from so-called *projection free inputs (PFIs)*, i.e. inputs that do not explicitly feature $\mathcal{P}$ or $\mathcal{Q}$, via a variety of pathways.[85] In what follows, we will focus on one such pathway, where the system's time evolution superoperator, $\mathcal{U}(t)$, serves as the PFI. $\mathcal{U}(t)$ is defined as follows:

$$\hat{\sigma}(t) = \mathcal{U}(t)\hat{\sigma}(0) = \mathrm{Tr}_b\left(e^{-i\mathcal{L}t/\hbar}\hat{\rho}_h^{eq}\otimes\hat{\rho}_c^{eq}\hat{\sigma}(0)\right) \quad . \tag{4.13}$$

Given $\mathcal{U}(t)$, $\mathcal{K}^{full}(\tau)$ can be obtained by numerically solving the following integral Volterra equation:[54,88,86]

$$\mathcal{K}^{full}(\tau) = -\ddot{\mathcal{U}}(\tau) - \frac{i}{\hbar}\dot{\mathcal{U}}(\tau)\mathcal{L}_s - \int_0^\tau d\tau'\dot{\mathcal{U}}(\tau-\tau')\mathcal{K}^{full}(\tau') \tag{4.14}$$

It should be noted that in practice, $\mathcal{U}(t)$ and $\mathcal{K}^{full}(\tau)$ are represented by $n^2\times n^2$ matrices in terms of a basis of the system's Hilbert space of one's choice, where n is the dimension of the system's Hilbert space. More specifically, Eqs. (4.11) and (4.14) in matrix form are

given by

$$\begin{aligned}\frac{d}{dt}\sigma_{jk}(t) = &-\frac{i}{\hbar}\sum_{mn}\mathcal{L}_{s,jk,mn}\sigma_{mn}(t) \\ &-\sum_{mn}\int_0^t d\tau \mathcal{K}_{jk,mn}(\tau)\sigma_{mn}(t-\tau) \quad ,\end{aligned} \tag{4.15}$$

$$\begin{aligned}\mathcal{K}_{jk,mn}(\tau) = &-\ddot{\mathcal{U}}_{jk,mn}(\tau) - \frac{i}{\hbar}\sum_{pq}\dot{\mathcal{U}}_{jk,pq}(\tau)\mathcal{L}_{s,pq,mn} \\ &-\sum_{pq}\int_0^\tau d\tau' \dot{\mathcal{U}}_{jk,pq}(\tau-\tau')\mathcal{K}_{pq,mn}(\tau') \quad ,\end{aligned} \tag{4.16}$$

with $\sigma_{jk}(t) = \langle j|\hat{\sigma}(t)|k\rangle$ and the (jk,lm) matrix element of a system superoperator $\mathcal{A}(\tau)$ given by

$$\mathcal{A}_{jk,lm}(\tau) = \mathrm{Tr}\Big\{|j\rangle\langle k|^\dagger \mathcal{A}(\tau)|l\rangle\langle m|\Big\} \quad , \tag{4.17}$$

where $\mathrm{Tr} = \mathrm{Tr}_s\mathrm{Tr}_h\mathrm{Tr}_c$ is the trace over the overall system's Hilbert space, $\mathcal{A} = \mathcal{L}_s, \mathcal{K}(\tau), \mathcal{U}(\tau), \dot{\mathcal{U}}(\tau)$ and $j,k,m,l,n,p,q = 1,\ldots,n$.

4.2.2.2 A Single Population/Coherence GQME

In addition to the full GQME formalism outlined in Sec. 4.2.2.1, which describes the dynamics of all system reduced density matrix elements, $\{\sigma_{ab}(t)\}$, we also consider reduced forms of the GQME obtained through specific choices of the projection operator, $\mathcal{P}$. The simplest case corresponds to a scalar projection onto a single population element, $\sigma_{jj}(t)$, or a single coherence element, $\sigma_{jk}(t)$. Within this formulation, the memory kernel and inhomogeneous term reduce to scalar quantities that govern the dynamics of only the selected population.

The equation of motion for $\sigma_{jj}(t)$ and $\sigma_{jk}(t)$, or the scalar single-population and scalar single-coherence GQMEs, can be obtained by substituting the following projection operators

into Eq. (4.8) and tracing over both system and bath Hilbert spaces ($\mathrm{Tr} = \mathrm{Tr}_s\mathrm{Tr}_b$):

$$\begin{aligned}\mathcal{P}^{jj}(\hat{A}) &= \mathrm{Tr}\Big\{[|j\rangle\langle j| \otimes \hat{I}_s]\hat{A}\Big\}\hat{\rho}_h^{eq} \otimes \hat{\rho}_c^{eq} \otimes |j\rangle\langle j|, \\ \mathcal{P}^{jk}(\hat{A}) &= \mathrm{Tr}\Big\{[|j\rangle\langle k| \otimes \hat{I}_s]\hat{A}\Big\}\hat{\rho}_h^{eq} \otimes \hat{\rho}_c^{eq} \otimes |j\rangle\langle k|\end{aligned} \tag{4.18}$$

$$\begin{aligned}\frac{d}{dt}\sigma_{jj}(t) &= -\int_0^t d\tau \mathcal{K}_{jj,jj}^{scalar}(\tau)\sigma_{jj}(t-\tau) + I_{jj}^{scalar}(t), \\ \frac{d}{dt}\sigma_{jk}(t) &= -\int_0^t d\tau \mathcal{K}_{jk,jk}^{scalar}(\tau)\sigma_{jk}(t-\tau) + I_{jk}^{scalar}(t)\end{aligned} \tag{4.19}$$

It is important to note, the presence of a non-zero inhomogeneous term depends on the initial state of the system. Specifically, the inhomogeneous term vanishes for the density matrix element corresponding to the initially populated state and is generally nonzero for all other density matrix elements. For example, if $\sigma_{00}(0) = 1$, then $I_{00}(t) = 0$, whereas the remaining inhomogeneous terms $I_{01}(t)$, $I_{10}(t)$, and $I_{11}(t)$ will be non-zero.

The memory kernels and inhomogeneous terms for the scalar single-population GQME and the scalar single-coherence GQME are explicitly given by:

$$\begin{aligned}\mathcal{K}_{jj,jj}^{scalar}(\tau) = \frac{1}{\hbar^2}\mathrm{Tr}_b\Big\{&(|j\rangle\langle j|)\mathcal{L}e^{-i\mathcal{Q}^{jj}\mathcal{L}\tau/\hbar} \\ &\times \mathcal{Q}^{jj}\mathcal{L}\hat{\rho}_h^{eq} \otimes \hat{\rho}_c^{eq} \otimes |j\rangle\langle j|\Big\}, \\ I_{jj}^{scalar}(t) = -\frac{i}{\hbar}\mathrm{Tr}_b\Big\{&(|j\rangle\langle j|)\mathcal{L}e^{-i\mathcal{Q}^{jj}\mathcal{L}t/\hbar} \\ &\times \Big[\hat{\rho}(0) - \hat{\rho}_h^{eq} \otimes \hat{\rho}_c^{eq} \otimes |j\rangle\langle j|\sigma_{jj}(0)\Big]\Big\}\end{aligned} \tag{4.20}$$

$$
\begin{aligned}
\mathcal{K}^{scalar}_{jk,jk}(\tau) &= \frac{1}{\hbar^2}\mathrm{Tr}_b\Big\{(|j\rangle\langle k|)\mathcal{L}e^{-i\mathcal{Q}^{jk}\mathcal{L}\tau/\hbar} \\
&\quad\times \mathcal{Q}^{jk}\mathcal{L}\hat{\rho}^{eq}_h\otimes\hat{\rho}^{eq}_c\otimes|j\rangle\langle k|\Big\}, \\
I^{scalar}_{jk}(t) &= -\frac{i}{\hbar}\mathrm{Tr}_b\Big\{(|j\rangle\langle k|)\mathcal{L}e^{-i\mathcal{Q}^{jk}\mathcal{L}t/\hbar} \\
&\quad\times\Big[\hat{\rho}(0)-\hat{\rho}^{eq}_h\otimes\hat{\rho}^{eq}_c\otimes|j\rangle\langle k|\sigma_{jk}(0)\Big]\Big\}
\end{aligned}
\tag{4.21}
$$

Here, $\mathcal{K}^{scalar}_{jj,jj}(\tau)$, $\mathcal{K}^{scalar}_{kk,kk}(\tau)$, $\mathcal{K}^{scalar}_{jk,jk}(\tau)$, $I^{scalar}_{kk}(t)$and $I^{scalar}_{jk}(t)$ are scalar quantities that can be obtained by solving the following Volterra equations, constructed from a subset of selected matrix elements of the full reduced propagator $\mathcal{U}(t)$ defined in Eq. (4.13) for the full GQME outlined in Sec. 4.2.2.1:

$$
\begin{aligned}
\mathcal{K}^{scalar}_{jj,jj}(\tau) &= -\ddot{\mathcal{U}}_{jj,jj}(\tau)-\int_0^\tau d\tau\dot{\mathcal{U}}_{jj,jj}(\tau-\tau')\mathcal{K}_{jj,jj}(\tau') \\
I^{scalar}_{kk}(t) &= \dot{\mathcal{U}}_{kk,jj}(t)-\int_0^t d\tau\dot{\mathcal{U}}_{kk,kk}(t-\tau)I_{kk}(\tau)
\end{aligned}
\tag{4.22}
$$

$$
\begin{aligned}
\mathcal{K}^{scalar}_{jk,jk}(\tau) &= -\ddot{\mathcal{U}}_{jk,jk}(\tau)-\int_0^\tau d\tau\dot{\mathcal{U}}_{jk,jk}(\tau-\tau')\mathcal{K}_{jk,jk}(\tau) \\
I^{scalar}_{jk}(t) &= \dot{\mathcal{U}}_{jk,kj}(t)-\int_0^t d\tau\dot{\mathcal{U}}_{jk,jk}(t-\tau)I_{jk}(\tau)
\end{aligned}
\tag{4.23}
$$

4.2.2.3 A Populations-Only GQME

We next consider a projection onto the full set of population elements, $\{\sigma_{jj}(t)\} = \{\sigma_{00}(t),...,\sigma_{nn}(t)\}$. The corresponding equation of motion for the populations can be obtained by substituting the following projection operator into Eq. (4.8), and tracing over the bath Hilbert space:

$$
\mathcal{P}^{pop}=\sum_{j=1}^{N_e}\mathcal{P}^{jj} \tag{4.24}
$$

This leads to the following populations-only GQME:

$$\frac{d}{dt}\sigma_{jj}(t) = -\sum_{j,k=1}^{N_e}\int_0^t d\tau \mathcal{K}^{pop}_{jj,kk}(\tau)\sigma_{kk}(t-\tau) \ , \tag{4.25}$$

where the individual memory kernel matrix elements and can be obtained by solving the following Volterra equation:

$$\begin{aligned}\mathcal{K}^{pop}_{jj,kk}(\tau) = \frac{1}{\hbar}Tr\Big\{&(|j\rangle\langle j|)\mathcal{L}e^{-iQ^{pop}\mathcal{L}\tau/\hbar} \\ &\times \mathcal{Q}^{pop}\mathcal{L}\hat{\rho}^{eq}_h \otimes \hat{\rho}^{eq}_c \otimes |k\rangle\langle k|\Big\}\end{aligned} \tag{4.26}$$

The memory kernel in this case reduces to an $n \times n$ matrix, in contrast to the memory kernel in the case of the GQME for the full system reduced density matrix, where the memory kernel corresponds to a $n^2 \times n^2$ matrix. It should also be noted that $I^{pop}_{jj}(t) = 0$ when the initial system reduced density matrix is diagonal, $\sigma_{jk}(0) = \delta(j,k)\sigma_{jj}(0)$.

Similarly to the memory kernels outlined in Eq. (4.20) and (4.21), $\mathcal{K}^{pop}_{jj,kk}(\tau)$ can also be obtained from the corresponding subset of PFIs obtained from the full system propagator, $\mathcal{U}(\tau)$, outlined in Eq. (4.13):

$$\begin{aligned}\mathcal{K}^{pop}_{jj,kk}(\tau) = &-\ddot{\mathcal{U}}_{jj,kk}(\tau) \\ &-\sum_l \int_0^\tau d\tau' \dot{\mathcal{U}}_{jj,ll}(\tau-\tau')\mathcal{K}_{ll,kk}(\tau') \ .\end{aligned} \tag{4.27}$$

In this formulation, the memory kernel acts only within the population subspace and has dimensionality $n \times n$.

4.2.2.4 A Coherences-Only GQME

The final case we consider corresponds to a projection onto only the off-diagonal elements (coherences) of the reduced density matrix, $\{\sigma_{jk}(t)\}$, with $j \neq k$. The corresponding projec-

tion operator is

$$\mathcal{P}^{\rm coh} = \sum_{j\neq k}^{N_e} \mathcal{P}^{jk}. \tag{4.28}$$

Substituting this into Eq. (4.8) and tracing over the bath Hilbert space yields the coherences-only GQME:

$$\begin{aligned}
&\frac{d}{dt}\sigma_{jk}(t) \\
&= -\sum_{l\neq m}^{N_e} \int_0^t d\tau\, \mathcal{K}^{\rm coh}_{jk,lm}(\tau)\, \sigma_{lm}(t-\tau) \\
&\quad + \sum_{j\neq k}^{N_e} I^{\rm coh}_{jk}(t)\ ,
\end{aligned} \tag{4.29}$$

where $\mathcal{K}^{coh}_{jk,lm}(\tau)$ and $I^{coh}_{jk}(t)$ is explicitly given by

$$\begin{aligned}
\mathcal{K}^{coh}_{jk,lm}(\tau) &= \frac{1}{\hbar}{\rm Tr_b}\Big\{ (|{\rm j}\rangle\langle{\rm k}|)\mathcal{L}{\rm e}^{-{\rm iQ^{coh}}\mathcal{L}\tau/\hbar} \\
&\quad \times \mathcal{Q}^{coh}\mathcal{L}\hat{\rho}^{eq}_h \otimes \hat{\rho}^{eq}_c \otimes |l\rangle\langle m|\Big\}, \\
I^{coh}_{jk}(t) &= \frac{i}{\hbar}{\rm Tr}_b\Big\{ (|j\rangle\langle k|)\mathcal{L}e^{-i\mathcal{Q}^{coh}\mathcal{L}t/\hbar} \\
&\quad \times \left[\hat{\rho}(0) - \hat{\rho}^{eq}_h \otimes \hat{\rho}^{eq}_c \otimes \sum_{l\neq m} |l\rangle\langle m|\sigma_{lm}(0)\right]\Big\}\ .
\end{aligned} \tag{4.30}$$

As with the memory kernels outlined above, $\mathcal{K}^{coh}_{jk,lm}(\tau)$ can also be obtained from the corresponding subset of PFIs obtained from the full system propagator, $\mathcal{U}(\tau)$, outlined in Eq. (4.13):

$$\begin{aligned}
\mathcal{K}^{coh}_{jk,lm}(\tau) &= -\ddot{\mathcal{U}}_{jk,lm}(\tau) \\
&\quad - \sum_{pq\in coh} \int_0^\tau d\tau' \dot{\mathcal{U}}_{jk,pq}(\tau-\tau')\mathcal{K}^{coh}_{pq,lm}(\tau'), \\
I^{coh}_{jk}(t) &= \dot{\mathcal{U}}_{jk,lm} - \int_0^t d\tau \dot{\mathcal{U}}_{jk,lm}(t-\tau) I^{coh}_{lm}(\tau)\ .
\end{aligned} \tag{4.31}$$

In this formulation, the memory kernel acts only within the coherence subspace and has

dimensionality $n \times n$.

A summary of the types of GQMEs, the corresponding projection operators, and the resulting subset of reduced system dynamics associated with each projection is outlined in Tab. 4.1. It is important to note, despite differences in formulation and dimensionality, the scalar single-population and scalar single-coherence GQMEs [Eq. (4.19)], populations-only GQME [Eq. (4.25)], and coherences-only GQME [Eq. (4.29)] all still remain formally exact equations of motion for the corresponding subsets of $\{\hat{\sigma}_{ab}(t)\}$.

Table 4.1: Types of GQMEs, the corresponding projection operators used in their construction, and the subsets of reduced system dynamics associated with each projection.

,

Model Parameters		
Type of GQME	Projection Operator	Two-State System
Full	$\mathcal{P}^{full}(\hat{\rho}) = \hat{\rho}_h^{eq} \otimes \hat{\rho}_c^{eq} \otimes \mathrm{Tr}_b(\hat{\rho})$	$\mathcal{P}^{full}\begin{pmatrix}\rho_{00} & \rho_{01}\\ \rho_{10} & \rho_{11}\end{pmatrix} = \hat{\rho}_b^{eq} \otimes \begin{pmatrix}\sigma_{00} & \sigma_{01}\\ \sigma_{10} & \sigma_{11}\end{pmatrix}$
Single-population	$\mathcal{P}^{jj}(\hat{\rho}) = \mathrm{Tr}\Big\{[\lvert j\rangle\langle j\rvert \otimes \hat{I}_s]\hat{\rho}\Big\} \times \hat{\rho}_h^{eq} \otimes \hat{\rho}_c^{eq} \otimes \lvert j\rangle\langle j\rvert$	$\mathcal{P}^{00}\begin{pmatrix}\rho_{00} & \rho_{01}\\ \rho_{10} & \rho_{11}\end{pmatrix} = \hat{\rho}_b^{eq} \otimes \begin{pmatrix}\sigma_{00} & 0\\ 0 & 0\end{pmatrix}$
Single-coherence	$\mathcal{P}^{jk}(\hat{\rho}) = \mathrm{Tr}\Big\{[\lvert j\rangle\langle k\rvert \otimes \hat{I}_s]\hat{\rho}\Big\} \times \hat{\rho}_h^{eq} \otimes \hat{\rho}_c^{eq} \otimes \lvert j\rangle\langle k\rvert$	$\mathcal{P}^{01}\begin{pmatrix}\rho_{00} & \rho_{01}\\ \rho_{10} & \rho_{11}\end{pmatrix} = \hat{\rho}_b^{eq} \otimes \begin{pmatrix}0 & \sigma_{01}\\ 0 & 0\end{pmatrix}$
Populations-only	$\mathcal{P}^{pop} = \sum_{j=1}^{N_e} \mathcal{P}^{jj}$	$\mathcal{P}^{pop}\begin{pmatrix}\rho_{00} & \rho_{01}\\ \rho_{10} & \rho_{11}\end{pmatrix} = \hat{\rho}_b^{eq} \otimes \begin{pmatrix}\sigma_{00} & 0\\ 0 & \sigma_{11}\end{pmatrix}$
Coherences-only	$\mathcal{P}^{\mathrm{coh}} = \sum_{j\neq k}^{N_e} \mathcal{P}^{jk}$	$\mathcal{P}^{coh}\begin{pmatrix}\rho_{00} & \rho_{01}\\ \rho_{10} & \rho_{11}\end{pmatrix} = \hat{\rho}_b^{eq} \otimes \begin{pmatrix}0 & \sigma_{01}\\ \sigma_{10} & 0\end{pmatrix}$

4.2.3 Projection-Dependent Breakdown of Kernel and Inhomogeneous Term Additivity

The four aforementioned GQMEs in [Eqs. (4.11), (4.25), (4.29), (4.19)], are exact equations of motion for a system coupled to *two* baths. However, the structure of the resulting reduced-dimensional dynamics depends explicitly on the choice of projection operator. In particular,

the projected memory kernel and the corresponding inhomogeneous terms that arise with reduced-dimensional projections both capture the influence of the two baths on the system's dynamics.

For a given projection operator, the influence of the two baths on the system dynamics is generally non-additive, such that

$$\mathcal{K}^{proj}(\tau) \neq \mathcal{K}_h^{proj}(\tau) + \mathcal{K}_c^{proj}(\tau) \ , \tag{4.32}$$

where $\mathcal{K}_h^{proj}(\tau)$ and $\mathcal{K}_c^{proj}(\tau)$ correspond to the projected memory kernels obtained when the system is coupled only to the hot bath or only to the cold bath, respectively. Similarly, for reduced-dimensional formulations that explicitly contain an inhomogeneous term,

$$I^{proj}(t) \neq I_h^{proj}(t) + I_c^{proj}(t) \ , \tag{4.33}$$

such that the breakdown of additivity of the dynamics are governed not only by the memory kernel, but also the contributions of the inhomogeneous term.

Importantly, the degree of non-additivity depends not only on the system-bath coupling strength, but also on the choice of projection operator. In the case of weak system-bath coupling, the full system memory kernel becomes additive, as shown in Chapter 3. However, the dynamics resulting from reduced-dimensional projections can exhibit significant breakdowns of additivity, even in the limit of weak system-bath coupling, reflecting the nontrivial effects of limiting the retained system degrees of freedom through the choice of projection operator. In particular, the projections corresponding to the most significant reduction in dimensionality generally lead to the strongest breakdown in additive behavior, with the scalar single-population and scalar single-coherence projections exhibiting the largest breakdown in additivity among the projections under consideration.

Thus, deviations from additivity quantify not only collective bath effects associated with increasing system-bath coupling strength, but also projection-dependent effects introduced

through reduced-dimensional representations of the system dynamics. Comparing the exact two-bath quantities with additive constructions based on combinations of single-bath memory kernels and single-bath inhomogeneous terms therefore provides a direct measure of the extent to which different projection-dependent GQME formulations preserve additive behavior of multi-bath dynamics.

4.3 Application to a Two-Level System Linearly Coupled to Hot and Cold Harmonic Baths

In this section, we demonstrate the theoretical framework outlined in Sec. 4.2, and the insights that can be obtained from it, on a benchmark model that consists of a two-level system linearly coupled to hot and cold harmonic baths using four types of GQMEs [Eqs. (4.11), (4.19), (4.25), (4.29)], each corresponding to a different subset of reduced system density matrix elements. To this end, we adopted a model Hamiltonian previously studied by Song and Shi in Ref. 123, which has the form of Eq. (4.1), with $\{\hat{H}_s, \hat{H}_h, \hat{H}_c, \hat{H}_{sh}, \hat{H}_{sc}\}$ given by

$$\begin{aligned}
\hat{H}_s &= \Delta\hat{\sigma}_x \\
\hat{H}_h &= \sum_{j=1}^{N}\left[\frac{\hat{P}_{hj}^2}{2} + \frac{\omega_{hj}^2\hat{R}_{hj}^2}{2}\right] \ , \ \hat{H}_c = \sum_{j=1}^{N}\left[\frac{\hat{P}_{cj}^2}{2} + \frac{\omega_{cj}^2\hat{R}_{cj}^2}{2}\right] \quad , \\
\hat{H}_{sh} &= \sum_{j=1}^{N} c_{hj}\hat{R}_{hj}\hat{\sigma}_z \ , \ \hat{H}_{sc} = \sum_{j=1}^{N} c_{cj}\hat{R}_{cj}\hat{\sigma}_z \quad .
\end{aligned} \tag{4.34}$$

Here, $\hat{\sigma}_x = |0\rangle\langle 1| + |1\rangle\langle 0|$, $\hat{\sigma}_y = -i(|0\rangle\langle 1| - |1\rangle\langle 0|)$ and $\hat{\sigma}_z = |0\rangle\langle 0| - |1\rangle\langle 1|$ are the Pauli operators, with $|0\rangle$ and $|1\rangle$ corresponding to the eigen states of $\hat{\sigma}_z$ with eigenvalues $+1$ and -1, respectively; $\{\hat{R}_{hj}, \hat{P}_{hj}, \omega_{hj}, c_{hj} | j = 1, \ldots, N\}$ and $\{\hat{R}_{cj}, \hat{P}_{cj}, \omega_{cj}, c_{cj} | j = 1, \ldots, N\}$ denote the mass-weighted coordinates, momenta, frequencies, and coupling coefficients of the hot and cold bath modes, respectively. It should be noted that for this model, the hot and cold baths' Hamiltonians are identical and coupled to the two-level system in the same way.

The values of $\{\omega_{hj}, c_{hj} | j = 1, \ldots, N\}$ and $\{\omega_{cj}, c_{cj} | j = 1, \ldots, N\}$ are extracted from spectral density functions, which are assumed to be identical for both baths and given by ($\alpha = h, c$):[123]

$$\begin{aligned} I_\alpha(\omega) &= \frac{\pi}{2} \sum_{j=1}^{N} \frac{c_{\alpha j}^2}{\omega_{\alpha j}} \delta(\omega - \omega_{\alpha j}) \\ &= \frac{\eta_\alpha \omega \gamma_{\alpha,1} \gamma_{\alpha,2} \gamma_{\alpha,3}}{(\omega^2 + \gamma_{\alpha,1}^2)(\omega^2 + \gamma_{\alpha,2}^2)(\omega^2 + \gamma_{\alpha,3}^2)} \quad . \end{aligned} \tag{4.35}$$

The initial state of the overall system is assumed to be given by Eq. (4.6), with $\hat{\sigma}(0) = |0\rangle\langle 0|$:

$$\hat{\rho}(0) = \hat{\rho}_h^{eq} \otimes \hat{\rho}_c^{eq} \otimes |0\rangle\langle 0| \quad . \tag{4.36}$$

Here, $\hat{\rho}_h^{eq}$ and $\hat{\rho}_c^{eq}$ are defined as in Eq. (4.5).

Calculations were performed for six realizations of this model that correspond to the values of the parameters outlined in Table 4.2. The values of β_h, β_c, $\gamma_{\alpha,1}$, $\gamma_{\alpha,2}$ and $\gamma_{\alpha,3}$ are the same for all six models. The models differ with respect to the values of Δ ($\Delta = 0.1$ for models 1-3, while $\Delta = 0.5$ for models 4-6) and η_α ($\eta_\alpha = 0.01$ for models 1 and 4, $\eta_\alpha = 0.1$ for models 2 and 5, and $\eta_\alpha = 1.0$ for models 3 and 6). It should be noted that quantum-mechanically exact results obtained via the HEOM method were reported in Ref. 123 for models 2,3,5 and 6. Models 1 and 4 were added in this study since they correspond to weaker system-bath coupling, in order to demonstrate the more additive nature of the memory kernel in this case.

Calculating the memory kernels of the four types of GQMEs outlined in Sec. 4.2.2.3, requires solving the Volterra equations, [Eqs. (4.14), (4.22), (4.23), (4.27), (4.31)], which requires $\mathcal{U}(\tau)$, as the PFI, Eq. (4.17). The different types of GQMEs only differ with respect to the specific matrix elements of $\mathcal{U}(\tau)$ that are required to calculate the memory kernel and inhomogeneous term. Calculating the memory kernel corresponding to the full set of reduced density matrix elements, [Eq. (4.17)], requires calculating all 16 matrix elements,

Table 4.2: Spin-Boson Model Parameters

Model Parameters								
Model #	ϵ	Δ	β_h	β_c	η_α	$\gamma_{\alpha,1}$	$\gamma_{\alpha,2}$	$\gamma_{\alpha,3}$
1	0.0	0.1	0.5	1.5	0.01	0.5	1.0	1.5
2	0.0	0.1	0.5	1.5	0.1	0.5	1.0	1.5
3	0.0	0.1	0.5	1.5	1.0	0.5	1.0	1.5
4	0.0	0.5	0.5	1.5	0.01	0.5	1.0	1.5
5	0.0	0.5	0.5	1.5	0.1	0.5	1.0	1.5
6	0.0	0.5	0.5	1.5	1.0	0.5	1.0	1.5

while the memory kernels of the populations-only GQME and the coherences-only GQME, [Eqs. (4.27), (4.29)], requires only a subset of four matrix elements, and calculating the memory kernel of the single-population/single-coherences GQMEs, [Eq. (4.19)], requires only a single matrix element. To this end, we calculated the 4×4 matrix that represents $\mathcal{U}(\tau)$ via the HEOM method, and its time derivatives, $\dot{\mathcal{U}}(\tau)$ and $\ddot{\mathcal{U}}(\tau)$, via the finite central difference method available on the NumPy Python library. The Volterra equations were then solved numerically via the iterative algorithm outlined in Refs. 88, 26, followed by propagation of the GQMEs using a fourth-order Runge-Kutta method.

It should be noted that the distinction between populations and coherences is basis-dependent. In what follows, populations and coherences refer to the diagonal and off-diagonal elements of the density matrix representing $\hat{\sigma}(t)$ in terms of the eigen-basis of $\hat{\sigma}_z$. Since the system Hamiltonian in this case is $\hat{H}_s = \Delta\hat{\sigma}_x$, the dynamics of σ_x correspond to energy relaxation, while the dynamics of σ_y and σ_z correspond to dephasing (both defined, as they usually are, in terms of the eigen-basis of $\hat{H}_s$). In other words, coherences and populations in the σ_z representation correspond to populations and coherences in the σ_x representation, respectively.

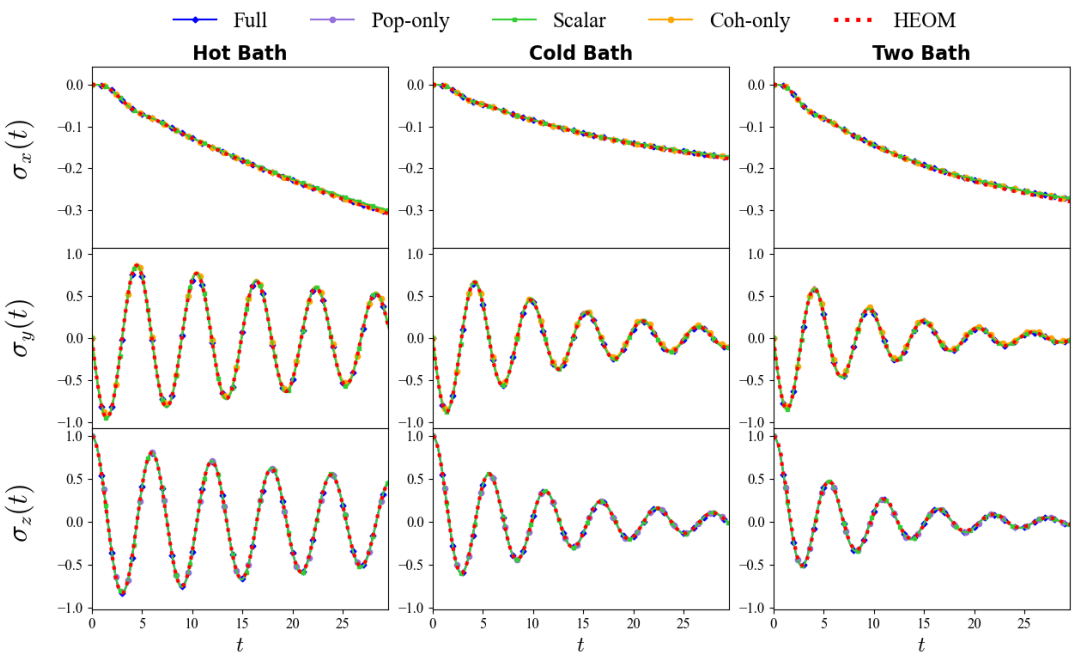


Figure 4.1: $\sigma_z(t)$, $\sigma_y(t)$, $\sigma_x(t)$ as a function of time for model 5 in Table 4.2. Shown are exact results calculated using HEOM (red dotted line), and four variations of GQME-based results with the exact memory kernel $\mathcal{K}(\tau)$: (1) the full GQME (solid blue line with diamonds), (2) a combination of single-population scalar GQMEs for $\sigma_{DD}(t)$, $\sigma_{AA}(t)$, $\sigma_{DA}(t)$, and $\sigma_{AD}(t)$ (solid green line with squares), (3) a coherences-only GQME (orange solid line with square), and (4) a populations-only GQME (solid purple line with circles).

4.3.1 Results

In Fig. 4.1, we begin by examining the effect of the four reduced-dimensional projection operators outlined in Sec. 4.2.2.3 on the dynamics of the system for model 5 (with analagous behavior observed across models 1-6). Specifically, we compare the dynamics of the three components of the Bloch vector, $[\sigma_x(t), \sigma_y(t), \sigma_z(t)]$, where $\sigma_u(t) = \langle \hat{\sigma}_u \rangle(t)$, obtained using four unique GQME formulations: (1) The full electronic GQME, Eq. (4.11), (2) A populations-only GQME, Eq. (4.25), (3) A coherences-only GQME, Eq. (4.29), (4) A scalar single-population/single-coherence GQME, Eq. (4.19).

We first note that the dynamics generated via all four reduced-dimensional GQME realizations using projections of HEOM-based exact single-bath memory kernels (hot and cold), and exact two-bath memory kernels, as well as the corresponding exact single-bath and two-

bath inhomogeneous terms that arise when necessary, directly coincide with those obtained via direct use of the HEOM method for all models considered. This agreement is to be expected because, regardless of the choice of projection, the corresponding GQMEs still remain formally exact equations of motion for the resulting full and corresponding subsets of the reduced system density matrix for both the single-bath and two-bath systems.

Having verified that the four reduced-dimensional GQME formulations recover the exact HEOM dynamics when obtained with projections of the exact two-bath memory kernels and corresponding inhomogeneous terms, we next examine the three components of the Bloch vector as obtained with the same four reduced-dimensionality GQMEs, but calculated instead with projections of the approximate additive memory kernels, $\mathcal{K}^{proj}(\tau) \approx \mathcal{K}_h^{proj}(\tau) + \mathcal{K}_c^{proj}(\tau)$, and the corresponding approximate additive inhomogeneous terms, $I(t) \approx I_h(t) + I_c(t)$ that arise when applicable. The results of this comparison for models 1-6 are shown in Fig. 4.2.

Inspection of Fig. 4.2 reveals several trends. First, we note that the non-additivity of the projected memory kernel depends not only on system-bath coupling strength (as measured by η_α), but also rather heavily on the degree of projection. More specifically, in the case of the full GQME, the non-additivity of the memory kernel is only evident in the presence of strong system bath coupling ($\eta_\alpha = 1.0$), with σ_x and σ_z showing the greatest sensitivity to the non-additive nature of the bath-induced effect, an effect that can be traced back to the fact that the Hamiltonian in Eq. (4.1) is expressed in terms of $\hat{\sigma}_x$ and $\hat{\sigma}_z$, but not $\hat{\sigma}_y$. In contrast, the system dynamics calculated from the reduced-dimensionality GQME frameworks exhibit substantial degrees of non-additivity, even in the weak system-bath coupling ($\eta_\alpha = 0.01$), where the resulting dynamics from the full system memory kernel is shown to be nearly additive across the range of system-bath coupling strengths under consideration. The magnitude of the observed breakdown in additivity further increases with the degree of dimensional reduction created by the projection, with the dynamics becoming increasingly non-additive in the case of the populations-only and coherences-only GQME frameworks, and the most pronounced degree of non-additivity arising in the case of the

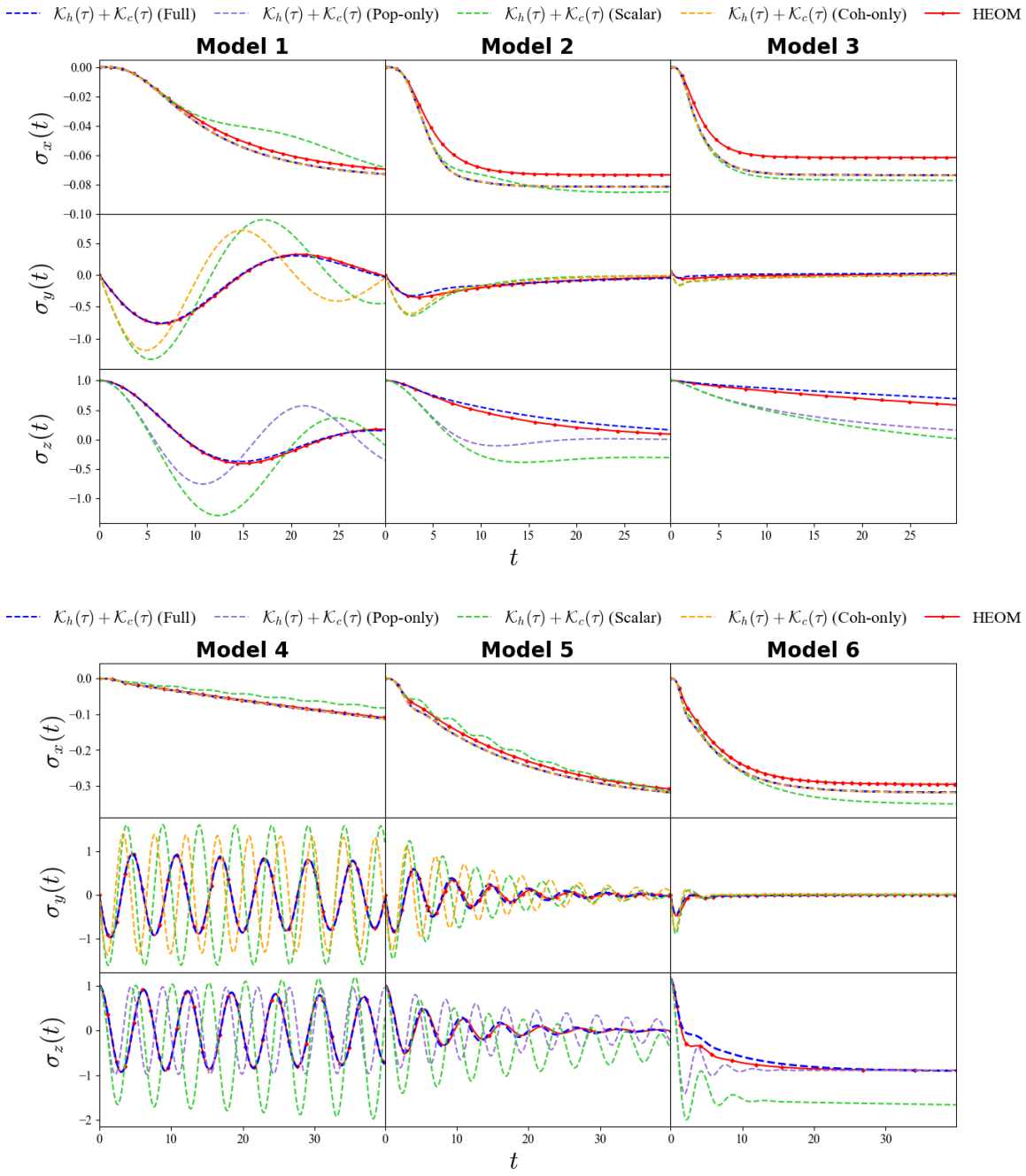


Figure 4.2: $\sigma_x(t)$, $\sigma_y(t)$ and $\sigma_z(t)$ as a function of time for models 1-3 (top panel) and models 4-6 (bottom panel) in Table 4.2. Shown are exact results calculated using HEOM (red dotted line), four variations of GQME-based results with the approximate additive memory kernel $\mathcal{K}_h(\tau)+\mathcal{K}_c(\tau)$: (1) the full GQME (dashed blue line), (2) a combination of single-population scalar GQMEs for $\sigma_{DD}(t)$, $\sigma_{AA}(t)$, $\sigma_{DA}(t)$, and $\sigma_{AD}(t)$ (dashed green line), (3) a coherences-only GQME (orange dashed line), (4) a populations-only GQME (purple dashed line).

scalar single-population and scalar single-coherence GQMEs.

This trend arises as a direct consequence of the fact that for a two-bath system, additivity is already an approximation on its own that neglects correlations arising between the hot and cold baths that are present in the exact two-bath kernel. When this approximation is combined with reduced-dimensional projections of the system, there is further restriction on the set of system degrees of freedom used to represent the dynamics. The resulting GQMEs become increasingly sensitive to the loss of collective bath-induced effects associated with the presence of multiple baths. As a result, lower-dimensional GQMEs exhibit progressively larger deviations from additive behavior with the most pronounced breakdown in additivity occurring in the single-scalar GQME formulation.

Further insight into the interplay of non-additivity arising from both the bath-induced effects and the reduced-dimensional descriptions of the system dynamics can be obtained by comparing $\mathcal{K}^{proj}(\tau)$ with $\mathcal{K}_h^{proj}(\tau)+\mathcal{K}_c^{proj}(\tau)$. It is important to note that the dimensionality of $\mathcal{K}^{proj}(\tau)$, $\mathcal{K}_h^{proj}(\tau)$, and $\mathcal{K}_c^{proj}(\tau)$ depends on the choice of projection operator. In each case, matrix elements vanish due to the symmetry of the spin-boson Hamiltonian in the $\hat{\sigma}_z$ eigen-basis, while additional symmetry relations between the remaining non-zero elements further reduce the number of independent matrix elements that must be evaluated.[88,71]

As a result, only a small subset of independent, non-vanishing matrix elements of $\mathcal{K}^{proj}(\tau)$ are present in the calculations of the GQMEs under consideration. For the populations-only GQME, the kernel is represented by a 2×2 matrix in the subspace $\{|0\rangle\langle 0|, |1\rangle\langle 1|\}$. Conservation of population imposes relationships among the kernel elements, reducing the number of independent matrix elements to $\{\mathcal{K}^{pop}_{00,00}(\tau), \mathcal{K}^{pop}_{00,11}(\tau)\}$. For the coherences-only GQME, the kernel is represented by a 2×2 matrix in the subspace $\{|0\rangle\langle 1|, |1\rangle\langle 0|\}$. Since, $\mathcal{K}_{jk,lm}(\tau) = \mathcal{K}^{coh*}_{kj,ml}(\tau)$, the memory kernel can be determined by the two independent elements: $\{\mathcal{K}^{coh}_{01,01}(\tau), \mathcal{K}^{coh}_{10,01}(\tau)\}$. For the scalar single-population and single-coherence GQMEs, the memory kernels reduce to single, independent elements, $\{\mathcal{K}^{scalar}_{00,00}(\tau)\}$ and $\{\mathcal{K}^{scalar}_{01,01}(\tau)\}$, respectively.

A comparison of projection-dependent nonzero matrix elements of $\mathcal{K}^{proj}(\tau)$ vs. $\mathcal{K}_h^{proj}(\tau) + \mathcal{K}_c^{proj}(\tau)$ is shown in Figs. 4.3–4.8 for models 1-6 (see Table 4.2). The non-additive contributions of the real and imaginary parts of the independent, non-vanishing matrix elements, $\Delta\mathcal{K}^{proj}(\tau) = \mathcal{K}^{proj}(\tau) - \mathcal{K}_h^{proj}(\tau) - \mathcal{K}_c^{proj}(\tau)$, are shown in Fig. 4.9.

While the scalar formulations of the kernels consistently exhibit the largest deviations from additive behavior, the populations-only and coherences-only GQME kernel elements display a more complex dependence on both system-bath coupling strength and the specific kernel element considered. In particular, weak system-bath coupling does not necessarily lead to uniformly smaller deviations in additivity. Even though the magnitude of the non-additive contribution arising from collective bath effects may decrease in the case of weak system-bath coupling, the populations-only, coherences-only, single-population/single-coherence memory kernels, $\mathcal{K}^{pop}(\tau)$, $\mathcal{K}^{coh}(\tau)$, $\mathcal{K}^{scalar}(\tau)$ exhibit deviations from additive behavior over comparatively long timescales, even in the weakest system-bath coupling considered here ($\eta = 0.01$). This observation suggests that the reduced-dimensional descriptions of the system dynamics are affected not only by the magnitude of the neglected multi-bath collective effects, but also by the timescale over which these effects persist and influence the projected dynamics. Additional details regarding the behavior of the memory kernels are provided in Appendix B, including a decomposition of the individual single-bath memory kernels and a comparison of their magnitudes with those of the corresponding two-bath memory kernels to further clarify the origins of the observed non-additive behavior shown in Figs. 4.3–4.8.

Finally, dimensional reduction affects not only the structure of the memory kernel, but also introduces inhomogeneous terms into the corresponding GQMEs. These terms arise as a result of the projected dynamics no longer explicitly retaining the full system density matrix elements which therefore must be accounted for. For the projections under consideration, and an initial condition of $\sigma_{00} = 1$, the inhomogeneous term is non-zero in the case of the acceptor population, σ_{11} in the scalar single-population, scalar single-coherence, and coherences-only GQME [Eqs. (4.21), (4.20) and (4.30)]. Consequently, the additivity of the inhomogeneous

term, $I^{proj}(t)$ can also be assessed in the same manner as the memory kernel by comparing the exact two-bath $I^{proj}(t)$ with the additive approximation, $I_h^{proj}(t) + I_c^{proj}(t)$. The real and imaginary components of the non-zero inhomogeneous terms, $I^{proj}(t)$ vs. $I_h^{proj}(t) + I_c^{proj}(t)$ are shown in Fig. 4.10.

For the coherence-based projections, a key feature is that the associated inhomogeneous terms are observed to generally not decay to zero at long times, suggesting a sustained contribution to the overall dynamics. However, this contribution is not independent of the coherence-based memory kernel elements, which also exhibit non-zero long-time behavior (see Figs. 4.3–4.8). As a result, it is only the combined sum of the inhomogeneous term and the convolution of the memory kernel that leads to an effective cancellation in the projected dynamics, rather than the individual contributions alone. This cancellation is further illustrated in Appendix B.

4.4 Concluding Remarks

The GQME framework provides a general approach for simulating energy, charge, and coherence transfer dynamics, as well as decoherence, in molecular systems embedded in complex environments. While Chapter 3 has focused primarily on the full system density matrix and the corresponding memory kernel, the present chapter extends the analysis to reduced-dimensionality GQMEs for a spin-boson model simultaneously coupled to hot and cold harmonic baths.

Using quantum-mechanically exact memory kernels obtained from hierarchical equations of motion (HEOM), we demonstrated that three GQMEs: (1) populations-only, (2) coherences-only, (3) single population/coherence scalar reproduce the exact dynamics despite retaining only a reduced subset of the system degrees of freedom. These results establish that even with a substantially-reduced description of the corresponding reduced density matrix, we retain formally exact equations of motion, provided that the memory kernels and inhomogeneous terms are also exact.

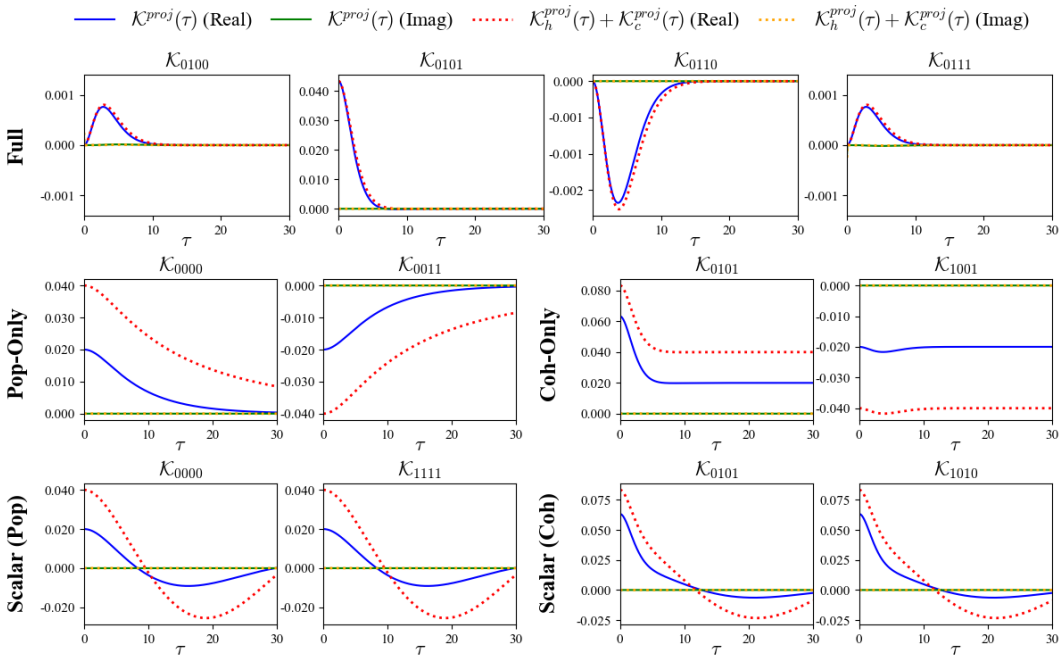


Figure 4.3: A comparison of the independent and non-vanishing matrix elements of $\mathcal{K}^{proj}(\tau)$ vs. $\mathcal{K}_h^{proj}(\tau) + \mathcal{K}_c^{proj}(\tau)$, for Model 1 (see Table 4.2). The independent matrix elements are projection dependent. For $\mathcal{K}^{full}(\tau)$, the four independent nonzero elements are (01,00), (01,01), (01,10), (01,11). For $\mathcal{K}^{pop}(\tau)$, the two independent elements are: (00,00), (00,11), and for $\mathcal{K}^{coh}(\tau)$, the two independent elements are: (01,01), (10,01). For $\mathcal{K}^{scalar}(\tau)$ the two population independent elements are: (00,00), (11,11), and the two coherence elements are: (01,01), (10,10).

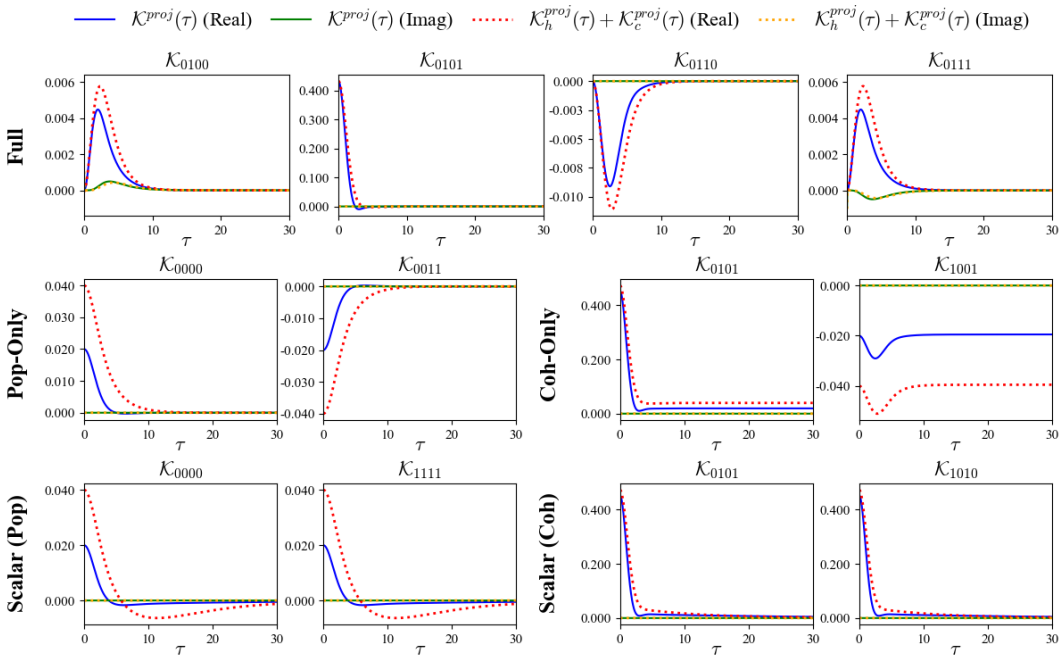


Figure 4.4: A comparison of the independent and non-vanishing matrix elements of $\mathcal{K}^{proj}(\tau)$ vs. $\mathcal{K}_h^{proj}(\tau) + \mathcal{K}_c^{proj}(\tau)$, for Model 2 (see Table 4.2). The independent matrix elements are projection dependent. For $\mathcal{K}^{full}(\tau)$, the four independent nonzero elements are (01,00), (01,01), (01,10), (01,11). For $\mathcal{K}^{pop}(\tau)$, the two independent elements are: (00,00), (00,11), and for $\mathcal{K}^{coh}(\tau)$, the two independent elements are: (01,01), (10,01). For $\mathcal{K}^{scalar}(\tau)$ the two population independent elements are: (00,00), (11,11), and the two coherence elements are: (01,01), (10,10).

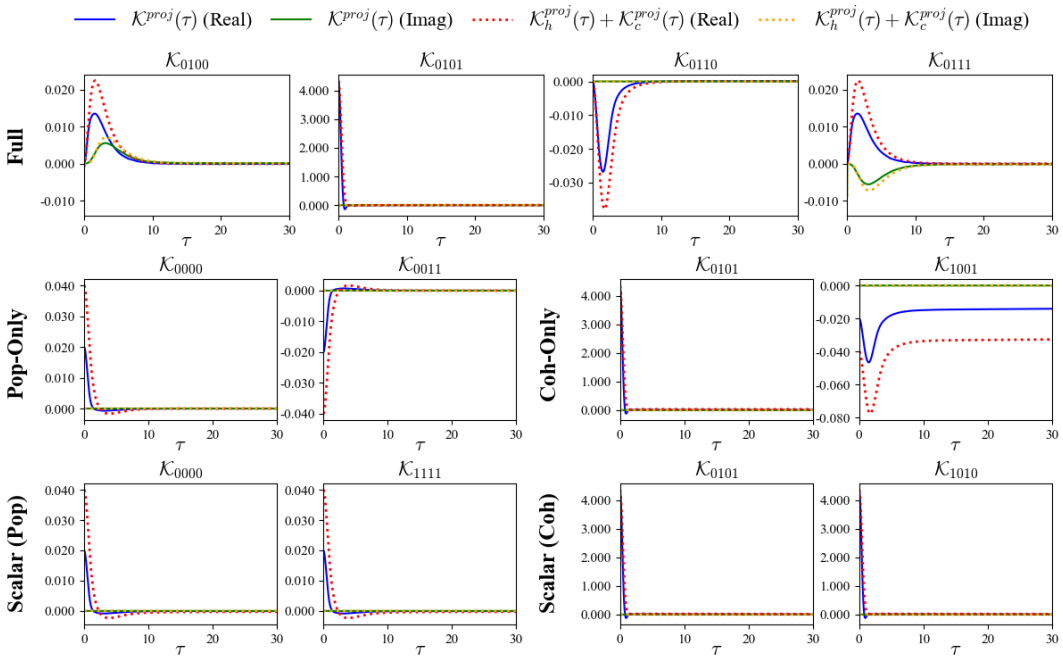


Figure 4.5: A comparison of the independent and non-vanishing matrix elements of $\mathcal{K}^{proj}(\tau)$ vs. $\mathcal{K}_h^{proj}(\tau) + \mathcal{K}_c^{proj}(\tau)$, for Model 3 (see Table 4.2). The independent matrix elements are projection dependent. For $\mathcal{K}^{full}(\tau)$, the four independent nonzero elements are (01,00), (01,01), (01,10), (01,11). For $\mathcal{K}^{pop}(\tau)$, the two independent elements are: (00,00), (00,11), and for $\mathcal{K}^{coh}(\tau)$, the two independent elements are: (01,01), (10,01). For $\mathcal{K}^{scalar}(\tau)$ the two population independent elements are: (00,00), (11,11), and the two coherence elements are: (01,01), (10,10).

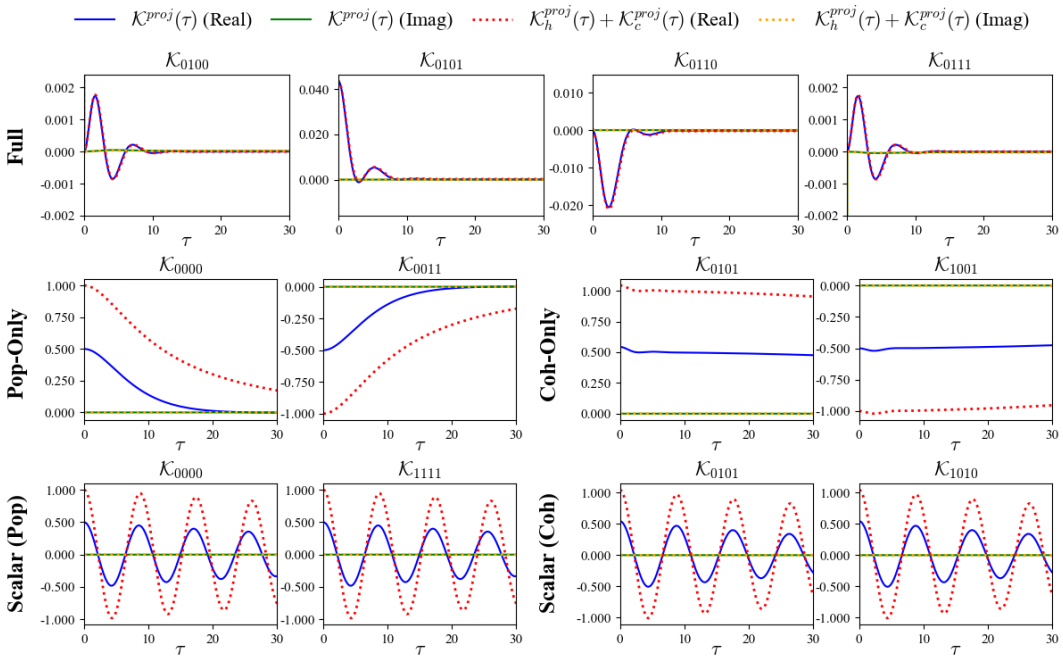


Figure 4.6: A comparison of the independent and non-vanishing matrix elements of $\mathcal{K}^{proj}(\tau)$ vs. $\mathcal{K}_h^{proj}(\tau) + \mathcal{K}_c^{proj}(\tau)$, for Model 4 (see Table 4.2). The independent matrix elements are projection dependent. For $\mathcal{K}^{full}(\tau)$, the four independent nonzero elements are (01,00), (01,01), (01,10), (01,11). For $\mathcal{K}^{pop}(\tau)$, the two independent elements are: (00,00), (00,11), and for $\mathcal{K}^{coh}(\tau)$, the two independent elements are: (01,01), (10,01). For $\mathcal{K}^{scalar}(\tau)$ the two population independent elements are: (00,00), (11,11), and the two coherence elements are: (01,01), (10,10).

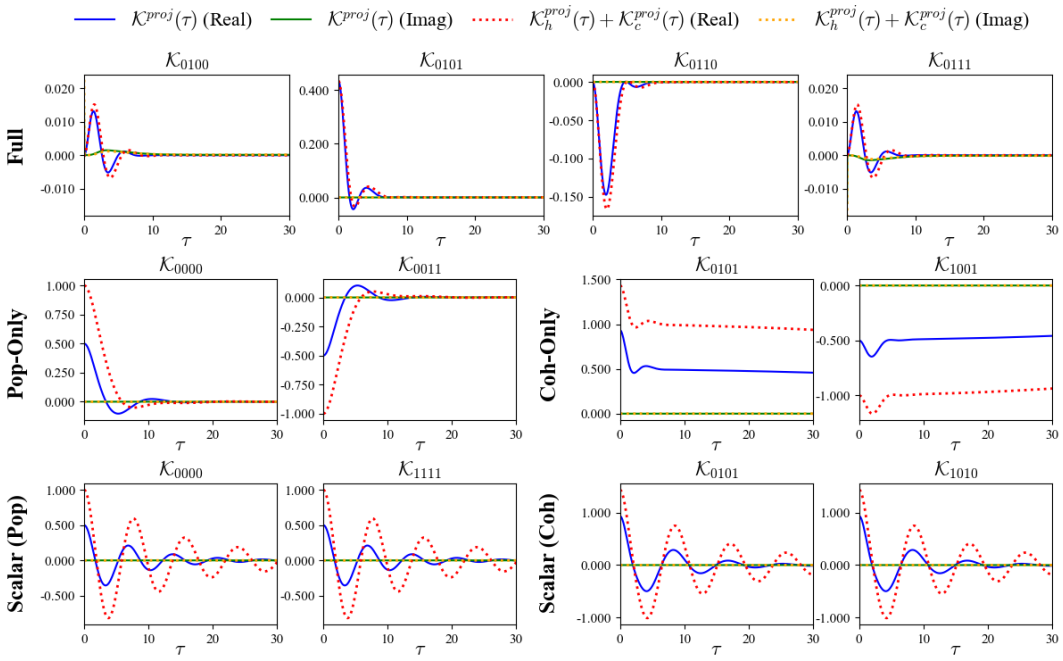


Figure 4.7: A comparison of the independent and non-vanishing matrix elements of $\mathcal{K}^{proj}(\tau)$ vs. $\mathcal{K}_h^{proj}(\tau) + \mathcal{K}_c^{proj}(\tau)$, for Model 5 (see Table 4.2). The independent matrix elements are projection dependent. For $\mathcal{K}^{full}(\tau)$, the four independent nonzero elements are (01,00), (01,01), (01,10), (01,11). For $\mathcal{K}^{pop}(\tau)$, the two independent elements are: (00,00), (00,11), and for $\mathcal{K}^{coh}(\tau)$, the two independent elements are: (01,01), (10,01). For $\mathcal{K}^{scalar}(\tau)$ the two population independent elements are: (00,00), (11,11), and the two coherence elements are: (01,01), (10,10).

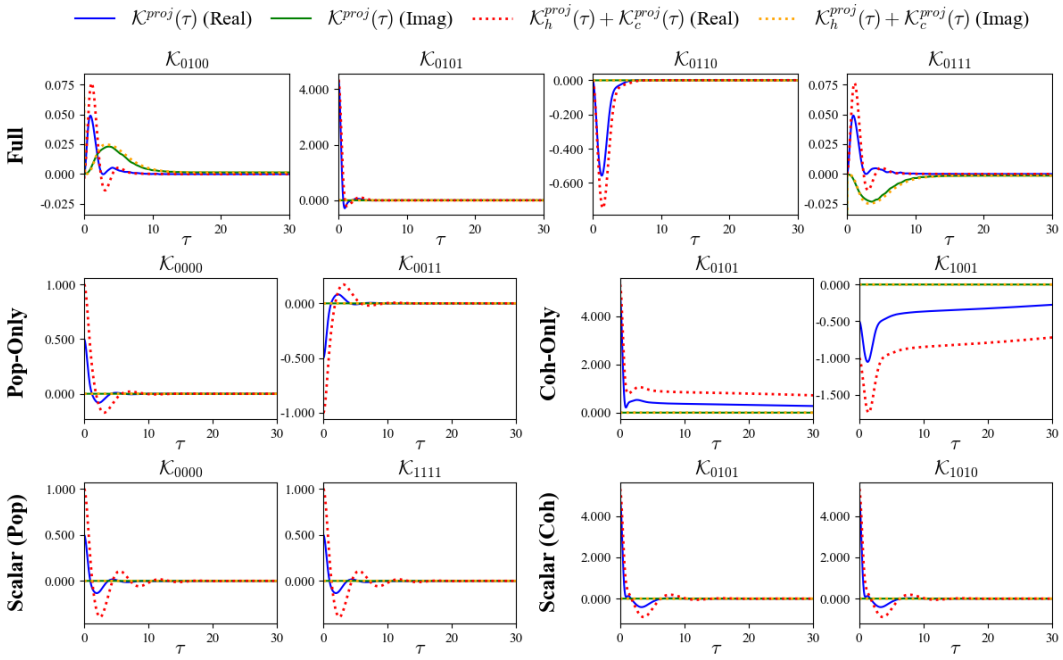


Figure 4.8: A comparison of the independent and non-vanishing matrix elements of $\mathcal{K}^{proj}(\tau)$ vs. $\mathcal{K}_h^{proj}(\tau) + \mathcal{K}_c^{proj}(\tau)$, for Model 6 (see Table 4.2). The independent matrix elements are projection dependent. For $\mathcal{K}^{full}(\tau)$, the four independent nonzero elements are (01,00), (01,01), (01,10), (01,11). For $\mathcal{K}^{pop}(\tau)$, the two independent elements are: (00,00), (00,11), and for $\mathcal{K}^{coh}(\tau)$, the two independent elements are: (01,01), (10,01). For $\mathcal{K}^{scalar}(\tau)$ the two population independent elements are: (00,00), (11,11), and the two coherence elements are: (01,01), (10,10).

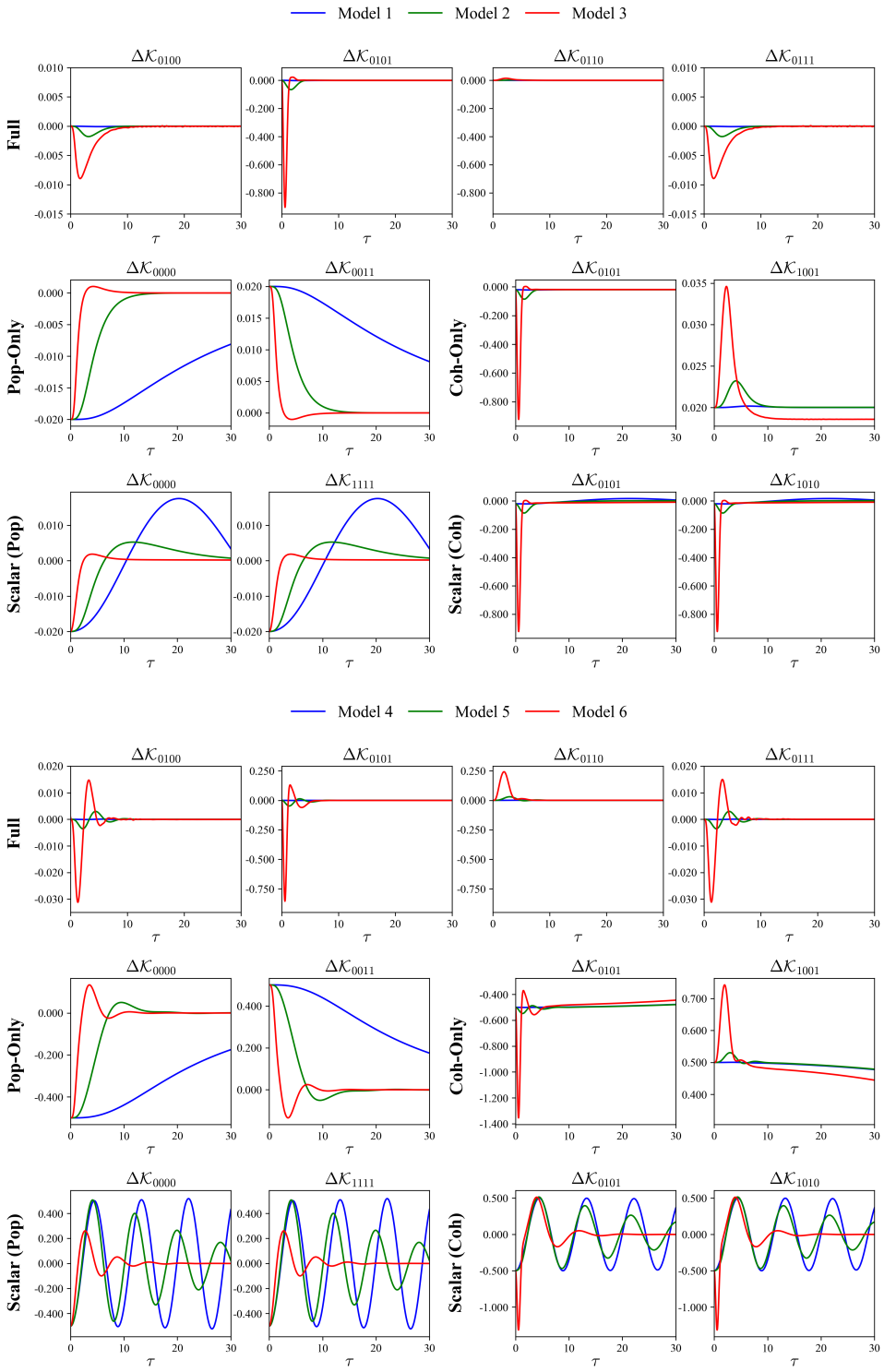


Figure 4.9: The real parts of the non-vanishing, independent kernel matrix elements of $\Delta\mathcal{K}^{proj}(\tau) = \mathcal{K}^{proj}(\tau) - \mathcal{K}_h^{proj}(\tau) - \mathcal{K}_c^{proj}(\tau)$ for the full GQME, populations-only and coherences-only GQMEs and the scalar population/coherence GQMEs, for the six spin-boson models under consideration. The number of independent kernel matrix elements are projection-dependent.

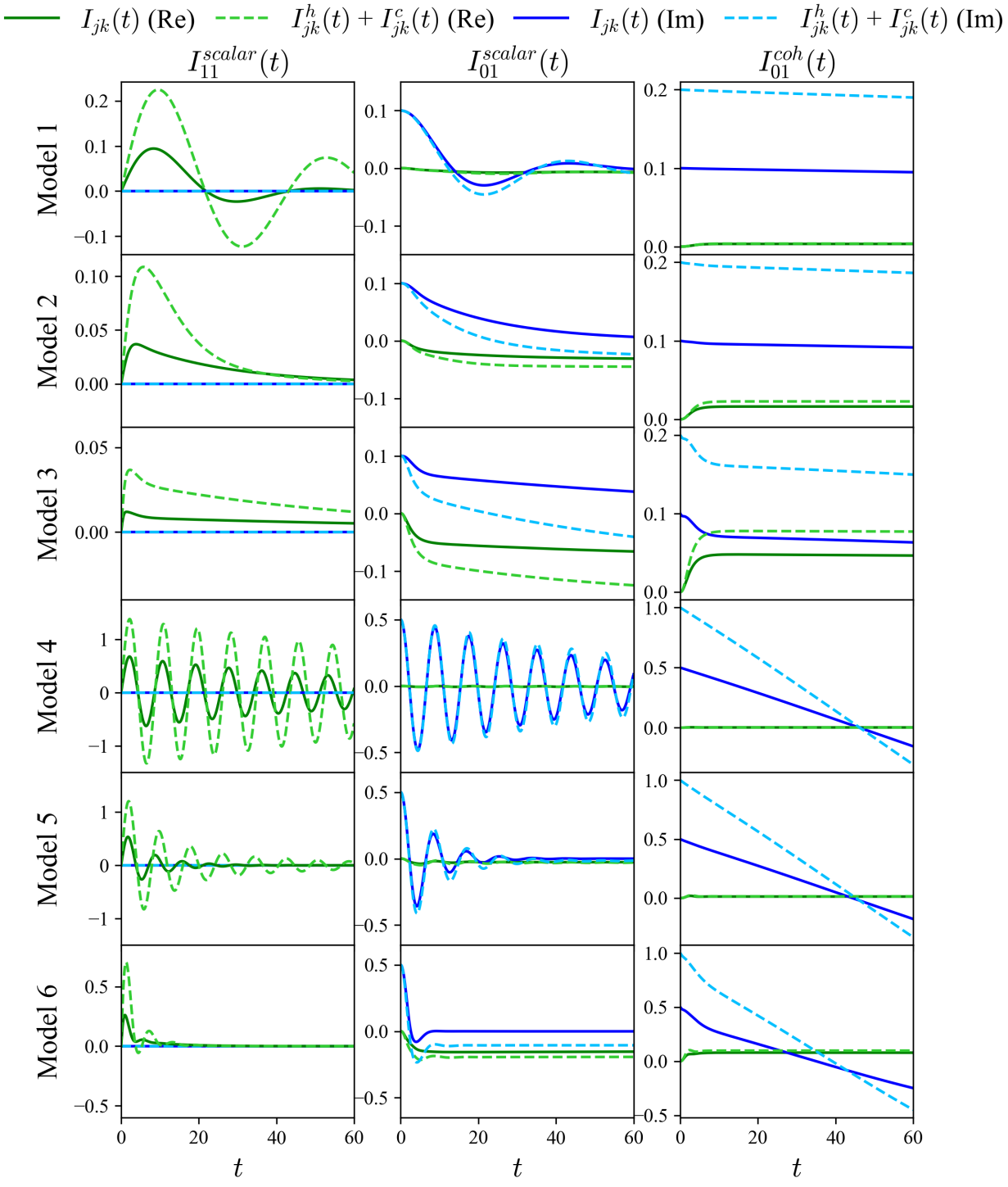


Figure 4.10: Shown are the real and imaginary parts of the independent non-zero inhomogeneous terms, $I_{11}^{scalar}(t)$, $I_{01}^{scalar}(t)$, and $I_{01}^{coh}(t)$ from Eqs. (4.20), (4.21), (4.30) for the six spin-boson models under consideration.

The reduced-dimensionality GQMEs under consideration also provide a useful framework for examining the influence of multi-bath environments on the system dynamics through the lens of investigating the additivity of the memory kernel and inhomogeneous terms. By comparing the exact two bath memory kernels and inhomogeneous terms with approximations constructed from the sum of single-bath memory kernels and inhomogeneous terms, we showed that the degree of non-additivity in the kernel depends not only on the strength of system-bath coupling, but also on the choice of projection. While the full system GQME remains relatively insensitive to this approximation, non-additivity becomes increasingly pronounced as the dimensionality of the projected density matrix is reduced, with the most prominent breakdown in additivity observed in the case of the scalar single-population/single-coherence GQMEs. These results indicate that the collective bath effects arising in a multi-bath model manifest differently under various projected descriptions of the dynamics, and the effect can be further amplified when more system degrees of freedom are projected out. One potential explanation for the observed breakdown in additivity is that reduced-dimensionality GQMEs may be sensitive to the choice of basis representation, unlike the full system GQME outlined in Chapter 3. Preliminary results suggest that formulating the single-bath, reduced-dimensionality GQMEs in the eigen-representation of the system will restore a more additive description of the dynamics.

The analysis presented in this work demonstrates that reduced-dimensionality GQMEs can accurately capture both population and coherence dynamics in multi-bath systems when combined with quantum-mechanically exact input methods. At the same time, they highlight the limitations of commonly used approximations, particularly in reduced formulations where projection choices become increasingly important. The quantum-mechanically exact memory kernels obtained from HEOM therefore provide a valuable benchmark for assessing the accuracy of approximate input methods in analogous systems.

CHAPTER 5

A Mixed Quantum-Classical Generalized Quantum Master Equation for a System Coupled to Multiple Heat Baths[1]

5.1 Introduction

A wide variety of approximate methods that can be used for simulating quantum dynamics have been developed, including the Ehrenfest (mean-field/MF) method,[77,88] as well as mapping Hamiltonian methods based on linearized semiclassical (LSC) approximations.[114,115,118,117,116,119,47,46,120,139,140,78] These approaches are particularly valuable because they provide a computationally cost-effective alternative to exact quantum dynamics methods. Within the generalized quantum master equation framework studied in Chapters 3 and 4, approximate methods can serve as inputs from which the memory kernels and corresponding equations of motion can be constructed, enabling an accurate description of system dynamics without the need to explicitly evaluate the exact memory kernel, which is often the primary computational bottleneck.

While these methods are well-tested for single-bath environments, their extension to multi-bath systems remains a relatively unexplored area of interest.[88,84,70,105] In particular, a central question is the effectiveness of approximate input methods at capturing the dynamical

[1]This work was conducted in collaboration with Professor Eitan Geva.

This chapter is based on a manuscript currently in preparation by Callie Wilson and Eitan Geva (2026).

Callie Wilson developed the theoretical analysis, implemented the numerical framework, performed the simulations, analyzed and interpreted the results, prepared the figures, and wrote the initial manuscript draft. Professor Eitan Geva supervised the research, contributed to the interpretation of the results, and provided overall scientific guidance and feedback during manuscript preparation.

effects arising from multiple bath environments. Among the various approximate methods available, the Ehrenfest method is a particularly useful choice due to its mixed quantum-classical formulation, in which the bath degrees of freedom are treated classically while the system degrees of freedom are treated quantum-mechanically. This enables a significant reduction in the overall computational cost while still retaining many of the key quantum-dynamical features of the system of interest. The goal of this chapter is therefore to extend the applicability of the Ehrenfest method to a system coupled to two baths, as described in Chapters 3 and 4.

The rest of this chapter is organized as follows. Sec. 5.2 outlines the Ehrenfest (MF) method and its application to the calculation of the projection-free inputs required for the memory kernel of the GQME. Sec. 5.3 presents results for the six spin-boson models coupled to a hot and a cold harmonic bath, outlined in Chapters 3 and 4, including both the direct Ehrenfest propagation of the reduced system dynamics and the populations-only GQME dynamics constructed from Ehrenfest-propagated projection-free inputs. Concluding remarks are given in Sec. 5.4.

5.2 Theory

In this section, we outline the theoretical framework for the mean-field Ehrenfest method used for direct propagation of reduced system dynamics, as well as for an input to GQMEs for a system coupled to multiple baths. To this end, we follow a convention, where a hat over a symbol, e.g. $\hat{A}$, indicates that the quantity is an operator, vector quantities are boldfaced, e.g., $\mathbf{R}$, and calligraphic font, e.g. $\mathcal{L}$, indicates that the quantity is a superoperator.

5.2.1 The GQME: Memory Kernel and Projection-Free Inputs

The dynamics of the reduced density operator for a system coupled to two baths,

$$\hat{\sigma}(t) = \mathrm{Tr_b}[\hat{\rho}(\mathrm{t})], \tag{5.1}$$

can be described through the generalized quantum master equation (GQME). As described in Chapters 3 and 4, the dynamics of the projected state, $\mathcal{P}\hat{\rho}(t)$ is given by the Nakajima-Zwanzig GQME,[90,149]

$$\frac{d}{dt}\hat{\sigma}(t) = -\frac{i}{\hbar}\mathcal{L}_s\hat{\sigma}(t) - \int_0^t d\tau \mathcal{K}(\tau)\hat{\sigma}(t-\tau), \tag{5.2}$$

where $\mathcal{L}_s\hat{\sigma}(t) = [\hat{H}_s, \hat{\sigma}(t)]$ and $\mathcal{K}(\tau)$ is the memory kernel,

$$\mathcal{K}(\tau) = \frac{1}{\hbar^2}\mathrm{Tr}_\mathrm{b}\Big\{\mathcal{L}\mathrm{e}^{-\mathrm{i}\mathcal{Q}\mathcal{L}\tau/\hbar}\mathcal{Q}\mathcal{L}\hat{\rho}_\mathrm{h}^\mathrm{eq}\otimes\hat{\rho}_\mathrm{c}^\mathrm{eq}\Big\}. \tag{5.3}$$

Eq. (5.2) is a formally exact equation of motion, however, direct evaluation of the projected propagator appearing in the exponential of the memory kernel makes it difficult to evaluate directly. A common strategy is to express the memory kernel in terms of projection-free inputs that can be obtained from either exact or approximate methods. In Chapters 3 and 4, these projection-free inputs were obtained using the hierarchical equations of motion (HEOM) method, resulting in quantum-mechanically exact memory kernels. In this chapter, the use of a semiclassical trajectory-based method is used instead to obtain the projection-free inputs, and assess the ability of the approximate method to reproduce the exact memory kernels and resulting GQME.

In Chapters 3 and 4, the memory kernel was expressed in terms of the projection-free reduced system propagator, $\mathcal{U}$, Eq. (5.3). The memory kernel can also be written in terms of the projection-free input, $\mathcal{F}(\tau)$, as a Volterra equation of the second-kind:

$$\mathcal{K}(\tau) = i\dot{\mathcal{F}}(\tau) - \frac{1}{\hbar}\mathcal{F}(\tau)\mathcal{L}_s + i\int_0^\tau d\tau'\mathcal{F}(\tau-\tau')\mathcal{K}(\tau')\ . \tag{5.4}$$

Here, the projection-free input $\mathcal{F}(\tau)$ is defined as:

$$\mathcal{F}(\tau) = \frac{1}{\hbar}\mathrm{Tr}_\mathrm{b}\Big\{\mathcal{L}\mathrm{e}^{-\mathrm{i}\mathcal{L}\tau/\hbar}\hat{\rho}_\mathrm{h}^\mathrm{eq}\otimes\rho_\mathrm{c}^\mathrm{eq}\Big\}\ . \tag{5.5}$$

$\mathcal{F}(\tau)$ is represented by a $n^2 \times n^2$ matrix in terms of the system basis (e.g. 4×4 matrix in the case of a two state system). The corresponding matrix elements of $\mathcal{F}(\tau)$ are given by:

$$\mathcal{F}_{jk,lm}(\tau) = \frac{1}{\hbar}\mathrm{Tr}\Big\{(|\mathrm{j}\rangle\langle\mathrm{k}|)^\dagger \mathcal{L}\mathrm{e}^{-\mathrm{i}\mathcal{L}\tau/\hbar}\hat{\rho}_{\mathrm{h}}^{\mathrm{eq}} \otimes \hat{\rho}_{\mathrm{c}}^{\mathrm{eq}}|\mathrm{l}\rangle\langle\mathrm{m}|\Big\} \tag{5.6}$$

5.2.2 Ehrenfest Method for Obtaining Projection-Free Inputs

In this section, we outline the protocol for calculating the projection-free inputs $\mathcal{F}_{jk,lm}(\tau)$ [Eq. (5.6)] via the Ehrenfest method. This starts by noting that the projection-free input, Eq. (5.6), can be given in terms of

$$\mathrm{Tr}\{\hat{\Omega}|\mathrm{l}\rangle\langle\mathrm{m}|\mathrm{e}^{\mathrm{i}\hat{\mathrm{H}}\tau/\hbar}\hat{\Gamma}|\mathrm{b}\rangle\langle\mathrm{a}|\mathrm{e}^{-\mathrm{i}\hat{\mathrm{H}}\tau/\hbar}\}. \tag{5.7}$$

Here, the bath operator, $\hat{\Omega}$ is $\hat{\rho}_b^{eq}$. The expression can be interpreted as the expectation value of $\hat{\Gamma}|b\rangle\langle a|$ at time t when the initial state is given by $\hat{\Omega}|l\rangle\langle m|$, and the dynamics are generated by the full Hamiltonian, $\hat{H}$. It is important to note that for a system coupled to two independent baths, the bath coordinates are partitioned as $\mathbf{R}_b = \{\mathbf{R}_h, \mathbf{R}_c\}$, where $b \in \{h, c\}$, where h and c denote the hot and cold bath degrees of freedom, respectively.

Within the Ehrenfest approximation, the bath DOF are treated classically, the system DOF are treated quantum-mechanically, and the impact of the system DOF on the bath DOF is treated in a mean-field manner. The initial positions and momenta of the bath DOF are sampled based on the Wigner transform of the equilibrium bath density operator, $\hat{\rho}_b^{eq}$, $\rho_{b,W}(\mathbf{R}_h, \mathbf{P}_h; \mathbf{R}_c, \mathbf{P}_c)\Big|_{t=0}$, or its classical limit, and expectation values are obtained by averaging over the corresponding ensemble of classical trajectories. For a given bath trajectory $\mathbf{R}_b(t)$, the system evolves under a time-dependent Hamiltonian,

$$\hat{H}_{sys}(t) = \sum_{j=1}^{N} V_j[(\mathbf{R}_h(t), \mathbf{R}_c(t))]|j\rangle\langle j| + \sum_{j,k=1,k\neq j}^{N} V_{jk}[(\mathbf{R}_h(t), \mathbf{R}_c(t))]|j\rangle\langle k|. \tag{5.8}$$

The effect of the system DOF on the bath DOF is included by propagating the bath DOF on the mean-field potential energy surface:

$$V_{mf}^{b}(\mathbf{R}_h, \mathbf{R}_c) = \sum_{j=1}^{N} \sigma_{jj}(t) V_j(\mathbf{R}_h, \mathbf{R}_c) + \sum_{j,k=1 k\neq j}^{N} \sigma_{jk}(t) V_{jk}(\mathbf{R}_h, \mathbf{R}_c) \ . \tag{5.9}$$

The use of Ehrenfest method is generally restricted to an initial system density operator that is Hermitian, since non-Hermitian initial conditions can lead to a complex-valued PES, and as a result, non-physical classical trajectories. To account for this, we switch to a basis of the system Liouville space consisting of operators that form a Hermitian, trace-preserving representation of the density matrix. It is important to note, the choice of basis is not unique, but a common choice that satisfies Hermiticity, trace one, and positivity corresponds to:[88]

$$\begin{aligned} \hat{X}_{lm} &= \frac{1}{2}\Big[|l\rangle\langle l| + |m\rangle\langle m| + |l\rangle\langle m| + |m\rangle\langle l|\Big] \ , \\ \hat{Y}_{lm} &= \frac{1}{2}\Big[|l\rangle\langle l| + |m\rangle\langle m| - i|l\rangle\langle m| + i|m\rangle\langle l|\Big] \ . \end{aligned} \tag{5.10}$$

In practice, we start with $\hat{X}_{lm}$ and $\hat{Y}_{lm}$ instead of $|l\rangle\langle m|$ and $|m\rangle\langle l|$ as initial states of the system, to obtain the Ehrenfest approximations of

$$\begin{aligned} &\mathrm{Tr}\{\hat{\Omega}\hat{\mathrm{X}}_{\mathrm{lm}} \mathrm{e}^{\mathrm{i}\hat{\mathrm{H}}\tau/\hbar} \Gamma(\hat{\mathbf{R}}_{\mathrm{h}}, \hat{\mathbf{R}}_{\mathrm{c}}) |\mathrm{b}\rangle\langle \mathrm{a}| \mathrm{e}^{-\mathrm{i}\hat{\mathrm{H}}\tau/\hbar}\} \\ &\mathrm{Tr}\{\hat{\Omega}\hat{\mathrm{Y}}_{\mathrm{lm}} \mathrm{e}^{\mathrm{i}\hat{\mathrm{H}}\tau/\hbar} \Gamma(\hat{\mathbf{R}}_{\mathrm{h}}, \hat{\mathbf{R}}_{\mathrm{c}}) |\mathrm{b}\rangle\langle \mathrm{a}| \mathrm{e}^{-\mathrm{i}\hat{\mathrm{H}}\tau/\hbar}\} \ . \end{aligned} \tag{5.11}$$

The results for $|u\rangle\langle v|$ and $|v\rangle\langle u|$ as the initial electronic states can therefore be expressed as linear combinations of the results in Eq. (5.11).

5.3 Application to a Two-Level System Linearly Coupled to a Hot and Cold Harmonic Bath

In this section, the applicability and accuracy of the semi-classical approximation, the Ehrenfest method, is demonstrated on a spin-boson model system coupled to a hot and cold harmonic bath, as outlined in Chapters 3 and 4. The accuracy of Ehrenfest is evaluated both in direct propagation of the reduced density matrix elements, $\{\sigma_{ab}(t)\}$, and as an approximate input method for obtaining the projection-free inputs required by the GQME, Eq. (5.2).

Our model Hamiltonian previously studied by Song and Shi in Ref. 123, which has the form of Eq. (4.1), with $\{\hat{H}_s, \hat{H}_h, \hat{H}_c, \hat{H}_{sh}, \hat{H}_{sc}\}$ given by

$$\begin{aligned}
\hat{H}_s &= \Delta\hat{\sigma}_x \\
\hat{H}_h &= \sum_{j=1}^{N}\left[\frac{\hat{P}_{hj}^2}{2} + \frac{\omega_{hj}^2\hat{R}_{hj}^2}{2}\right] \ , \ \hat{H}_c = \sum_{j=1}^{N}\left[\frac{\hat{P}_{cj}^2}{2} + \frac{\omega_{cj}^2\hat{R}_{cj}^2}{2}\right] \quad , \\
\hat{H}_{sh} &= \sum_{j=1}^{N} c_{hj}\hat{R}_{hj}\hat{\sigma}_z \ , \ \hat{H}_{sc} = \sum_{j=1}^{N} c_{cj}\hat{R}_{cj}\hat{\sigma}_z \quad .
\end{aligned} \tag{5.12}$$

Here, $\hat{\sigma}_x = |0\rangle\langle 1| + |1\rangle\langle 0|$, $\hat{\sigma}_y = -i(|0\rangle\langle 1| - |1\rangle\langle 0|)$ and $\hat{\sigma}_z = |0\rangle\langle 0| - |1\rangle\langle 1|$ are the Pauli operators, with $|0\rangle$ and $|1\rangle$ corresponding to the eigenstates of $\hat{\sigma}_z$ with eigenvalues $+1$ and -1, respectively; $\{\hat{R}_{hj}, \hat{P}_{hj}, \omega_{hj}, c_{hj} | j = 1, \ldots, N\}$ and $\{\hat{R}_{cj}, \hat{P}_{cj}, \omega_{cj}, c_{cj} | j = 1, \ldots, N\}$ denote the mass-weighted coordinates, momenta, frequencies, and coupling coefficients of the hot and cold bath modes, respectively. It should be noted that for this model, the hot and cold baths' Hamiltonians are identical and coupled to the two-level system in the same way.

The values of $\{\omega_{hj}, c_{hj} | j = 1, \ldots, N\}$ and $\{\omega_{cj}, c_{cj} | j = 1, \ldots, N\}$ are extracted from spectral density functions, which are assumed to be identical for both baths and given by

$(\alpha = h, c)$:[123]

$$
\begin{aligned}
I_\alpha(\omega) &= \frac{\pi}{2}\sum_{j=1}^{N}\frac{c_{\alpha j}^2}{\omega_{\alpha j}}\delta(\omega-\omega_{\alpha j}) \\
&= \frac{\eta_\alpha \omega \gamma_{\alpha,1}\gamma_{\alpha,2}\gamma_{\alpha,3}}{(\omega^2+\gamma_{\alpha,1}^2)(\omega^2+\gamma_{\alpha,2}^2)(\omega^2+\gamma_{\alpha,3}^2)} \quad .
\end{aligned}
\tag{5.13}
$$

The initial state of the overall system is assumed to be given by Eq. (4.6), with $\hat{\sigma}(0) = |0\rangle\langle 0|$:

$$
\hat{\rho}(0) = \hat{\rho}_h^{eq} \otimes \hat{\rho}_c^{eq} \otimes |0\rangle\langle 0| \quad . \tag{5.14}
$$

Here, $\hat{\rho}_h^{eq}$ and $\hat{\rho}_c^{eq}$ are defined as:

$$
\hat{\rho}_b^{eq} = \hat{\rho}_h^{eq} \otimes \hat{\rho}_c^{eq} = \frac{e^{-\beta_h \hat{H}_h}}{\mathrm{Tr_h}\{\mathrm{e}^{-\mathrm{i}\beta_\mathrm{h}\hat{\mathrm{H}}_\mathrm{h}}\}} \otimes \frac{e^{-\beta_c \hat{H}_c}}{\mathrm{Tr_c}\{\mathrm{e}^{-\mathrm{i}\beta_\mathrm{c}\hat{\mathrm{H}}_\mathrm{c}}\}} \tag{5.15}
$$

where $\hat{H}_h$, $\hat{H}_c$ are as defined in Eq. (5.12) and the initial bath position and momenta are sampled based on the Wigner transform of Eq. (5.15), such that $\rho_{b,W}(\mathbf{R}_h, \mathbf{P}_h, \mathbf{R}_c, \mathbf{P}_c; 0) = \rho_{h,W}(\mathbf{R}_h, \mathbf{P}_h; 0)\rho_{c,W}(\mathbf{R}_c, \mathbf{P}_c; 0)$, with:

$$
\rho_{\alpha,W}(\mathbf{R}_\alpha, \mathbf{P}_\alpha; 0) = \prod_{i=1}^{N} \frac{\tanh\left(\beta_\alpha \hbar\omega_i/2\right)}{\pi\hbar} \exp\left[-\frac{2\tanh\left(\beta_\alpha\hbar\omega_i/2\right)}{\hbar\omega_i}\left(\frac{P_{\alpha,i}^2}{2} + \frac{1}{2}\omega_i^2 R_{\alpha,i}^2\right)\right] , \tag{5.16}
$$

where $\alpha \in \{h, c\}$. Note, the system and baths are assumed to start out uncorrelated, with the hot and cold baths each prepared in thermal equilibrium at their respective temperatures. As a result, the total bath Wigner distribution factorizes into the product of the hot and cold bath equilibrium Wigner distributions.

Calculations were carried out for the six different realizations of the spin-boson model linearly coupled to a hot and cold harmonic bath, as outlined in Table 3.1, averaged over 10^5 trajectories. The results in this chapter focus exclusively on the populations-only GQME framework in order to assess the performance of the Ehrenfest method for calculating the corresponding two-bath projection-free input, Eq. (5.5) and two-bath memory kernel, Eq. (5.4).

Therefore, we define the following projection operator corresponding to the populations-only subspace:

$$\mathcal{P}^{pop} = \sum_{j=1}^{N_e} \mathcal{P}^{jj} \ , \tag{5.17}$$

Here, $\mathcal{P}^{jj}$ is defined as in Eq. (4.20) in Chapter 4. For the spin-boson model under consideration, $n = 2$, therefore the populations-only PFI and memory kernel, $\mathcal{F}^{pop}(\tau)$ and $\mathcal{K}^{pop}(\tau)$, are represented by 2×2 matrices in the population subspace $\{|0\rangle\langle 0|, |1\rangle\langle 1|\}$. In this chapter, the PFI $\mathcal{F}(\tau)$ is calculated directly from Ehrenfest dynamics as described above. The corresponding time derivative, $\dot{\mathcal{F}}(\tau)$ was calculated via the finite central difference method available in the NumPy Python library. The Volterra equation was then solved numerically via the iterative algorithm outlined in Refs. 88, 26, followed by propagation of the populations-only GQME using a fourth-order Runge-Kutta method. The results are presented in terms of the eigen-basis $\hat{\sigma}_z$ ($\{|0\rangle, |1\rangle\}$, such that $\hat{\sigma}_z|0\rangle = |0\rangle$ and $\hat{\sigma}_z|1\rangle = |1\rangle$.

5.3.1 Results

We start by comparing the two PFI matrix elements, $\mathcal{F}_{0000}(\tau)$ and $\mathcal{F}_{0011}(\tau)$, Eq. (5.6), obtained using HEOM and Ehrenfest, and the respective time derivatives, $\dot{\mathcal{F}}_{0000}(\tau)$ and $\dot{\mathcal{F}}_{0011}(\tau)$, evaluated using numerical differentiation. Results for these elements across models 1-6 are presented in Figs. 5.1 and 5.2. Inspection of these results show that Ehrenfest, combined with a numerical evaluation of the time-derivative, is capable of accurately reproducing the exact two-bath PFIs obtained from HEOM. As a result, a comparison of the two-bath memory kernels constructed via HEOM-based PFIs and Ehrenfest-based PFIs, shown in Fig. 5.3, are also found to be in excellent agreement across all six models under consideration.

In Fig. 5.4, the resulting population dynamics is shown in terms of the population difference, $\sigma_z(t) = |0\rangle\langle 0| - |1\rangle\langle 1|$. The dynamics were obtained through four approaches: (1) direct application of the Ehrenfest method (MF); (2) the populations-only MF-GQME method where the memory kernel was constructed from Ehrenfest-propagated PFIs; (3) the exact

populations-only GQME constructed from HEOM-based PFIs; (4) the direct application of HEOM. The results demonstrate that the populations-only MF-GQME results are shown to yield excellent agreement across both weak and strong coupling regimes in comparison to the exact populations-only GQME results obtained with HEOM. Interestingly, the direct applicaiton of Ehrenfest also reproduces the exact population dynamics with high accuracy across all six models considered for the two-bath system. This suggests that, for the parameters under consideration, the population dynamics are well-captured by the propagated Ehrenfest dynamics, and as a result, the MF-GQME provides an effective approximation for reproducing the exact reduced dynamics without requiring the explicit construction of the exact two-bath memory kernel.

5.4 Concluding Remarks

Multi-bath systems are of considerable interest due to the presence of nonequilibrium dynamics. However, because of the complexity that arises from the presence of multiple baths, the exact evaluation of these dynamics can become very computationally expensive. As a result, the extension of approximate input methods capable of reproducing exact two-bath dynamics is of considerable interest, as these methods provide a means to forgo the need for explicit construction of the exact memory kernel.

In this chapter, the semiclassical Ehrenfest method was outlined and applied in two distinct ways: first through the direct propagation of the reduced system density matrix elements $\{\sigma_{ab}(t)\}$, and second as an approximate input method for constructing the memory kernel of the populations-only GQME. The application of the Ehrenfest method was extended to a spin-boson system linearly coupled to a hot and cold harmonic bath, as previously outlined in Chapters 3 and 4. The results presented in Sec. 5.3 demonstrate the utility of Ehrenfest for accurately reproducing the exact two-bath PFIs and memory kernels required for the populations-only GQME, providing a computationally cost-effective pathway to approximating the dynamics of $\sigma_z(t)$ for a two-bath model, a key quantity of interest

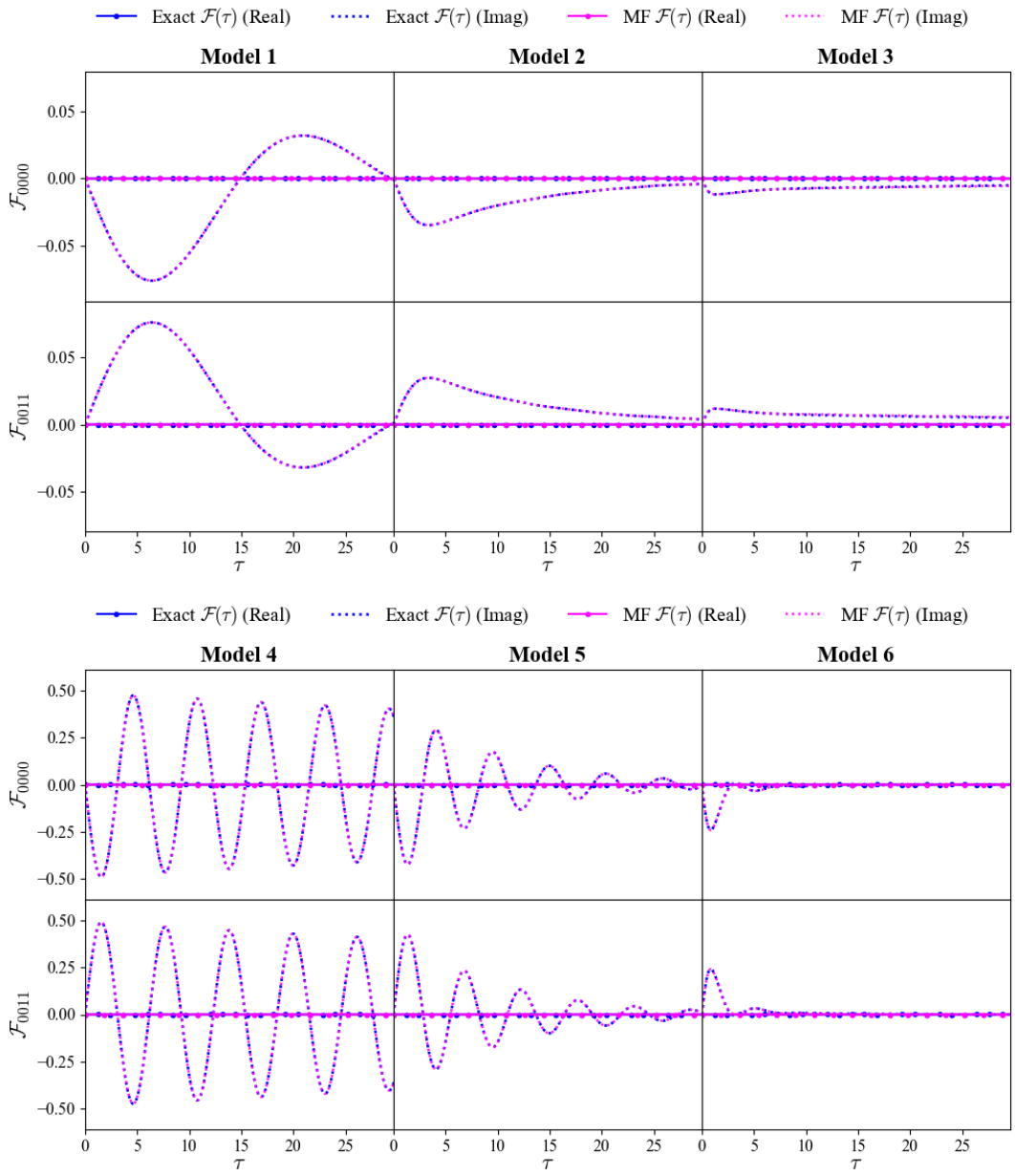


Figure 5.1: A comparison of the two projection-free input matrix elements, $\mathcal{F}_{0000}(\tau)$ and $\mathcal{F}_{0011}(\tau)$, used to construct the populations-only GQME memory kernel for the six spin-boson models under consideration. The exact HEOM results are shown in blue, while the Ehrenfest results are shown in magenta, with solid lines denoting the real parts and dotted lines denoting the imaginary parts of $\mathcal{F}(\tau)$.

in charge-transfer processes, both directly and in conjunction with the GQME framework.

For multi-bath systems, however, the use of approximate methods, requires further exploration to assess their accuracy and computational advantages. This includes comparisons

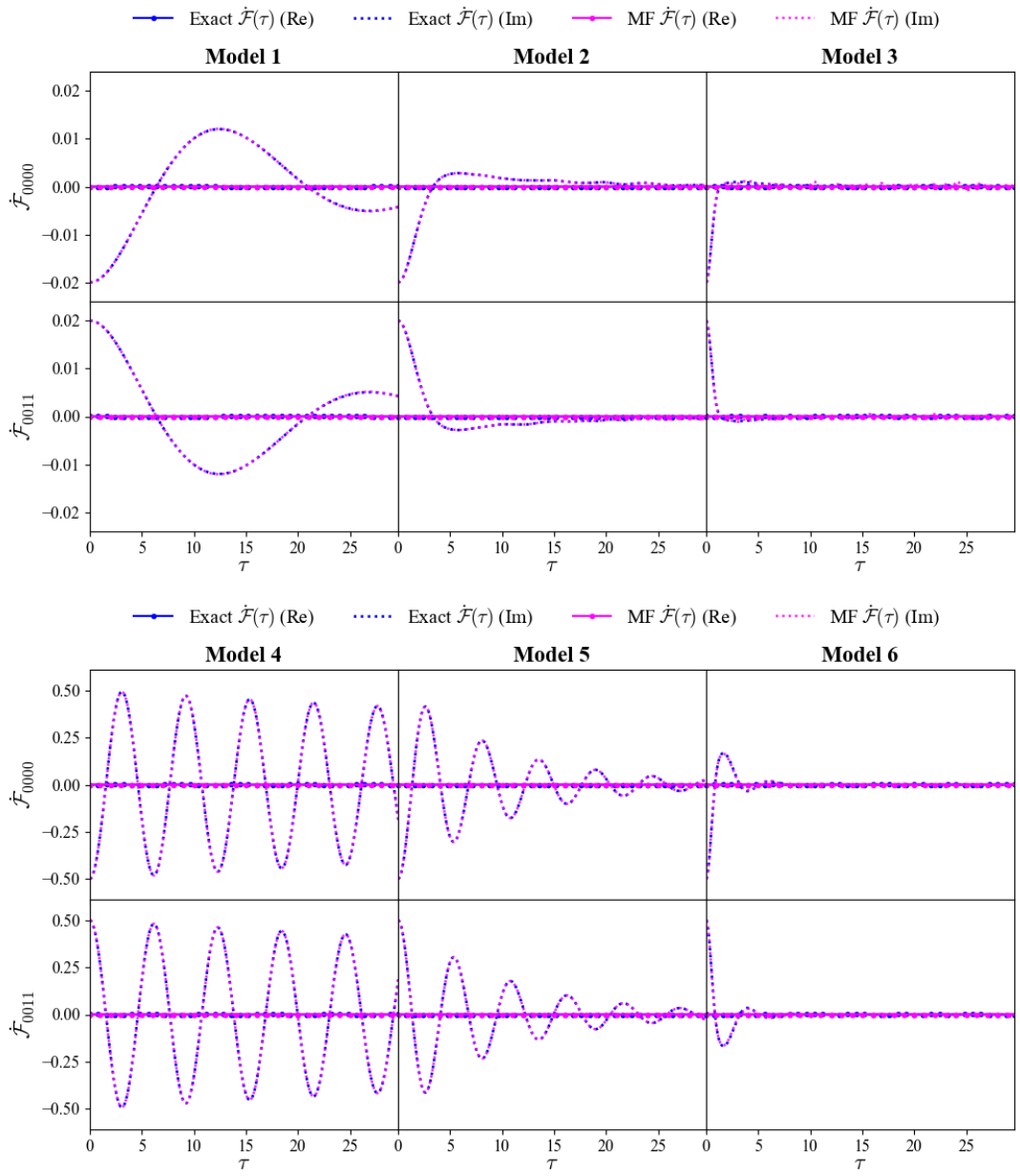


Figure 5.2: A comparison of the two projection-free input matrix elements, $\dot{\mathcal{F}}_{0000}(\tau)$ and $\dot{\mathcal{F}}_{0011}(\tau)$, used to construct the populations-only GQME memory kernel for the six spin-boson models under consideration. The exact HEOM results are shown in blue, while the numerical derivatives of the Ehrenfest PFIs are shown in magenta, with solid lines denoting the real parts and dotted lines denoting the imaginary parts of $\dot{\mathcal{F}}(\tau)$.

with other semiclassical approaches, such as mapping Hamiltonian methods based on linear semiclassical (LSC) dynamics, as well as extensions to other GQME formulations, including the full GQME, in order to evaluate their capabilities in describing other dynamical ob-

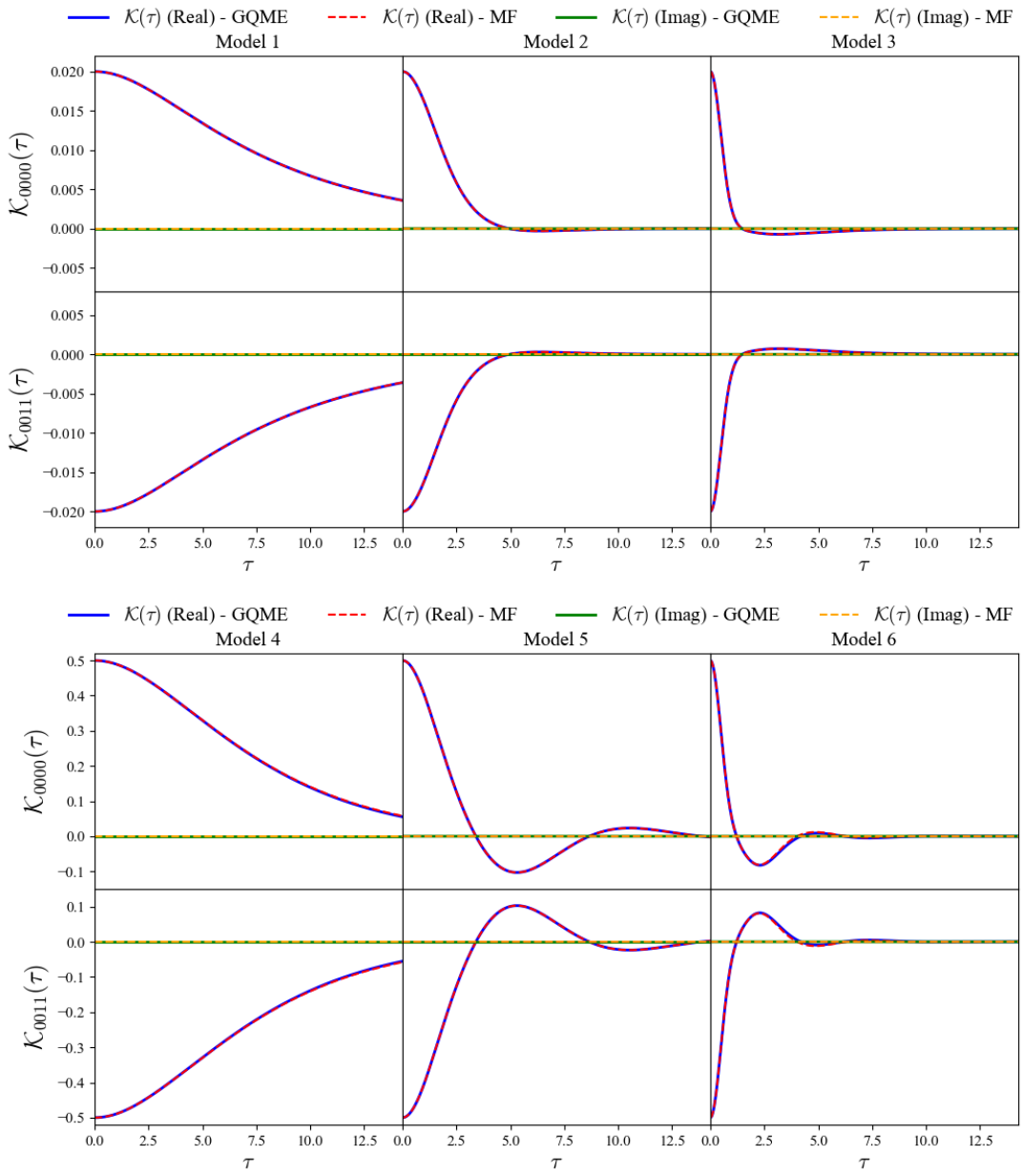


Figure 5.3: A comparison of the real and imaginary parts of two memory kernel matrix elements, $\mathcal{K}_{0000}(\tau)$ and $\mathcal{K}_{0011}(\tau)$, used in the populations-only GQME for the six spin-boson models under consideration. The real parts (solid blue line) and imaginary parts (solid green line) of the exact HEOM memory kernels are shown, while the real parts (dashed red line) and imaginary parts (dashed green line) of the Ehrenfest-based memory kernels are also shown.

servables of interest, such as $\sigma_x(t)$, a quantity of interest relevant for studying heat transfer processes.

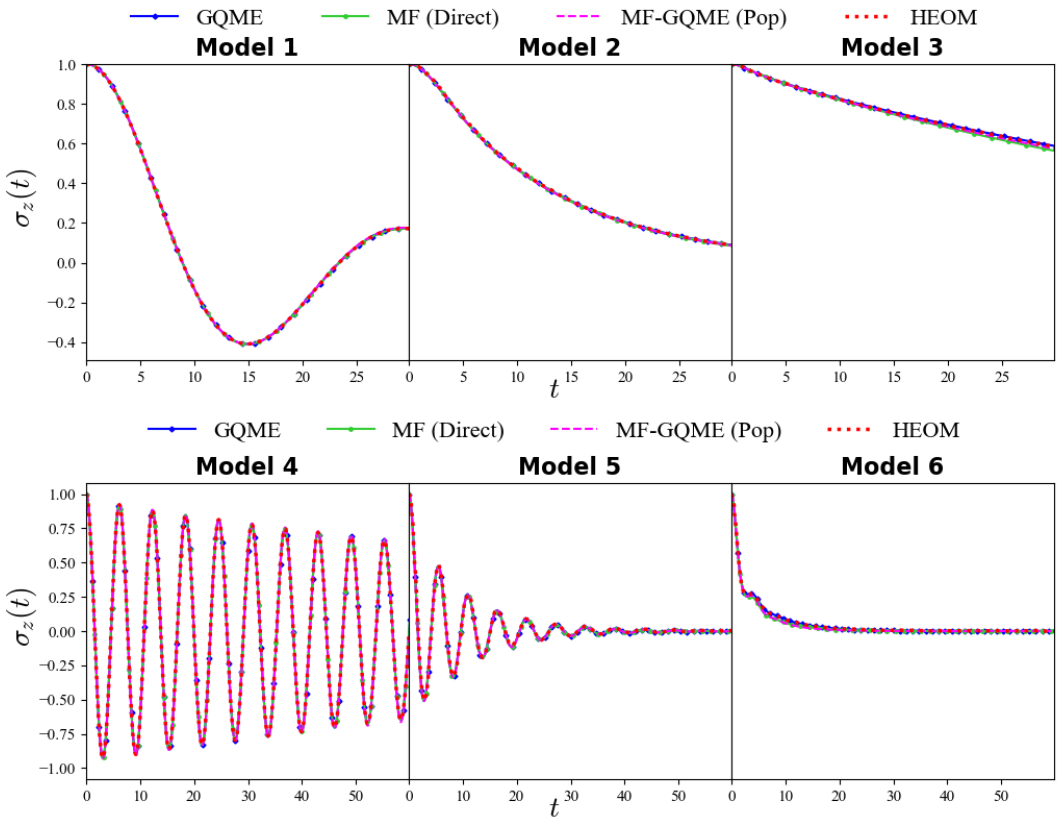


Figure 5.4: $\sigma_z(t)$ as a function of time for models 1-3 (top panel) and models 4-6 (bottom panel) in Table 3.1. Shown are exact HEOM-based results (dotted red line), populations-only GQME-based results with the exact memory kernel, $\mathcal{K}(\tau)$, calculated from HEOM-based PFIs (solid blue line), populations-only MF-GQME results using an approximate memory kernel constructed from Ehrenfest-based PFIs (solid green line), and results from direct propagation of Ehrenfest (MF) dynamics (dashed magenta line).

CHAPTER 6

Conclusion

6.1 Summary

Many chemically, biologically, and technologically-relevant processes involve open quantum systems operating under nonequilibrium conditions, where interactions with the surrounding environment have a significant influence on the electronic energy and charge transfer dynamics. Developing accurate and computationally-feasible methods to simulate these processes remains a key challenge in theoretical and computational chemistry. Quantum master equation approaches provide a powerful framework for addressing this challenge, ranging from perturbative methods to the formally exact generalized quantum master equation, with the flexibility to describe any arbitrary subset of reduced density matrix elements of interest.

The presence of nonequilibrium conditions, including an external driving field or a multi-bath environment introduce a new set of challenges into the dynamics of open quantum systems. In Chapter 2, the OD-QME framework first introduced in Ref. 60 was extended to treat externally driven systems. The resulting field-driven OD-QME was applied to the GOA model in the presence of a continuous-wave (CW) driving field, and the resulting dynamics were compared to those obtained in the absence of the field. This study demonstrated that the presence of the driving field introduces an additional radiative transition pathway that is an additive contribution to the overall transition rates, with the greatest enhancement occurring in the case when the field frequency was considered to be in resonance with the

transition frequency of the system. These results highlight the flexibility of the OD-QME framework to account for a time-dependent Hamiltonian, as well as its ability to recover behavior consistent with classical Marcus rate theory predictions.

In Chapter 3, the GQME framework was extended to systems coupled to multi-bath environments. The resulting formally exact GQME corresponding to the full electronic reduced density matrix was applied to a spin-boson model simultaneously coupled to hot and cold harmonic baths. The validity of approximating the two-bath environment as a sum of single-bath coupling was investigated through the construction of an additive memory kernel corresponding to the sum of exact single bath memory kernels and compared to the exact two-bath memory kernel. A comparison of the resulting population and coherence dynamics with the additive two-bath secular, Markovian and non-Markovian Redfield QMEs was also investigated. This analysis highlighted the limitations of the additivity approximation. In the strong system-bath coupling regime, bath additivity was shown to breakdown, leading to significant deviations in the population and coherence dynamics arising from the exact two-bath memory kernel and the sum of the exact single-bath memory kernels. Additionally, the degree of additivity was found to depend strongly on the specific transition pathway: the memory kernels describing population-to-coherence, coherence-to-coherence, and coherence-to-population transfer exhibited the strongest non-additive behavior.

In Chapter 4, the flexibility and accuracy of the GQME for a two-bath model was investigated by considering projections of additional subsets of interest of the reduced density matrix. Four reduced-dimensionality GQMEs were compared in the context of the spin-boson model coupled to a hot and cold harmonic bath outlined in Chapter 3, including the full electronic, populations-only, coherences-only, and single-population/single-coherence GQMEs. The bath additivity was also studied in the context of the reduced-dimensional memory kernels and the corresponding inhomogeneous terms. The results revealed that in addition to a dependence on the system-bath coupling strength, the breakdown of additivity was also influenced by the type of projection, with the highest degree of non-additivity

observed in the case of the single-population/single-coherence GQMEs. The observed breakdown in additivity is believed to be a basis-dependent outcome arising from working in a representation different than the eigen-representation of the system.

In Chapter 5, the two-bath model explored in Chapters 3 and 4 is extended to a mixed quantum-classical method in order to assess the ability of an approximate method to capture the two-bath dynamics. Specifically, the approximate Ehrenfest method is applied to the spin boson model simultaneously coupled to a hot and cold harmonic bath both through direct propagation of reduced system dynamics and as an input to the populations-only GQME framework. The approximate PFIs and memory kernels are shown to accurately reproduce the corresponding exact two-bath PFIs and memory kernels. Additionally, both the directly-propagated and GQME-derived population dynamics were shown to be in good agreement with the exact results obtained from HEOM, demonstrating the utility of Ehrenfest in capturing the non-equilibrium dynamics arising from a multi-bath environment.

6.2 Outlook

This dissertation presented the development, exploration, and application of several quantum master equation approaches to nonequilibrium quantum systems, including systems subject to time-dependent external driving fields and systems simultaneously coupled to a hot and a cold thermal bath. While the studies presented here demonstrate the applicability of quantum master equation approaches to a variety of nonequilibrium processes, several extensions would be of interest for future investigation.

For externally-driven systems, one natural extension from the model explored in Chapter 2 would be the study of multi-excitonic systems in which the driving field selectively couples to specific electronic states. For example, stimulated Raman adiabatic passage (STIRAP)-like systems are an area of interest in physics and chemistry due to their ability to achieve efficient and controllable population transfer of a quantum system through pulse sequences.[38] Additional studies of interest include exploring external fields with more tunable temporal

profiles, such as a pulsed field that periodically turns on and off, or multiple competing fields that would generate more complex, nonequilibrium dynamical behavior.[66] While the OD-QME framework shown in Chapter 2 was a suitable choice for the model and parameters under consideration, an extension to stronger driving fields where this perturbative treatment of the system-field coupling breaks down could instead be achieved using the non-perturbative GQME framework. This would allow for the study of strong-field phenomena, such as Rabi oscillations, that cannot be fully captured within a perturbative approach.[94]

For multi-bath systems, there are several future areas of interest, including studying a system with asymmetrical system-bath coupling in which case the orientation of the bath coupling and the resulting strength of the bath interaction can be systematically varied.[30,101,3,12] Another interesting direction would be the application of quantum master equation approaches to quantum heat engines or refrigerators coupled to multiple thermal baths. In these systems, an external driving field performs work on the quantum system, while heat is exchanged between baths at different temperatures. Depending on the operating regime, the system can convert heat into an output of work, as in the case of a heat engine, or consume work to drive heat from a colder reservoir to a hotter reservoir, in the case of a refrigerator.[2,43,57] The interplay between the driving field and the multi-bath coupling would be of particular interest, as both mechanisms could act simultaneously on the system to control energy and heat flow.

Additionally, the work in Chapter 4 raises the question of whether bath additivity in projection-dependent GQME formulations is sensitive to the choice of representation of the projected dynamics. The natural extension would therefore be to derive the reduced-dimensionality GQME formalisms in the eigen-basis representation of the system, which in the case of Chapter 4 would be the σ_x representation, and verify whether additivity is restored, as is the case for Redfield theory.

Finally, the results in Chapter 5 provide a foundation for further exploration of alternative approximate methods capable of accurately capturing nonequilibrium dynamics in multi-

bath environments. The value and computational feasibility of such approximate methods is of significant importance when considering more complex, realistic chemical systems, where solving for the numerically exact dynamics is often computationally infeasible due to the size and complexity of the system-bath coupling. The use of approximate methods, both directly and as inputs to the GQME, provides a means to overcoming these computational challenges because they do not require exact input quantities or a fully quantum-mechanical treatment of both the system and bath degrees of freedom. Consequently, these approaches are well suited for studying systems beyond the spin-boson model considered in this work, including molecular junctions and molecular wires, in which a molecule bridges two or more bath reservoirs each held at different chemical potentials or temperatures. Such systems are of considerable interest because their nonequilibrium, multi-bath quantum dynamics govern charge and energy transport processes that underly a wide range of technological applications, including molecular electronics, quantum sensing, and quantum information processing.[108,56,110,107] Collectively, these research directions provide a foundation for understanding the relationship between quantum dynamics and thermodynamic properties of systems operating under nonequilibrium conditions.

APPENDIX A

Driven OD-QMEs: Additional Driven OD-QME Variations and Discussion of Experimental Validity

A.1 OD-QMEs for Full Electronic Density Matrix and Populations-Only TC

The OD-QMEs presented in the main text are referred to as *populations-only* since their derivation is based on the projection superoperator in Eq. (2.16), which projects onto the electronic populations of the donor and acceptor states, $\tilde{\sigma}_{DD}(t)$ and $\tilde{\sigma}_{AA}(t)$, as the quantity of interest. In this case, the p-tc-OD-QME and p-tcl-OD-QME in Eqs. (2.19) and (2.21), respectively, describe the dynamics of the electronic populations, with the information on the projected out nuclear DOF and electronic coherences, $\tilde{\sigma}_{DA}(t)$ and $\tilde{\sigma}_{AD}(t)$, limited to the minimum necessary to account for their impact on the electronic populations [as captured in the correlation functions in Eq. (2.20)].

However, other choices of projection superoperators are possible, which lead to different types of OD-QMEs. For example, using the following projection superoperator would lead to OD-QMEs for the full 2×2 electronic density matrix, $\tilde{\sigma}(t)$, including both electronic populations and coherences:

$$\mathcal{P}(\hat{\xi}) = \hat{p}_B(0) \otimes Tr_B[\hat{\xi}]. \tag{A.1}$$

Using the projection superoperator in Eq. (A.1) and following the procedure outlined in

Ref. 60 leads to the following time-convolution and time-convolutionless OD-QMEs for $\tilde{\sigma}(t)$ as the quantity of interest:

$$\frac{d}{dt}\tilde{\sigma}(t) = -\frac{i}{\hbar}\langle \mathcal{L}_I(t)\rangle \tilde{\sigma}(t) - \frac{1}{\hbar^2}\int_0^t d\tau \mathcal{K}(t,\tau)\tilde{\sigma}(\tau), \tag{A.2}$$

$$\frac{d}{dt}\tilde{\sigma}(t) = -\frac{i}{\hbar}\langle \mathcal{L}_I(t)\rangle \tilde{\sigma}(t) - \frac{1}{\hbar^2}\left[\int_0^t d\tau \mathcal{K}(t,\tau)\right]\tilde{\sigma}(t). \tag{A.3}$$

In what follows, we will refer to Eqs. (A.2) and (A.3) as the *full time-convolution OD-QME (f-tc-OD-QME)* and *full time-convolutionless OD-QME (f-tcl-OD-QME)*, respectively.

In Eqs. (A.2) and (A.3), $\mathcal{K}(t,\tau)$, and $\langle \mathcal{L}_I(t)\rangle$ are superoperators, which are defined by:

$$\langle \mathcal{L}_I(t)\rangle = Tr_B[\hat{\rho}_B(0)\mathcal{L}_I(t)], \tag{A.4}$$

$$\mathcal{K}(t,\tau) = \langle \mathcal{L}_I(t)\mathcal{L}_I(\tau)\rangle - \langle \mathcal{L}_I(t)\rangle\langle \mathcal{L}_I(\tau)\rangle \tag{A.5}$$

The matrix elements of $\mathcal{K}(t,\tau)$, which is referred to as the memory kernel, are given by (where each of the indices j,k,m,n can be either D or A):

$$\begin{aligned}\mathcal{K}_{jk,mn}(t,\tau) = {} & \delta(k,n)\sum_{l\neq j,m}\langle \delta\hat{V}_{jl}(t)\delta\hat{V}_{lm}(\tau)\rangle \\ & + \delta(j,m)\sum_{l\neq k,n}\langle \delta\hat{V}_{kl}(t)\delta\hat{V}_{ln}(\tau)\rangle^* \\ & - \langle \delta\hat{V}_{nk}(t)\delta\hat{V}_{jm}(\tau)\rangle - \langle \delta\hat{V}_{mj}(t)\delta\hat{V}_{kn}(\tau)\rangle^*,\end{aligned} \tag{A.6}$$

where

$$\delta\hat{V}_{jk}(t) = \hat{V}_{jk}(t) - \langle \hat{V}_{jk}(t)\rangle \tag{A.7}$$

such that

$$\langle \delta\hat{V}_{jk}(t)\delta\hat{V}_{mn}(\tau)\rangle = \langle \hat{V}_{jk}(t)\hat{V}_{mn}(\tau)\rangle - \langle \hat{V}_{jk}(t)\rangle\langle \hat{V}_{mn}(\tau)\rangle \quad . \tag{A.8}$$

Quantum-mechanically exact expressions for the quantities on the R.H.S. of Eq. (A.8) can be obtained in closed form for the GOA model off-diagonally driven by a CW field:

$$\begin{aligned}\langle \hat{V}_{DA}(t)\hat{V}_{DA}(\tau)\rangle = (V_{DA}^2 + 2(\chi_{DA}^0)^2\cos(\omega\tau))e^{i\omega_{DA}(t-\tau)} \\ \times \exp\Bigg\{ \sum_n \frac{\tilde{\omega}_n (R_n^{eq})^2}{2\hbar}\coth(\frac{1}{2}\beta\hbar\tilde{\omega}_n) \\ \times [\cos(\tilde{\omega}_n(t-\tau)) - 1]\Bigg\} \\ \times \exp\Bigg\{ -i\sum_n \frac{\tilde{\omega}_n (R_n^{eq})^2}{2\hbar} \\ \times \sin(\tilde{\omega}_n(t-\tau))\Bigg\},\end{aligned} \tag{A.9}$$

$$\begin{aligned}\langle \hat{V}_{DA}(t)\rangle = (V_{DA} + \chi_{DA}^0(e^{i\omega t} + e^{-i\omega t}))e^{i\omega_{DA}(t)} \\ \times \exp\Bigg\{ \sum_n \frac{\tilde{\omega}_n (R_n^{eq})^2}{2\hbar}\coth(\frac{1}{2}\beta\hbar\tilde{\omega}_n) \\ \times [\cos(\tilde{\omega}_n(t)) - 1]\Bigg\} \\ \times \exp\Bigg\{ -i\sum_n \frac{\tilde{\omega}_n (R_n^{eq})^2}{2\hbar}\sin(\tilde{\omega}_n(t))\Bigg\}\end{aligned} \tag{A.10}$$

The results reported in Chapter 2 of the main text were based on the p-tcl-OD-QME. However, similar calculations that were performed based on the p-tc-OD-QME, f-tcl-OD-QME and f-tc-OD-QME were found to yield indistinguishable results for the model parameters under consideration. This is demonstrated in Fig. A.1 for models A and B discussed in the main text, which were chosen to be consistent with typical CT reactions. The p-tcl-OD-QME emerged as the method of choice because its computational cost is the lowest among the four OD-QMEs tested, and because it is the most straightforward to interpret.

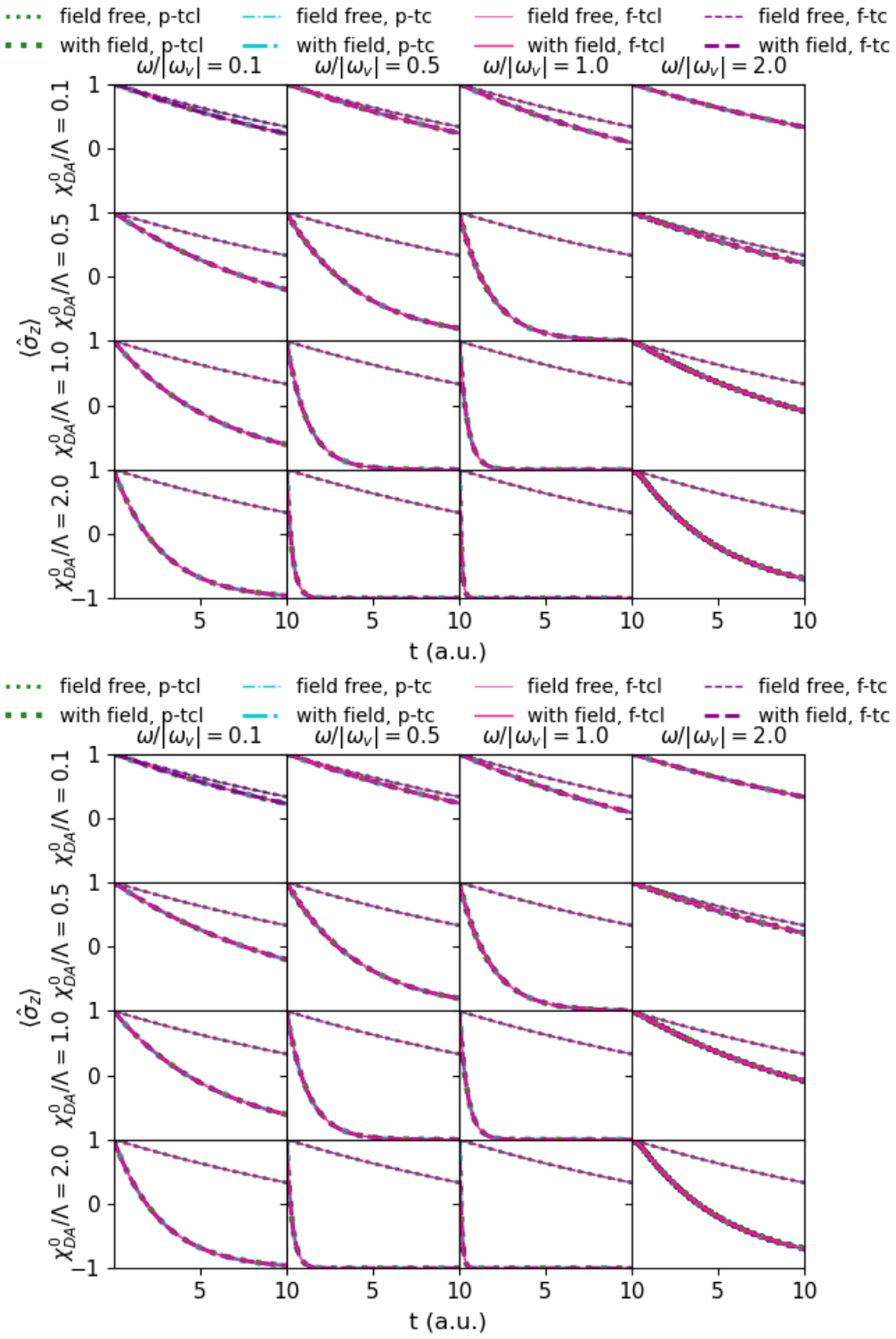


Figure A.1: The effect of the driving field's intensity and frequency on the CT dynamics within models A (top panel) and B (bottom panel), simulated at $T = 300$K based on four different OD-QMEs (p-tcl-OD-QME, p-tc-OD-QME, f-tcl-OD-QME and f-tc-OD-QME). The difference between the populations of the donor and acceptor states, $\langle\hat{\sigma}_z\rangle = \langle D|\hat{\sigma}|D\rangle - \langle A|\hat{\sigma}|A\rangle$ is plotted as a function of time for different combinations of $\chi^0_{DA}/\Lambda = \{0.1, 0.5, 1.0, 2.0\}$ and $\omega/|\omega_v| = \{0.1, 0.5, 1.0, 2.0\}$.

A.2 The Rotating Wave Approximation

Substituting $V_{DA}(t) = V_{DA} + \chi^0_{DA}(e^{i\omega t} + e^{-i\omega t})$ into the expression for $C_{D\to A}(t)$ in Eq. (2.20), and then substituting it back into Eq. (2.22), we obtain:

$$\begin{aligned} k_{D\to A}(t) &= \frac{2}{\hbar^2} V_{DA}^2 Re \int_0^t d\tau C^0_{DA}(\tau) \\ &+ \frac{2}{\hbar^2}\left(\frac{\chi^0_{DA}}{V_{DA}}\right)^2 Re\Big[(1+e^{2i\omega t})\int_0^t d\tau e^{-i\omega\tau} C^0_{D\to A}(\tau) \\ &+ (1+e^{-2i\omega t})\int_0^t d\tau e^{i\omega\tau} C^0_{D\to A}(\tau)\Big] \\ &+ \frac{2}{\hbar^2}\frac{\chi^0_{DA}}{V_{DA}} Re\Big(e^{i\omega t} + e^{-i\omega t}\Big)\int_0^t d\tau C^0_{D\to A} \\ &+ \frac{2}{\hbar^2}\frac{\chi^0_{DA}}{V_{DA}} Re\Big(e^{i\omega t}\int_0^t d\tau e^{-i\omega\tau} C^0_{D\to A} \\ &+ e^{-i\omega t}\int_0^t d\tau e^{i\omega\tau} C^0_{D\to A}\Big) \ . \end{aligned} \tag{A.11}$$

Applying the RWA corresponds to neglecting terms containing $e^{\pm i\omega t}$ and $e^{\pm 2i\omega t}$ factors, which leads to Eq. (2.23).

To justify the RWA, note that based on Eq. (2.21):

$$\begin{aligned} \sigma_{DD}(t) = \sigma_{DD}(0) &- \int_0^t dt' k_{D\to A}(t')\sigma_{DD}(t') \\ &+ \int_0^t dt' k_{A\to D}(t')\sigma_{AA}(t'). \end{aligned} \tag{A.12}$$

As shown above, $k_{D\to A}(t')$ and $k_{A\to D}(t')$ are given in terms of $k^0_{D\to A}(t')$, $k^0_{A\to D}(t')$, $k^0_{D\to A}(\pm\omega, t')$ and $k^0_{A\to D}(\pm\omega, t')$. For a typical CT reaction (e.g. models A and B in this paper), the time dependence of those rate coefficients is on the *ps* timescale. This timescale is considerably longer than the timescale associated with the oscillatory terms, $e^{\pm i\omega t}$ and $e^{\pm 2i\omega t}$, in which ω is typically of the order of the vertical transition frequency, $\langle U\rangle_{eq}/\hbar$, which is of the order 0.5-1.0 eV, corresponding to a timescale of 5-10 fs. Given this separation of timescales, integrals of the form $\int_0^t dt' e^{\pm i\omega t'} k^0_{D\to A}(t')\sigma_{DD}(t')$ and $\int_0^t dt' e^{\pm 2i\omega t'} k^0_{D\to A}(t')\sigma_{DD}(t')$ would be negligible compared to $\int_0^t dt' k^0_{D\to A}(t')\sigma_{DD}(t')$ due to the highly oscillatory nature

of the integrands.

The RWA was also validated numerically by simulating the dynamics without employing the RWA and verifying that the results are indistinguishable from the results obtained with the RWA.

A.3 Estimation of Experimental Feasibility

According to Eq. (2.23), in order for the radiative CT pathway to be competitive with the non-radiative CT pathway, χ^0_{DA} needs to be comparable to V_{DA}. In this appendix, we show that this is indeed the case for typical values of laser intensity[93] and molecular dipole moment.

We start by noting that the energy density of the field, u_F, the field amplitude, E_0, the laser intensity, I, and the laser peak power, P_{peak}, are related as follows:[93]

$$u_F = \frac{1}{2}\epsilon_0 E_0^2 = \frac{I}{c} = \frac{P_{peak}}{cA}, \tag{A.13}$$

Here, ϵ_0 is vacuum permittivity, and A is the cross-sectional area of the laser beam. (note that we denoted the field amplitude by E_0 instead of ϵ_0 as in the text in order not to get it confused with the vacuum permittivity).

Given the typical values[93] $P_{peak} \approx 1 \times 10^6 Js^{-1}$ and $r \approx 75 \times 10^{-6}$ m, we obtain $E_0 \sim 2.1 \times 10^8\,\mathrm{J\,C^{-1}\,m^{-1}}$. Given a typical value of the transition dipole moment, $\mu_{DA} \sim -10\,\mathrm{D} = 3.3 \times 10^{-29}\,\mathrm{C\,m}$, we obtain $\chi_{DA} \sim 43$meV, which is comparable to typical values of the electronic coupling coefficient, V_{DA}.

APPENDIX B

Reduced-Dimensionality GQMEs: Proofs of Memory Kernels and Inhomogeneous Terms

This appendix outlines the mathematical proof of the initial values of the reduced memory kernel elements, a comparison of the magnitudes of the projection-dependent, individual single-bath memory kernels, $\mathcal{K}_h^{proj}(\tau)$ and $\mathcal{K}_c^{proj}(\tau)$, with the exact two-bath memory kernel, $\mathcal{K}^{proj}(\tau)$, as well as an explanation of the behavior of the inhomogeneous terms corresponding to the coherence-only GQME [Eq. (4.29)] shown in Chapter 4.

B.1 Analytical Proof of Initial Value of Reduced Memory Kernel Elements

To understand the origin of the initial value of the populations-only memory kernel, we consider the following Volterra equation for population $|0\rangle$:

$$\mathcal{K}_{00,00}(\tau) = -\ddot{\mathcal{U}}_{00,00}(\tau) - \int_0^\tau d\tau \dot{\mathcal{U}}_{00,00}(\tau - \tau')\mathcal{K}_{jj,jj}(\tau') \tag{B.1}$$

At $\tau = 0$, the integral vanishes so the kernel element becomes:

$$\mathcal{K}_{00,00}^{pop}(0) = -\ddot{\mathcal{U}}_{00,00}(0) \tag{B.2}$$

Therefore, the initial value of the memory kernel element is determined entirely by the second derivative of the system propagator at $t = 0$:

$$\begin{aligned}\ddot{\mathcal{U}}_{00,00}(0) &= \frac{1}{\hbar^2}\mathrm{Tr}\Big\{|0\rangle\langle 0|\mathcal{L}\mathrm{e}^{-\mathrm{i}\mathcal{L}(0)/\hbar}\mathcal{L}\rho_{\mathrm{b}}^{\mathrm{eq}}\otimes|0\rangle\langle 0|\Big\} \\ &= \frac{1}{\hbar^2}\mathrm{Tr}\Big\{|0\rangle\langle 0|\mathcal{L}^2\rho_{\mathrm{b}}^{\mathrm{eq}}\otimes|0\rangle\langle 0|\Big\}\ .\end{aligned} \tag{B.3}$$

Using the definition of the Liouvillian, $\mathcal{L}\hat{A} = [\hat{H}, \hat{A}]$, the quantity of interest $\mathcal{L}^2\rho_b^{eq}$ can be defined as the following:

$$\mathcal{L}^2\rho_b^{eq} = [\hat{H}, [\hat{H}, \rho_b^{eq}]]\ , \tag{B.4}$$

where $\hat{H} = \hat{H}_s + \hat{H}_b + \hat{H}_{bs}$. Since, the bath equilibrium density operator commutes with the bath Hamiltonian, $[\hat{H}_b, \rho_b^{eq}] = 0$, the inner commutator becomes:

$$[\hat{H}, \rho_b^{eq}] = [\hat{H}_s, |0\rangle\langle 0|]\rho_b^{eq} + [\hat{H}_{bs}, |0\rangle\langle 0|](B_h)\rho_b^{eq}\ . \tag{B.5}$$

Based on the spin-boson Hamiltonian, outlined in Sec. 3.3, $\hat{H}_s = \Delta\sigma_x$ and $\hat{H}_{bs} = \sigma_z(B)$ so:

$$\begin{aligned}[\hat{H}_s, \rho_b^{eq}] &= [\Delta\sigma_x, |0\rangle\langle 0|]\rho_b^{eq} \\ &= \Delta(|1\rangle\langle 0| - |0\rangle\langle 1|)\rho_b^{eq}\ , \\ [\hat{H}_{bs}, \rho_b^{eq}] &= [\sigma_z B_h, |0\rangle\langle 0|]\rho_b^{eq} = 0\end{aligned} \tag{B.6}$$

The outer commutator will also contain both system and system-bath contributions,

$$[\hat{H}, [\hat{H}_s, \rho_b^{eq}] = [\hat{H}_s, [\hat{H}_s, \rho_b^{eq}]] + [\hat{H}_{bs}, [\hat{H}_s, \rho_b^{eq}]]\ . \tag{B.7}$$

From the system contribution:

$$\begin{aligned}[\hat{H}_s,[\hat{H}_s,\rho_b^{eq}]] &= [\Delta(|0\rangle\langle 1|+|1\rangle\langle 0|),\Delta(|1\rangle\langle 0|-|0\rangle\langle 1|)]\rho_b^{eq} \\ &= \Delta^2((-|0\rangle\langle 0|+|1\rangle\langle 1|)-(|1\rangle\langle 1|-|0\rangle\langle 0|)) \\ &= \Delta^2(\sigma_z-(-\sigma_z)) = 2\Delta^2\sigma_z \ .\end{aligned} \tag{B.8}$$

For the system-bath contribution:

$$\begin{aligned}[\hat{H}_{sb},[\hat{H}_s,\rho_b^{eq}]] &= [\sigma_z(B_h),[(\Delta(|1\rangle\langle 0|-|0\rangle\langle 1|)\rho_b^{eq}]]\rho_b^{eq} \\ &= (-2\Delta\sigma_x B)\rho_b^{eq} \ .\end{aligned} \tag{B.9}$$

However, when projected onto population $|0\rangle\langle 0|$, the system-bath contribution will not survive. Therefore, the only contribution to the initial value of $\mathcal{K}^{pop}_{00,00}(0)$ comes from the double commutator of the system Hamiltonian outlined above.

For models 1-3, $\Delta = 0.1$, while for models 4-6 (see Tab. 3.1), the initial values of the populations-only kernel become:

$$\begin{aligned}\mathcal{K}^{pop}_{00,00}(0) &= 2\Delta^2 = 0.02 \ , \\ \mathcal{K}^{pop}_{00,00}(0) &= 2\Delta^2 = 0.5 \ .\end{aligned} \tag{B.10}$$

These values coincide with the numerically observed initial values for the populations-only memory kernel element $\mathcal{K}^{pop}_{00,00}$. Because the system Hamiltonian is independent of bath identity, the same result applies to the hot bath kernel element, the cold bath kernel element, and the two bath kernel element. Therefore,

$$\begin{aligned}\mathcal{K}^{pop,h}_{00,00}(0) = \mathcal{K}^{pop,c}_{00,00}(0) &= \mathcal{K}^{pop}_{00,00}(0), \\ \mathcal{K}^{pop,h}_{00,00}(0) + \mathcal{K}^{pop,c}_{00,00}(0) &= 2\mathcal{K}^{pop}_{00,00}(0).\end{aligned} \tag{B.11}$$

B.2 Breakdown of Memory Kernel Additivity by Projection

Figs. B.1–B.6 compare the exact single bath memory kernels, $\mathcal{K}_h^{proj}(\tau)$ and $\mathcal{K}_c^{proj}(\tau)$, with the corresponding exact two-bath memory kernel, $\mathcal{K}^{proj}(\tau)$. These results illustrate the projection-dependent nature of the breakdown in additivity observed in the population and coherence dynamics. In particular, for the single-population/single-coherence GQMEs, described by Eq. (4.19), the individual hot and cold bath memory kernels are each comparable in magnitude to the exact two-bath memory kernel for the timescale considered. As a result, the additive approximation, $\mathcal{K}^{proj}(\tau) \approx \mathcal{K}_h^{proj}(\tau) + \mathcal{K}_c^{proj}(\tau)$ becomes a significant overestimation of the magnitude of the exact two-bath memory kernel, resulting in the clear breakdown of bath additivity discussed in Chapter 4.

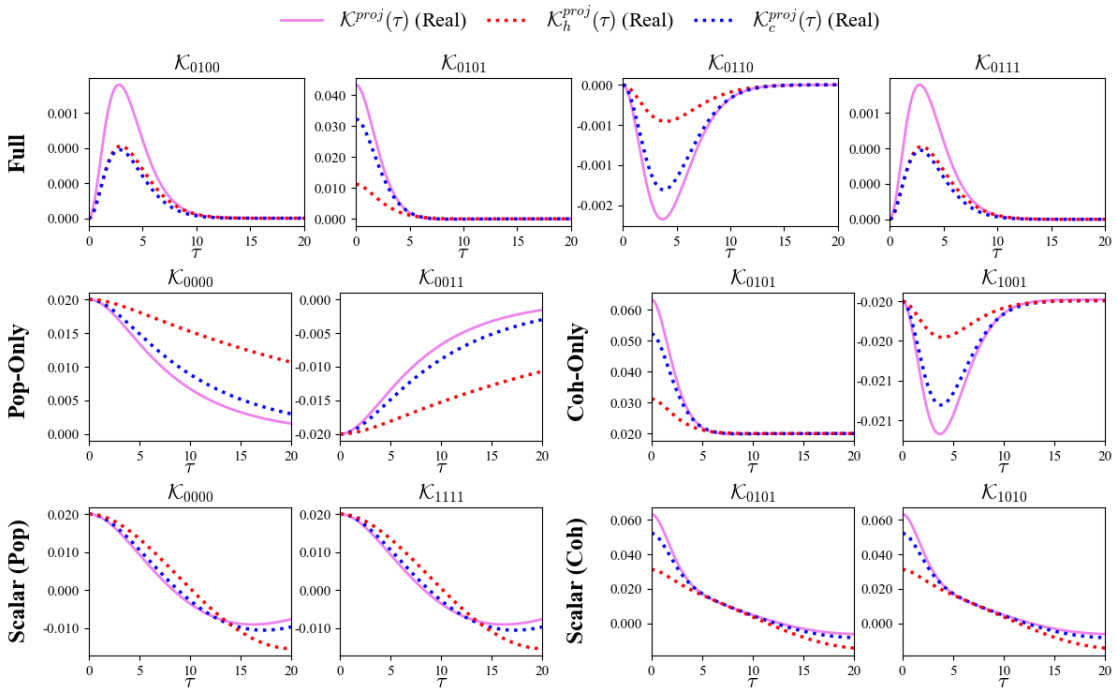


Figure B.1: Shown are the real parts of the exact single-bath memory kernels, $\mathcal{K}_h^{proj}(\tau)$ (red dotted line) and $\mathcal{K}_c^{proj}(\tau)$ (blue dotted line), and the exact two-bath memory kernel, $\mathcal{K}^{proj}(\tau)$ for Model 1 (see Tab. 4.2).

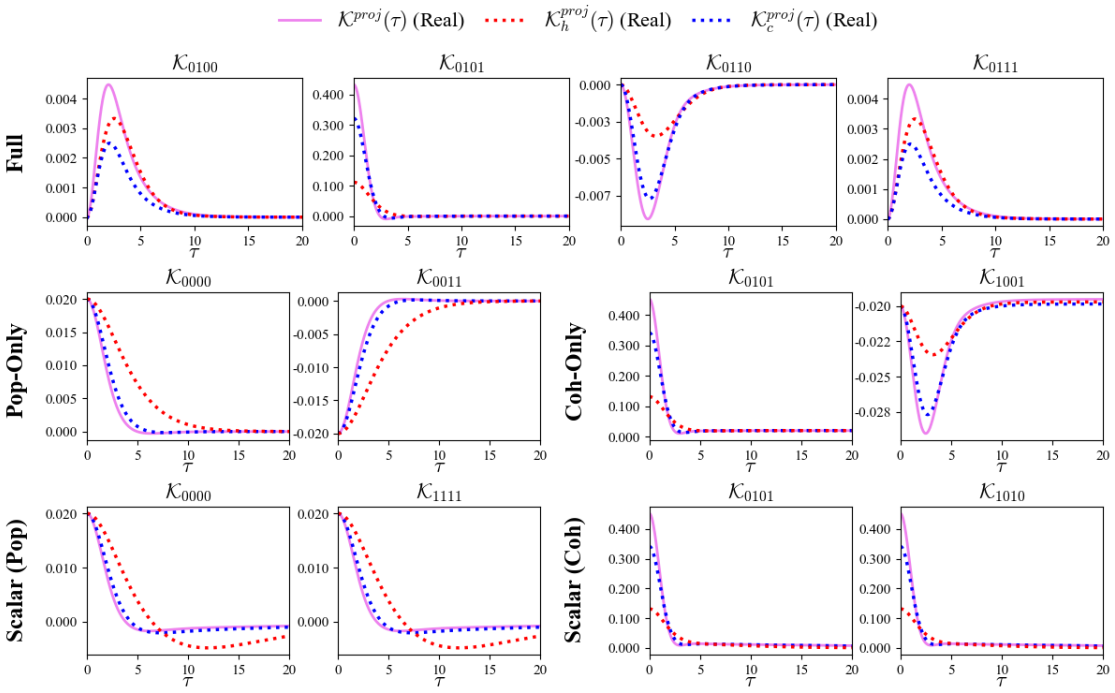


Figure B.2: Shown are the real parts of the exact single-bath memory kernels, $\mathcal{K}_h^{proj}(\tau)$ (red dotted line) and $\mathcal{K}_c^{proj}(\tau)$ (blue dotted line), and the exact two-bath memory kernel, $\mathcal{K}^{proj}(\tau)$ for Model 2 (see Tab. 4.2).

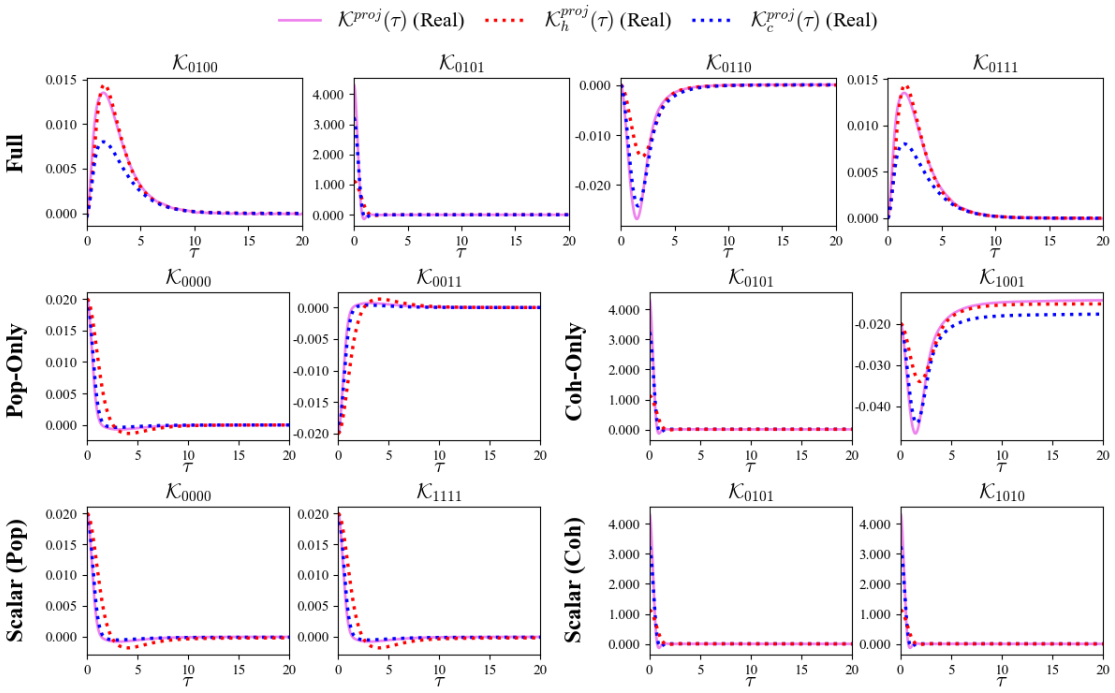


Figure B.3: Shown are the real parts of the exact single-bath memory kernels, $\mathcal{K}_h^{proj}(\tau)$ (red dotted line) and $\mathcal{K}_c^{proj}(\tau)$ (blue dotted line), and the exact two-bath memory kernel, $\mathcal{K}^{proj}(\tau)$ for Model 3 (see Tab. 4.2).

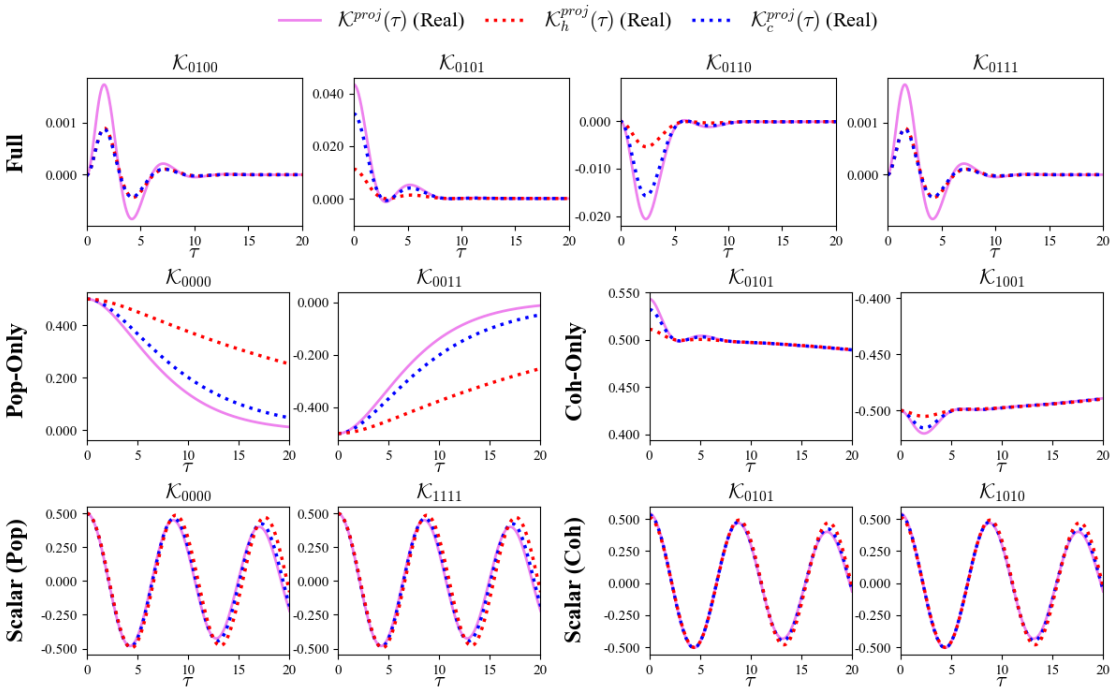


Figure B.4: Shown are the real parts of the exact single-bath memory kernels, $\mathcal{K}_h^{proj}(\tau)$ (red dotted line) and $\mathcal{K}_c^{proj}(\tau)$ (blue dotted line), and the exact two-bath memory kernel, $\mathcal{K}^{proj}(\tau)$ for Model 4 (see Tab. 4.2).

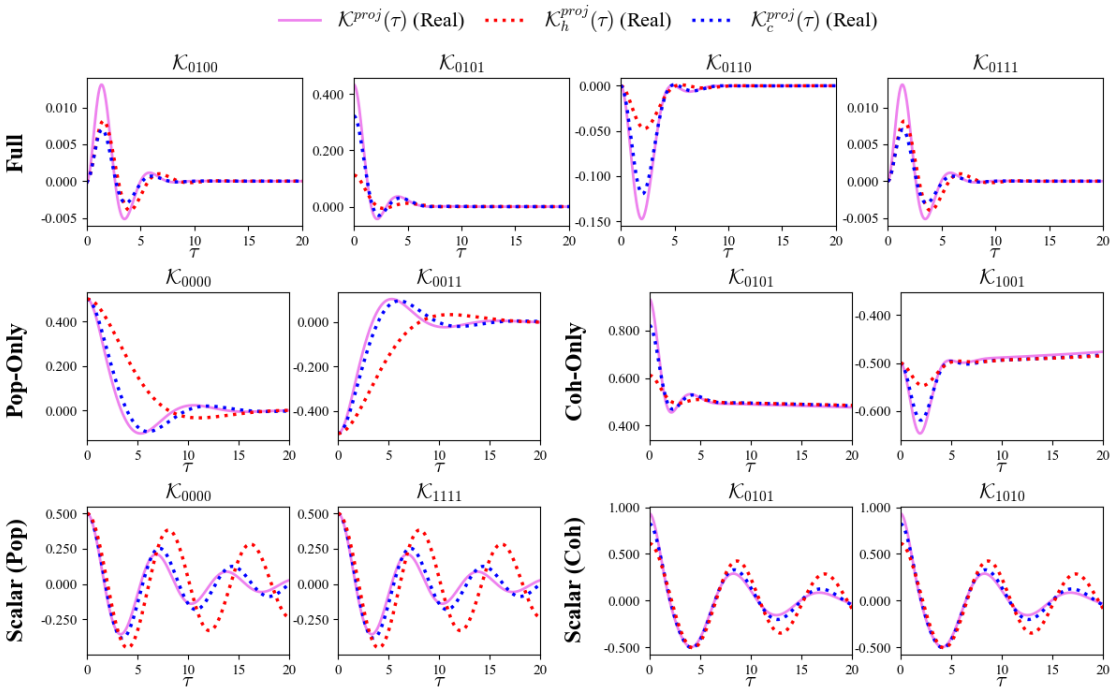


Figure B.5: Shown are the real parts of the exact single-bath memory kernels, $\mathcal{K}_h^{proj}(\tau)$ (red dotted line) and $\mathcal{K}_c^{proj}(\tau)$ (blue dotted line), and the exact two-bath memory kernel, $\mathcal{K}^{proj}(\tau)$ for Model 5 (see Tab. 4.2).

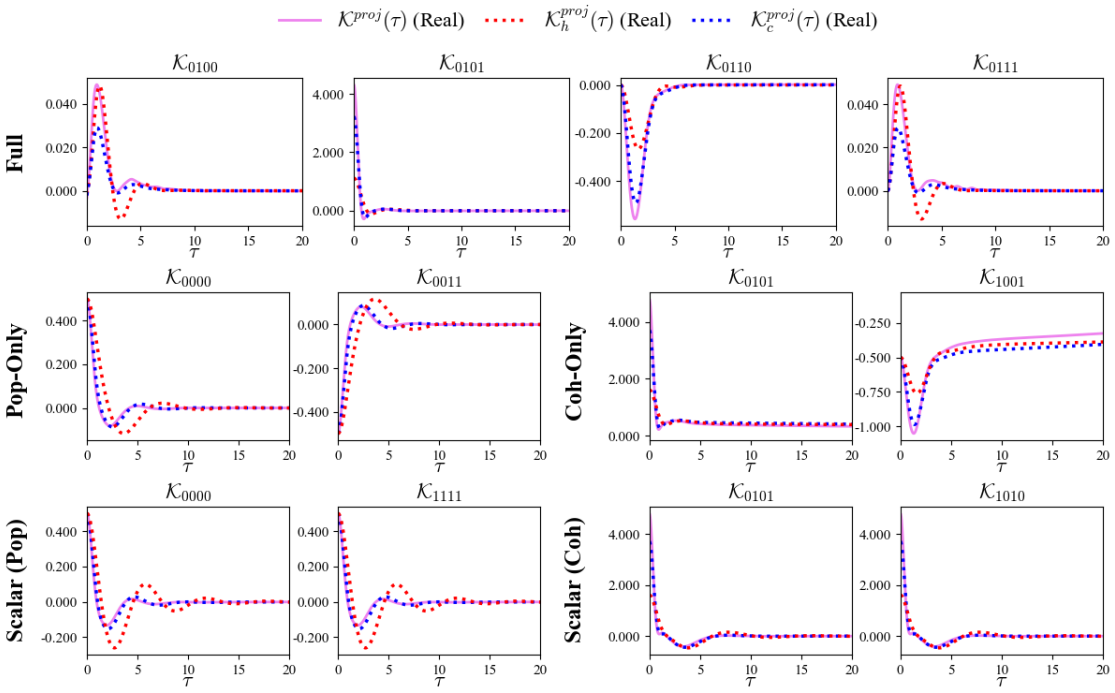


Figure B.6: Shown are the real parts of the exact single-bath memory kernels, $\mathcal{K}_h^{proj}(\tau)$ (red dotted line) and $\mathcal{K}_c^{proj}(\tau)$ (blue dotted line), and the exact two-bath memory kernel, $\mathcal{K}^{proj}(\tau)$ for Model 6 (see Tab. 4.2).

B.3 Cancellation of the Coherence-Projected Inhomogeneous Term with the Memory Kernel at Long Times

Fig. B.11 shows the convolution of the memory kernel, the inhomogeneous term $I^{coh}(t)$, and the sum of both terms for the coherence-only GQME for Models 1-6 (see Tab. 4.2). While the inhomogeneous term is shown to approach a constant at long times, this result is canceled out by an equal and opposite contribution from the memory-kernel convolution. Because of this, the memory time is determined by the decay of the combined contribution rather than by the individual lifetimes of the memory kernel or inhomogeneous term alone. Therefore, beyond the long-time limit, the memory kernel and inhomogeneous terms are assumed to vanish and do not contribute to the dynamics.

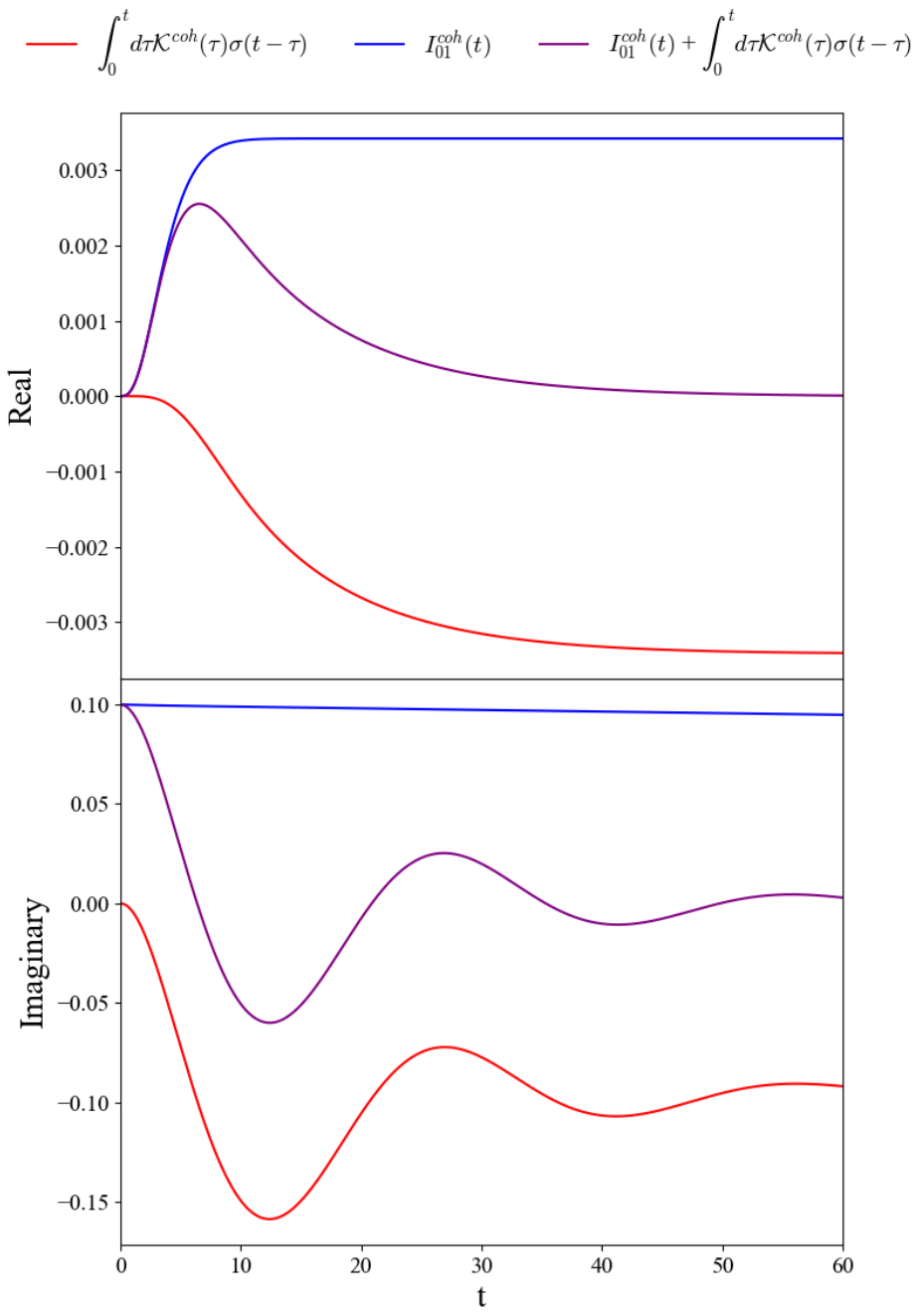


Figure B.7: Shown are the real (top) and imaginary (bottom) contributions of the convolution of the memory kernel, $\int_0^t \mathcal{K}^{coh}(\tau)\sigma(t-\tau)$ (red line), the inhomogeneous term for the coherences-only GQME, $I_{01}^{coh}(t)$ (see Eq. 4.29) (blue line), and the sum of the two contributions (purple line) for Model 1 (see Tab. 4.2).

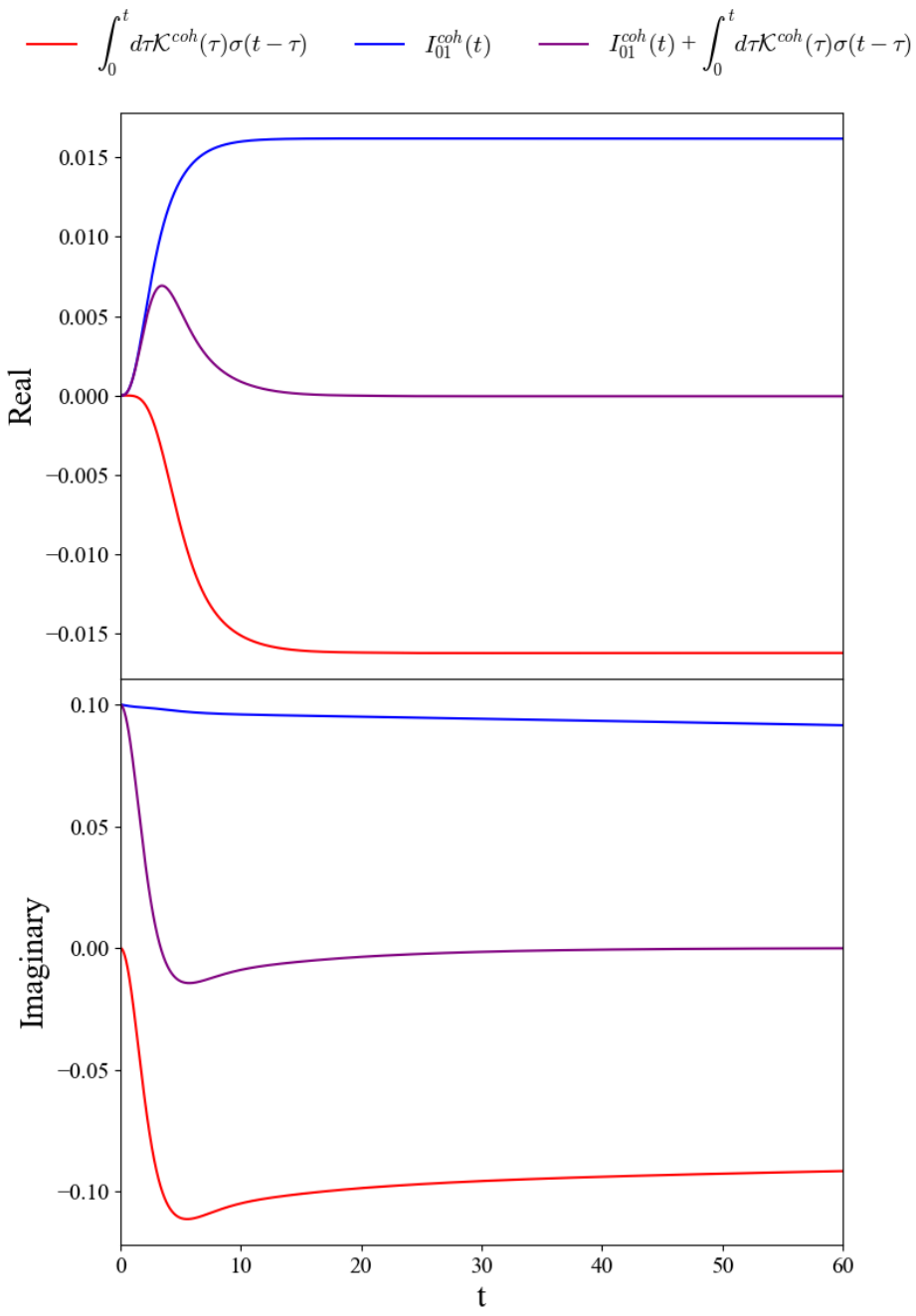


Figure B.8: Shown are the real (top) and imaginary (bottom) contributions of the convolution of the memory kernel, $\int_0^t \mathcal{K}^{coh}(\tau)\sigma(t-\tau)$ (red line), the inhomogeneous term for the coherences-only GQME, $I_{01}^{coh}(t)$ (see Eq. 4.29) (blue line), and the sum of the two contributions (purple line) for Model 2 (see Tab. 4.2).

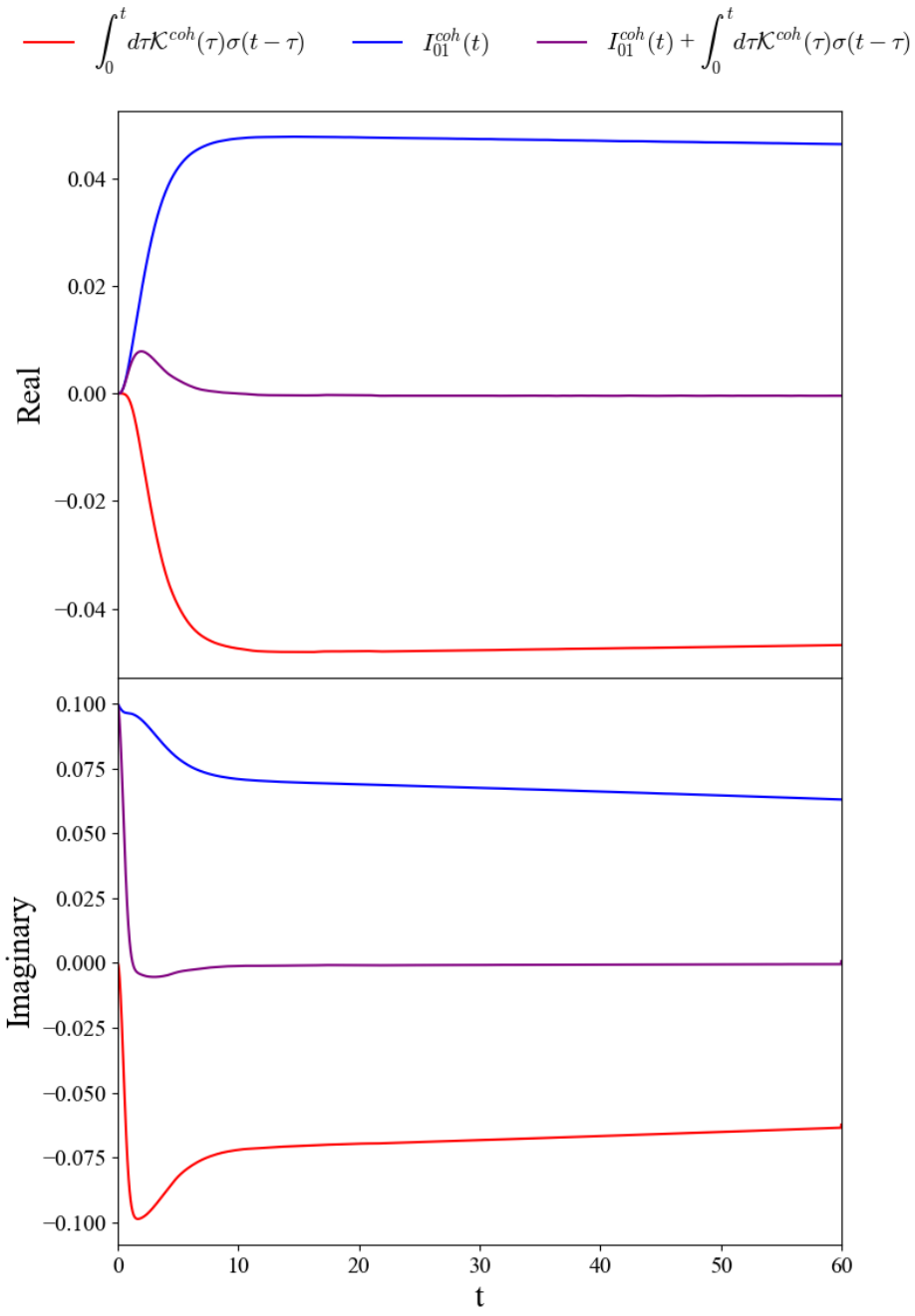


Figure B.9: Shown are the real (top) and imaginary (bottom) contributions of the convolution of the memory kernel, $\int_0^t \mathcal{K}^{coh}(\tau)\sigma(t-\tau)$ (red line), the inhomogeneous term for the coherences-only GQME, $I_{01}^{coh}(t)$ (see Eq. 4.29) (blue line), and the sum of the two contributions (purple line) for Model 3 (see Tab. 4.2).

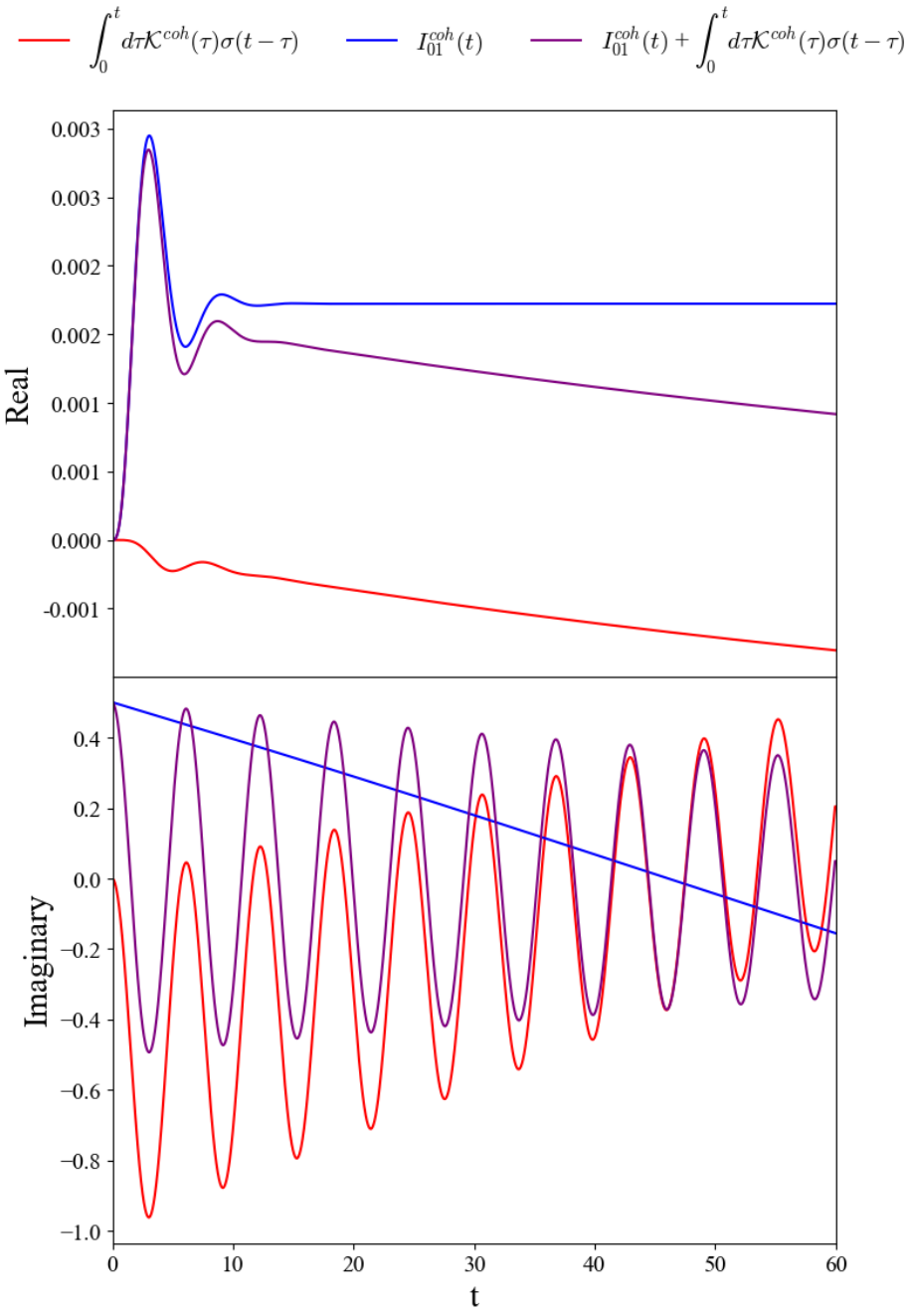


Figure B.10: Shown are the real (top) and imaginary (bottom) contributions of the convolution of the memory kernel, $\int_0^t \mathcal{K}^{coh}(\tau)\sigma(t-\tau)$ (red line), the inhomogeneous term for the coherences-only GQME, $I_{01}^{coh}(t)$ (see Eq. 4.29) (blue line), and the sum of the two contributions (purple line) for Model 4 (see Tab. 4.2).

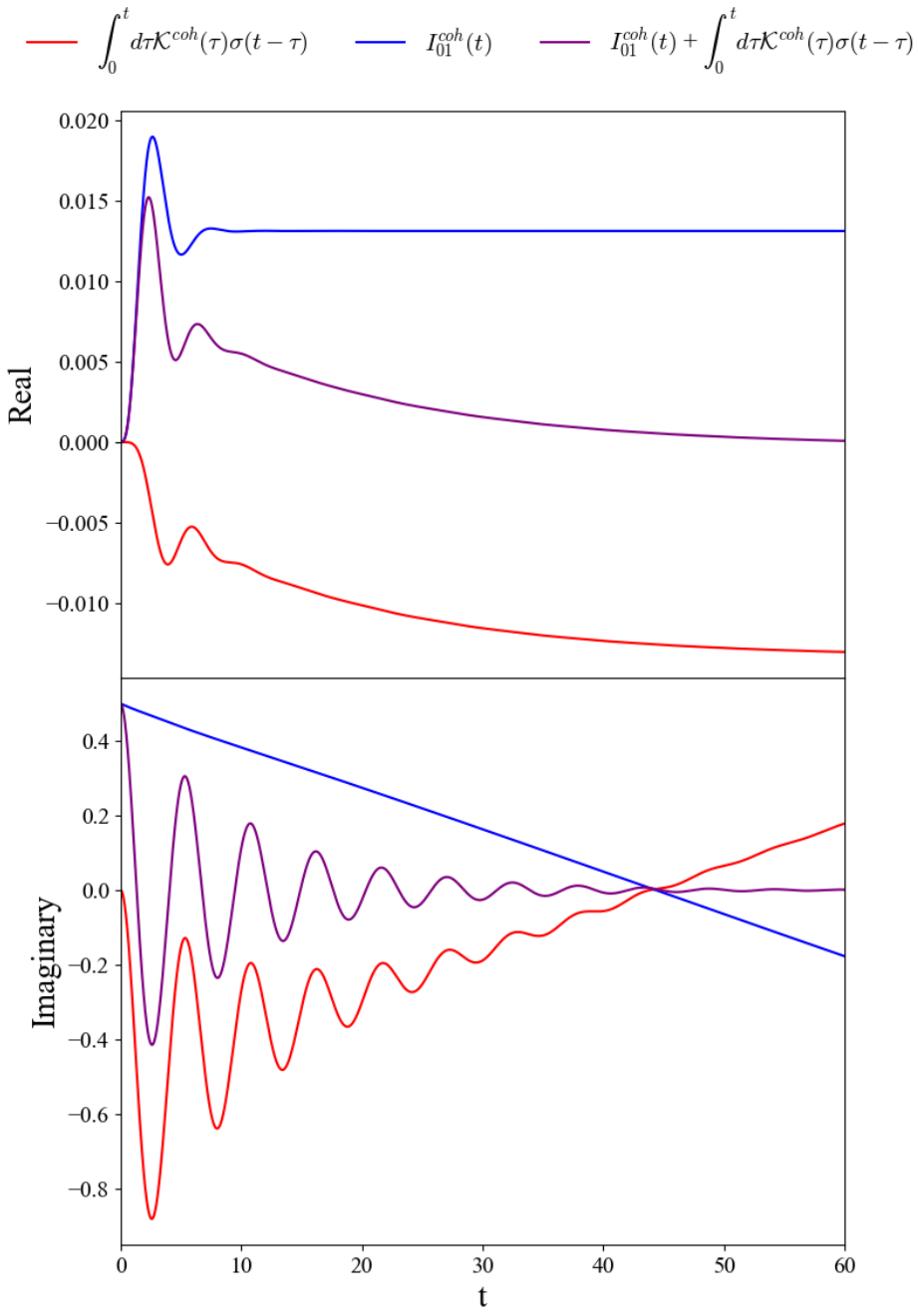


Figure B.11: Shown are the real (top) and imaginary (bottom) contributions of the convolution of the memory kernel, $\int_0^t \mathcal{K}^{coh}(\tau)\sigma(t-\tau)$ (red line), the inhomogeneous term for the coherences-only GQME, $I_{01}^{coh}(t)$ (see Eq. 4.29) (blue line), and the sum of the two contributions (purple line) for Model 5 (see Tab. 4.2).

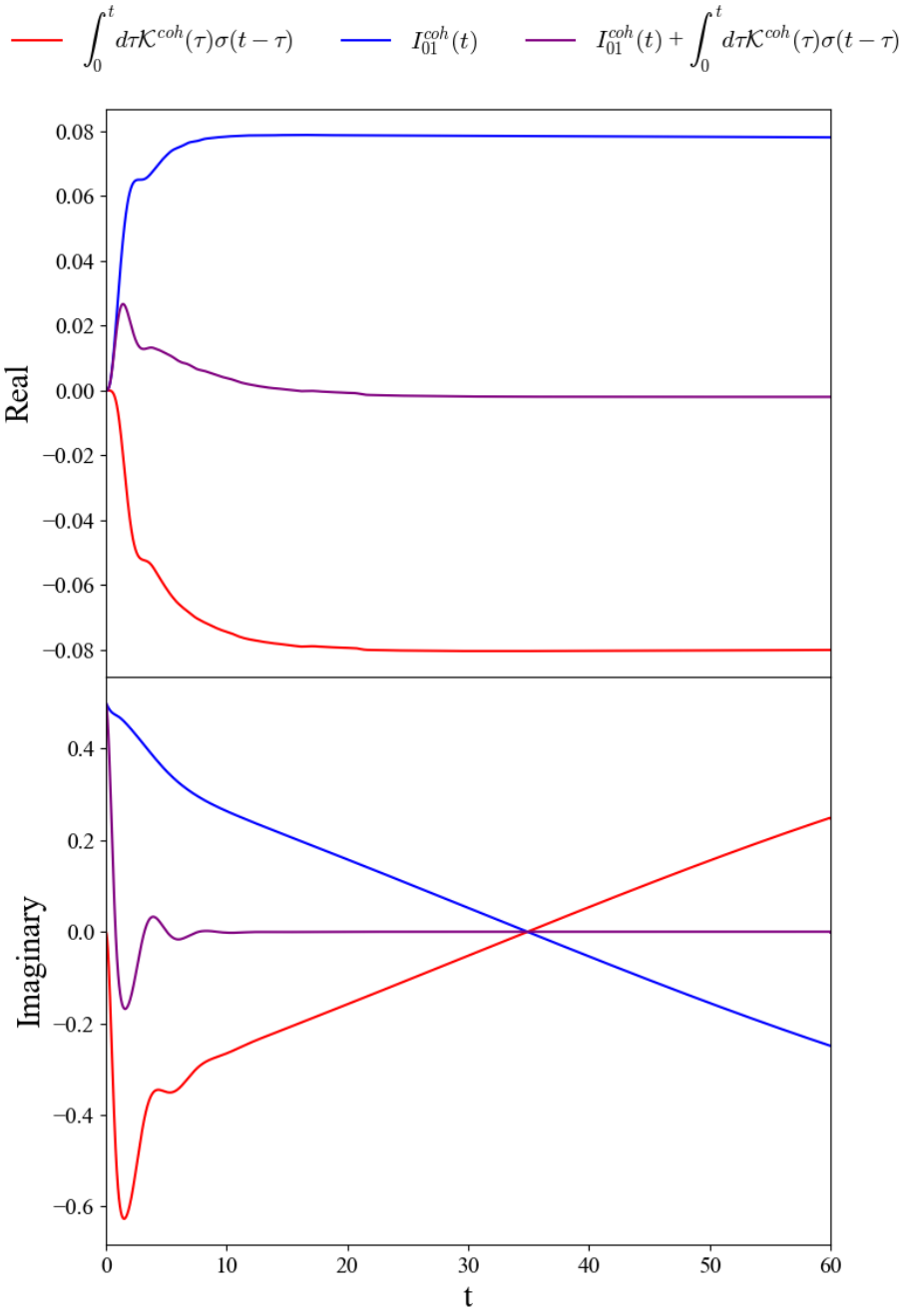


Figure B.12: Shown are the real (top) and imaginary (bottom) contributions of the convolution of the memory kernel, $\int_0^t \mathcal{K}^{coh}(\tau)\sigma(t-\tau)$ (red line), the inhomogeneous term for the coherences-only GQME, $I_{01}^{coh}(t)$ (see Eq. 4.29) (blue line), and the sum of the two contributions (purple line) for Model 6 (see Tab. 4.2).

BIBLIOGRAPHY

[1] I. I. Abram and R. Silbey. J. Chem. Phys., 63:2317, 1975.

[2] B. K. Agarwalla, J. Jiang, and D. Segal. Quantum efficiency bound for continuous heat engines coupled to noncanonical reservoirs. Phys. Rev. B, 96:104304, 2017.

[3] Y. Aiache, A. El Allati, İ. Demir, and K. El Anouz. Nonequilibrium quantum thermometry with noncommutative system-bath couplings. Phys. Rev. A, 112:062229, 2025.

[4] R. Alicki and K. Lendi. Quantum Dynamical Semigroups and Applications. Springer-Verlag, Berlin, 1987.

[5] G. Amati, M.A.C. Saller, A. Kelly, and J. O. Richardson. Quasiclassical approaches to the generalized quantum master equation. J. Chem. Phys., 157:234103, 2022.

[6] N. Anto-Szrtirkacs and D. Segal. Quantum thermal transport beyond second order with the reaction coordinate mapping. J. Chem. Phys., 156:214107, 2022.

[7] N. Anto-Sztricaks, F. Ivander, and D. Segal. Quantum thermal transport beyond second order with the reaction coordinate mapping. J. Chem. Phys., 156:214107–14, 2022.

[8] N. Anto-Sztricaks, A. Nazir, and D. Segal. Effective-hamiltonian theory of open quantum systems at strong coupling. PRX QUANTUM, 4:020307–35, 2023.

[9] C.R. Baiz, K.J. Kubarych, and E. Geva. Molecular theory and simulation of coherence transfer in metal carbonyls and its signature on multidimensional infrared spectra. J. Phys. Chem. B, 115:5322–5339, 2011.

[10] N. Boujada and D. Segal. From dissipative dynamics to studies of heat transfer at the nanoscale: analysis of the spin-boson model. J. Phys. Chem. A, 118:11323–11336, 2014.

[11] J-L Brédas, D. Beljonne, V. Coropceanu, and J. Cornil. Charge-Transfer and Energy-Transfer Processes in π-Conjugated Oligomers and Polymers: A Molecular Picture. Chem. Rev., 104:4971–5004, 2004.

[12] M. Brenes, J. Garwoła, and D. Segal. Optimal qubit-mediated quantum heat transfer via noncommuting operators and strong coupling effects. Phys. Rev. B, 111:235440, 2025.

[13] H.P. Breuer and F. Petruccione. The Theory of Open QuantumSystems. Oxford University Press, New York, 2006.

[14] Brian and X. Sun. Generalized Quantum Master Equation: A Tutorial Review and Recent Advances. CHINESE JOURNAL OF CHEMICAL PHYSICS, 5:497–524, 2022.

[15] D. Brian, Z. Liu, B.D. Dunietz, E. Geva, and X. Sun. Three-state harmonic models for photoinduced charge transfer. J. Chem. Phys., 154:174105–18, 2021.

[16] H. B. Callen. Thermodynamics. Jhon-Wiley, New York, 1979.

[17] J. Cerrillo and J. Cao. Non-Markovian Dynamical Maps: Numerical Processing of Open Quantum Trajectories. Phys. Rev. Lett., 112:110401–5, 2014.

[18] S. Chandrasekaran, M. Aghtar, S. Valleau, A. Aspuru-Guzik, and U. Kleinekathöfer. Influence of Force Fields and Quantum Chemistry Approach on Spectral Densities of BChl a in Solution and in FMO Proteins. J. Phys. Chem. B, 119:9995–10004, 2015.

[19] S. Chaturvedi and F. Shibata. Time-Convolutionless Projection Operator Formalism for Elimination of Fast Variables. Applications to Brownian Motion. Z. Physik. B, 35:297, 1979.

[20] J. Chen, J. Grawola, and D. Segal. Suppression of decoherence dynamics by a dissipative bath at strong coupling. Phys. Rev. A, 112:022209–17, 2025.

[21] S.N. Chowdhury, A. Mandal, and P. Huo. Ring polymer quantization of the photon field in polariton chemistry. J. Chem. Phys., 154:044109–11, 2021.

[22] R. D. Coalson, D. G. Evans, and A. Nitzan. A nonequilibrium golden rule formula for electronic state populations in nonadiabatically coupled systems. J. Chem. Phys., 101:436–448, 1994.

[23] G. Cohen, E. Gull, D.R. Reichman, A.J. Millis, and E. Rabani. Numerically exact long-time magnetization dynamics at the nonequilibrium Kondo crossover of the Anderson impurity model. Phys. Rev. B, 87:195108–5, 2013.

[24] G. Cohen and E. Rabani. Memory effects in nonequilibrium quantum impurity models. Phys. Rev. B, 84:075150–5, 2011.

[25] G. Cohen, E.Y. Wilner, and E. Rabani. Generalized projected dynamics for non-system observables of non-equilibrium quantum impurity models. New J. Phys. , 15:073018–21, 2013.

[26] Xiaohan Dan, Pouya Khazaei, Brandon C Allen, Ningyi Lyu, Callie Wilson, Ellen Mulvihill, Yuchen Wang, Saurabh Shivpuje, Sabre Kais, Victor S Batista, and Eitan Geva. Qflux: An open-source toolkit for quantum dynamics simulations on quantum computers. part vi - the generalized quantum master equation. ChemRxiv, 2026(0130), 2026.

[27] Xiaohan Dan, Meng Xu, J. T. Stockburger, J. Ankerhold, and Qiang Shi. Efficient low-temperature simulations for fermionic reservoirs with the hierarchical equations of motion method: Application to the Anderson impurity model. Phys. Rev. B, 107:195429, May 2023.

[28] Xiaohan Dan, Meng Xu, Yaming Yan, and Qiang Shi. Generalized master equation for charge transport in a molecular junction: Exact memory kernels and their high order expansion. J. Chem. Phys., 156(13):134114, 2022.

[29] P. de Bree and D. A. Wiersma. Application of Redfield theory to optical dephasing and line shape of electronic transitions in molecular mixed crystals. J. Chem. Phys., 70:790–801, 1979.

[30] Chenru Duan, Chang-Yu Hsieh, Junjie Liu, Jianlan Wu, and Jianshu Cao. Unusual transport properties with noncommutative system–bath coupling operators. J. Phys. Chem. Lett., 11(10):4080–4085, 2020.

[31] D. Egorova, A. Kühl, and W. Domcke. Modeling of ultrafast electron-transfer dynamics: Multi-level Redfield theory and validity of approximation. Chem. Phys., 268:105–120, 2001.

[32] S. M. Feldt, E. A. Gibson, E. Gabrielsson, L. Sun, G. Boschloo, and A. Hagfeldt. Design of organic dyes and cobalt polypyridine redox mediators for high-efficiency dye-sensitized solar cells. J. Am. Chem. Soc., 132:16714–16724, 2010.

[33] A. Garg, J. N. Onuchic, and V. Ambegaokar. Effect of friction on electron transfer in biomolecules. J. Chem. Phys., 83:4491–4503, 1985.

[34] J. Garwola and D. Segal. Open quantum systems with noncommuting coupling operators: An analytic approach. Phys. Rev. B, 110:174304, 2024.

[35] E. Geva. Chapter 4: The quantum master equation. Unpublished lecture notes, Department of Chemistry, University of Michigan.

[36] E. Geva and R. Kosloff. Three-level quantum amplifier as a heat engine: A study in finite-time thermodynamics. Phys. Rev. E, 49:3903, 1994.

[37] E. Geva and R. Kosloff. The quantum heat engine and heat pump: An irreversible thermodynamic analysis of the three-level amplifier. J. Chem. Phys., 104:7681, 1996.

[38] E. Geva, R. Kosloff, and J. L. Skinner. On the relaxation of a two-level system driven by a strong electro-magnetic field. J. Chem. Phys., 102:8541, 1995.

[39] Z. Hu, Z. Tong, M. S. Cheung, B. D. Dunietz, E. Geva, and X. Sun. Photoinduced charge transfer dynamics in the carotenoid-porphyrin-c_{60} triad via the linearized semiclassical nonequilibrium fermi's golden rule. J. Chem. Theory Comput., 124:9579–9591, 2020.

[40] A. Ishizaki and G.R. Fleming. On the adequacy of the Redfield equation and related approaches to the study of quantum dynamics in electronic energy transfer. J. Chem. Phys., 130:234110–9, 2009.

[41] A. Ishizaki and G.R. Fleming. Theoretical examination of quantum coherence in a photosynthetic system at physiological temperature. Proc. Natl. Acad. Sci. U.S.A., 106:17255–17260, 2009.

[42] A. Ishizaki and G.R. Fleming. Quantum Coherence in Photosynthetic Light Harvesting. Annu. Rev. Condens. Matter Phys., 3:333–361, 2012.

[43] Felix Ivander, Nicholas Anto-Sztrikacs, and Dvira Segal. Strong system-bath coupling reshapes characteristics of quantum thermal machines, 2021.

[44] A.F. Izmaylov, D. Mendive-Tapia, M.J. Bearpark, M.A. Robb, J.C. Tully, and M.J. Frisch. Nonequilibrium Fermi golden rule for electronic transitions through conical intersections. J. Chem. Phys., 135:234106–14, 2011.

[45] S. J. Jang. Dynamics of Molecular Excitons. Elsevier, 2020.

[46] B.J. Ka and E. Geva. Vibrational energy relaxation of polyatomic molecules in liquid solution via the linearized semiclassical method. J. Phys. Chem. A, 110:9555–9567, 2006.

[47] B.J. Ka, Q. Shi, and E. Geva. Vibrational energy relaxation rates via the linearized semiclassical approximations: Applications to neat diatomic liquids and atomic-diatomic liquid mixtures. J. Phys. Chem. A, 109:5527–5536, 2005.

[48] B.J. Ka, M-L. Zhang, and E. Geva. Homogeneity and Markovity of electronic dephasing in liquid solutions. J. Chem. Phys., 125:124509–8, 2006.

[49] A.A. Kananenka, C-Y Hsieh, J. Cao, and E. Geva. Accurate Long-Time Mixed Quantum-Classical Liouville Dynamics via the Transfer Tensor Method. J. Phys. Chem. Lett., 7:4809–4814, 2016.

[50] A. Kelly, N. Brackbill, and T.E. Markland. Accurate nonadiabatic quantum dynamics on the cheap: Making the most of mean field theory with master equations. J. Chem. Phys., 142:094110–9, 2015.

[51] A. Kelly and T.E. Markland. Efficient and accurate surface hopping for long time nonadiabatic quantum dynamics. J. Chem. Phys., 139:014104–10, 2013.

[52] A. Kelly, A. Montoya-Castillo, L. Wang, and T.E. Markland. Generalized quantum master equations in and out of equilibrium: When can one win? J. Chem. Phys., 144:184105–5, 2016.

[53] V. M. Kenkre and R. S. Knox. Generalized-master-equation theory of excitation transfer. Phys. Rev. B, 9:5279–5290, Jun 1974.

[54] L. Kidon, H. Wang, M. Thoss, and E. Rabani. On the memory kernel and the reduced system propagator. J. Chem. Phys., 149:104105–3, 2018.

[55] L. Kidon, E.Y. Wilner, and E. Rabani. Exact calculation of the time convolutionless master equation generator: Application to the nonequilibrium resonant level model. J. Chem. Phys., 143:234110–9, 2015.

[56] M. Kilgour and D. Segal. Charge transport in molecular junctions: From tunneling to hopping with the probe technique. J. Chem. Phys., 143(2):024111, 2015.

[57] M. Kilgour and D. Segal. Coherence and decoherence in quantum absorption refrigerators. Phys. Rev. E, 98:012117, 2018.

[58] A. Kimura. J. Chem. Phys., 161:124102, 2024.

[59] A. Kühl and W. Domcke. Multilevel redfield description of the dissipative dynamics at conical intersections. J. Chem. Phys., 116:263–274, 2002.

[60] Y. Lai and E. Geva. On simulating the dynamics of electronic populations and coherences via quantum master equations based on treating off-diagonal electronic coupling terms as a small perturbation. J. Chem. Phys., 155:204101–19, 2021.

[61] B. B. Laird, J. Budimir, and J. L. Skinner. J. Chem. Phys., 94:4391, 1991.

[62] M. H. Lee, B. D. Dunietz, and E. Geva. Calculation from first principles of intramolecular golden-rule rate constants for photo-induced electron transfer in molecular donor-acceptor systems. J. Phys. Chem. C, 117:23391–23401, 2013.

[63] M. H. Lee, B. D. Dunietz, and E. Geva. Calculation from first principles of golden-rule rate constants for photo-induced subphthalocyanine/fullerene interfacial charge transfer and recombination in organic photovoltaic cells. J. Phys. Chem. C, 118:9780–9789, 2014.

[64] M.H. Lee, B.D. Dunietz, and E. Geva. Donor-to-donor vs. donor-to-acceptor interfacial charge transfer states in the phthalocyanine-fullerene organic photovoltaic system. J. Phys. Chem. Lett., 5:3810–3816, 2014.

[65] L. Li and X. Cao. Coherent destruction of tunneling of quantum energy transport in a driven nonequilibrium spin-boson model. Phys. Rev. B, 110:075403, 2024.

[66] S. Li, B. Jochim, J. Stamm, D. Peng, H. Shao, J. Djiokap, and M. Dantus. Pulse shaping in strong-field ionization: Theory and experiments. Phys. Rev. A, 105:053105, 2022.

[67] P.A. Liddell, G. Kodis, A.L. Moore, T.A. Moore, and D. Gust. Photo switching of photoinduced electron transfer in a dithienylethene-porphyrin-fullerene triad molecule. J. Am. Chem. Soc., 124:7668–7669, 2002.

[68] P.A. Liddell, D. Kuciauskas, J.P. Sumida, B. Nash, D. Nguyen, A.L. Moore, T.A. Moore, and D. Gust. Photoinduced charge separation and charge recombination to a triplet state in a carotene-porphyrin-fullerene triad. J. Am. Chem. Soc., 119:1400–1405, 1997.

[69] G. Lindblad. On the generators of quantum dynamical semigroups. Commun. Math. Phys., 48:119, 1976.

[70] Y. Liu, E. Mulvihill, and E. Geva. Combining the generalized quantum master equation approach with quasiclassical mapping Hamiltonian methods to simulate the dynamics of electronic coherences. J. Chem. Phys., 161:164101, 2024.

[71] N. Lyu, E. Mulvihill, M. Soley, E. Geva, and V. Batista. Tensor-train thermo-field memory kernels for generalized master equations. J. Chem. Theory Comput., 19:1111–1129, 2023.

[72] N. Makri. The Linear Response Approximation and Its Lowest Order Corrections: An Influence Functional Approach. J. Phys. Chem. B, 103(15):2823–2829, 1999.

[73] N. Makri. Discrete Generalized Quantum Master Equations. J. Chem. Theory Comput., 21:50375048, 2025.

[74] R.A. Marcus. Electron transfer reactions in chemistry: Theory and experiment (nobel lecture). Angew. Chem. lnt. Ed. Engl., 32:1111–1121, 1993.

[75] Maria José Martínez-Pérez, Antonio Fornieri, and Francesco Giazotto. Rectification of electronic heat current by a hybrid thermal diode. Nature nanotechnology, 10(4):303–307, 2015.

[76] V. May and O. Kühn. Charge and Energy Transfer Dynamics in Molecular Systems. Willey-VCH, Berlin, 2000.

[77] A.D. McLachlan. A variational solution of the time-dependent schrodinger equation. Mol. Phys., 8:39–44, 1964.

[78] P.L. McRobbie and E. Geva. A benchmark study of different methods for calculating one- and two-dimensional optical spectra. J. Phys. Chem. A, 113:10425–10434, 2009.

[79] C. Meier and D. Tannor. Non-Markovian evolution of the density operator in presence of strong laser fields. J. Chem. Phys., 111:3365, 1999.

[80] A. Mishra, M.K.R. Fischer, and P. Bäuerle. Metal-Free Organic Dyes for Dye-Sensitized Solar Cells: From Structure: Property Relationships to Design Rules. Angew. Chem. Int. Ed., 48:2474–2499, 2009.

[81] M. Mohseni, A. Shabani, S. Lloyd, and H. Rabitz. Energy-scales convergence for optimal and robust quantum transport in photosynthetic complexes. J. Chem. Phys., 140(3):035102, 2014.

[82] A. Montoya-Castillo and D.R. Reichman. Approximate but accurate quantum dynamics from the Mori formalism: I. Nonequilibrium dynamics. J. Chem. Phys., 144:184104–16, 2016.

[83] S. Mukamel. Principles of Nonlinear Optical Spectroscopy. Oxford University Press, Oxford, 1995.

[84] E. Mulvihill, X. Gao, Y. Liu, A. Schubert, B.D. Dunietz, and E. Geva. Combining the mapping Hamiltonian linearized semiclassical approach with the generalized quantum master equation to simulate electronically nonadiabatic molecular dynamics. J. Chem. Phys., 151:074103–16, 2019.

[85] E. Mulvihill and E. Geva. A Road Map to Various Pathways for Calculating the Memory Kernel of the Generalized Quantum Master Equation. J. Phys. Chem. B, 125:9834–9852, 2021.

[86] E. Mulvihill and E. Geva. Simulating the dynamics of electronic observables via reduced-dimensionality generalized quantum master equations. J. Chem. Phys., 156:044119–13, 2022.

[87] E. Mulvihill, K.M. Lenn, X. Gao, A. Schubert, B.D. Dunietz, and E. Geva. Simulating energy transfer dynamics in the Fenna-Matthews-Olson complex via the modified generalized quantum master equation. J. Chem. Phys., 154:204109–13, 2021.

[88] E. Mulvihill, A. Schubert, X. Sun, B.D. Dunietz, and E. Geva. A modified approach for simulating electronically nonadiabatic dynamics via the generalized quantum master equation. J. Chem. Phys., 150:034101–20, 2019.

[89] M. Naher, D.C. Milan, O.A. Al-Owaedi, I.J. Plunje, S. Bock, J. Hurtado-Gallego, P. Bastante, Z. Murtada, A. Dawood, L. Rincon-Garcia, G. Rubio-Bollinger, S.J. Higgins, N. Agrait, C.J. Lambert, R.J. Nichols, and P.J. Low. Molecular structure(thermo)electric property relationships in single-molecule junctions and comparisons with single- and multiple-parameter models. J. Am. Chem. Soc., 143:3817, 2021.

[90] S. Nakajima. On the quantum theory of transport phenomena. Prog. Theor. Phys., 20:948–959, 1958.

[91] A. Nitzan. Chemical Dynamics in Condensed Phases. Oxford University Press, New York, 2006.

[92] V.I. Novoderezhkin, A.G. Yakovlev, R. van Grondelle, and V.A. Shuvalov. Coherent Nuclear and Electronic Dynamics in Primary Charge Separation in Photosynthetic Reaction Centers: A Redfield Theory Approach. J. Phys. Chem. B, 108:7445–7457, 2004.

[93] Catrina P Oberg, Leah C Spangler, David F Coker, and Gregory D Scholes. Chirped laser pulse control of vibronic wavepackets and energy transfer in phycocyanin 645. The Journal of Physical Chemistry Letters, 15:7125–7132, 2024.

[94] S. Pan, C. Hu, and W. Zhang et. al. Rabi oscillations in a stretching molecule. Light Sci. Appl., 12:235440, 2023.

[95] R Peng, L. P. Lindoy, and J. Lee. On the discretization error of the discrete generalized quantum master equation. J. Chem. Phys., 163:134101, 2025.

[96] A. Pereverzev and E. R. Bittner. Time-convolutionless master equation for mesoscopic electron-phonon systems. J. Chem. Phys., 125:104906–7, 2006.

[97] W. C. Pfalzgraff, A. Kelly, and T. E. Markland. Nonadiabatic Dynamics in Atomistic Environments: Harnessing Quantum-Classical Theory with Generalized Quantum Master Equations. J. Phys. Chem. Lett., 6:4743–4748, 2015.

[98] W.C. Pfalzgraff, A. Montoya-Castillo, A. Kelly, and T.E. Markland. Efficient construction of generalized master equation memory kernels for multi-state systems from nonadiabatic quantum-classical dynamics. J. Chem. Phys., 150:244109–16, 2019.

[99] W. T. Pollard, A. K. Felts, and R. A. Friesner. The Redfield equation in condensed-phase quantum dynamics. Adv. Chem. Phys., XCIII:77, 1996.

[100] W.T. Pollard and R.A. Friesner. Solution of the Redfield equation for the dissipative quantum dynamics of multilevel systems. J. Chem. Phys., 100:5054–5065, 1994.

[101] A. Prositto, C. Ramon-Escandell, and D. Segal. Collisional model with dissipative and dephasing baths: nonadditive effects at strong coupling. New J. Phys., 28:014502, 2026.

[102] A. G. Redfield. On the theory of relaxation processes. IBM Jr., 1:19, 1957.

[103] A.C. Rizzi, M. van Gastel, P.A. Liddell, R.E. Palacios, G.F. Moore, G. Kodis, A.L. Moore, T.A. Moore, D. Gust, and S.E. Braslavsky. Entropic changes control the charge separation process in triads mimicking photosynthetic charge separation. J. Phys. Chem. A, 112:4215–4223, 2008.

[104] Keiji Saito and Takeo Kato. Kondo signature in heat transfer via a local two-state system. Phys. Rev. Lett., 111:214301, 2013.

[105] M.A.C. Saller, A. Kelly, and E. Geva. Benchmarking Quasiclassical Mapping Hamiltonian Methods for Simulating Cavity-Modified Molecular Dynamics. J. Phys. Chem. Lett., 12:3163–3170, 2021.

[106] M.A.C. Saller, Y. Lai, and E. Geva. Cavity-modified fermi's golden rule rate constants from cavity-free inputs. J. Phys. Chem. C, 127:3154–3164, 2023.

[107] D. Segal and B. K. Agarwalla. Vibrational heat transport in molecular junctions. Annu. Rev. Phys. Chem., 67:185–209, 2016.

[108] D. Segal, A. Nitzan, and P. Hänggi. Thermal conductance through molecular wires. J. Chem. Phys., 119(13):6840–6855, 2003.

[109] Dvira Segal. Heat transfer in the spin-boson model: A comparative study in the incoherent tunneling regime. Phys. Rev. E, 90:012148, 2014.

[110] Dvira Segal and Abraham Nitzan. Heat rectification in molecular junctions. J. Chem. Phys., 122:194704, 2005.

[111] Dvira Segal and Abraham Nitzan. Spin-boson thermal rectifier. Phys. Rev. Lett., 94:034301, 2005.

[112] Q. Shi, L-P. Chen, G-J. Nan, R-X. Xu, and Y-J. Yan. Electron transfer dynamics: Zusman equation versus exact theory. J. Chem. Phys., 130:164518, 2009.

[113] Q. Shi and E. Geva. A new approach to calculating the memory kernel of the generalized quantum master equation for an arbitrary system-bath coupling. J. Chem. Phys., 119:12063–12076, 2003.

[114] Q. Shi and E. Geva. A semiclassical theory of vibrational energy relaxation in the condensed phase. J. Phys. Chem. A, 107:9059–9069, 2003.

[115] Q. Shi and E. Geva. Vibrational energy relaxation in liquid oxygen from a semiclassical molecular dynamics simulation. J. Phys. Chem. A, 107:9070–9078, 2003.

[116] Q. Shi and E. Geva. A derivation of the mixed quantum-classical Liouville equation from the influence functional formalism. J. Chem. Phys., 121:3393–3404, 2004.

[117] Q. Shi and E. Geva. Nonradiative electronic relaxation rate constants from approximations based on linearizing the path-integral forward-backward action. J. Phys. Chem. A, 108:6109–6116, 2004.

[118] Q. Shi and E. Geva. A semiclassical generalized quantum master equation for an arbitrary system-bath coupling. J. Chem. Phys., 120:10647–10658, 2004.

[119] Q. Shi and E. Geva. A comparison between different semiclassical approximations for optical response functions in nonpolar liquid solutions. J. Chem. Phys., 122:064506–10, 2005.

[120] Q. Shi and E. Geva. A comparison between different semiclassical approximations for optical response functions in nonpolar liquid solution II. the signature of excited state dynamics on two-dimensional spectra. J. Chem. Phys., 129:124505, 2008.

[121] F. Shibata and T. Arimitsu. Expansion formulas in nonequilibrium statistical mechanics. J. Phys. Soc. Japan., 49:891–897, 1980.

[122] F. Shibata, Y. Takahashi, and N. Hashitsume. A Generalized Stochastic Liouville Equation. Non-Markovian Versus Memoryless Master Equations. J. Stat. Phys., 17:171–187, 1977.

[123] L. Song and Q. Shi. Hierarchical equations of motion method applied to nonequilibrium heat transport in model molecular junctions: Transient heat current and high-order moments of the current operator. Phys. Rev. B, 95:064308, 2017.

[124] Y. Song, A. Schubert, X. Liu, S. Bhandari, S.R. Forrest, B.D. Dunietz, E. Geva, and J.P. Ogilvie. Efficient Charge Generation via Hole Transfer in Dilute Organic Donor-Fullerene Blends. J. Phys. Chem. Lett., 11:2203–2210, 2020.

[125] Y. Song, A. Schubert, E. Maret, R.K. Burdick, B.D. Dunietz, E. Geva, and J.P. Ogilvie. Vibronic structure of photosynthetic pigments probed by polarized two-dimensional electronic spectroscopy and ab initio calculations. Chem. Sci., 10:8143–8153, 2019.

[126] M. Sparpaglione and S. Mukamel. Dielectric friction and the transition from adiabatic to nonadiabatic electron transfer. I. Solvation dynamics in Liouville space. J. Chem. Phys., 88:3263, 1988.

[127] X. Sun and E. Geva. Equilibrium Fermi's Golden Rule Charge Transfer Rate Constants in the Condensed Phase: The Linearized Semiclassical Method vs Classical Marcus Theory. J. Phys. Chem. A, 120:2976–2990, 2016.

[128] X. Sun and E. Geva. Exact vs. Asymptotic Spectral Densities in the Garg-Onuchic-Ambegaokar Charge Transfer Model and its Effect on Fermi's Golden Rule Rate Constants. J. Chem. Phys., 144:044106–4, 2016.

[129] X. Sun and E. Geva. Non-Condon Equilibrium Fermi's Golden Rule Electronic Transition Rate Constants Via The Linearized Semiclassical Method. J. Chem. Phys., 144:244105–12, 2016.

[130] X. Sun and E. Geva. Non-Condon nonequilibrium Fermi's golden rule rates from the linearized semiclassical method. J. Chem. Phys., 145:064109–19, 2016.

[131] X. Sun and E. Geva. Nonequilibrium Fermi's Golden Rule Charge Transfer Rates via the Linearized Semiclassical Method. J. Chem. Theory Comput., 12:2926 – 2941, 2016.

[132] X. Sun, P. Zhang, Y. Lai, K.L. Williams, M.S. Cheung, B.D. Dunietz, and E. Geva. Computational Study of Charge-Transfer Dynamics in the Carotenoid-Porphyrin-C_{60} Molecular Triad Solvated in Explicit Tetrahydrofuran and Its Spectroscopic Signature. J. Phys. Chem. C, 122:11288–11299, 2018.

[133] Y. Tanimura. Numerically "exact" approach to open quantum dynamics: The hierarchical equations of motion (HEOM). J. Chem. Phys., 153:020901–23, 2020.

[134] Y. Tanimura and R. Kubo. Time Evolution of a Quantum System in Contact with Nearly Gaussian-Markoffian Noise Bath. J. Phys. Soc. Jpn., 58:101–114, 1989.

[135] Yoshitaka Tanimura. Stochastic Liouville, Langevin, Fokker–Planck, and Master Equation Approaches to Quantum Dissipative Systems. J. Phys. Soc. Jpn., 75(8):082001–39, August 2006.

[136] H. Tian, Z. Yu, A. Hagfeldt, L. Kloo, and L. Sun. Organic Redox Couples and Organic Counter Electrode for Efficient Organic Dye-Sensitized Solar Cells. J. Am. Chem. Soc., 133:9413–9422, 2011.

[137] Z. Tong, X. Gao, M.S. Cheung, B.D. Dunietz, E. Geva, and X. Sun. Charge transfer rate constants for the carotenoid-porphyrin-C_{60} molecular triad dissolved in tetrahydrofuran: The spin-boson model vs the linearized semiclassical approximation. J. Chem. Phys., 153:044105–10, 2020.

[138] A. Trushechkin. Calculation of coherences in Förster and modified Redfield theories of excitation energy transfer. J. Chem. Phys., 151:074101–19, 2019.

[139] F. X Vazquez, I. Navrotskaya, and E. Geva. Vibrational energy relaxation rate constants via the linearized semiclassical method without force derivatives. J. Phys. Chem. A, 114:5682–5688, 2010.

[140] F. X Vazquez, S. Talapatra, and E. Geva. Vibrational energy relaxation in liquid HCl and DCl via the linearized semiclassical method: Electrostriction versus quantum delocalization. J. Phys. Chem. A, 115:9775–9781, 2011.

[141] Y. Wang, E. Mulvihill, Z. Hu, N. Lyu, S. Shivpuje, Y. Liu, M. B. Soley, E. Geva, V. S. Batista, and S. Kais. Simulating Open Quantum System Dynamics on NISQ Computers with Generalized Quantum Master Equations. J. Chem. Theory Comput., 19:48514862, 2023.

[142] E.Y. Wilner, H. Wang, G. Cohen, M. Thoss, and E. Rabani. Bistability in a nonequilibrium quantum system with electron-phonon interactions. Phys. Rev. B, 88:045137, 2013.

[143] C. Wilson, Z. Huang, and E. Geva. Quantum master equations for systems off-diagonally driven by a time-dependent external field. J. Chem. Phys., 163(9):094101, 2025.

[144] D. Xu and K. Schulten. Coupling of protein motion to electron transfer in a photosynthetic reaction center: Investigating the low temperature behavior in the framework of the spin–boson model. Chem. Phys., 182:91–117, 1994.

[145] M. Yang and G.R. Fleming. Influence of phonons on exciton transfer dynamics: comparison of the Redfield, Förster, and modified Redfield equations. Chem. Phys., 282:163–180, 2002.

[146] M-L. Zhang, B. J. Ka, and E. Geva. Nonequilibrium quantum dynamics in the condensed phase via the generalized quantum master equation. J. Chem. Phys., 125:044106–12, 2006.

[147] W. M. Zhang, T. Meier, V. Chernyak, and S. Mukamel. Exciton-migration and three-pulse femtosecond optical spectroscopies of photosynthetic antenna complexes. J. Chem. Phys., 108:7763–7774, 1998.

[148] Y. Zhao and W. Liang. Charge transfer in organic molecules for solar cells: Theoretical perspective. Chem. Soc. Rev., 41:1075–1087, 2012.

[149] R. Zwanzig. Lectures in Theoretical Physics (Boulder), 3:106, 1960.

[150] R. Zwanzig. Ensemble method in the theory of irreversibility. J. Chem. Phys., 33:1338–1341, 1960.

[151] R. Zwanzig. Nonequilibrium Statistical Mechanics. Oxford University Press, New York, 2001.